Christian Oberdorfer

Numeric Simulation of Atom Probe Tomography

2014

Materialphysik

Numeric Simulation of Atom Probe Tomography

Inaugural-Dissertation
zur Erlangung des Doktorgrades
der Naturwissenschaften im Fachbereich Physik
der Mathematisch-Naturwissenschaftlichen Fakultät
der Westfälischen Wilhelms-Universität Münster

vorgelegt von
Christian Oberdorfer
aus Münster

– 2014 –

URN: urn:nbn:de:hbz:6-72369452076
URL: http://nbn-resolving.de/urn:nbn:de:hbz:6-72369452076

Dekan | *Dean*:	Prof. Dr. M. Donath
Erster Gutachter | *First Referee*:	Prof. Dr. Dr. h.c. G. Schmitz
Zweiter Gutachter | *Second Referee*:	Prof. Dr. G. Wilde
Tag der mündlichen Prüfung | *Day of Defense*:	14.07.2014
Tag der Promotion | *Day of Graduation*:	14.07.2014

Zusammenfassung

Die Arbeit beschreibt einen neuen Ansatz zur Simulation von Messdaten, wie sie bei der Durchführung von Experimenten mit der Atomsondentomographie erzeugt werden. Derartige Simulationen stellen einen komplementären Ansatz dar, mit dessen Hilfe die Interpretation der Messergebnisse verbessert werden soll.

Als Grundlage dient ein flexibles Rechengitter, auf dem die Poisson-Gleichung gelöst wird. Die atomare Struktur der zu untersuchenden Probe wird hierbei maßstabsgerecht durch Wigner-Seitz-Zellen beschrieben. Im Anschluss wird die Probe schrittweise, Atom für Atom, durch simulierte Feldverdampfung abgetragen. Aus der Berechnung der Trajektorien feldemittierter Ionen ergeben sich zweidimensionale Detektorkoordinaten, vergleichbar zu den Messdaten, die beim Experiment aufgezeichnet werden.

Eine Analyse der simulierten Trajektorien zeigt qualitativ vergleichbare Abbildungseigenschaften, wie sie auch mit anderen Simulationsverfahren und in Experimenten ermittelt wurden. Die Flexibilität in der Beschreibung der Probenstruktur beim hier verwendeten Ansatz zeigt sich darin, dass Felddesorptionsbilder für beliebige Gitterstrukturen und -orientierungen berechnet werden können (z. B. kubisch, hexagonal). Für eine bestimmte Probe stellt sich im Detail heraus, dass die Detektorposition feldverdampfter Atome nicht eindeutig festgelegt ist, sondern von der genauen Reihenfolge der Verdampfung abhängt. Unterschiede im Emissionswinkel identischer Atome von ca. 1,1° sind möglich. Ergebnisse für Simulationen bei erhöhter Probentemperatur lassen eine Verringerung der Tiefenauflösung in der dreidimensionalen Probenrekonstruktion erwarten, die im Bereich typischer Gitterabstände liegen kann. Ein Vergleich der ursprünglichen Probengestalt mit dem Ergebnis nach der Simulation und der Rekonstruktion offenbart eine falsche Tiefenskalierung, falls der weit verbreitete Rekonstruktionsalgorithmus von Bas et al. benutzt wird. Eine Korrektur ergibt sich, wenn das Volumen einer dünnen Schale an der Spitzenoberfläche in Abhängigkeit vom Emissionswinkel berücksichtigt wird. Die mittels Fouriertransformation bestimmte Auflösung in der berechneten Rekonstruktion beträgt ca. 0,8 Å in der Tiefe und ca. 1,5 Å in lateraler Richtung.

Anhand von Beispielrechnungen werden die erweiterten Fähigkeiten des Simulationsverfahrens verdeutlicht. Feldinduzierte Kräfte, die auf ein in die Probenmatrix eingebettetes Partikel einwirken, werden abgeschätzt. Die Zugspannung auf das Partikel ändert sich quadratisch zum relativen Unterschied im Verdampfungsfeld. Die neue Möglichkeit, Proben mit komplexen Gitterstrukturen zu untersuchen, wird am Beispiel eines Schichtsystems von abwechselnd kristallinen und amorphen Bereichen illustriert. In den 3D Rekonstruktionen von Proben mit einer Σ5-Korngrenze, ist eine deutliche Verringerung der Atomdichte in der Korngrenzebene zu finden. Im Fal-

le von Korngrenzsegregation sind inhomogene Verdampfungsfelder für zusätzliche Artefakte verantwortlich. Ermittelte Konzentrationsprofile zeigen sich daher stark verfälscht.

Abstract

This thesis deals with a new approach for the simulation of measurement data as they are usually obtained in atom probe experiments. Simulations represent a complementary method which enables an improved interpretation of such measurement results. As a general basis, a flexible computational mesh is used on which the Poisson equation is solved. The detailed atomic structure of the sample to be analysed is described true to scale by differently shaped Wigner-Seitz cells. By the simulated field evaporation, the sample shrinks atom by atom. From the calculated trajectories of field emitted ions, two-dimensional detector coordinates comparable to the recorded measurement data in the experiments are obtained.

An analysis of the trajectories reveals qualitatively the same imaging properties as they have been determined before based on other simulation approaches or in experiments. The offered flexibility in the description of arbitrary sample structures by this approach is demonstrated on the basis of calculated field desorption maps for different lattice types and orientations, e.g. for cubic and hexagonal lattices. In particular, it is shown that the determined detector positions are not unique. They depend on the respective evaporation sequence. A shift in the launch angle of about 1.1° for identical atoms is possible. In addition, simulations at elevated sample temperatures indicate a degrading depth resolution of the 3D reconstruction in the range of typical lattice distances.

A comparison of the original sample with the result subsequent to the calculated 3D reconstruction clearly reveals a wrong depth scaling if the reconstruction is computed following the common protocol of Bas et al. A correction is possible if the volume of a thin shell at the sample surface as a function of the emission angle is considered. Based on an in this way corrected reconstruction, the resolution is determined by Fourier transformation. The depth resolution amounts to 0.8 Å and in lateral direction it is 1.5 Å.

The enhanced abilities of the simulation approach are illustrated by exemplary calculations. An estimation of the field-induced force, which acts on an embedded particle in a sample matrix is presented. The tensile stress changes with the square of the relative difference in the critical evaporation threshold. The new possibility to take account for complex lattice structures is demonstrated by the example of a layer system with alternating crystalline and amorphous stacking. The 3D reconstruction of samples, which contain a $\Sigma 5$ grain boundary (GB), shows depletion of the atom density in the GB plane. In the case of segregation, an inhomogeneous evaporation threshold of the GB is responsible for additional artifacts. Determined concentration profiles appear strongly distorted.

Contents

1. Introduction **1**

2. Background: Atom Probe Microscopy **7**
2.1. Field emission . . . 8
2.1.1. Historic context: field electron emission . . . 8
2.1.2. Field ion emission . . . 10
2.1.3. Field desorption and field evaporation . . . 11
2.2. Basic principles of atom probe tomography . . . 14
2.2.1. Sample geometry and image formation . . . 17
2.2.2. Field desorption experiments . . . 20
2.2.3. Outline of the APT measurement process . . . 22
2.2.4. Constitution of the 3D reconstruction . . . 25
2.2.5. Enhanced reconstruction approach dedicated to wide angle instruments . . . 28
2.3. Present challenges . . . 30

3. Numeric and algorithmic prerequisites **33**
3.1. Foundations of mesh generation . . . 34
3.1.1. Geometric convexity . . . 35
3.1.2. Properties of simplices . . . 36
3.1.3. Delaunay tessellation . . . 41
3.1.4. Voronoi tessellation . . . 50
3.2. Discrete solution of the Poisson equation in electrostatics . . . 56
3.2.1. Basic electrostatics . . . 57
3.2.2. Regular mesh . . . 59
3.2.3. Irregular mesh . . . 62
3.3. Ion trajectories and the electric field . . . 64

4. Implemented simulation approaches **69**
4.1. Basic model according to Vurpillot's approach . . . 72
4.1.1. Increasing numeric resolution . . . 74
4.1.2. Distinguished evaporation thresholds . . . 75
4.1.3. Statistic evaporation . . . 77
4.1.4. Extension to include dielectricity . . . 78
4.1.5. Discussion . . . 80
4.2. New generalized approach . . . 82
4.2.1. Foundation by an irregular mesh . . . 83

4.2.2. Assisted mesh generation 85
4.2.3. Properties of the electrostatic solution 86
4.2.4. Consideration of the polarization force for evaporation 90

5. Imaging characteristics of detector events 93
5.1. Field properties and trajectories 94
5.1.1. Field factor 96
5.1.2. Image compression 98
5.1.3. Interdependence of surface field and image compression . . . 99
5.2. Detector event maps 100
5.2.1. Surface imaging mode 100
5.2.2. Desorption mode 103
5.2.3. Atom displacements in the desorption mode 108
5.3. Statistic desorption under the influence of temperature 111

6. Quality of the 3D reconstruction 121
6.1. Geometric consistency 122
6.2. Spatial resolution determined by 3D Fourier analysis 124

7. Evaluation of model emitter structures 131
7.1. Exerted stress on an embedded particle 132
7.2. Simulated evaporation of a complex multi-layer structure 136
7.2.1. Curvature changes at the apex 137
7.2.2. Consistent control of the evaporation sequence 141
7.2.3. Additional information required for direct comparison with experimental data 141
7.3. Investigation of a grain boundary in copper 143
7.3.1. Different inclination angles 145
7.3.2. Segregation effects 150

8. Conclusion 153

A. Derivation of the discrete Poisson equation on the regular mesh 159

B. Computing the electric field on the irregular mesh (2nd order) 161

Bibliography 165

1. Introduction

Atom probe tomography (APT) is a high resolution measurement technique with application in materials science and engineering. The three-dimensional (3D) chemical composition at the apex of small needle shaped tips is accessed by the controlled field evaporation of atoms. Typical measurements include tenth of millions of atoms corresponding to nano-metric volumes of about $50\,\mathrm{nm} \times 50\,\mathrm{nm} \times 250\,\mathrm{nm}$.

In recent years, APT has seen a remarkable progress. Not so long ago, only a handful of research institutes in the world were equipped with atom probe instruments. The deployed devices were mainly self-constructed and needed to be operated by trained specialists. But nowadays, this situation is changing. Comparable to transmission electron microscopy (TEM), APT has evolved into a standard method in materials research. In particular, it plays a leading role for analyses which require for 3D imaging, high spatial resolution, and highest chemical sensitivity. The rise of APT began early in the last decade with decisive innovations [KM07; Aud+09]:

- The analysis of a broadened range of materials classes (e.g. insulators and composites) was enabled by a new type of instruments utilizing laser-assisted field evaporation.
- The probed volume was increased by a factor of four, while the overall measurement time was shortened by at least twenty times.
- Sample preparation and measurements of selective features (e.g. grain boundaries, triple lines) were facilitated.

Besides, the application of APT by researchers who are not dedicated experts was eased. On this background, a large-scale commercial distribution of instruments all over the world has started.[1] Indeed, the commercial success may be seen as best evidence for the new status of APT. On the other side, this success was made possible not at least because of the clear demand for its unique analytic capabilities. The access to the 3D stoichiometry at the nano-scale is getting in general increasingly important for modern technologies [Gle89; Gle00]. Therefore, a further increasing demand for appropriate analysis methods in the future can be expected. For instance, the ongoing trend for miniaturization in the semiconductor industry as described by Moore's law [Moo65] requires higher resolving characterization techniques beyond the limits of secondary ion mass spectrometry (SIMS) which is

[1] At the time of writing, at least 61 instruments have been sold since 2006 on a commercial basis (*www.atomprobe.com*). Important customers are public research facilities but also the industry.

the current standard method. Here, APT can fill the needs [Lar+11b; Lar+11a; Pro+13].

In contrast to this success story, the achieved instrumental progress cannot hide the fact that APT measurement results still suffer from intrinsic inaccuracies. Artifacts are likely encountered in the 3D reconstructions if materials with different evaporation properties are investigated [Mil87; MH91; MV08]. Current state of the art reconstruction protocols do not take into account such material dependent effects [Gau+11; Lar+13; Vur+13]. Thus, the next step for improving APT must consist in the development of a reliable model of the field evaporation process. First, this should allow to reveal present artifacts by the comparison of measured data with those derived from the model. The procedure resembles the similar practice in high resolution TEM. Second, such a model may be further utilized to directly guide the 3D reconstruction process of actual measurement data. In both directions, the numeric simulation of atom probe experiments provides invaluable information.

In this work, two dedicated approaches for APT simulation are addressed. Both are founded on the numeric solution of the Poisson equation. In this way, surface fields at a modelled 3D emitter structure are enabled and trajectories of field emitted ions are derived. The approaches are dynamic: protruding atoms, exposed to stronger fields at the emitter apex, are removed preferentially one after the other. Therefore, the computed electrostatic solution must be repeatedly updated so that the simulation reflects field conditions comparable to the experiments.

The development of the first simulation approach has originally been motivated from atom probe analyses of insulating oxide films (WO_3, NiO, Al_20_3, ...) by means of laser assisted evaporation [Obe+07]. For this application, an extended possibility to account for dielectric effects at the emitter has been added [OS11]. But apart from this, the approach mostly follows the established standard procedure for APT simulation introduced by Vurpillot et al. [Vur+99; VBB00; Vur+00] about twelve years ago.

In the course of the first work on APT simulation, deliberations for a different second simulation approach have been initiated [OES13]. Related results are mainly addressed in this thesis. This so called "generalized approach" features major improvements:

- in the possible treatment of the physics of field evaporation and
- in the way the atomic structure of the field emitter sample is represented.

The new approach is deeply founded on the 3D Voronoi tessellation. This way, existing geometric constraints by the simulation mesh are removed. For example,

the new approach can operate at largely different scales in space. The microscopic field at the atoms of a simulated emitter tip as well as the field at the mesoscopic scale is considered. Such a coherent treatment has not been possible before.

Having a nice idea is one thing, filling it with live is another: the programming part of this work took by far most of the time. The involved numerics with 3D geometry may be fairly tricky and complex. All together about 50.000 lines of source code in C++ have been written — not just for operating the simulation but also for additional presentation and analysis tools. Only a little part of this programming work is directly apparent from the descriptions in the thesis. In this regard, any presented results are only the cherry on the cake.

However, a practical outcome in addition to the thesis is the *TAPSim*[2] software package which is dedicated to APT simulation. It is freely offered to all "atom probers" in the IFES[3] community.

[2]Download opportunity and description: *www.uni-muenster.de/physik.mp/schmitz/tapsim*
[3]International field emission society (*www.fieldemission.org*)

Outline

The next chapter provides an introduction to APT. Besides the description of the theoretical basis of the field emission effects, broad emphasis is put on the application of APT as an experimental measurement method. With this focus, details of the ion projection and the geometric reconstruction process will be described. Assorted experimental results may ease the understanding of the presented background information. Readers who are familiar with the technique may skip this part.

The numeric foundations of the simulations are elaborated in chapter 3. Notable concepts like the partitioning of space, the constitution by a point mesh, and associated topological properties are described in detail. In the application to physics, the approaches for the discrete solution of the Poisson equation and for extracting the field in the simulations are derived. The standard simulation approach by Vurpillot et al. operates on a regular mesh, whereas for the new "generalized approach" an irregular mesh applies. Descriptions are treated separately for each type of mesh. The general application of both simulation approaches to APT is described in chapter 4. The next chapters exclusively demonstrate features of the newly introduced approach:

- The imaging properties of the evaporation process are characterized (chapter 5). Desorption patterns mainly of the cubic lattices are investigated. The effect of disturbed evaporation sequences under the influence of temperature is shown.

- The output of the simulations can be directly fed into existing algorithms for APT reconstruction. Test results for the consistency and the spatial resolution of computed reconstructions are presented in chapter 6.

- The new ability to account for the detailed atomic structure of simulated emitter samples is demonstrated in chapter 7. Here, inter alia, results for the simulated evaporation of an amorphous phase and for the case of samples with a grain boundary are presented.

Finally, the main results of the thesis are concluded.

2. Background: Atom Probe Microscopy

This chapter aims to give essential background information on atom probe tomography (APT). The text is constrained to the relevant topics as far as they are suited to improve the understanding of the present work. For a general introduction to APT, the reader is referred to the increasing collection of textbooks [MS89; Tso90; Mil00; Gau+12a].

First, the physics behind APT is described, thereafter the basics of the method from the view of the experimenter. Recently, improved capabilities of the technique, mainly focused on instrumentation, have been achieved. As a consequence, aspects, which are ought to be already known, appear in different light. But also solutions for newly raised problems are required. These issues are addressed at the end of this chapter.

2.1. Field emission

In a historic view, the evolution of APT cannot be thought without the scientific genius of Erwin Müller (* 1911 - † 1977) [Mel13] and his original work on field emission. Starting in the 1930s dealing with field induced electron emission, he continued later in the 1950s focussing on field ion emission. Müller initiated a completely new field in physics which is in modern language termed *high-field nanoscience*. It deals with investigations on the solid state in the presence of extraordinary high electric fields ($\sim 10\,\mathrm{GV\,m^{-1}}$). Müller's particular merit lies not so much in the role as a discoverer of new physical effects or in that of a theorist finding a solution for a tricky problem but rather in pushing forward the application of the emission phenomena which led to a new type of microscope and finally to the atom probe.

2.1.1. Historic context: field electron emission

Nowadays, the era of electric light bulbs is drawing to an end. The long period of more than hundred years in which they have been in use is remarkable. In contrast to the application as a light source, a light bulb represents perhaps the easiest example of an electron emitter besides conventional cathode rays[1]. We consider the electrons inside a metal as a gas enclosed in a potential well formed by the positively charged atom cores. The height of the well is given by the work function Φ. The kinetic energy of the electrons follows a statistic distribution. Thus, it happens that at equilibrium at a given temperature T some of the electrons gain enough energy to overcome the barrier and leave the bulk. The flux for this so

[1] Philipp Lenard (* 1862 - † 1947), Nobel prize 1905

called thermionic emission is described by Richardson's law[2] [Ric24]

$$\Psi \sim T^2 \cdot \exp\left(-\frac{\Phi_0}{k_B T}\right) \tag{2.1}$$

with k_B denoting the Boltzmann constant. On the other hand, electron emission may be seen as the thermal activated jump over the potential barrier with an activation energy equal to Φ_0. This is indicated by the exponential Boltzmann relation.

Electrons are charged particles. Therefore, it is natural to expect an effect on the observed emission if a positive electric field additionally applies. This approach has been followed by Walter Schottky (* 1886 - † 1976)[3]. He discovered that by the presence of the field E at the metal vacuum interface, the activation energy for the electron emission becomes decreased. In this way, the field accelerates the emission. The effect is attributed to the interaction of the escaping electron with its own image force

$$F(x) = -\frac{e^2}{4\pi\epsilon_0 (2x)^2} \tag{2.2}$$

Here, e and ϵ_0 denote the electron charge and the vacuum permittivity, respectively.

The electron potential well, formerly described by a step-function, then approximately writes as

$$\Phi(x) = -\frac{e^2}{16\pi\epsilon_0} \cdot \frac{1}{x} - e\,E \cdot x \;(x > 0) \tag{2.3}$$

This function has a maximum at $x_{\max} = \sqrt{\frac{e}{16\pi\epsilon_0 E}}$. The consequence of this so called Schottky effect [Sch23] is a reduction of the barrier height by $\Delta\Phi = \sqrt{\frac{e^3 E}{4\pi\epsilon_0}}$. The electron flux (eqn. 2.1) gets decisively enhanced due to the field:

$$\Psi_{\text{Schottky}} \sim T^2 \cdot \exp\left(-\frac{\Phi_0 - \Delta\Phi}{k_B T}\right) \tag{2.4}$$

At very high field strengths, above about $0.1\,\mathrm{GV\,m^{-1}}$, the barrier gets so narrow that quantum mechanical tunneling is the dominant mechanism. Then field emission becomes independent of temperature. Therefore, it is often referred to as *cold emission* because it takes equally part at ambient or cryogenic conditions. In a theoretical paper dated 1928, Fowler and Nordheim [FN28] calculated the tunneling

[2] O. W. Richardson (* 1879 - † 1959), Nobel prize 1928
[3] A former PhD student of Max Planck (* 1858 - † 1947) who was awarded the 1919 Nobel prize.

flux by considering a triangular shape for the tunneling barrier:

$$\Psi_{\mathrm{FN}} \sim \exp\left(-\frac{4\sqrt{2m_e\Phi_0^3}}{3\hbar eE}\right) \tag{2.5}$$

Here, m_e and $\hbar \equiv h/(2\pi)$ denote the electron mass and Planck's constant, respectively. Equation (2.5) forms the theoretical basis of modern electron emitters applied in the field emission gun of state of the art transmission electron microscopes (TEM).

Interestingly, at about the same time, Erwin Müller was engaged with his PhD research under the supervision of Gustav Hertz (* 1887 - † 1975) in Berlin. In 1935 he constructed the first field electron microscope (FEM) and analysed the voltage-current characteristics of the observed emission. The FEM is directly based on the described field effects [Mül36b; Mül36a]. The instrumental setup was very simple: It consists of an evacuated bulb. Inside, a needle shaped electron emitter is placed opposite to an anode. For operation, the emitter is subjected to a negative potential of a few hundred volts. Produced electrons get captured by the anode. In later instruments, the anode was replaced by a phosphor screen which allowed for studying the spatial distribution of the emission. Furthermore, cooling to cryogenic temperature reduced thermal velocities of the electrons and allowed for less disturbed imaging conditions.

2.1.2. Field ion emission

Considering the same setup as described before but with a positive voltage applied to the emitter, emission of field-induced ions becomes possible. The field ion microscope (FIM) presented by Erwin Müller in 1951 [Mül51] follows this principle. Ions are routinely imaged by the use of a phosphor screen. Because higher fields are necessary, the applied voltage shifts into the range of some kilovolts, up to 20 kV are quite common.

The usual FIM operation mode utilizes a so called imaging gas (typical is He, Ne or another inert gas). Caused by the diverging emitter field, gas atoms are polarized and attracted to the emitter apex where they get trapped and lose their kinetic energy by thermal accommodation. Figure 2.1a shows the potential diagram for such an trapped atom in front of a metallic tip in the view of its electron. The binding potential is decisively deformed by the applied field. I denotes the ionization energy, Φ_F the Fermi level, respectively. Assuming a sufficient high field, ionization may appear by tunneling of an electron from the potential well of the

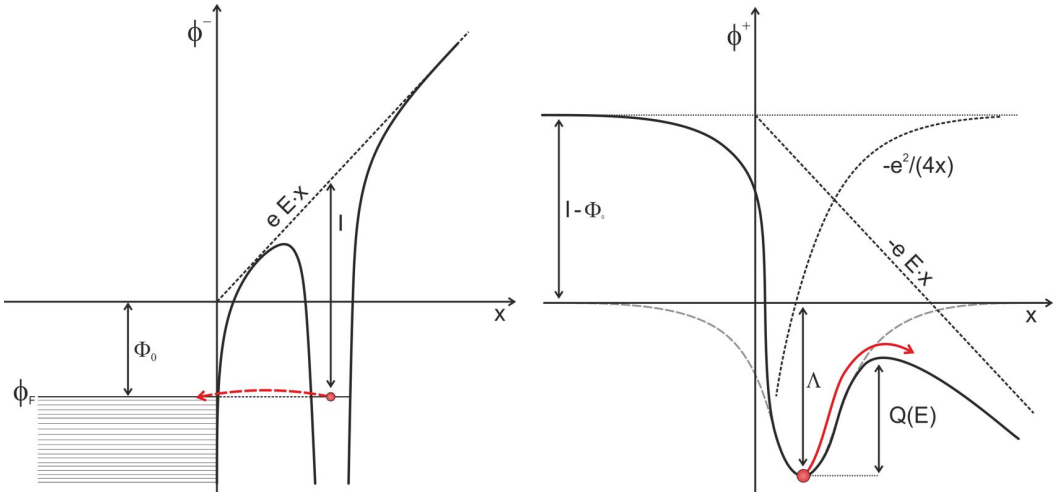

(a) field ionization **(b)** field desorption & evaporation

Figure 2.1.: Potential curves for (a) an electron and (b) an adatom in the vicinity to the emitter metal-vacuum interface with applied field.

adatom into the metal. Clearly, this is only possible if the binding level of the electron is shifted above the Fermi level of the metal. The critical distance x_c for this to happen reads

$$x_c = \frac{I - \Phi_0}{e\,E} \tag{2.6}$$

In the case of a tungsten tip imaged with He for example, this distance amounts to about 5 Å or almost two lattice spacings. Imaging contrast in the FIM mostly develops owing to the local varying surface field. Protruding positions like kinks or edges of atomic terraces concentrate the field and are therefore responsible for bright contrast while, for instance, the inner parts of atomic terraces appear dark. Related properties of the projective images will be addressed in section 2.2.1 in more detail.

2.1.3. Field desorption and field evaporation

If the applied field is further increased beyond the necessary threshold for gas ionization, direct desorption of atoms from the surface is observed. If the removed ions have formerly been part of the emitter bulk, one speaks more precisely of field evaporation. Field desorption is the more general term that addresses also the removal of adatoms. For explaining the physics of the effect, various models have been proposed [Gom59; GS63; Kin82a; Kin82b] and also numeric approaches based on Density Functional Theory (DFT) calculations have been tested [KN87].

But nevertheless, most popular is the image hump model already introduced by Müller [Mül56] — although it is severely questioned [BF82]. Its origin is the energy balance of the ionized state after desorption with the neutral bound state (without any field). The basic idea is analogue to the case of electron emission: In order to remove a neutral atom from the bulk, one has to spend the sublimation energy Λ and the ionization energy (fig. 2.1b). On the other hand, an electron is drained into the bulk during ionization. Therefore, one times the work function is retrieved. In summary, the energy balance writes as

$$Q_0 = \Lambda + I - \Phi_0 \tag{2.7}$$

Considering in addition the field dependency as mainly determined by the image potential of the formed ion, the final outcome is Müller's formula. The height of the activation barrier in the presence of a field then reads

$$Q(E) = Q_0 - \sqrt{\frac{e^3}{4\pi\epsilon_0} E} \tag{2.8}$$

A naive application of this equation derives an estimate for the critical field strength at which the barrier completely vanishes:

$$E_{\mathrm{Crit}} \cong \frac{4\pi\epsilon_0}{e^3} Q_0^2 \tag{2.9}$$

This field is commonly called the materials *evaporation field*.

A comparison of predicted evaporation fields with experimentally observed ones is presented by figures 2.2a and 2.2b for different materials. As a general trend, we see that the evaporation field of the materials correlates with their melting temperature. The higher the melting temperature the higher is the evaporation field which can be expected. To some part, this can be easily understood because the binding energy is essential for both field induced evaporation and melting. Nevertheless, in a second view, the correlation between the evaporation field and melting is still astonishing as for field evaporation additional electric effects have an impact.

On the other hand, details of field evaporation theory are rudimentary understood and even surprising insights may still arise in the future. Avoiding theoretical pitfalls, two general relations confirmed by experimental evidence turn out to be useful:

First, experiments which have been conducted with constant desorption flux in-

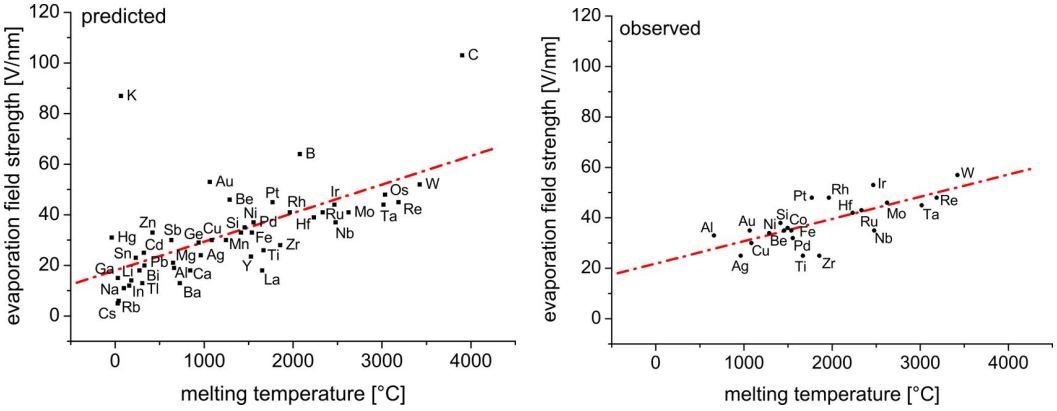

(a) **(b)**

Figure 2.2.: Evaporation fields plotted versus temperature: (a) predicted by the image hump model and (b) observed in experiments. For the image hump an extension to multiple charged ionic appearances was considered. Derived fields refer to the most prominent charge states observed in experiments. The original data are tabulated in [MS89] and [Tso90]. Melting temperatures are taken from [Sto00].

dicate that a linear relation between the acting field and the activation barrier is realistic [Vur+06]. Although this result contradicts at first sight with the described dependence (eqn. 2.8), this finding is nevertheless consistent if the particular field conditions close to the critical threshold are adressed. A Taylor approximation of equation (2.8) with $E \approx E_{\mathrm{Crit}}$ clearly predicts this linear field dependence:

$$Q(E) \approx \frac{Q_0}{2}\left(1 - \frac{E}{E_{\mathrm{Crit}}}\right) \tag{2.10}$$

In turn, this form represents a useful starting point for further experimental or theoretical considerations. — Fairly, this is at the cost of treating Q_0 and E_{Crit} as free parameters.

Second, experiments with constant field reveal an Arrhénius dependency when the temperature is raised [Kel84]:

$$\Psi_{\mathrm{Ions}} \sim \exp\left(-\frac{Q(E)}{k_B T}\right) \tag{2.11}$$

This observation is a strong hint to a thermally controlled process. Thus, kinetic models of field evaporation [WK90] appear justified. Equation (2.11) is also the theoretical basis for understanding effects with laser-assisted field evaporation for which a short heat pulse to the tip is assumed [KT80; Vel+06; Gau+06; Obe+07].

2.2. Basic principles of atom probe tomography

APT represents the direct application of field desorption as a measurement technique. Under common experimental conditions, the necessarily high field strengths in the order of $10\,\mathrm{GV\,m^{-1}}$ are difficult to reach. Even if best vacuum conditions apply, the dielectric strength is about three orders of magnitude to low. A simple setup consisting of a plate capacitor would suffer from breakdown before a sufficiently high field is reached.

For this reason, a particular geometric setup is considered in APT. By making use of small needle shaped samples, a sufficient field is then already achieved if only moderate voltages in the range of some kilovolts apply. Indeed, utilizing the needle like geometry is one of Erwin Müller's first merits. Figure 2.3 shows the basic geometric setup which is used for FIM as well. Due to the tip geometry, the enhanced field is constricted to the apex of the emitter as the curvature is highest there. For the experiments, a micro-channel plate combined with a position sensitive delay-line detector or phosphor screen acts as counter electrode in order to catch the emitted ions. As mentioned before, cooling of the emitter to cryogenic temperatures is favourable as thermal noise becomes reduced this way.

An approximate analytic solution for the potential and field of this setup may be obtained if the geometry of two confocal paraboloids as electrode surfaces is considered [SW78]. By virtue of rotational symmetry, two independent coordinates (y,z) are sufficient for the description. With the origin taken to be in the common focus, the small paraboloid representing the emitter is given by $y^2 = 4Z_r \cdot (Z_r - z)$. The curvature radius at the tip is $r = 2Z_r$. For the second paraboloid, a focal length Z_R is used which is considered equal to the distance between emitter and counter electrode (fig. 2.4). With this, the solution of the potential writes as

$$\varphi(y,z) = \ln\left(\frac{z+\sqrt{z^2+y^2}}{2\,Z_R}\right) \cdot \frac{U}{\ln(Z_r/Z_R)} \tag{2.12}$$

Parameter U denotes the applied voltage. The field $(E_y, E_z)^\top(y,z)$ is given by the gradient. So we get

$$\begin{aligned} E_y &= \frac{U}{\ln(Z_R/Z_r)} \cdot \frac{y}{z^2+y^2+Z\sqrt{z^2+y^2}} \\ E_z &= \frac{U}{\ln(Z_R/Z_r)} \cdot \frac{1}{\sqrt{z^2+y^2}} \end{aligned} \tag{2.13}$$

(a)

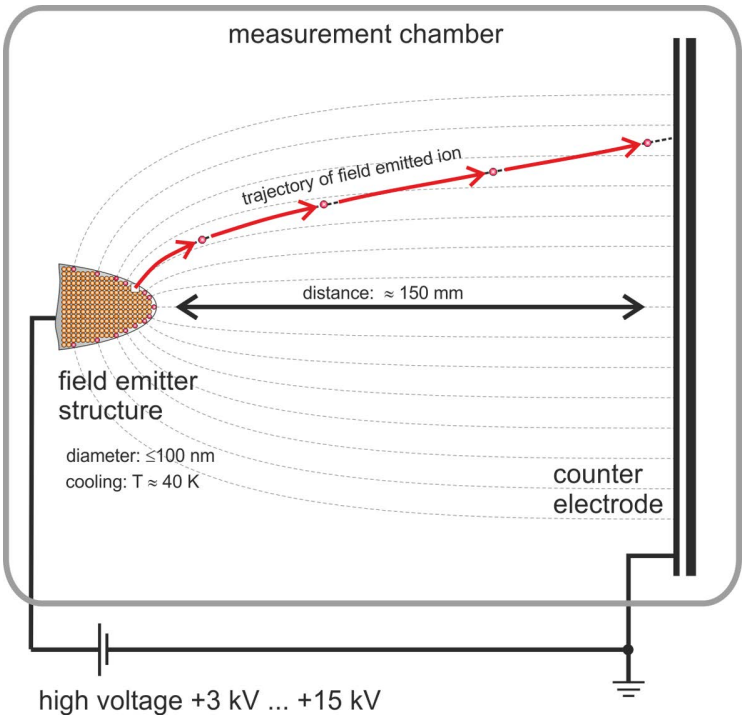

(b)

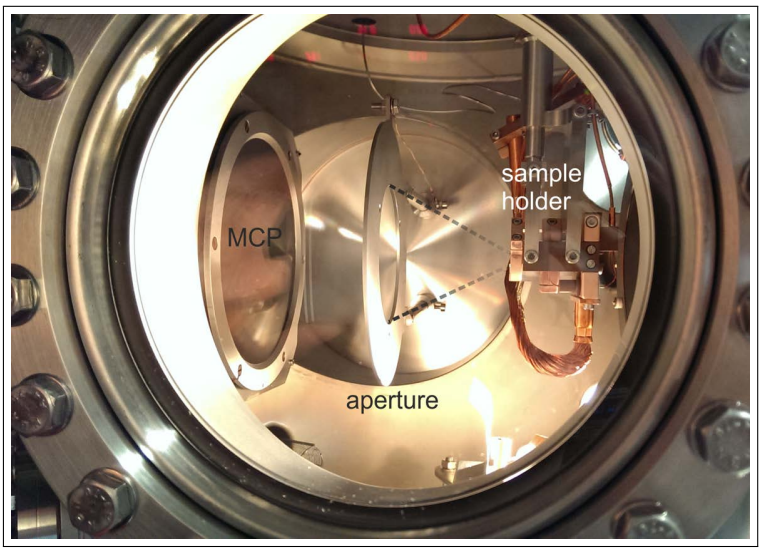

Figure 2.3.: Basic setup for APT measurements: (a) schematic sketch of the field emitter structure in front of the counter electrode. With an applied voltage, the trajectories of emitted ions approximately follow the field. (b) View inside the measurement chamber of the atom probe at Münster University [Ste+07] showing the same basic arrangement. The emitter is fixed inside the sample holder. The micro-channel plate (MCP) on the left acts as the counter electrode. The additional aperture is grounded to 0 V and enables slightly enhanced field conditions for emitted ions.

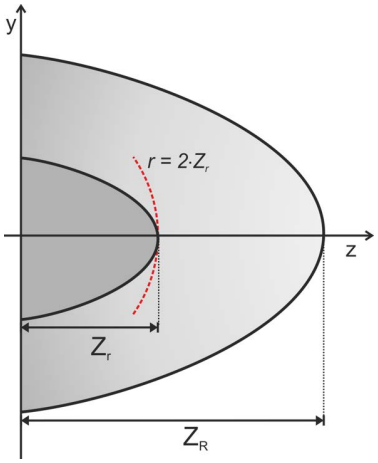

Figure 2.4.: The analytic solution of the Laplace equation considers the geometry of two confocal paraboloids with different heights Z_r and Z_R.

Although this solution turns out to be of limited use in order to describe the real electrostatic conditions of the experiments, particularly if an additional aperture or a sophisticated lens system is present, this analytic approach provides nevertheless interesting clues. For instance, the field along the emitter axis with $(0, z)$ equates to

$$E_z = \frac{U}{\ln(Z_R/Z_r)\, z}$$

In particular, it reads

$$E(z = Z_r) = \frac{2}{\ln(Z_R/Z_r)} \cdot \frac{U}{r} \tag{2.14}$$

at the apex. Here, the pre-factor only weakly depends on geometric parameters as $Z_R \gg Z_r$. This leads us to consider the apex field to be in general expressible in the form

$$E_{\text{Apex}} = \frac{U}{\beta\, r} \tag{2.15}$$

with a practically constant β as it is common practice in APT. The here newly introduced factor β replaces the logarithm in equation (2.14) and is called *field-factor*. It is generally considered as a sample and instrument related parameter. Usual experimental values are in the range between three and twelve. — If, for example, in the application to the paraboloidal model, a curvature radius of 50 nm and a distance of $Z_R = 15$ cm are used, the calculated "analytic" field factor yields $\beta = 7.5$.

Vice versa, equation (2.14) can also be used to determine the curvature at the apex if β and the voltage are known. In an experiment starting at zero voltage, the emitter begins to form itself on the onset of field desorption until a steady shape is established. Observed curvature changes are then proportional to the

submitted voltage and to the coefficient $(\beta E_{\mathrm{Crit}})^{-1}$ which is essentially controlled by the critical evaporation field of the material.

The so established desorption is very sensitive to the applied field or voltage (eqn. 2.11). The ability for the fine grained control and to trigger single desorption events establishes the core of any APT measurement approach.

2.2.1. Sample geometry and image formation

The way in which the field factor has been introduced here already emphasizes the crucial role of the emitter geometry for APT experiments. In practice, a more simple geometry than the paraboloidal one is used as approximation. The tip is considered to be assembled of a truncated cone and a half-spherical closing cap (see fig. 2.5a). Decisive parameters are the taper angle γ_{tip} and the curvature radius r_{tip}. (The particular advantage of this practice will become clear in the latter part of this section, when the 3D reconstruction is discussed.) Although the preparation of the required needle shaped samples seems to be tedious, this constraint does not really represent a bottle neck in modern APT. For instance, the samples depicted in figure 2.5 have been prepared utilizing conventional electrolytic etching techniques. If this etching is used in combination with a polishing step in the FIM, such samples can also serve well as substrate for deposition of even more complex multi-layer structures (fig. 2.5b).

Less tricky but requiring an expensive instrumental equipment, state-of-the art APT sample preparation is enabled by the focused ion beam (FIB) technique [KL12]. This not only allows for site specific preparation directly from a bulk source, but also enables a verifiable control of the milling process which finally results in perfectly shaped samples with improved measurement yield.

As a lens-less microscope, APT is really unique: Each sample acts as its own projective imaging system. In the FIM mode as well as in APT measurements, the trajectories of emitted ions are controlled by the emitter apex. For illustration, figure 2.6 shows two field ion micrographs which have been obtained both at a low voltage (fig. 2.6a) and at an elevated voltage (fig. 2.6b). In the first case, the estimated curvature amounts to about 8 nm which represents a very sharp tip and results in a high magnification. Clearly, these conditions are way sufficient to easily resolve individual atoms at the apex. In the latter case, the curvature amounts to about 40 nm. The magnification is much lower. We see, the continuous erosion of the tip apex by increasing the voltage not only results in a blunting of the tip but is also responsible for a dramatic change in magnification.

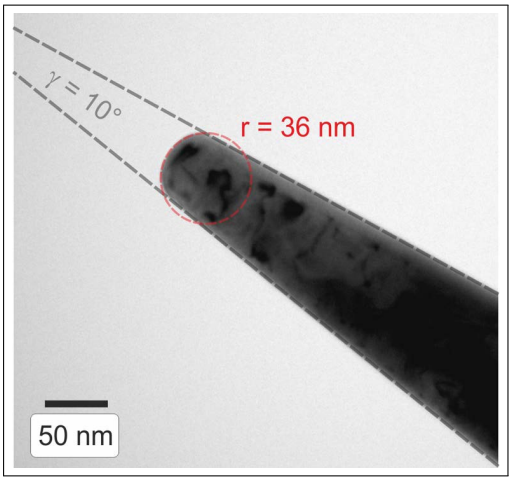

(a) Measurement of the emitter shape by determining its taper angle and the curvature radius at the apex. Before imaging with the TEM, the emitter has been submitted to a voltage of 13 kV (Courtesy of M. Roussel, University of Münster).

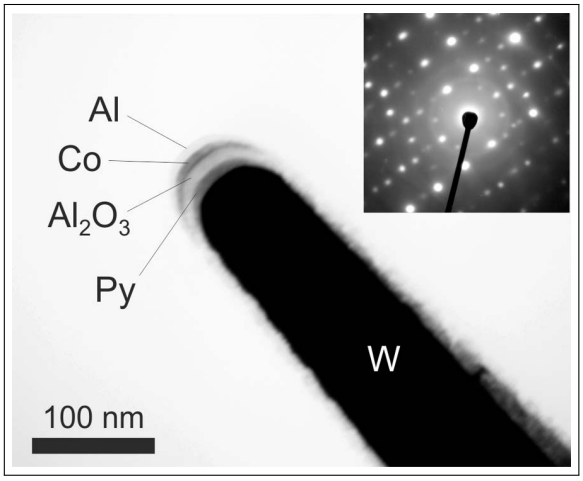

(b) Typical sample geometry in the application to material analysis [Sch+10]. Four different layers prepared by sputter-deposition onto a pre-sharpened tungsten tip are seen (Py ≡ $Fe_{19}Ni_{81}$).

Figure 2.5.: Exemplary TEM micrographs of used APT field emitter samples

The general image formation is described by a point projection, with the origin of the projection off-centred of the half-sphere at the apex. As an effect of the needle shaft, the origin shifts somewhat backwards along the emitter axis. In consequence, the imaging conditions are best described by an intermediate projection between a central and a stereographic projection [Bas+95; AlK+03].

In detail, the ring like pole patterns, which are easily visible in the FIM mode, coincide with distinct crystal orientations. A careful microscopic description of the projection therefore derives from the angular relations of the image at the FIM screen and the comparison with the lattice orientations [WSS74]. As the result, a linear relationship between the imaging angle and the corresponding launch angle for field emitted ions is revealed (See figure 2.7 for the definition of the

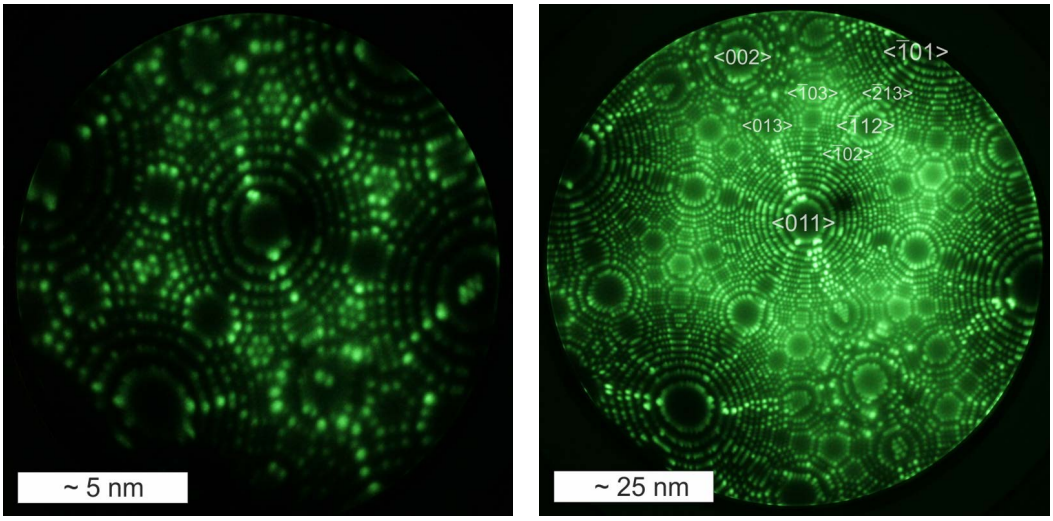

(a) Low voltage: $\approx 3.0\,\mathrm{kV}$, high magnification: $\geq 5 \cdot 10^6$

(b) Elevated voltage: $\approx 15.0\,\mathrm{kV}$, low magnification: $\leq 10^6$

Figure 2.6.: Field ion micrographs of a tungsten emitter. Crystallographic orientations are revealed by distinguished pole patterns.

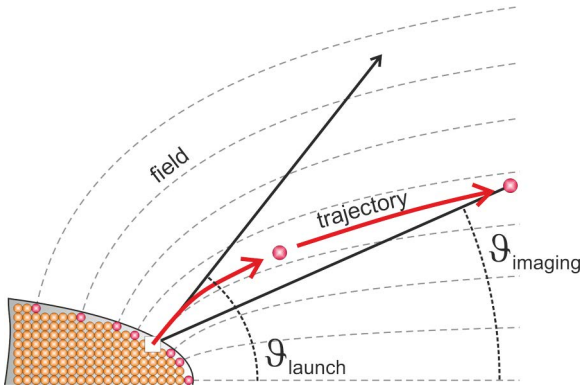

Figure 2.7.: Sketch of the angles which become considered for the image compression.

angles.) [CWS99]:

$$\vartheta_{\mathrm{imaging}} = \xi \cdot \vartheta_{\mathrm{launch}} \tag{2.16}$$

The controlling factor denoted by ξ is called the image compression ($0.0 < \xi \leq 1.0$). The image compression establishes the link between the original location at the apex and the final position in the image. Therefore, it is essential for the application in APT reconstruction, as we will shortly see. But firstly, we can use it to give the equation for the magnification of the projection. According to the principle of intercepting lines, the magnification simply becomes

$$M := \frac{l\,\xi}{r} \tag{2.17}$$

if the emitter to screen distance is l.

2.2.2. Field desorption experiments

Figure 2.8 shows in atomic detail the crystal structure at the apex of an Al field emitter which has been imaged with an high resolution TEM. Atomic columns of the fcc structure are seen. From this, the present lattice orientation can be determined. Most remarkably here is the rough morphology with kinks and edges at the boundary to the vacuum. This picture makes immediately clear that for the details of the desorption and the following trajectories towards the detector the surface does play an essential role. Whereas the usual imaging properties described before are determined by the macroscopic field, the local field in direct vicinity to the surface is responsible for observed patterns and also for possible imaging artifacts. In order to understand this relation it is instructive to compare the imaging process in the FIM (fig. 2.6) with its counterpart in APT.

Detailed results from the literature about the image projection have been almost exclusively been gathered by FIM experiments, despite the process of field ionization and field induced desorption are not identic. In FIM, the whole apex surface is imaged simultaneously by means of field ionization of an imaging gas, whereas APT is based on the consecutive evaporation of single apex atoms. — For sure, the latter process is also routinely observed in FIM. But the important difference is that FIM does not really image the evaporation: the image of the emitter apex

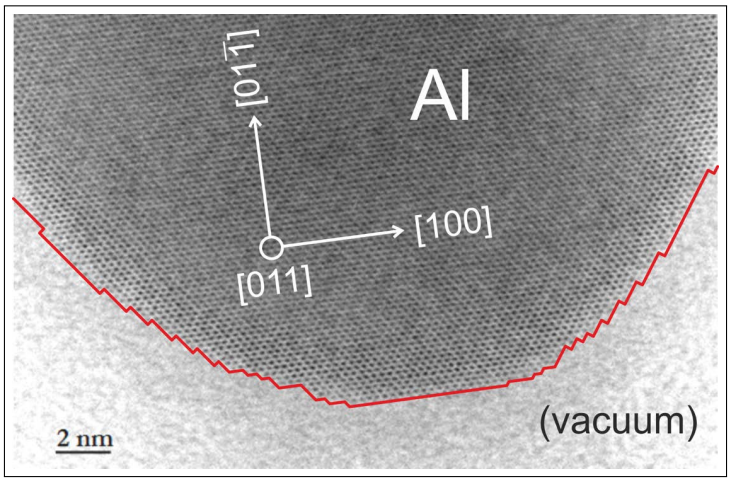

Figure 2.8.: High resolution TEM image of an Al field emitter sample after preparation with FIB (Courtesy of W. Levebvre, Institut des Matériaux, Universite de Rouen). The atomic rough surface morphology of the apex is clearly predetermined by the crystal lattice.

before and after the evaporation event is visible. In contrast, what is not visible, is the image of the evaporated atom itself at the screen, like it is the case in APT.

The insight that both processes obey somewhat different rules is emphasized by patterns captured with the so called field desorption microscope (FDM). The basic instrumental setup of the instrument is the same as for the FIM, but in this case, the device operates without any image gas. Instead, the imaging screen is coupled with a timing gate which is used to activate the screen for preset time slots right after a high voltage pulse has been applied [WDJ75; WDJ76; KMM77]. The magnitude of these trigger pulses is adjusted such that the atoms of a few mono-layers at the apex are removed. Unintended contribution of noise due to residual ions in the chamber is prevented by means of the time gated detector screen. This way, incoming ions are filtered by their time-of-flight.

FDM experiments must be conducted with great care for the best possible vacuum and temperature conditions in order to avoid misleading results. For example, the presence of residual gases in the chamber like H_2, H_2O or He and Ne from a previous operation as a FIM does selectively promote the desorption of atoms [Kel84]. Unfortunately, most of the available FDM micrographs [WDJ76; KMM77], which are almost exclusively published in the 1970s of the last century, probably suffer from less than optimal conditions.

A counter example is given by figure 2.9 published by Geiser et al. in 2009 [Gei+09]. This extraordinary detailed desorption map of a high-purity Al field emitter was obtained using a modern commercial atom probe instrument[4]. The shown pattern is the cumulative result of many single desorption events which have been captured. It is one of the best measurements known to the author. Very good vacuum conditions ($\sim 10^{-11}$ mbar) at the lowest possible temperature (~ 20 K) offered by the instrument have been ensured. A complex pattern with rings around low indexed crystallographic poles appears which has some similarities to typical FIM micrographs, although the origin here is from field desorption. Particularly striking is the detailed appearance of clear zone lines of the crystalline Al apex which are revealed by dark stripes depleted in hit intensity. Different widths are also recognized. Most remarkably, in the stripe center, a bright contrast is restored. Thus, no or at least less depletion of atoms seems to be present here.

In comparison to other FDM images, this observation is unique and a result of the excellent measurement conditions. Notably, in older publications, the zone lines appeared also with *elevated* intensity but a detailed inner structure could not be

[4] Cameca LEAP 3000 X Si

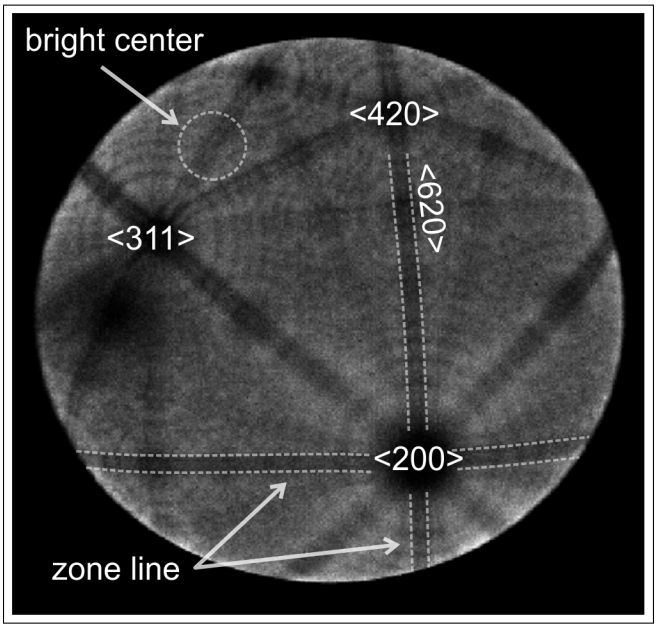

Figure 2.9.: Al desorption pattern obtained at a very low temperature of T=20 K and particular clean vacuum conditions [Gei+09] (Courtesy of M. Moody, Department of Materials, Oxford University).

observed. Elevated intensity is presumably a result of promoted desorption. It is well known that in particular at zone lines elevated fields are present which must be considered to play a decisive role [Pan74]. The observed loss of internal structure is presumably due to degraded vacuum conditions in combination with an in general elevated emitter temperature ($\geq$ 70 K).

2.2.3. Outline of the APT measurement process

Practically, the FDM almost operates like a modern atom probe but with the notable limitation that only cumulative desorption events could be reasonably detected and no further information on the desorbing atoms is accessed. Actually, the capability of the detection system of determining the 2D hit position for each of the incoming ions is one of the main instrumental characteristics of the so called "three-dimensional" (3DAP) [CGS88] or "tomographic" (TAP) [Bla+93] atom probe instruments.

In state of the art devices, fast delay line detectors are used for this purpose. Unfortunately, these detectors have only limited capacity to discriminate the position information in the case of multiple hits at a time. For this reason, atom probe measurements are conducted in a sequential manner, atom by atom. The controlled

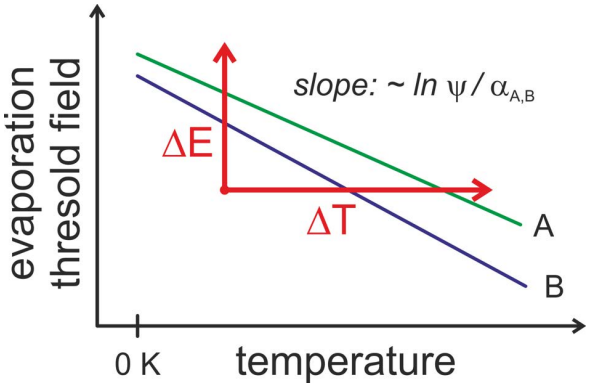

Figure 2.10.: Sketch of the dependence of the desorption on both field and temperature.

desorption of mostly single atoms is enabled by pulsed high-voltage or laser-assisted field evaporation in combination with a standing voltage (fig. 2.10): While without any pulse, the actual emitter field is not sufficient, suited evaporation conditions are either achieved by a short high-voltage pulse superimposed to the standing voltage or by illumination with a laser pulse which leads to a shortly increased temperature at the tip. This latter approach has the same promoting effect on the desorption rate but leaves the field constant (eqn. 2.11). If species with different evaporation fields are present, denoted by A and B in figure 2.10, the magnitude of the applied pulses must be chosen with care so that preferential evaporation does not appear. The actual desorption rate in the measurement (i.e. atoms per pulse) is adjusted by increasing or decreasing the standing voltage insofar it is necessary.

Besides the sophisticated measurement control, pulsed field evaporation enables mass-spectrometry on the detected ions. Simultaneous with each trigger pulse submitted to the emitter, a clock is started and it is stopped once a detector event is registered. From the measured time-of-flight and the accelerating voltage, the respective mass-to-charge ratio is calculated from which in turn the chemical nature can be deduced.

Each APT measurement results in a unique data set. For each detected evaporation event,

- the 2D detector position,
- the measured time-of-flight, and
- the actual measurement voltage

are recorded. The stored sequence of such data records notably matches the sequence in which the atoms have been evaporated from the analysed emitter structure. Hence, first records depict information on atoms which have been located at

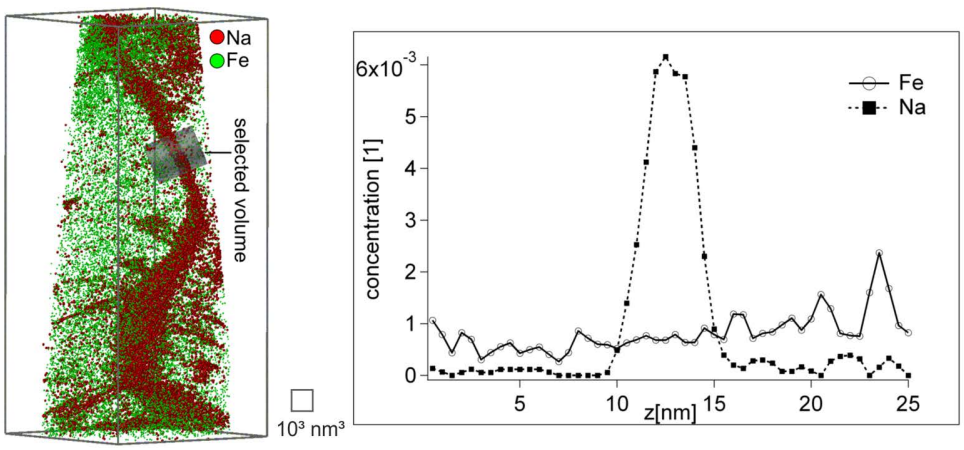

Figure 2.11.: APT analysis of a $Cu(In, Ga)Se_2$ (CIGS) thinfilm solar cell (Courtesy of R. Schlesiger, University of Münster [Sch+10]). (a) 3D impurity distribution of Fe and Na. Segregation of Fe clearly reveals a grain boundary. In contrast, Na appears equally distributed. (b) Determined atom concentration in the marked cylinder.

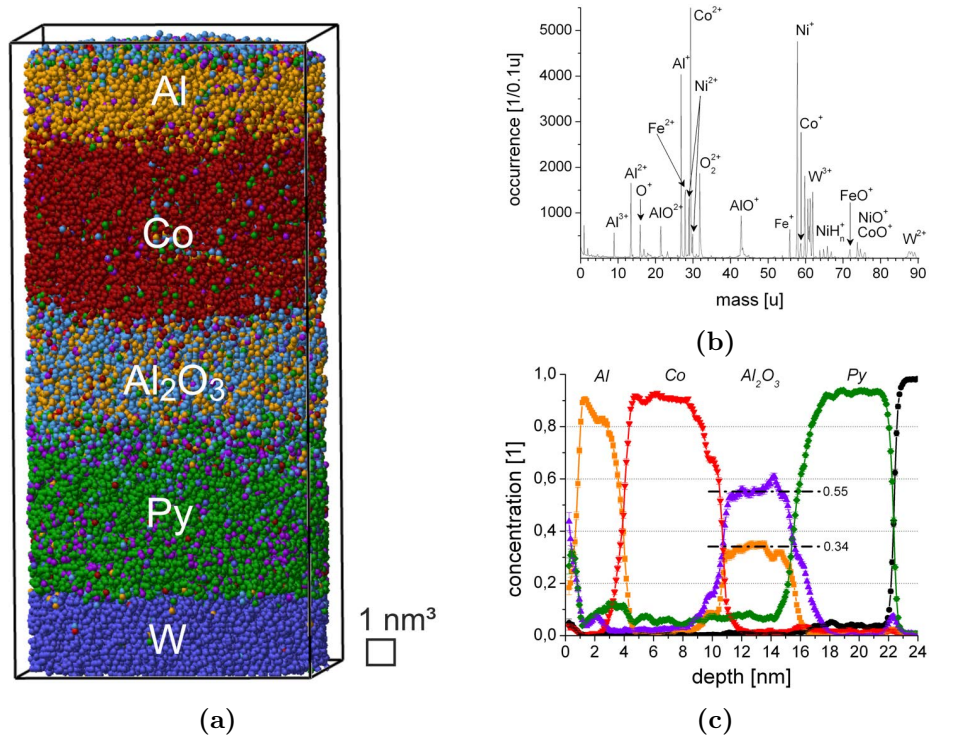

Figure 2.12.: APT analysis of the emitter sample depicted before in figure 2.5b [Sch+10]. (a) 3D reconstruction. At the bottom part, lattice planes in W are revealed ($d_{\langle 011 \rangle} = 2.23\,\text{Å}$). (b) Mass spectrum. Atomic and molecular species with different charge state are identified. (c) 1D concentration analysis. Stoichiometry of Al oxide almost matches the nominal value for Al_2O_3.

the surface of the sample structure, whereas the following records depict information on the volume underneath. Thanks to the continuously progressing erosion of the emitter, the depth information is preserved in the obtained sequence. We will describe in the next section how the collected information can be used to reconstruct the original 3D atomic positions within the analysed volume. Examples of reconstructed sample volumes from such data sets are presented in figures 2.11 and 2.12.

2.2.4. Constitution of the 3D reconstruction

The standard approach for reconstruction has been introduced by Bas et al. at a time when the first instruments equipped with position-sensitive detectors were available [Bas+95]. Although APT instrumentation has seen a vast progress since then, the original reconstruction approach still almost represents the state of the art. Most of the conducted 3D atom probe analyses conceptually still rely on this early work.

As a general premise, the measured emitter apex is assumed to maintain an approximately uniform spherical surface at any time. A suited description of the geometry is therefore enabled by deliberately accounting for the curvature radius, denoted by r, and the emitter height z_{Apex}. Both parameters are subject of continuous changes during measurement and different approaches exist in order to account for the variation. Another premise is that a central projection holds which gets only slightly modified by the image compression factor ξ.

Provided that the sample emitter is not tilted and coincides with the instrument axis, the procedure for reconstructing the sample volumes can be conveniently divided into two parts. In a first step, the 2D coordinate at the detector (x', y') is considered (fig. 2.13). From the distance l between the detector and the sample the respective imaging angle

$$\vartheta' = \arctan\left(\frac{\sqrt{x'^2 + y'^2}}{l}\right) \tag{2.18}$$

is computed. — Here and in the following, primed symbols refer to the situation at the detector, whereas the plain symbols are valid for the emitter. — The extension to 3D takes the presumed emitter curvature into account. The launch angle ϑ of the detected ions amounts to ϑ'/ξ, whereas the azimuth within the image plane

$$\varphi = \arctan\left(\frac{y'}{x'}\right) \tag{2.19}$$

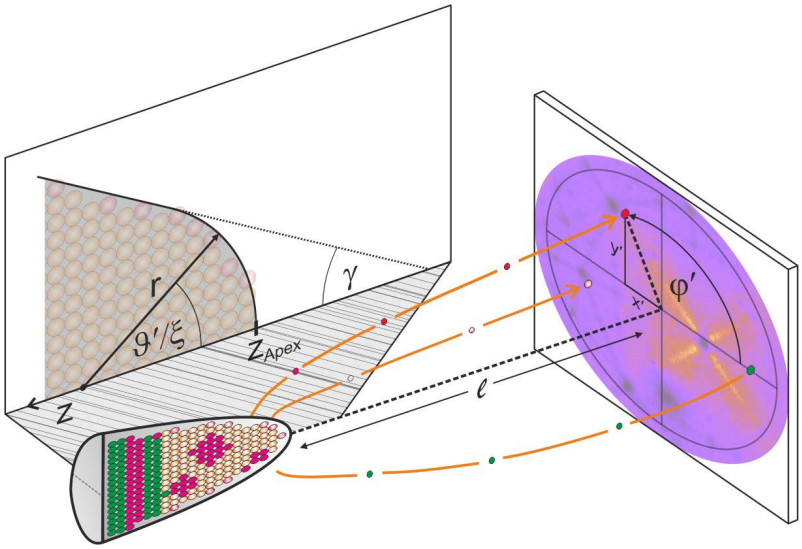

Figure 2.13.: Geometrical relations which become considered for the 3D reconstruction

remains the same both at the detector plane and at the emitter due to rotational symmetry. The image transfer relation is best expressed by using spherical coordinates $(r, \varphi', \vartheta')$, so that the 3D launch position at the emitter may be written as

$$\begin{pmatrix} x \\ y \\ z \end{pmatrix} = \begin{pmatrix} 0 \\ 0 \\ z_{\mathrm{Apex}} \end{pmatrix} + r \cdot \begin{pmatrix} \sin(\vartheta'/\xi)\,\cos(\varphi) \\ \sin(\vartheta'/\xi)\,\sin(\varphi) \\ 1 - \cos(\vartheta'/\xi) \end{pmatrix} \tag{2.20}$$

The z-axis is directed along the tip-shaft. As a consequence of the curvature, the reconstructed z-coordinates are larger for events located at the center of the detector than for those located more outwards. Particularly for $\vartheta' = 0°$, one directly receives $z = z_{\mathrm{Apex}}$, which is the actual height of the apex. By the described inverse projection, we are basically able to trace back the 3D launch positions of each single event. But that is not enough. In order to reconstruct the full volume with several millions of atoms, further effort is necessary to appropriately account for the shrinkage of the tip. This change is addressed by a separate, second reconstruction step.

Emitter shrinkage

The usual approach is to distribute the shrinkage due to the discontinuous erosion of atomic terraces as it is usually observed in FIM continuously to all events in the APT measurement sequence. Thus, once the 3D atom position of the ith event has

been computed, the actual emitter height changes by a small decrement Δz which is then used for the reconstruction of the *(i+1)*th event:

$$z_{\mathrm{Apex}}^{(i+1)} = z_{\mathrm{Apex}}^{(i)} - \Delta z \tag{2.21}$$

The value for the applied decrement can be estimated by considering the volume of a thin shell of the apex which is delimited by the aperture angle ϑ_{max}. If the thickness of this shell is Δr and a fixed atom volume Ω applies, the respective number of atoms located in the shell becomes

$$N = A(\vartheta_{\mathrm{max}}) \cdot \Omega^{-1} \cdot \Delta r \tag{2.22}$$

$A(\vartheta)$ is derived from the detector area with regard to the magnification of the projection (eqn. 2.17):

$$N = \frac{A_{\mathrm{Det}}}{M^2} \cdot \Omega^{-1} \cdot \Delta r \tag{2.23}$$

The limited detection efficiency of the detector must also be considered. In order to correct for missed events, a factor $1/p_{\mathrm{Det}}$ is additionally introduced. At the end, the desired emitter shrinkage attributed with each single atom is then given by

$$\Delta z \approx \left(\frac{dN}{d(\Delta r)}\right)^{-1} = \frac{\Omega}{p_{\mathrm{Det}}} \cdot \frac{M^2}{A_{\mathrm{Det}}} \tag{2.24}$$

Tip blunting

Owing to the cone-shape, erosion of the tip also leads to an increase of apex curvature. In order to track this tip blunting, basically two approaches are established [JS02]. The obvious way is to determine the curvature changes directly from the applied voltage which is recorded together with each measurement event (eqn. 2.15). Clearly, this is only possible if preset values for the field factor and the evaporation field, which appear in equation (2.15), are provided. Although this approach offers a high reliability, it practically suffers from the requirement of uniform evaporation properties of the analysed materials. However, most of the analysed samples usually exhibit complex composite structures with decisively different field evaporation properties. The commonly applied approach is therefore to predict the curvature changes by considering a conical emitter geometry. Then, the provided values are an initial apex curvature and the taper angle γ. Straight forward geometry leads to the relation

$$\Delta r = \frac{\sin\gamma}{1 - \sin\gamma} \cdot \Delta z \tag{2.25}$$

for the curvature change as a function of the shrinkage. Because both of the described reconstruction steps are applied one after the other, a unique set of 3D coordinates results for each event. Together with the continuously progressing z-coordinate the curvature radius advances as well.

2.2.5. Enhanced reconstruction approach dedicated to wide angle instruments

In the evaluation of data collected by instruments with limited field of view ($\sim 5°$), the approach by Bas et al. has proven sufficient quality in terms of atom positioning and spatial calibration of the reconstructed 3D volume. A famous example in this regard is the analysis of the Cotrell atmosphere of Boron close to an edge dislocation in FeAl by Blavette et al. [Bla+99]. Exhibiting a dopant concentration of 400 ppm, enrichment of the Boron atoms could be clearly resolved in addition to the simultaneous imaging of the Burgers circuit in the host lattice.

Anyhow, facing the extended aperture offered by modern instruments — up to 40° are state of the art — the highest possible resolution of the 3D reconstructions remains limited to volumes located close to or at the center of the emitter apex parallel to the specimen axis. The origin for this lies to some part in the applied back projection procedure and the assumption of a unique apex curvature. Improved results after the reconstruction are therefore generally enabled by treating a not so ideally formed apex shape. For example, this can be achieved by an image compression factor which is a function of the imaging angle [Lar+10]. As the main drawback here, the evolving emitter shape depends on parameters which are not a-priori known for a conducted measurement, e.g. faceting in dependence on the crystal lattice and/or composition is important but complicated to predict. This uncertainty prevents the general application for reconstruction.

In addition, the lateral resolution is known to be degraded by aberrations in the trajectories of emitted ions [WCS98; Gau+09]. Moreover, these aberrations do eventually combine with directed diffusion prior to launching from the surface under the presence of the acting field ("rolling up motion") [Gau+12c]. Because off-axis trajectories are necessarily curved, degrading effects on the resolution get worse with an increasing imaging angle. Clearly, by their statistic nature such effects cannot be really corrected for.

In contrast, a fundamental improvement is achieved by an enhanced approach to account more precisely for the overall emitter shrinkage (eqn. 2.24). Starting point for this attempt is an emitter geometry with a simple cylindric shaft (fig. 2.14).

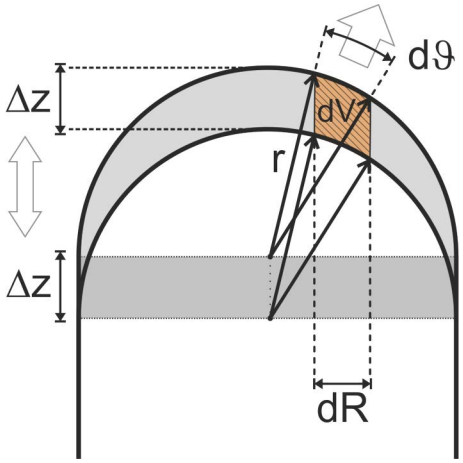

Figure 2.14.: Eroded volume at the emitter apex related to a small shrinkage of Δz. The angular desorption flux $\Psi(\vartheta)\,d\vartheta$ is linked to the hatched volume denoted by dV.

The curvature radius at the apex remains constant independent of the measurement progress ($dr(\vartheta, z) \equiv 0$). Therefore, the loss in volume associated with a shrinkage of Δz directly compares to a disc with

$$\Delta V = \pi r^2\,\Delta z \tag{2.26}$$

Since only a fraction of this volume can be accessed due to a limited measurement aperture, we need to take particular care for the angular distribution for which

$$\Delta V = \int_0^{\vartheta_{\max}} \frac{dV}{d\vartheta}\,d\vartheta \tag{2.27}$$

holds. From the hatched region in figure 2.14, it is clear that the linked volume segment $dV(\vartheta)$ severely changes with the desorption angle. With regard to the depicted geometry we get

$$\begin{aligned} dV(\vartheta) &= \Delta z \cdot R\,dR\,d\varphi \\ &= \Delta z \cdot r^2 \sin(\vartheta)\cos(\vartheta)\,d\vartheta\,d\varphi \end{aligned} \tag{2.28}$$

such that the angular desorption flux yields

$$\Psi_{\mathrm{Tip}}(\vartheta)\,d\vartheta = \frac{dN}{d\vartheta}\,d\vartheta = \Omega^{-1} \cdot \frac{dV}{d\vartheta}\,d\vartheta = \frac{2\pi r^2 \Delta z}{\Omega} \cdot \sin(\vartheta)\cos(\vartheta)\,d\vartheta \tag{2.29}$$

at the apex. Alternatively, this becomes

$$\Psi_{\mathrm{Det}}(\vartheta')\,d\vartheta' = \frac{2\pi r^2 \Delta z}{\Omega} \cdot \sin\left(\frac{\vartheta'}{\xi}\right) \cos\left(\frac{\vartheta'}{\xi}\right) \frac{d\vartheta'}{\xi} \tag{2.30}$$

if detector coordinates are used instead. Then, ϑ' refers to the imaging instead of the launching angle. Therefore, image compression, again denoted by ξ, must be considered.

If a limited aperture with $\vartheta'_{\max} \leq 90°$ is regarded, the relation between emitter shrinkage and the number of measured atoms ΔN at the detector equates as

$$\Delta z = \frac{\Omega}{p_{\mathrm{Det}}} \cdot \frac{\Delta N}{\pi r^2 \cdot \sin^2\left(\frac{\vartheta'_{\max}}{\xi}\right)} \tag{2.31}$$

which is not at all the same as it is commonly assumed in the frame of the Bas et al. approach (eqn. 2.24).

The expression for the shrinkage in the special case of a cylindric shaft is consistent with a result of Geiser et al. which has been published in [Gau+12a] but without giving any further description or proof. The impact of the here presented formulation on the computed reconstructions will be further examined in chapter 6.

2.3. Present challenges

Enabled by the computed 3D reconstructions, APT offers materials analysis at the ultimate limit as at the same time a high chemical resolution combined with a high spatial resolution is delivered. For sure, facing the progress in instrumentation and utilizing sample preparation by FIB, there exists nowadays practically no limitation on the type of possible samples: metals, semiconductors, ceramics or even solidified biologic materials, and complex compound structures can in principle be successively applied. But as much as the collection of measurement data has been facilitated, e.g. in particular by utilizing laser assisted field evaporation, the need for more sophisticated data processing techniques and for a better physical understanding of the basic processes has also increased. The demand to understand the involved physics has even increased with the now possible investigations of electrically more "exotic" materials than metals. For instance, in the case of semiconductors, such effects like band bending with at least partial field penetration into the bulk probably alters field evaporation [Tso79]. Also, it is well known that in samples which exhibit heterogeneous evaporation properties for different species severe artifacts in the computed reconstructions are encountered [VBB00; Vur+04b; MV08; Mar+10].

In order to illustrate the effect, a TEM tomography footage of a SiGe superlattice structure before and after performing the APT measurement is shown in figure 2.15.

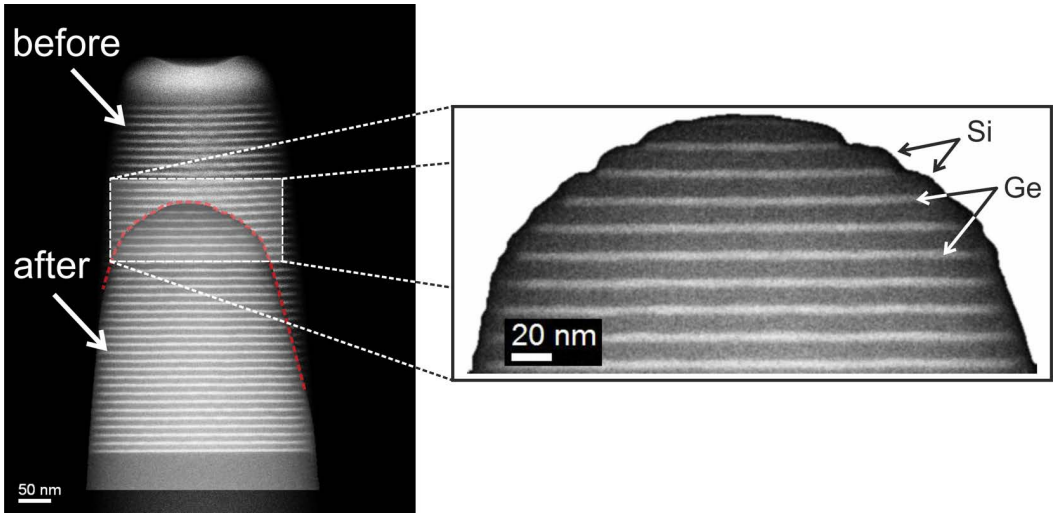

Figure 2.15.: TEM tomography capture of a SiGe superlattice before and after the field evaporation experiment (Courtesy of S. S. A. Gerstl & E. Mueller, EMEZ – Electron Microscopy Center at ETH Zürich).

The expected evaporation fields from the literature are $33\,\mathrm{V\,nm^{-1}}$ and $29\,\mathrm{V\,nm^{-1}}$ for Si and Ge, respectively [MS89]. As it is clearly depicted by the magnified view of the partially measured sample apex, a clearly heterogeneous surface morphology evolves. Deviations in the local curvature, as they are here encountered, are responsible for different imaging conditions of the ion trajectories which are finally also responsible for artifacts in the computed 3D reconstruction. Local density fluctuations in the reconstruction and unexpected sharp or intermixed interfaces are typical if a 1D concentration plot is evaluated. If lattice planes are recognized, they may appear bent close to such interfaces.

Currently, there exists no satisfactory solution for dealing with such type of artifacts. In the long term, it would therefore be desirable if the applied reconstruction procedure would be improved in such a way that it can correct artifacts. But this seems not feasible at the moment.

In this situation, simulations of APT measurements can play an important role. Provided they reflect the important physical mechanisms to a sufficient extent, possible evaporation artifacts in real measurements might get more easily revealed by comparison with simulations. If, in addition, also the magnitude of the present distortions could be quantified, the general reliability of the conducted APT analyses can be improved despite the artifacts. Besides, the simulation of APT measurements may play a key role in testing, improving and correcting present and newly developed analysis techniques which are applied to the 3D reconstructed data. Also

the ultimate goal to overcome the limitations of the present reconstructions may be finally reached on this path.

3. Numeric and algorithmic prerequisites

APT simulation models are based on two assumptions: First, if an atom evaporates, it almost loses instantly an electron during the process. Thereafter, it is accelerated off the apex. Second, realistic field conditions both at the emitter surface and for the trajectories are enabled if the rigid atom structure of the vacuum-emitter interface is treated as the decisive electrostatic interface, like it is visible in the high resolution TEM image of the Al emitter apex in the previous chapter (see fig. 2.8).

The implementation of the simulation model takes account to these assumptions by making use of a discrete mesh. The topology of the mesh permits a suited geometric and electric description of the emitter structure. In the following, foundations for the numeric treatment of meshes are addressed and related algorithms are explained. In a second part, discrete equations for the treatment of classical electrostatics on the meshes are derived.

3.1. Foundations of mesh generation

The topological description of a particular mesh is closely related to the notion of tessellations. A tessellation is the filling of space with well-defined geometric objects in which the single elements seamlessly fit together. In a different view, a tessellation represents a certain kind of partition of space into subspaces with a distinguished centroid and an implicit connectivity. For this reason, tessellations serve well as the foundation for computing meshes in numeric simulations.

The simplest kind of tessellation is the regular one which directly results from equidistant distributed points along the basis axes of a given coordinate system. In 2D, the obtained geometric objects are equally shaped squares or parallelograms (fig. 3.1a). If used as a computing mesh, the periodicity supports algorithmic and numeric treatment. However, not every problem is suited to be handled by this

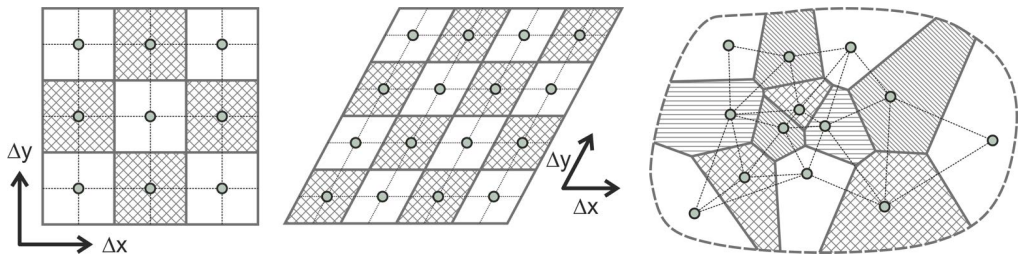

(a) regular type **(b)** irregular type

Figure 3.1.: Examples of fundamentally different tessellations

regularity. For instance, it is not practical to make use of a fine equidistant mesh in an application which covers different length scales. Inefficient use of resources, in computing power, or available memory put constraints on this approach. In such a situation, switching to irregular tessellations (fig. 3.1b) is beneficial, despite their increased complexity. Regular meshes are not explicitly addressed here furthermore, because each regular mesh can be considered as the specialization of an irregular one.

The Delaunay and the Voronoi tessellation, which are described in the following, represent two kinds of familiar irregular tessellations. Both rely on fundamental geometric considerations which are valid in any dimension of space. First, we introduce the tessellations by giving their general definition. Thereafter, we specialize to fixed dimensions (2D, 3D) and describe the algorithms and data-structures which have been applied in this work. This approach increases the level of abstraction, but it has been chosen in the hope that it will be more instructive.

3.1.1. Geometric convexity

As preparation, we introduce the concept of convexity. We identify a geometric object in $\mathbb{R}^n$ with the bounded sub-domain $\Omega \subset \mathbb{R}^n$. The object is termed convex, if — visually speaking — any two points $\boldsymbol{p}_1, \boldsymbol{p}_2 \in \Omega$ can be joined by a line segment which does not intersect the boundary of $\partial\Omega$ (fig. 3.2a). More formally, the line segment is defined by the point set

$$\mathrm{L}(\boldsymbol{p}_1, \boldsymbol{p}_2) := \{\boldsymbol{x} \in \mathbb{R}^n \,|\, \boldsymbol{x} = \lambda\, \boldsymbol{p}_1 + (1-\lambda)\, \boldsymbol{p}_2, \lambda \in \mathbb{R} : 0 \leq \lambda \leq 1\}$$

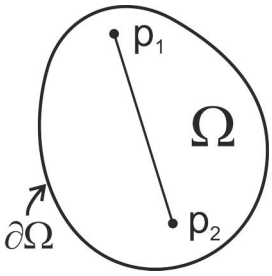

(a) Ω represents a plain convex domain.

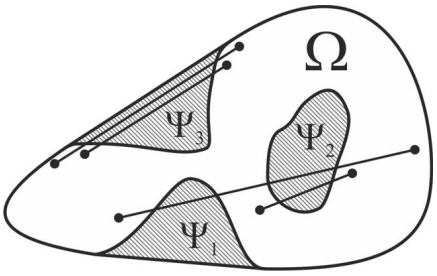

(b) The convex hull $\mathrm{CH}(\Omega) \equiv \Omega \cup \Psi_1 \cup \Psi_2 \cup \Psi_3$ denotes the smallest convex extension to Ω.

Figure 3.2.: Illustration of two simple convex sets

and we call Ω a convex set if

$$\mathrm{L}(\boldsymbol{p}_1, \boldsymbol{p}_2) \subset \Omega \,\forall\, \boldsymbol{p}_1, \boldsymbol{p}_2 \in \Omega \tag{3.1}$$

In particular, every line segment is by definition convex. This property turns out to be useful if we examine the intersection of two arbitrary convex sets Ω_1 and Ω_2. Let $\boldsymbol{p}_1, \boldsymbol{p}_2 \in \Omega_1 \cap \Omega_2$. In this case holds $\mathrm{L}(\boldsymbol{p}_1, \boldsymbol{p}_2) \subset \Omega_1$ as well as $\mathrm{L}(\boldsymbol{p}_1, \boldsymbol{p}_2) \subset \Omega_2$, and we conclude that the intersection $\Omega_1 \cap \Omega_2$ is a convex set because the finding holds in general for all included points.

What can we do about non-convex sets? — Suppose Ω to be non-convex and simply connected as it is shown in figure 3.2b. We look at the union of the line segments $\bigcup \mathrm{L}(\boldsymbol{p}_1, \boldsymbol{p}_2)$ with $\boldsymbol{p}_1, \boldsymbol{p}_2 \in \Omega$. The result is called the convex hull (CH). The hatched regions in figure 3.2b depict the part of $\mathrm{CH}(\Omega) \setminus \Omega$. In this view, $\mathrm{CH}(\Omega)$ describes the smallest convex extension. In a general definition, the convex hull is obtained by considering the intersection of all possible convex supersets X:

$$\mathrm{CH}(\Omega) := \bigcap_{\substack{\Omega \subseteq X \\ X \text{ convex}}} X \tag{3.2}$$

3.1.2. Properties of simplices

A special class of geometric objects which are identically equal to their convex hull are simplices. They are the geometric core elements by which the Delaunay tessellation is constructed. As we will see, they have some really interesting properties. Consider a set of $n+1$ points in n-dimensional space:

$$P := \{\boldsymbol{p}_0, \ldots, \boldsymbol{p}_n \mid \boldsymbol{p}_i \in \mathbb{R}^n \wedge \boldsymbol{p}_i \neq \boldsymbol{p}_j \,\forall\, i \neq j\}.$$

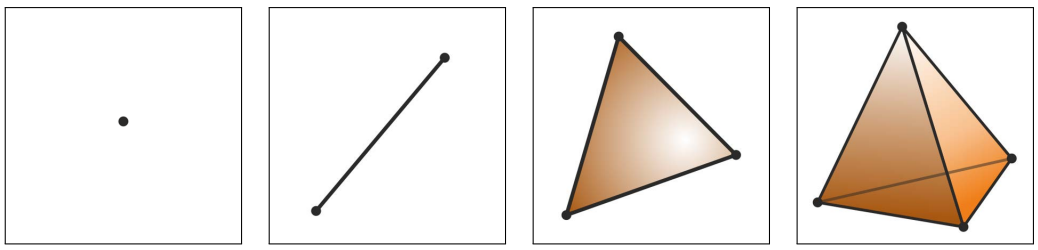

0-simplex: *point* | 1-simplex: *line segment* | 2-simplex: *triangle* | 3-simplex: *tetrahedron*

Figure 3.3.: Assorted types of simplices

If the points are affinely independent, a regular basis of the $\mathbb{R}^n$ may be derived. But here, we use P and define the n-simplex Δ^n as the domain which is spanned by the linear combinations

$$\Delta^n(P) := \left\{ \boldsymbol{x} \in \mathbb{R}^n \mid \boldsymbol{x} = \sum_{i=0}^{n} \lambda_i \boldsymbol{p}_i,\ 0 \leq \lambda_i \leq 1 \wedge \sum_{i=0}^{n} \lambda_i = 1 \right\} \tag{3.3}$$

A simplex represents the most simple kind of polytope (a generalization of a polygon to arbitrary space). The points $\boldsymbol{p}_i \in P$ define the vertices of the polytope. In figure 3.3 exemplary shapes of simplices in ordinary space are presented.

The boundary of the general n-simplex is composed of $(n-1)$-simplices. Their boundaries in turn are composed from $(n-2)$-simplices. Thus, any simplex consists of all $0-$ to $(n-1)$-dimensional types in a hierarchical order. This way, properties are inherited and also extend to higher dimensions in space. Particularly, the $(n-1)$-simplices are called facets and the $(n-2)$-simplices are called sub-facets or ridges.

Signed volume

The first presented property of simplices is an equation for the volume $V^n \in \mathbb{R}$. It may be easily computed by evaluating the determinant of the following matrix [Ste66]:

$$V^n(P) := \frac{1}{n!} \cdot \underbrace{\begin{vmatrix} p_{n,1} - p_{0,1} & \cdots & p_{1,1} - p_{0,1} \\ \vdots & \ddots & \vdots \\ p_{n,n} - p_{0,n} & \cdots & p_{1,n} - p_{0,n} \end{vmatrix}}_{n \times n} = \frac{1}{n!} \cdot \underbrace{\begin{vmatrix} p_{0,1} & \cdots & p_{0,n} & 1 \\ \vdots & \ddots & \vdots & \vdots \\ p_{n,1} & \cdots & p_{n,n} & 1 \end{vmatrix}}_{(n+1) \times (n+1)} \tag{3.4}$$

The sign of the determinant indicates a sense of direction. If the vertices $\boldsymbol{p}_0, \ldots, \boldsymbol{p}_n$ are given in counter-clockwise order, it is positive, it is negative for clockwise order, and, if the vertices are affinely dependent, V^n equals zero.

As an application, equation (3.4) can be used to determine orientation relationships in space. For example, the points $\boldsymbol{p}_0$ and $\boldsymbol{p}_1$ in figure 3.4 depict the vertices of a 1-simplex (a line segment). In combination with a third point, denoted by $\boldsymbol{x}$, a triangle is formed. With respect to the direction of the line segment, the position of $\boldsymbol{x}$ may be either *left* or *right* of the line depending on the sign of the determinant.

In general, the orientation test for any points $\boldsymbol{p}_0, \ldots, \boldsymbol{p}_{n-1} \in \mathbb{R}^n$ given in counter-

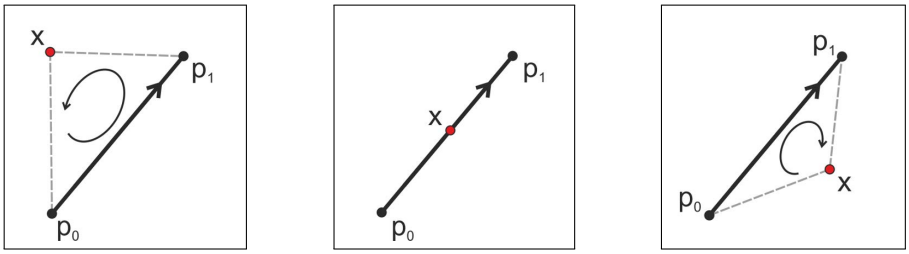

"left" of the line (> 0) degenerated ($= 0$) "right" of the line (< 0)

Figure 3.4.: Illustration of the orientation test considering a line segment and a point in 2D.

clockwise order with respect to a separate point $\boldsymbol{x} \in \mathbb{R}^n$ is declared as follows:

$$\text{Orient}(\boldsymbol{p}_0, \ldots, \boldsymbol{p}_{n-1}, \boldsymbol{x}) := \begin{vmatrix} p_{0,1} & \cdots & p_{0,n} & 1 \\ \vdots & \ddots & \vdots & \vdots \\ p_{n-1,1} & \cdots & p_{n-1,n} & 1 \\ x_1 & \cdots & x_n & 1 \end{vmatrix} = \begin{cases} < 0 \\ = 0 \\ > 0 \end{cases} \tag{3.5}$$

Circum-Hypersphere

A second property of simplices is the existence of the so called circum-hypersphere. Each simplex possesses a unique hypersphere (fig. 3.5). In 2D, this is the circum-circle of a triangle (fig. 3.5b). The centre $\boldsymbol{c} \in \mathbb{R}^n$ of the hypersphere is computed from the requirement that the euclidian distances $|\boldsymbol{p}_i - \boldsymbol{c}|$ to each of the vertices must be necessarily equal. This approach results in a system of n linear equations:

$$\begin{pmatrix} p_{1,1} - p_{0,n} & \cdots & p_{1,n} - p_{0,n} \\ \vdots & \ddots & \vdots \\ p_{n,1} - p_{n,n} & \cdots & p_{n,n} - p_{0,n} \end{pmatrix} \cdot \begin{pmatrix} c_1 \\ \vdots \\ c_n \end{pmatrix} = \frac{1}{2} \cdot \begin{pmatrix} \sum_{i=1}^{n} \left(p_{1,i}^2 - p_{0,i}^2 \right) \\ \vdots \\ \sum_{i=1}^{n} \left(p_{n,i}^2 - p_{0,i}^2 \right) \end{pmatrix} \tag{3.6}$$

With the solution for the center, the circum-radius $r \in \mathbb{R}$ directly becomes

$$r = \sqrt{(\boldsymbol{p}_j - \boldsymbol{c})^2} \quad (0 \leq j \leq n)$$

Again, we can apply this finding and define a geometric test. In this case, the position of $\boldsymbol{x} \in \mathbb{R}^n$ in terms of *inside* or *outside* shall be determined. This so called in-sphere-test is an essential subroutine in algorithms for computing the Delaunay tessellation. In an easy implementation, the test is enabled by the comparison of the distance $|\boldsymbol{x} - \boldsymbol{c}|$ with the circum-radius. However, therefore equation (3.6) must

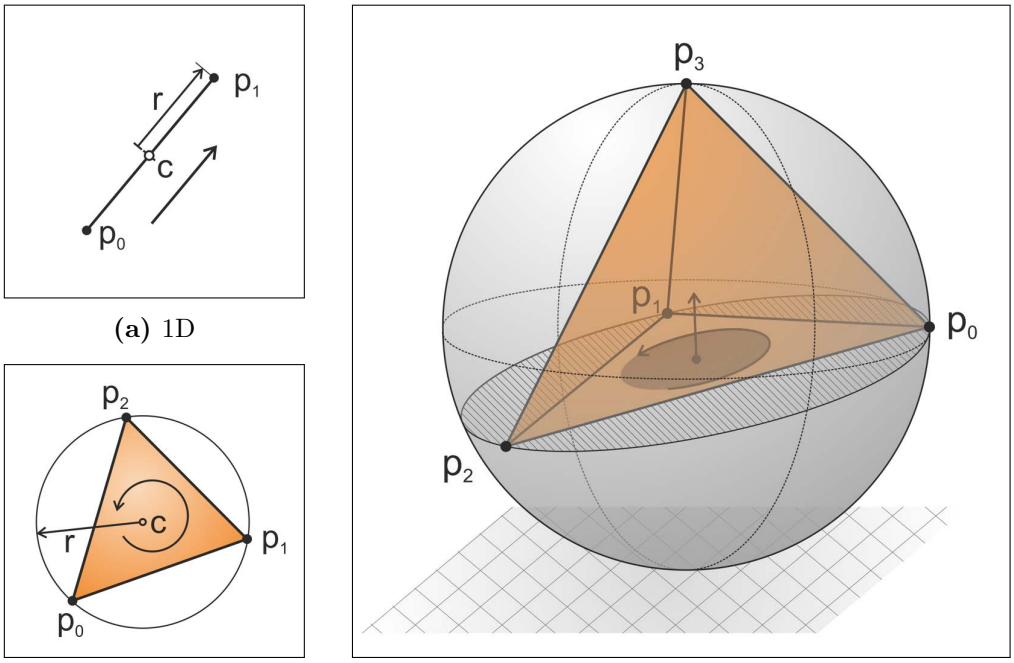

(a) 1D **(b)** 2D **(c)** 3D

Figure 3.5.: Example of the circum-hypersphere about a simplex in one, two, and three dimensions.

be solved, which is expensive to compute. In contrast, an efficient alternative is enabled by treating the problem in $\mathbb{R}^{n+1}$. For this purpose, we make use of the following so called "lift-up"-transformation:

$$\boldsymbol{p}^* : \boldsymbol{p} \in \mathbb{R}^n \mapsto \boldsymbol{p}^*(\boldsymbol{p}) := \left(p_1, \ldots, p_n, \sum_{i=1}^{n} p_i^2 \right)^\top \subset \mathbb{R}^{n+1} \tag{3.7}$$

The transformation is convex. All points of the $\mathbb{R}^n$ are mapped into a hyper-paraboloidal sub-domain of the $\mathbb{R}^{n+1}$.

For the sake of simplicity, we demonstrate the effect for the 1D case in the following. The 1-simplex is the line segment with the endpoints $p_1, p_2 \in \mathbb{R}$. The domain of the circum-hypersphere is simply the interval $[p_1, p_2]$ with the centre at $(p_1 + p_2)/2$. The circum-radius is $|(p_2 - p_1)/2|$. As a prerequisite, we demand the vertices to be given in clockwise orientation. In 1D this is equivalent to the condition $p_1 \leq p_2$. The mapping (eqn. 3.7) describes a parabola in 2D: $\boldsymbol{p}^*(p) = (p, p^2)^\top$. Now, we introduce the test point $x \in \mathbb{R}$. Without limiting the generality, we shift coordinates so that the position is fixed at the minimum of the parabola (see fig. 3.6). We see that the three points $\boldsymbol{p}^*(p_1)$, $\boldsymbol{p}^*(p_2)$, and $\boldsymbol{p}^*(x)$ form a 2-simplex

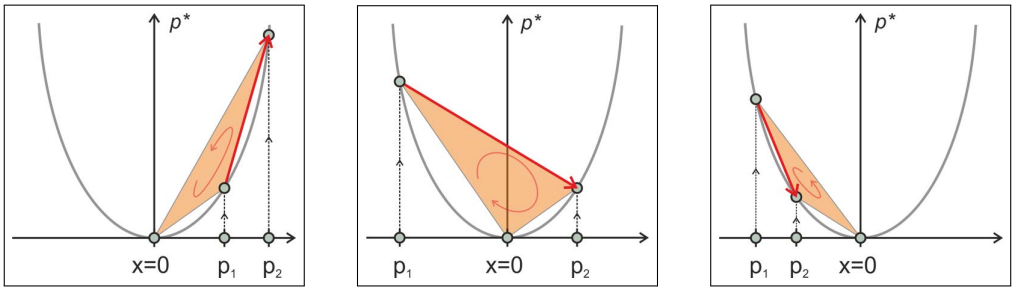

$\boldsymbol{x} < \boldsymbol{p}_1 < \boldsymbol{p}_2$ $\quad$ $\boldsymbol{p}_1 < \boldsymbol{x} < \boldsymbol{p}_2$ $\quad$ $\boldsymbol{p}_1 < \boldsymbol{p}_2 < \boldsymbol{x}$

Figure 3.6.: Example of the application of the lift-up transformation to 1D points. Mapped points are located on a parabola in 2D.

(a triangle). Also we notice that the orientation of the simplex is counter-clockwise if $x \notin [p_1, p_2]$, else it is clockwise. The degenerate case with $x = p_1$ or $x = p_2$ is not addressed. However, we already came across the analog relations when we discussed the orientation test (eqn. 3.5). Here, we will adapt the same consideration.

For the general case of the in-sphere-test, we demand the points $\boldsymbol{p}_0, \ldots, \boldsymbol{p}_n$ to be in *counter-clockwise* order. Then, we declare the test condition for the location of the extra point $\boldsymbol{x}$ with regard to the circum-hypersphere in the following way:

$$\text{InSphere}(\boldsymbol{p}_0, \ldots, \boldsymbol{p}_n, \boldsymbol{x}) := \underbrace{\begin{vmatrix} p_{0,1} & \cdots & p_{0,n} & \sum_{i=1}^{n} p_{0,i}^2 & 1 \\ \vdots & \ddots & \vdots & \vdots & \vdots \\ p_{n,1} & \cdots & p_{n,n} & \sum_{i=1}^{n} p_{n,i}^2 & 1 \\ x_1 & \cdots & x_n & \sum_{i=1}^{n} x_i^2 & 1 \end{vmatrix}}_{(n+2)\times(n+2)} = \begin{cases} < 0 \\ = 0 \\ > 0 \end{cases} \tag{3.8}$$

Thus, instead of solving a linear system of equations and conducting a comparison for the distance $|\boldsymbol{x} - \boldsymbol{c}|$, it is sufficient to compute the sign of the respective determinant.

Local coordinates

When we introduced the simplices, it was mentioned that a regular basis of the $\mathbb{R}^n$ may be derived from their vertices. A particularly useful representation is thereby enabled by barycentric coordinates. They are addressed here shortly as they will be used in a later part of this work as means for interpolation.

Consider a point $\boldsymbol{q} \in \mathbb{R}^n$ and a simplex $\triangle^n(P)$. The barycentric coordinates of $\boldsymbol{q}$ with respect to the vertices in P are obtained like this: At first, n new simplices $\Delta^n(\tilde{P}_i)$ are constructed from the vertices in P by consecutively replacing one vertex

$\boldsymbol{p}_i \in P$ after the other with $\boldsymbol{q}$. In a second step, the new coordinates are determined straight forward from the volume ratio:

$$\lambda_i := \frac{V^n(\tilde{P}_i)}{V^n(P)} \quad (1 \leq i \leq n) \tag{3.9}$$

The case with $\boldsymbol{q} \in \Delta^n(P)$ is of special interest, because then the newly assembled simplices represent a disjoint partition

$$\Delta^n(P) \equiv \bigcup_{i=1}^{n} \Delta^n(\tilde{P}_i)$$

with

$$[\Delta^n(\tilde{P}_i) \setminus \partial\Delta^n(\tilde{P}_i)] \cap [\Delta^n(\tilde{P}_j) \setminus \partial\Delta^n(\tilde{P}_j)] = \emptyset \quad \forall\, i \neq j$$

Accordingly, the components of the transformed coordinates form a partition of unity, $\sum \lambda_i = 1$, and are constrained to the interval $[0, 1]$.

3.1.3. Delaunay tessellation

For a preset distribution of M non-coinciding points

$$G := \left\{ \boldsymbol{p}_1, \ldots, \boldsymbol{p}_M \,|\, \boldsymbol{p}_i \neq \boldsymbol{p}_j \,\forall\, i \neq j \wedge M \geq n+1 \right\} \subset \mathbb{R}^n \tag{3.10}$$

a set of n-simplices

$$\tilde{\Delta}(G) := \{\Delta^n(G_1), \ldots, \Delta^n(G_N) \mid G_i \subset G\}$$

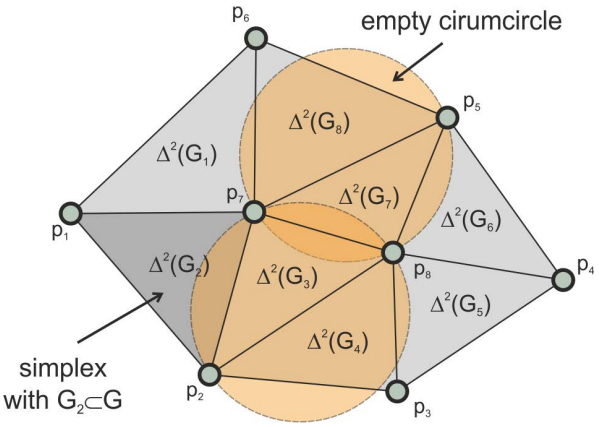

Figure 3.7.: Example of the Delaunay tessellation which has been constructed from $G = \{\boldsymbol{p}_1, \ldots, \boldsymbol{p}_8\} \subset \mathbb{R}^2$.

with pairwise disjoint interior

$$[\Delta^n(G_i) \setminus \partial\Delta^n(G_i)] \cap [\Delta^n(G_j) \setminus \partial\Delta^n(G_j)] = \emptyset \quad \forall\, i \neq j$$

is constructed (fig. 3.7). Such a set is called the Delaunay tessellation $\mathcal{DT}(G)$[1] if it meets the following two requirements:

- For any simplex $\Delta^n(G_i) \in \tilde{\Delta}(G)$ no additional points of $G \setminus G_i$ are included in the circum-hypersphere.

- The spanned space is convex such that $\mathrm{CH}(G) \equiv \bigcup \tilde{\Delta}(G)$.

The first property is called the empty circum-hypersphere criterion. A simplex $\Delta^n(G_i)$ is called to be "Delaunay" if it has an empty circum-hypersphere. In the degenerate case of the Delaunay tessellation, more than $n+1$ points are located exactly on a single circum-hypersphere which makes the partition ambiguous (fig. 3.8). But apart from this exception, the Delaunay tessellation represents a unique partition of $\mathrm{CH}(G)$. The points in G are called the generator points. From the inversion of the second property follows that the boundary of the convex hull can always be decomposed into $(n-1)$-simplices.

In this regard, an interesting connection exists between $\mathcal{DT}(G)$ and the facets of the convex hull $\mathrm{CH}(G^*)$ of the lifted set of generators. Figure 3.9 shows the Delaunay tessellation and the associated lift-up transformation of a point set in 2D. All points $G^*(G)$ are located on the boundary of the paraboloid with $z \geq 0$ (eqn. 3.7). Due to the downward convex property of G^*, the mapped points constitute the convex hull in 3D. The orthographic projection of the facets of $\mathrm{CH}(G^*)$ to the basic $x-y$ plane results in $\mathcal{DT}(G)$.

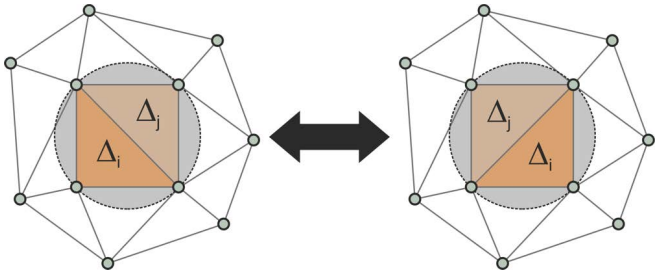

Figure 3.8.: Ambiguous case of the Delaunay triangulation with four points located on a circum-circle.

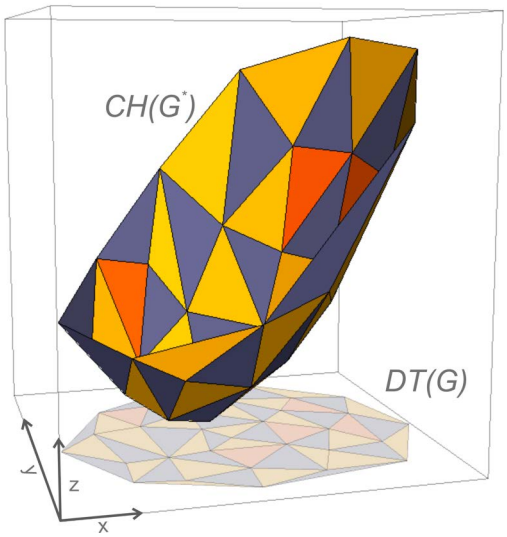

Figure 3.9.: Example of the lift-up transformation in 2D. The projection of $CH(G^*)$ to the $x-y$ base plane depicts the Delaunay tessellation $\mathcal{DT}(G)$.

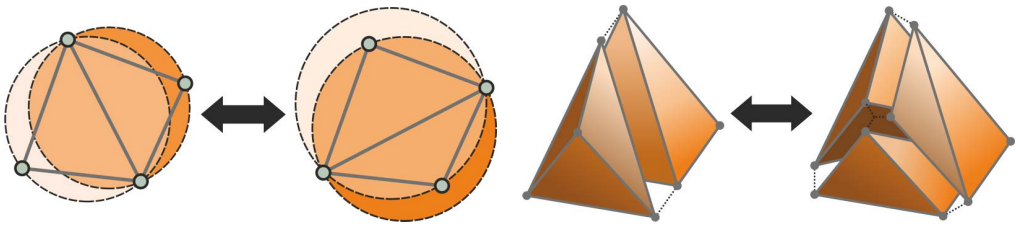

(a) edge flip in 2D

(b) example for a bistellar flip in 3D (type $2 \leftrightarrow 3$)

Figure 3.10.: Modification of the Delaunay tessellation by flipping: (a) Triangles on the left-hand-side are Delaunay whereas those on the right hand site are not. (b) The analogous transformation in 3D changes in addition the number of tetrahedra.

Construction

Special algorithms for the construction of the Delaunay tessellation have been developed [For86; GKS92; Ber+08]. The brute-force approach is based on the observation that the boundary $\partial\mathrm{CH}(G)$ is necessarily equivalent to $\partial\mathcal{DT}(G)$ and that the number of possible partitions is limited. Therefore, any partition $\tilde{\Delta}(G) \neq \mathcal{DT}(G)$ can be switched by a finite sequence of simple transformations until it becomes a Delaunay tessellation. In 2D, this is enabled by the application of edge flips to the triangles. The analogous transformations in 3D are bistellar flips (fig. 3.10). Clearly, the brute-force approach is only feasible for small generator sets as otherwise the

[1] In 2D, the tessellation represents a triangulation. For this reason, the synonymous naming "Delaunay triangulation" is more popular in this context. Accordingly, the naming "Delaunay tetrahedralization" is used for the 3D case.

number of possible combinations, which must be tested, gets too large.

A sophisticated algorithm, which elegantly circumvents this problem, has been introduced by Bowyer and Watson [Bow81; Wat81]. In this approach, the generator points are consecutively inserted into an already pre-existing tessellation $\mathcal{DT}(\tilde{G} \subset G)$. Subsequent to the insertion step, the tessellation gets refined until the "delaunayness" has been recovered. In detail, the following sequence of tasks is processed (fig. 3.11) [She12]:

- An additional point is added to the tessellation. A search for the simplex which contains the new point is conducted. Due to the additional point, this simplex is marked as invalid (fig. 3.11a).
- A *breadth-first search*[2] on adjacent simplices is performed and the InSphere-test is applied to each candidate. Additional invalid simplices are collected (fig. 3.11b).
- All invalid simplices are removed from the tessellation and a cavity is created (fig. 3.11c).
- For any facet of the cavity, a new simplex is constructed by joining the respective vertices with the newly inserted point. In this way, the cavity is filled with new simplices (fig. 3.11d).
- Continue with the first step until all points have been inserted ...

If no initial tessellation is present, a super-simplex is initially constructed which completely encloses all points in G. It acts as seed for the algorithm and will be removed in a clean-up step after finishing the insertion.

The Bowyer-Watson algorithm effectively takes advantage of the only locally confined changes to the tessellation which are processed. This way, an optimal run-time complexity of $\mathcal{O}(n \log n)$ is enabled. In this work on APT simulation, an implementation of the Bowyer-Watson algorithm provided by Hang Si's TetGen-package [Si11] applies for the mesh generation.

In practice, hard to fight difficulties emerge in computational geometry from the inaccuracies of the floating point arithmetic in modern computer systems. In the context of the Delaunay tessellation, the sign of the determinants in the Orient- and InSphere-tests becomes highly sensitive to implicit rounding errors. Such errors occur, when for almost coplanar vertices the absolute value approaches zero.

[2] Adjacent neighbours will be recursively inspected.

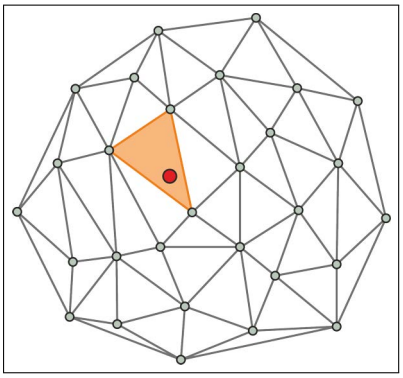

(a) Find enclosing simplex for the new point.

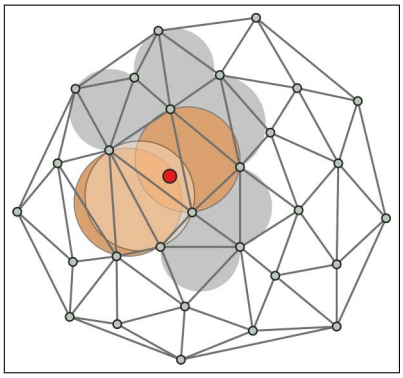

(b) Breadth-first search for invalid simplices.

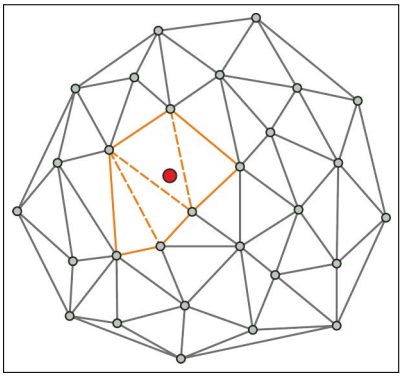

(c) Formation of a cavity.

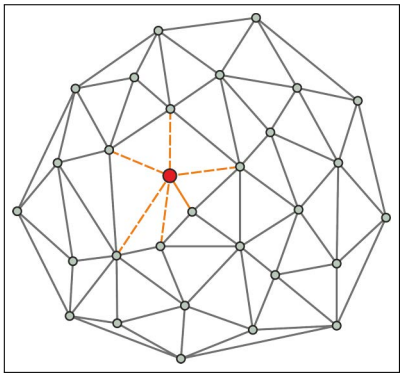

(d) Triangulation of the cavity.

Figure 3.11.: Description of the Bowyer-Watson algorithm

For this reason, a numerically robust implementation of these tests, provided by Shewchuck [She97] has been applied.

Data structure

As we have seen before, the tessellation can be incrementally constructed based on the Bowyer-Watson algorithm. But besides an efficient assembly, the use of an appropriate data structure for storing and accessing the tessellation is at least equally important. Before we describe the storage concept, let us briefly consider possible data requests of more elaborated algorithms operating on the Delaunay tessellation. This will help to get an impression of the requirements in effective data organization:

- *Effective look-up routines for generator points are required.*

For a given generator point, we want to find its next neighbour points and any incident simplices efficiently. With "neighbour points" we mean neighbourhood in the sense of the Delaunay tessellation, which is different from spatial neighbourhood: Any generator which is joined by a common edge with another point is termed a "natural" neighbour. E.g. all vertices in a simplex are mutually natural neighbours. The task to find the full set of natural neighbours of a selected generator is therefore equivalent to the problem of finding all simplices with that generator as common vertex. Higher order neighbourhoods are analog. They can be accessed by examining respective simplices recursively.

- *Routines for obtaining adjacent simplices are required.*

  The spatial alignment of simplices is a basic characteristic of the tessellation. Adjacent simplices should be easily obtained. At the same time, shared facets, edges, and vertices should be easily recognized.

- *Information on the boundary (of the convex hull) must be supplied.*

- *Runtime complexity of the algorithms and memory consumption of the data structures should be within acceptable limits.*

  Because we intend to deal with tessellations which are constructed from millions of points and which in turn form simplices, facets and edges, the administrative overhead (e.g. by internal references, pointers, index tables etc.) should be kept to a minimum.

Keeping this requirements in mind, the Delaunay tessellation may be managed based on an astonishingly minimalist approach. All needed information is stored using two kinds of lists: The first one contains the set of generators (fig. 3.12a), the second one is for administrative information regarding the simplices and their contiguity (fig. 3.12b). In the following description, we will specialize to 3D, but there is no reason why the same approach should not be equally efficient in any other dimension; e.g. figure 3.12 shows the application to 2D.

In 3D, the Delaunay tessellation becomes a tetrahedralization. The data records in the first list are termed *node data* and records of the latter *tetrahedron data*. The *node data* record consists of the (x, y, z)-coordinates of the generator points. In addition, we supply a boundary marker indicating if the generator is part of the convex hull or not. Furthermore, a reference, which links the generator to an arbitrary tetrahedron that contains this generator as a vertex, is used. This reference

(a) *node data* list

#	coordinates	boundary	triangle
0	(x_0, y_0)	✓	C
⋮	⋮	⋮	⋮
2	(x_2, y_2)	□	⋮
3	(x_3, y_3)	✓	⋮
⋮	⋮	⋮	⋮
10	(x_{10}, y_{10})	✓	L

(b) *triangle data* list

#	vertices	neighbours
A	(4,3,2)	(B,G,∅)
B	(0,2,3)	(A,∅,C)
⋮	⋮	⋮
E	(2,9,6)	(J,F,D)
⋮	⋮	⋮
L	(9,1,10)	(∅,K,D)

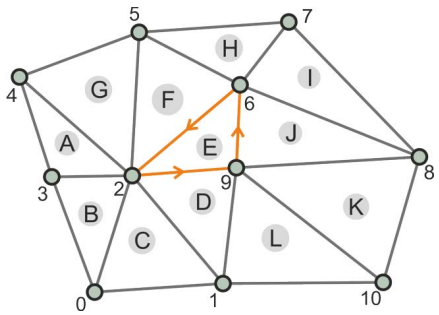

(c) related 2D topology

Figure 3.12.: Data structure used for representing Delaunay tessellations. The numeric administration is based on two plain lists (a,b). Depicted data refers to the exemplary Delaunay triangulation plotted in (c).

is not strictly mandatory but helps to speed-up respective look-ups. Alternatively, the point location routine, which is described in the subsequent section, might be applied instead. This way, an increase in runtime costs would be balanced by lower memory consumption.

Remarkably, all the essential information about the tetrahedra can be stored in the *tetrahedron data* records by using two quadruples of references. The first quadruple depicts the vertices of a tetrahedron. It consists of four links to *node data* elements. Implicitly, we demand the vertices to be given in counter-clockwise order (see sec. 3.1.2). The second quadruple points to those four *tetrahedron data* elements of the adjacent tetrahedra. As before for the *node data*, a fixed order is established: We take advantage of the condition that two adjacent tetrahedra share a common facet which is defined by three common vertices. Vice versa, one vertex in both tetrahedra is not part of the common facet. This relation mutually exists for all vertices. Therefore, we can make use of the position of the respective "unbound" vertex in the first quadruple (of vertices) and use the same position in the second quadruple (of adjacent tetrahedra) for the reference to the respective

adjacent tetrahedron.[3] If a facet is part of the boundary of the convex hull, there is no adjacent tetrahedron. We indicate this condition by assigning an *invalid* reference value ("∅" in tab. 3.12b).

The complete data structure reflects a direct approach for an efficient treatment of all the required information. The topology of the Delaunay tessellation is essentially maintained by making use of implicit rules which have been derived from the basic orientation test (eqn. 3.5). This reduces computing effort and saves memory.

Finally, we come back to the initially declared requirements and give a short outline how to retrieve the requested information:

- The set of natural neighbours of a given generator is obtained by applying a breadth-first search on the simplices: all the neighbours of an initial simplex containing the depicted generator are successively inspected for having the same generator as a vertex. The search is extended to the next neighbouring simplices as long as they still contain the demanded generator. In a second step, the vertices are extracted from the obtained simplices. Duplicates will be ignored.

- Adjacent simplices are directly referenced in the data structure. Therefore, they are easily accessible.

- Boundary points are labeled using a positive boundary marker. Facets of the convex hull are obtained by looking for simplices with an *invalid* neighbour reference entry.

- Memory consumption is comparably low and grows proportionally with the number of generators and simplices.

Delaunay walk algorithm

The proposed storage structure is also beneficial when we encounter the need to locate a specific simplex in the Delaunay tessellation. Initially, only the position of a query point $\boldsymbol{x} \in \mathbb{R}^n$ is known and we want to obtain the distinguished simplex which includes this point. The problem can be solved efficiently by performing a directed walk on the simplices of the tessellation [GS78; DMZ98].

[3] The triangle labeled E in table 3.12b and figure 3.12c is adjacent to the three triangles J, F, and D. The common facet between E and J is the line segment $\overline{9,6}$. The "unbound" vertex is 2. This vertex is placed first in the triplet of vertices. Therefore, the reference to J becomes placed first in the triplet of adjacent triangles etc.

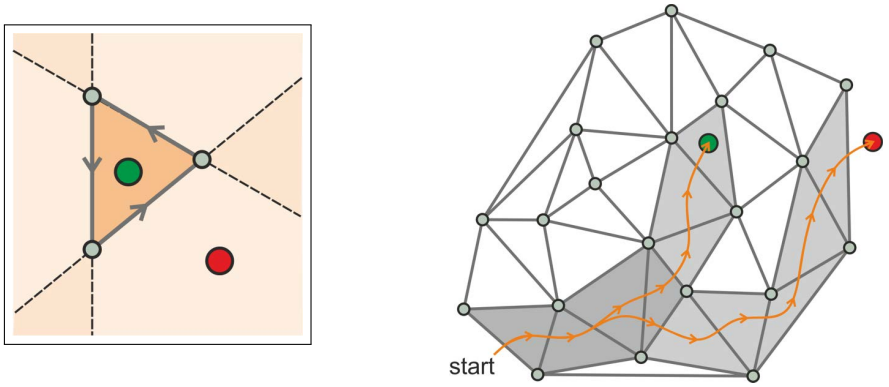

(a) A point is located inside the triangle only if the position is on the same side of all edges.

(b) Application: location of the enclosing triangle by a series of directed jumps in the triangle mesh for two different query points.

Figure 3.13.: Operation of the Delaunay walk algorithm in 2D

In order to illustrate the basic idea, we first consider the most simple situation with only one single simplex. Clearly, only two results for the position are possible: either $\boldsymbol{x}$ is located inside or it is located outside the simplex. — So, where is it? The answer is determined straight-forward from a series of orientation tests (eqn. 3.5) applied to the present facets of the simplex and the query point. If it happens that the position of $\boldsymbol{x}$ is located on different sides of the facets, the query point is located outside; otherwise, it must be inside the simplex (fig. 3.13a depicts an example in 2D).

This finding extends to a network of Delaunay simplices. Whenever the location-test for $\boldsymbol{x}$ indicates that the position is not inside the examined simplex, we continue by selecting the adjacent simplex opposite to the actually fail tested facet. Because every facet divides the space into two bisectors — one which is containing $\boldsymbol{x}$ and one which does not — the newly selected simplex will be in any case a better candidate.

In this way, a directed walk in the network of simplices is conducted until, finally, the only simplex which includes $\boldsymbol{x}$ is found. If the query point is not included in the convex hull of the Delaunay tessellation, the walk will leave the tessellation. An example of the detailed approach is illustrated in figure 3.13b. The needed information about the next adjacent simplices is directly supplied by the *simplex data* structure which facilitates a fast traversal with a minimum of computational costs.

Basically, the origin for the walk can be arbitrarily chosen. However, significant time may be saved if the walk distance is shortened by providing a suitable guess for a starting simplex. If no particular information is available, an effective guess

is obtained from a random sample of the present simplices. For this, the vertex distances of the sampled simplices to the query points are evaluated. In 3D, this combined approach runs with $\mathcal{O}(n^{1/4})$ expected time for the search, where n denotes the number of generators in the tessellation [MSZ99].

3.1.4. Voronoi tessellation

Based on the same set of generator points, the Voronoi tessellation is closely related to the Delaunay tessellation. But contrary to the construction of simplices with several generators as vertices, well-defined sub-domains of the underlying space are assigned to each generator point. For any $\boldsymbol{p}_i \in G$ the domain is termed the Voronoi cell denoted by $\mathcal{V}(\boldsymbol{p}_i)$. Formally, such a cell may be constructed by the successive intersection of half-spaces which are determined by $\boldsymbol{p}_i$ in combination with each of the remaining points $\boldsymbol{p}_j \in G \setminus \{\boldsymbol{p}_i\}$. Vividly, $\mathcal{V}(\boldsymbol{p}_i)$ includes all those points in space which are closer to $\boldsymbol{p}_i$ than to any other generator point:

$$\begin{aligned} \mathcal{V}(\boldsymbol{p}_i) &:= \bigcap_{j \neq i} \{\boldsymbol{x} \in \mathbb{R}^n : |\boldsymbol{x} - \boldsymbol{p}_i| \leq |\boldsymbol{x} - \boldsymbol{p}_j|\} \\ &= \{\boldsymbol{x} \in \mathbb{R}^n : |\boldsymbol{x} - \boldsymbol{p}_i| \leq |\boldsymbol{x} - \boldsymbol{p}_j| \; \forall j \neq i\} \end{aligned} \tag{3.11}$$

Having in mind what we have said about the intersection of convex domains, it is clear that every Voronoi cell is always a convex polytope. However, a Voronoi cell is not necessarily constrained. It may be infinite in space. In particular holds

$$[\mathcal{V}(\boldsymbol{p}_i) \setminus \partial\mathcal{V}(\boldsymbol{p}_i)] \cap \left[\mathcal{V}(\boldsymbol{p}_j) \setminus \partial\mathcal{V}(\boldsymbol{p}_j)\right] = \emptyset$$

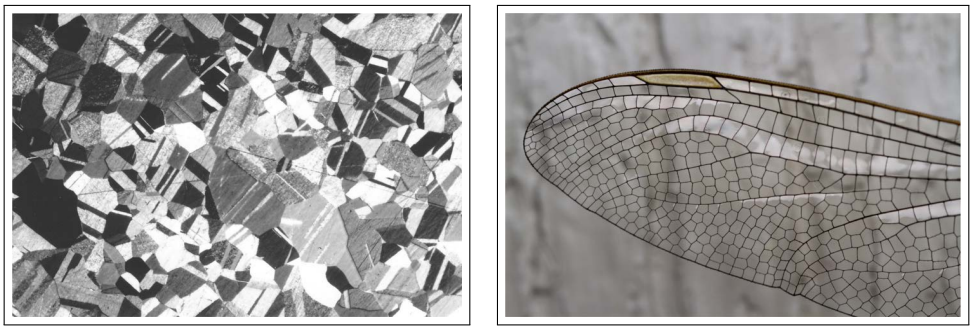

(a) Microscopic grains (and twins) in polycrystalline brass

(b) Detailed wing structure of a dragon fly (Courtesy of S. Begin [Beg13])

Figure 3.14.: Examples for the occurrence of Voronoi patterns in nature

for the interior of any disparate cells $\mathcal{V}(\boldsymbol{p}_i)$ and $\mathcal{V}(\boldsymbol{p}_j)$ so that the set of unbounded Voronoi cells forms a partition. This leads us to define the Voronoi tessellation $\mathcal{VT}(G)$ analogously to the Delaunay tessellation by

$$\mathcal{VT}(G) := \bigcup_{\boldsymbol{p}_i \in G} V(\boldsymbol{p}_i) \equiv \mathbb{R}^n \tag{3.12}$$

Reviewing the literature, it seems that the Voronoi tessellation has been reinvented independently several times in the past because there exist so many synonyms. In physics, the tessellation is known as Wigner-Seitz cell partition, other terms are Dirichlet tessellation or, constrained to 2D and with application in metrology, Thiessen polygons. Generally, the specialization to 2D is called "Voronoi diagram". Whatever name is used, the partition obviously reflects common principles for pattern formation. For this reason, we face Voronoi tessellations in many different contexts in everyday life. Particularly, structures, which are the result of self-organized growth processes in nature, show often a (microscopic) texture similar to Voronoi patterns (fig. 3.14).

Geometric dual relation to the Delaunay tessellation

An important property of the Voronoi tessellation is its close relationship to the Delaunay tessellation: The Delaunay tessellation is the geometric dual graph of the Voronoi tessellation. Geometric properties of one tessellation are opposite or related to similar properties in the other one. For instance, if we look at a vertex of a Voronoi cell, we recognize that it represents the centre of a circum-hypersphere which is associated to a simplex of the Delaunay tessellation. A not fully exhaustive

Table 3.1.: Interrelation of geometric elements in the Delaunay tessellation $\mathcal{DT}(G)$ with their analogons in the Voronoi tessellation $\mathcal{VT}(G)$. It is assumed that both are constructed from the same set of generators $G \subset \mathbb{R}^n$.

category	$\mathcal{DT}(\mathbf{G})$	$\mathcal{VT}(\mathbf{G})$
covered domain	convex hull	infinite space
basic objects	simplices	convex polytopes
hierarchic order of geometric related objects	n-simplex	Voronoi vertex (0-polytope)
	$(n-1)$-simplex	Voronoi edge (1-polytope)
	$(n-2)$-simplex	Voronoi facet (2-polytope)
	$\vdots$	$\vdots$
	0-simplex	Voronoi cell (n-polytope)

overview of the existing relations is presented in table 3.1.[4]

The duality extends to surprising details of the present geometry, although this is not obvious at first glance: As we already have explained in section 3.1.3, the Delaunay tessellation is ambiguous if there are more than n coincident points on a circum-hypersphere. If this happens, we expect this should have some effect to the Voronoi tessellation. But astonishingly, the Voronoi tessellation remains a unique partition in any case. Instead, the ambiguity of the Delaunay tessellation effects the Voronoi tessellation in the way that degenerate n-polytopes are constructed, e.g. the polygonal facet of a cell becomes an edge or even a point. An illustration for this case is shown in figure 3.15. Depicted are the Voronoi and Delaunay tessellations for a set of four generator points. Generators are denoted by circles, Voronoi vertices are squares, respectively. The downright point is moving from inside the inscribed circum-circle to the outside: in frame (1), we have a Voronoi edge aligned perpendicular to the dashed auxiliary line. In frames (2) and (3), the downright generator crosses the circle. The Delaunay tessellation becomes ambiguous in this situation. The considered Voronoi edge degenerates to a point. Finally, in frame (4) the edge appears again, but this time, the orientation changed and it is aligned parallel to the auxiliary line. Accordingly, the triangles in the Delaunay tessellation have flipped their edges.

Recipe for the construction of Voronoi cells in 3D space

A practical benefit of the dual relation is that it may be utilized to construct the Delaunay from the Voronoi tessellation and vice versa. As we have seen, effective

[4] An annotated example of the 2D Voronoi tessellation is shown in fig. 3.16, p. 53. In 2D, Voronoi cells are 2-polytopes (polygons) and the related dual elements are 2-simplices (triangles).

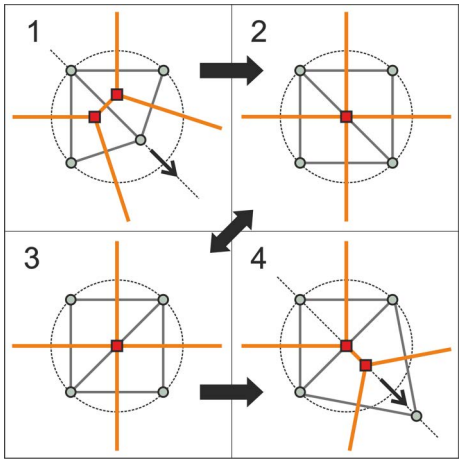

Figure 3.15.: Degeneration of a Voronoi edge. Disc symbols depict generator points (vertices) of the Delaunay tessellation, square symbols vertices of the Voronoi tessellation, respectively. In (1), the bottom right vertex of the Delaunay tessellation is inside the inscribed circum-circle. (2)-(4) show the changes in both tessellations if the vertex moves outward and crosses the circum-circle (see text for details).

data structures and algorithms already exist for dealing with the Delaunay tessellation. Therefore, we expect only little extra effort if these can be reused for the construction of the Voronoi tessellation as well.

Subsequently, we will describe an algorithm which is able to obtain a Voronoi cell from the Delaunay tessellation in 3D. But first, we take a step backwards in order to describe the basic idea in 2D. Here, Voronoi cells have simply the shape of convex polygons (fig. 3.16). We can distinguish two different cases: either the polygon is bounded and has a finite area or it is unbounded with infinite area. The latter is always the case if the generator point of the Voronoi cell is located on the convex hull. In the algorithmic approach, each polygon represents itself by an ordered list of Voronoi vertices (as indicated by the arabic numbering in fig. 3.16). If the polygon is bounded, the start and end vertex in the list coincide. In the opposite case that they differ, we know that we are dealing with an unbounded polygon and additional information about the direction of the infinite edges of the respective Voronoi cell is needed. Now, we apply a trick: instead of the Voronoi vertices, the geometric dual elements of the Delaunay tessellation, references to simplices (tab. 3.1), will be stored in the list (labeled by latin numbers in fig. 3.16). Thus, the problem of finding the Voronoi vertices reduces to conduct a circular

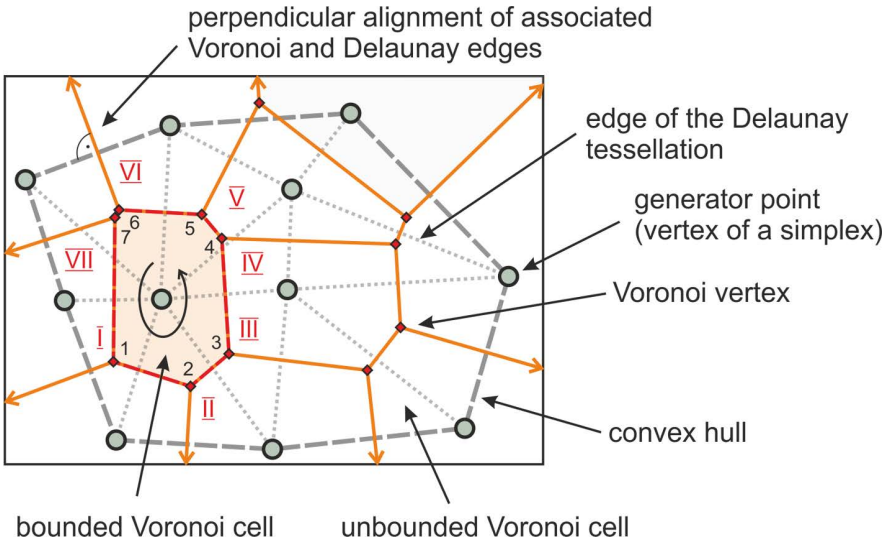

Figure 3.16.: Example of a 2D Voronoi tessellation: The polygonal domain of each bounded Voronoi cell is completely determined by the ordered sequence of Voronoi vertices (arabic numbering). Due to the geometric dual relation, equivalent use can be made of the corresponding simplices of the Delaunay tessellation (latin numbering). Infinite edges of unbounded Voronoi cells, as indicated by the arrows, are regarded by considering their orientation perpendicular on a line segment of the convex hull.

walk in the Delaunay triangulation about a single generator point. The complete functional algorithm writes as follows:

- We start at an arbitrary triangle which contains the given generator point. The respective reference will be the first entry in our list.
- Next, all adjacent triangles which also contain the generator point are examined counter-clockwise and the respective references are enqueued to the end of the list.
- The operation is stopped if we encounter again the triangle which is the first in the list. Then, we know that the Voronoi cell is bounded and we finish.
- If we detect that there is no further triangle present in counter-clockwise orientation (because the algorithm arrived at the boundary of the convex hull), we switch the search direction and look for adjacent triangles clockwise. Therefore, we start again at the first triangle, but this time, any additionally collected triangle is enqueued, each to the beginning of the list. Again, this process stops if a boundary facet has been reached.
- In the case that a simplex of an unbounded cell has been traced, the normal vector of the unbounded facets is computed and is additionally recorded.

Later, the actual coordinates of the Voronoi vertices are calculated at runtime by evaluating the circum-center of the respective simplices (eqn. 3.6).

For 3D, we can adopt almost the same prescription using the same trick: The 3D Voronoi facets are convex polygons in a plane. From the dual relation (tab. 3.1) we know that the corresponding elements of the Delaunay tessellation are tetrahedra edges (line segments). Hence, we can construct each facet by selecting all those tetrahedra which have the same edge in common. Analog to 2D, an ordered sequence of the polygon vertices is obtained by conducting a circular walk about this common edge (fig. 3.17a). Coordinates of the Voronoi vertices are computed as the center of the circum-sphere about each tetrahedron. The Voronoi cell completely assembles from its facets if all incident edges to the generator point in the center are considered (fig. 3.17b). The necessary edges and by this the Voronoi facets are determined by the natural neighbour points of the generator (see p. 46).

If the considered generator point is located on the boundary of the convex hull, additional effort is needed to cope with the present infinite facets. The circular walk about the common edge is not closed in this case. The orientation of infinite

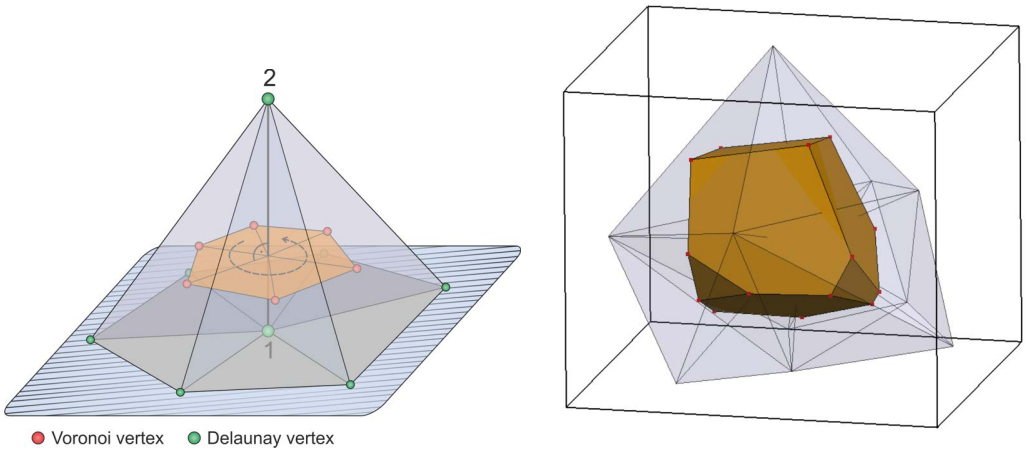

(a) Construction of the facets

(b) Completely assembled Voronoi cell and its defining tetrahedra.

Figure 3.17.: Construction of a Voronoi cell in 3D: (a) Each facet is a polygon and is constructed by inspecting all adjacent tetrahedra of the Delaunay tessellation which have an edge in common, e.g. like the edge $\overline{1,2}$ here. The vertices of the polygon are computed from the circum-center of the obtained tetrahedra. (b) The complete cell is assembled by taking account of all incident edges to the generator point in the center.

Voronoi edges is then defined by the normal vector of the respective tetrahedra facets (triangles) which constitute the convex hull.

Computing properties of the Voronoi cell in 3D space

Enabled by equation 3.4, we have seen that the volume of any n-simplex is easily computed from a determinant. For the application in the context of the numeric treatment of differential equations on the Voronoi mesh, we wish to have the equal ability for determining the volume and the surface area of Voronoi cells. Although the shape in 3D appears comparably complex, this task turns out to be easier than one might think because of the convex properties of the Voronoi tessellation.

The volume can be easily computed if we subdivide the Voronoi cell into a set of pyramids. Each pyramid is constructed from one facet of the Voronoi cell at the base and shares the tip with the remaining pyramids. The number of pyramids is equal to the number of Voronoi facets. In the case that the common tip is in the interior of the Voronoi cell, the set of pyramids represents a disjunct partition. Accounting to classic geometry, the volume of a pyramid amounts to one third the base area times the height of the pyramid. A particular easy access to the cell volume is therefore enabled if we choose the generator point of the Voronoi

cell, denoted by $\boldsymbol{p}_0$, as common tip for the pyramids, because, in this case, the height of the pyramids coincides with half the length of the Delaunay edges. The edges as well as the Voronoi facets are determined by the natural neighbour points $\boldsymbol{p}_1, \ldots, \boldsymbol{p}_N$ of the generator. Due to the dual relation, each Delaunay edge $\overline{\boldsymbol{p}_0, \boldsymbol{p}_i}$ is necessarily perpendicular to its associated Voronoi facet. Both intersect at the midpoint of the Delaunay edge. Thus, the volume of a single pyramid is given by:

$$V(\boldsymbol{p}_0, \boldsymbol{p}_i) = \frac{1}{3} \cdot A(\boldsymbol{p}_0, \boldsymbol{p}_i) \cdot \frac{|\boldsymbol{p}_0 - \boldsymbol{p}_i|}{2}.$$

Accordingly, the complete volume of the Voronoi cell yields

$$V(\boldsymbol{p}_0) = \frac{1}{6} \cdot \sum_{i=1}^{N} A(\boldsymbol{p}_0, \boldsymbol{p}_i) \cdot |\boldsymbol{p}_0 - \boldsymbol{p}_i| \tag{3.13}$$

and it only remains to retrieve the value of the facet area $A(\boldsymbol{p}_0, \boldsymbol{p}_i)$. That is again not too complicated because the Voronoi facets are convex as well. We simply adopt the same approach once more, except this time, the facets become subdivided into triangles. For each edge $(\boldsymbol{p}_0, \boldsymbol{p}_i)$, we denote the respective Voronoi vertices of the associated facet with $\{\boldsymbol{v}_1, \ldots, \boldsymbol{v}_N\} \in \mathbb{R}^3$ and use

$$\boldsymbol{c}_F := \frac{1}{N} \cdot \sum_{i=1}^{N} \boldsymbol{v}_i$$

as common center. The area then writes as[5]

$$A(\boldsymbol{p}_0, \boldsymbol{p}_i) := \frac{1}{2} \cdot \sum_{i=1}^{N} \left| (\boldsymbol{v}_{(i \bmod N)+1} - \boldsymbol{c}_F) \times (\boldsymbol{v}_i - \boldsymbol{c}_F) \right| \tag{3.14}$$

For Voronoi cells at the boundary, we set the volume directly to infinity. We do the same when we encounter an infinite facet.

3.2. Discrete solution of the Poisson equation in electrostatics

On the basis of the described geometric relations, two approaches for computing the numeric solution of the Poisson equation will be introduced. The first approach particularly applies to regular meshes, whereas the second approach depicts the

[5] By the modulo operator, the first Voronoi vertex is selected again if $i \equiv N$.

general case with application to an irregular mesh.

Under a *mesh* we understand here a preset distribution of non coincident points in space. We call each of these locations a node. In particular, we resume with the subject of the previous chapter and identify the set of nodes as the basis of a tessellation. To each node, a well-defined part of space is attributed which we term a *cell*. With regard to the Poisson equation, the mesh represents the necessary support on which the discrete approximation is obtained. The electric potential, different values for dielectricity, and charges become explicitly related to the nodes and cells in the considered types of meshes.

Although it is true that in general a regular mesh represents a specialization of the irregular one, we will soon see which subtle differences exist in the way the respective solution depicts the details of the considered geometry. E.g. electric interfaces are not equally considered in both meshes. For this reason, the derivations for both approaches are treated independently in two different sections.

In any case, the basic idea is to rewrite the continuous form of the governing equations into an analogous discrete form which remains valid if it is applied to an arbitrary network of nodes. The result is an implicit equation for the potential and a corresponding system of equations which accounts for all nodes in the mesh. The solution may be obtained either directly in the frame of the finite-element method (FEM) or asymptotically in the frame of the finite-difference method (FDM). Details of the latter method will be treated by the description of the implemented simulation models in the next chapter.

3.2.1. Basic electrostatics

Let us begin with a quick reminder to the macroscopic Maxwell equations which apply for the electrostatic condition and introduce the necessary basic definitions. Different material properties are explicitly taken into account. We express the electric field $\boldsymbol{E}$ by the electric displacement field $\boldsymbol{D}$. The respective relation is

$$\boldsymbol{D} = \epsilon_0 \epsilon_r \boldsymbol{E} \tag{3.15}$$

Permittivity of free space is denoted by ϵ_0 and relative dielectricity by ϵ_r. If we further denote the charge density with ρ, the first Maxwell equation becomes

$$\operatorname{div} \boldsymbol{D} = \rho \tag{3.16}$$

as the charge is the source of the field. The electrical field is conservative. This statement is expressed by the second Maxwell equation:

$$\operatorname{rot} \boldsymbol{E} = 0 \tag{3.17}$$

This latter equation implies the existence of the electric potential, which is defined by

$$\varphi(\boldsymbol{r}) := -\int_{\boldsymbol{r}_0}^{\boldsymbol{r}} \boldsymbol{E}(\boldsymbol{r}')\, d\boldsymbol{r}' \Leftrightarrow \boldsymbol{E}(\boldsymbol{r}) = -\operatorname{grad} \varphi(\boldsymbol{r}) \tag{3.18}$$

The Poisson equation expresses the dependence of the potential on the respective charge distribution. The equation results directly from the basic relations if we replace the field in equation (3.16) with the derivative of equation (3.18). As we want to keep the possibility of dealing with different charges and anisotropic dielectricity, we explicitly write here the general expression:

$$\operatorname{div} (\epsilon_r \operatorname{grad} \varphi) + \frac{\rho}{\epsilon_0} = 0 \tag{3.19}$$

Accordingly, we can apply the Gaussian law and integrate over the surface of a given volume in 3D. If we assume an isotropic charge density, the Poisson equation yields

$$\int_{\partial V} \epsilon_0 \epsilon_r \operatorname{grad} \varphi \; d\boldsymbol{A} + \rho \cdot V = 0 \tag{3.20}$$

Equation (3.20) is the basis for all the numeric treatment which will be described next. Apart from the inverted sign, the first term denotes the electric flux

$$\Psi := \int_{\partial V} \boldsymbol{D}\, d\boldsymbol{A} \tag{3.21}$$

and the second term the interior charge. We see that the Poisson equation is just a valuable expression for flux conservation.

We complete this part reminding to the contiguity conditions for the electric field and the displacement field at a dielectric interface. If we consider the general situation with arbitrary orientation of the fields with respect to the interface, it can be compiled of the two special cases of the field either aligned parallel or perpendicular. As it is illustrated in figure 3.18, the interface is described by different values for dielectricity on either side, denoted by $\epsilon_\uparrow$ and by $\epsilon_\downarrow$, respectively.

We first consider the inscribed Gaussian box and make use of equation (3.16).

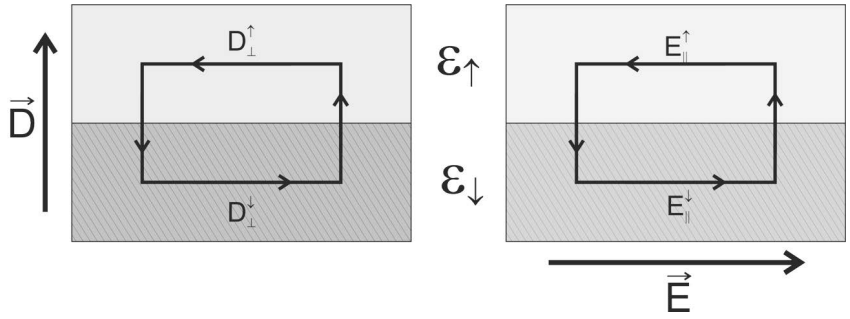

(a) perpendicular field **(b)** parallel field

Figure 3.18.: Contiguity conditions for the electric field $\boldsymbol{E}$ and displacement field $\boldsymbol{D}$ at a dielectric interface ($\epsilon_\uparrow \neq \epsilon_\downarrow$)

Integration over the box volume yields the surface integral

$$\oiint_{\partial V} \boldsymbol{D}\, d\boldsymbol{A} = 0$$

which we can easily evaluate (fig. 3.18a) to the requirement

$$\boldsymbol{D}_\uparrow^\perp = \boldsymbol{D}_\downarrow^\perp \quad \wedge \quad \boldsymbol{E}_\uparrow^\perp \epsilon_\uparrow = \boldsymbol{E}_\downarrow^\perp \epsilon_\downarrow \tag{3.22}$$

for the contiguity conditions of the normal components of the fields. Similarly, we apply equation (3.17) to the second case depicted in figure 3.18b. Regarding Stokes' theorem then yields the line integral

$$\oint_{\partial A} \boldsymbol{E}\, d\boldsymbol{s} = 0$$

from which we obtain the additional contiguity conditions

$$\boldsymbol{D}_\uparrow^\parallel \epsilon_\downarrow = \boldsymbol{D}_\downarrow^\parallel \epsilon_\uparrow \quad \wedge \quad \boldsymbol{E}_\uparrow^\parallel = \boldsymbol{E}_\downarrow^\parallel \tag{3.23}$$

for the parallel components.

3.2.2. Regular mesh

Prepared in this way, we now address an approach for the numeric solution of the Poisson equation on a regular mesh. As a basis we use the regular tessellation with isotropic spacing $\Delta a \in \mathbb{R}$ (p. 34). Coordinates of the nodes in the mesh are given

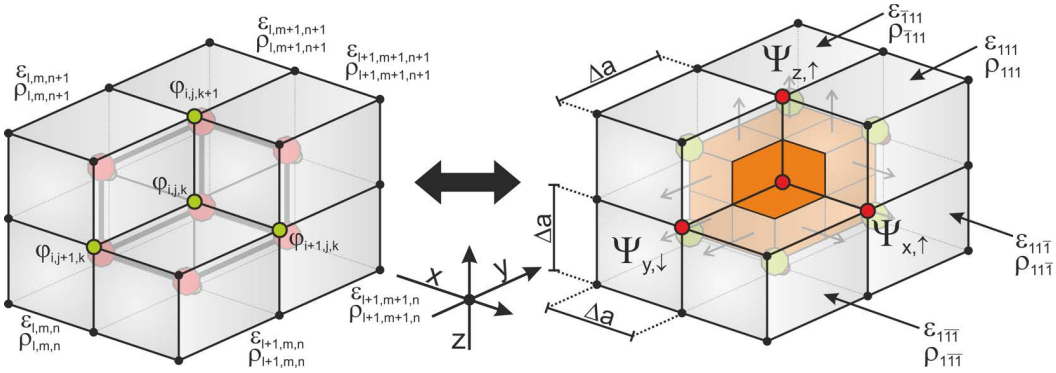

(a) material nodes adjacent to $\varphi(i,j,k)$ **(b)** potential nodes adjacent to $\varphi(i,j,k)$

Figure 3.19.: Sketch of the computation mesh for the regular case. (a) Cubic domains denoted by coordinates (l,m,n) are attributed with different values for dielectricity and charge density. Potential nodes are located at the corners of the cubes for which shifted coordinates (i,j,k) apply. (b) The sphere of influence about each potential node depicts a nested cube within the basic mesh. For the six fluxes $\Psi_{\{x,y,z\},\{\uparrow,\downarrow\}}$ through the facets, electrical properties in each four different octants must be considered.

by

$$(i,j,k) \in \mathbb{Z}^3 \mapsto \boldsymbol{r}(i,j,k) := \Delta a \cdot \begin{pmatrix} i \\ j \\ k \end{pmatrix}, \ \boldsymbol{r} \in \mathbb{R}^3 \tag{3.24}$$

The value of the unknown potential $\varphi(i,j,k)$ shall be determined at each node. For this, an additional mesh is constructed from a shifted set of coordinates

$$(l,m,n) \in \mathbb{Z}^3 \mapsto \boldsymbol{r}(l,m,n) := \Delta a \cdot \begin{pmatrix} l \\ m \\ n \end{pmatrix} + \frac{\Delta a}{2} \cdot \begin{pmatrix} 1 \\ 1 \\ 1 \end{pmatrix}, \ \boldsymbol{r} \in \mathbb{R}^3 \tag{3.25}$$

to which different material properties are assigned. Values for dielectricity and charge density are denoted by $\epsilon_r(l,m,n)$ and $\rho(l,m,n)$, respectively. The combination of the nested meshes is shown in figure 3.19. In both depicted meshes, the associated cell volume centred about a node is the cube with $V = (\Delta a)^3$. This cube represents a sphere of influence. From the perspective of the mesh carrying the material properties, the potential is evaluated at the corner sites of the cells (fig. 3.19a). This allows for both well-defined equipotential surfaces and sharp interfaces at the respective cell boundaries. In contrast, the sphere of influence for any single potential node intersects with eight adjacent cells which may possess different dielectricity $\epsilon_r(l,m,n)$ and charge density $\rho(l,m,n)$ (fig. 3.19b). All these

cells do contribute to the evaluated potential.

In the following, we refer to the notation given in the figures. Adopting equation (3.20) with equation (3.21) yields

$$\sum_{\partial V(i,j,k)} \Psi_{\{x,y,z\},\{\uparrow,\downarrow\}} - q(i,j,k) = 0 \tag{3.26}$$

for the balanced flux through the cube about $\varphi(i,j,k)$. The sum extends to six (3×2) terms according to the cube facets. The flux at each facet writes as

$$\Psi_{\{x,y,z\},\{\uparrow,\downarrow\}} = \epsilon_0 \epsilon_r^{\{x,y,z\},\{\uparrow,\downarrow\}} E^{\{x,y,z\},\{\uparrow,\downarrow\}} \cdot \left(\frac{\Delta a}{2}\right)^2$$

Due to the setup with the nested meshes, every facet consists of four quadrants with different dielectricity. Fortunately, we can assume that the field across the quadrants remains approximately the same (arrows in fig. 3.19b). For the lateral components of the field vector, this is concluded from the contiguity relation (eqn. 3.23) and for the normal component no different dielectricity applies at all. If we consider the marked stencil of the six adjacent potential nodes in figure 3.19, an approximation of the effective field is enabled using standard first-order finite differences:

$$\begin{aligned} \boldsymbol{E}_{x,\downarrow}^{(i,j,k)} &\equiv -\operatorname{grad}\varphi\Big|_{\boldsymbol{r}-\frac{\Delta a}{2}\hat{e}_x} \cong -\frac{\varphi(i-1,j,k)-\varphi(i,j,k)}{\Delta a}\cdot\hat{e}_x \\ &\dots \\ \boldsymbol{E}_{z,\uparrow}^{(i,j,k)} &\equiv -\operatorname{grad}\varphi\Big|_{\boldsymbol{r}+\frac{\Delta a}{2}\hat{e}_z} \cong -\frac{\varphi(i,j,k+1)-\varphi(i,j,k)}{\Delta a}\cdot\hat{e}_z \end{aligned} \tag{3.27}$$

Whereas for the effective dielectricity, the summed value for each facet is appropriate:

$$\begin{aligned} \epsilon_{x,\downarrow}^{(i,j,k)} &= \epsilon_{\bar{1}\bar{1}\bar{1}}^{(i,j,k)} + \epsilon_{\bar{1}\bar{1}1}^{(i,j,k)} + \epsilon_{\bar{1}1\bar{1}}^{(i,j,k)} + \epsilon_{\bar{1}11}^{(i,j,k)} \\ &\dots \\ \epsilon_{z,\uparrow}^{(i,j,k)} &= \epsilon_{\bar{1}\bar{1}1}^{(i,j,k)} + \epsilon_{\bar{1}11}^{(i,j,k)} + \epsilon_{1\bar{1}1}^{(i,j,k)} + \epsilon_{111}^{(i,j,k)} \end{aligned} \tag{3.28}$$

It remains to compute the included charge. Therefore, the different charge densities in each of the contributing cells are considered:

$$q^\star \equiv q(i,j,k) = \left(\frac{\Delta a}{2}\right)^3 \cdot \left[\rho_{\bar{1}\bar{1}\bar{1}}^{(i,j,k)} + \ldots + \rho_{111)}^{(i,j,k)}\right] \tag{3.29}$$

Finally, we are able to derive the discrete approximation for the potential. The potential at $\varphi(i,j,k)$ only depends on the values at adjacent nodes in the mesh and on the respective electric properties [OS11]:

$$\varphi(i,j,k) \cong \frac{\epsilon^{(i,j,k)}_{x,\{\uparrow,\downarrow\}}\varphi(i\pm1,j,k) + \epsilon^{(i,j,k)}_{y,\{\uparrow,\downarrow\}}\varphi(i,j\pm1,k) + \epsilon^{(i,j,k)}_{z,\{\uparrow,\downarrow\}}\varphi(i,j,k\pm1) + \frac{q^\star}{\epsilon_0}}{\epsilon^{(i,j,k)}_{x,\{\uparrow,\downarrow\}} + \epsilon^{(i,j,k)}_{y\{\uparrow,\downarrow\}} + \epsilon^{(i,j,k)}_{z,\{\uparrow,\downarrow\}}} \tag{3.30}$$

Besides the charge, it is notably independent from the imposed mesh spacing. The contribution of the potential at the adjacent nodes gets weighted by the effective dielectricity. The effect of the different values for the dielectricity appears equivalent to the picture of the multiple conductances in a parallel electric circuit.

3.2.3. Irregular mesh

For the analogous treatment of an irregular mesh, we account here for the combination of the Delaunay and the Voronoi tessellation in 3D. Despite the more complex effort accompanied with the construction of these tessellations, the introduced approach remains astonishingly simple.

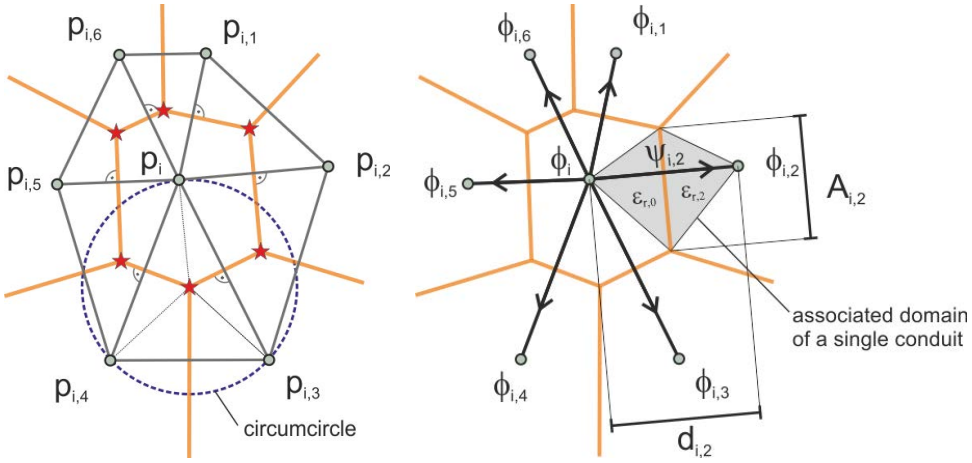

(a) Voronoi tessellation and Delaunay tessellation about a single Voronoi cell

(b) Alternative view of the Delaunay tessellation as a conduit network

Figure 3.20.: Irregular computing mesh compiled from the Voronoi and the Delaunay tessellation. The potential is computed at the generator points of the tessellations. Different values for dielectricity and charge density are assigned to each Voronoi cell [OES13].

We examine a single Voronoi cell (fig. 3.20a). It is determined by the generator $\boldsymbol{p}_i$ and its associated set of natural neighbour points, denoted by $\boldsymbol{p}_{i,1}, \ldots, \boldsymbol{p}_{i,N}$. As before in the regular case, we wish to evaluate the flux through the boundary formed by the cell facets — or, in an alternative view, we may consider the dual representation by the Delaunay tessellation: Then the facets correspond to edges of the tetrahedra which are incident to $\boldsymbol{p}_i$. Mathematically speaking, the Delaunay edges represent a directed graph. Hence, we may treat the Delaunay tessellation as a conduit network for the electric flux. Consequently, the driving force for the fluxes is in this picture due to different potentials at the end of both sides of a conduit (fig. 3.20b) and we yield

$$\sum_{j=1}^{N} \Psi_{i,j} = \sum_{j=1}^{N} D_{i,j} \cdot A_{i,j} = q_i \tag{3.31}$$

for the balanced flux through $\boldsymbol{p}_i$ [SB03]. The displacement fields hold for the direction of the respective Delaunay edges. The capacity of each such conduit is proportional to the area of the depicted Voronoi facet in the dual Voronoi mesh denoted by $A_{i,j}$.

Different values of the potential, dielectricity, and charge density exist at each node of the Delaunay tessellation. Hence, we immediately recognize at this point a notable difference to the geometry in the regular mesh: the spheres of influence for the unknown potential and the electric properties coincide in the chosen representation. As a consequence, any boundary conditions which apply for the potential have a different effect. They do not explicitly hold for the boundary of the cells with different properties as it was the case before. For this reason, the present approach is termed *cell-centered*, whereas the former is termed *vertex-centered*.

However, in order to obtain the solution for the potential at the given generator node, we firstly evaluate the charge in equation (3.31). It directly amounts to

$$q_i = \rho_i \cdot V_i \tag{3.32}$$

if we take into account the volume of the Voronoi cell denoted by V_i (eqn. 3.13).

Next, we consider the displacement fields $D_{i,j}$ which are responsible for the fluxes. In the picture of the conduits, the situation corresponds to a plate capacitor in 1D with a dielectric interface at half the distance between the two electrodes at $\boldsymbol{p}_i$ and $\boldsymbol{p}_j$. Due to the contiguity equation (3.22) we know that the electric field is not contiguous across the interface. For this reason, we cannot directly apply the first

order finite differences approximation as before. But by means of equations (3.18) and (3.15), a suitable expression for the potentials at the ends of the conduit may be obtained, if we consider that the displacement field remains unchanged:

$$\varphi_i - \varphi_j = \frac{D_{i,j}}{\epsilon_0} \cdot \int_{\boldsymbol{p}_i}^{\boldsymbol{p}_j} \frac{1}{\epsilon_r(r)}\, dr = \frac{D_{i,j}}{\epsilon_0} \cdot \frac{d_{i,j}}{2} \cdot \left(\frac{1}{\epsilon_{r,i}} + \frac{1}{\epsilon_{r,j}} \right) \tag{3.33}$$

Here, $d_{i,j}$ denotes the distance between the nodes $\boldsymbol{p}_i$ and $\boldsymbol{p}_j$, according to the length of the conduit.

If we rearrange equation (3.33) for $D_{i,j}$ and insert the result in equation (3.31), we finally obtain

$$\varphi_i = \left(\sum_{j=1}^{N} \gamma_{i,j} \cdot \varphi_j + \frac{q_i}{\epsilon_0} \right) \Bigg/ \left(\sum_{j=1}^{N} \gamma_{i,j} \right) \tag{3.34}$$

as the expression for the potential at a given node of the irregular mesh. Weighting factors are defined as

$$\gamma_{i,j} := 2 \cdot \left(\frac{1}{\epsilon_{r,i}} + \frac{1}{\epsilon_{r,j}} \right)^{-1} \cdot \frac{A_{i,j}}{d_{i,j}} \tag{3.35}$$

Interestingly, the reciprocal values for dielectricity reveal their effect on the flux. It is equivalent to multiple conductances of an in series-connected resistor network.

3.3. Ion trajectories and the electric field

The electric field in the simulation mesh can be derived by virtue of the known potential. In the application to the simulation, the field enables the analysis of charged particle trajectories. Since the maximum velocity of the ions will be moderate in the studied cases ($v_{\mathrm{Ion}} < 2\,\mathrm{km\,s^{-1}}\,@\,20\,\mathrm{kV}$), trajectories are sufficiently described by classical physics based on Newton's equation of motion:

$$m \cdot \frac{\partial^2 \boldsymbol{r}}{\partial t^2} = n \cdot e \cdot \boldsymbol{E}(\boldsymbol{r}) \tag{3.36}$$

Here, m denotes the mass, n the charge state, and e the unit charge, respectively. If we explicitly introduce the ion momentum denoted by $\boldsymbol{p}$, the second order ordinary

differential equation can be replaced by two coupled first order differential equations

$$\left| \begin{array}{l} \dfrac{\partial \boldsymbol{p}(\boldsymbol{r},t)}{\partial t} = n \cdot e \cdot \boldsymbol{E}(\boldsymbol{r}) \\ \dfrac{\partial \boldsymbol{r}(t)}{\partial t} = \dfrac{1}{m} \cdot \boldsymbol{p}(\boldsymbol{r},t) \end{array} \right| \tag{3.37}$$

from which the trajectory is computed by simultaneous numeric integration. At each integration step, respective values for the position $\boldsymbol{r}(t)$ and momentum $\boldsymbol{p}(t)$ are recorded according to the progressing time $t^{(i+1)} = t_i + \Delta t$. Therefore, the final result represents a time dependent path in the phase space. The stepwise integration algorithm continues until a preset abortion criterion, e.g. the ion passes the boundary of the mesh, has been reached.

For the numeric integration of equation (3.37), an embedded fourth order Runge-Kutta method [CK90] has been employed, which allows for an economic processing as the time steps are determined adaptively with respect to a preset limit of the numeric error. Of course, other standard integration approaches are equally appropriate, but whatever method applies, the prerequisite of providing a value for the field at arbitrary position remains. In fact, computing the electric field from the discrete potential nodes turns out to be the major obstacle for the trajectory computation.

Computing the electrical field

The easy case is the regular mesh. As the field is the derivative of the potential (eqn. 3.18), it can be directly computed by reversing equation (3.27). The (negated) standard symmetric numeric derivative writes as

$$\boldsymbol{E}(i,j,k) = \frac{\varphi(i-1,j,k) - \varphi(i+1,j,k)}{2\,\Delta a} \cdot \hat{e}_x + \ldots \tag{3.38}$$

For each component of the field vector, the potential differences are equated at a discrete node. Subsequently, the field at an arbitrary position within the mesh is obtained by linear interpolation considering the field vectors at the next neighbour nodes.

Unfortunately, obtaining the field in the irregular mesh is more complicated. Due to the arbitrary distribution of the potential nodes, a clear basis for establishing the derivative is missing. Therefore, a fitting approach based on the least squares method applies. The potential in the vicinity of a given node at $\boldsymbol{p_0}$ is expressed by

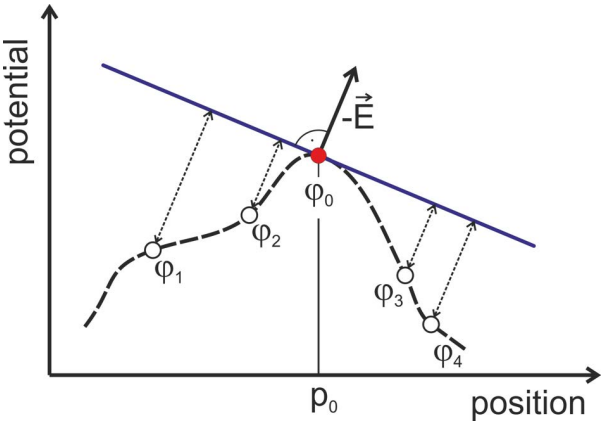

Figure 3.21.: Graphical representation of the approach which applies for the field computation on an irregular mesh. A linear fit to the potential landscape with regard to the next $1, \ldots, N$ neighbour potentials is conducted. By the fitting, the normal vector of a hyperplane (a plane in 3D) at the offset $\boldsymbol{p}_0$ is obtained. The result is identic to the field except for the sign.

the Taylor expansion

$$\begin{aligned} \varphi(\boldsymbol{p}) &= \varphi(\boldsymbol{p}_0) - \operatorname{grad}\varphi\big|_{\boldsymbol{r}=\boldsymbol{p}_0} \cdot \big(\boldsymbol{p} - \boldsymbol{p}_0\big) + \mathcal{O}(2) \\ &\cong \varphi(\boldsymbol{p}_0) - \sum_{i=1}^{3} \underbrace{\frac{\partial\varphi}{\partial r_i}\hat{e}_i}_{\lambda_i} \cdot \underbrace{\big(\boldsymbol{p} - \boldsymbol{p}_0\big)}_{\Delta\boldsymbol{p}} \end{aligned} \tag{3.39}$$

The unknown electric field appears in the form of the gradient term denoted by $\boldsymbol{\lambda}$. Graphically, $\boldsymbol{\lambda}$ depicts an approximation to the tangent plane for the potential at the node φ_0. This is illustrated in figure 3.21. For the fitting function $\varphi(\boldsymbol{p})$ the potential values φ_n at the $1, \ldots, N$ local neighbour nodes of the mesh are considered. In the case of the Delaunay tessellation, the natural neighbours apply.

Next, we demand the least square error defined by

$$\begin{aligned} \chi(\boldsymbol{\lambda})^2 &= \sum_{n=1}^{N} \Big(\varphi_n - \varphi(\boldsymbol{p}_n)\Big)^2 \\ &\overset{(3.39)}{=} \sum_{n=1}^{N} \Big(\varphi_n - \varphi(\boldsymbol{p}_0) + \sum_{i=1}^{3} \lambda_i \Delta\boldsymbol{p}_{n,i}\Big)^2 \end{aligned} \tag{3.40}$$

to be minimal. An equal statement is to set the differential $d\chi^2$ to zero. As $\boldsymbol{\lambda}$ is arbitrary, the result are three equations for the partial derivatives

$$d\chi^2 = \sum_{i=1}^{3} \frac{\partial\chi^2}{\partial\lambda_i} \cdot d\lambda_i \overset{!}{=} 0 \Leftrightarrow \frac{\partial\chi^2}{\partial\lambda_i} = 0 \;\forall i \tag{3.41}$$

which form a system of linear equations:

$$\frac{\partial \chi^2}{\partial \lambda_i} = \sum_{k=1}^{3} \underbrace{\left(\sum_{n=1}^{N} \Delta \boldsymbol{p}_{n,k} \cdot \Delta \boldsymbol{p}_{n,i} \right)}_{D_{ik}} \cdot \lambda_k = \underbrace{\sum_{n=1}^{N} \left(\varphi(\boldsymbol{p}_0) - \varphi_n \right) \cdot \Delta \boldsymbol{p}_{n,i}}_{B_i} \tag{3.42}$$

By making use of the given abbreviations it writes as

$$\begin{pmatrix} D_{11} & \dots & D_{13} \\ \vdots & \ddots & \vdots \\ D_{31} & \dots & D_{33} \end{pmatrix} \cdot \begin{pmatrix} \lambda_1 \\ \lambda_2 \\ \lambda_3 \end{pmatrix} = \begin{pmatrix} B_1 \\ B_2 \\ B_3 \end{pmatrix} \tag{3.43}$$

Hence, solving for $(\lambda_1, \lambda_2, \lambda_3)$ yields the field $\boldsymbol{E}(\boldsymbol{p}_0)$.

A numerically stable approach involves to obtain first the LU decomposition of the matrix D_{ik} which then leads to the solution by forward-backward substitution line-by-line applied to both the triangular matrices [Pre+07]. Due to the symmetry ($D_{ik} \equiv D_{ki}$), only six matrix elements need to be computed. Therefore, the described approach turns out to be astonishingly efficient.

For the field at arbitrary positions $\boldsymbol{r}$ within the irregular mesh, linear interpolation applies: In a first step, the tetrahedron with $\boldsymbol{r}$ in the interior is located by conducting a Delaunay walk (sec. 3.1.3, p. 48) in the mesh. Second, the discrete fields at the vertices of the tetrahedron are computed based on equation (3.43). Finally, the interpolated field results by using the barycentric coordinates (sec. 3.1.2, p. 40) of $\boldsymbol{r}$ with respect to the tetrahedron vertices as weights.

The described approach for the field computation may be further refined by using the extended Taylor series for the least squares fitting (appendix, chap. B). Besides an improved accuracy, an additional second order term — the trace of the Hesse matrix — enables information about the (free) local charge density according to the Poisson equation $\nabla^2 \varphi = -\frac{\rho}{\epsilon_0}$ which is a nice supplement. Of course, this additional information is not for free because the numeric effort increases at the same time considerably.

4. Implemented simulation approaches

In this chapter, the method of operation of two distinguished approaches for modelling the field evaporation and ion trajectories in APT will be described. Both approaches have been implemented for this work.

Although recently, research in this field has raised considerable interest, investigating the properties of field emitted ions by means of electrostatic modelling is not a new attempt at all. Starting point for the modelling is a common simplification. The electrostatic condition of a real measurement setup becomes reduced to consist of three main parts (see fig. 2.3, p. 15):

- the emitter structure, which represents the sample to be analysed,
- the counter electrode, as electrostatic representation of a sensitive detector or imaging system, and
- the enclosing measurement chamber.

Even if, the influence of the measurement chamber is almost negligible in the experiment, it is indeed mandatory in order to establish appropriate boundary conditions in the numeric treatment.

A crucial point of this general setup is the large difference in the covered length scales. The field emitter has a diameter of usually less than 100 nm, whereas the counter electrode and the measurement chamber have macroscopic extents of several centimeters.

Here, we want to restrict ourselves to classical physics and therefore do not intend to account for the quantum mechanical origins of field evaporation or field ionization. Nevertheless, it is clear that the local electric field in the (sub)nanometer range close to the field emitter surface, does effect the trajectories of emitted ions decisively. Therefore, the solution for the potential may demand to bridge six orders of magnitude in order to address all important properties.

In the generality, this is only possible by accepting a considerable level of numeric complexity. On the other hand, such a general approach is not always required. Depending on the respective focus of interest, it can be beneficial to make use of some natural simplifications. For example, if only the part in a small distance to the tip apex is taken into account, e.g. about two times the curvature radius of the emitter apex, a small simulation box with adapted boundary conditions can be used. Similarly, rotational symmetry may be assumed for the emitter structure and its surroundings. This reduces the effective dimensionality of the problem from 3D to 2D. If, in addition, the atomically rough nature of the emitter surface is neglected, even an analytic solution for the potential becomes possible (e.g. like the

paraboloidal model, see p. 16). Of course, this is at the expense of a considerable loss in generality.

Besides these geometrical considerations linked to the scaling problem, a fundamental classification of APT modelling approaches into *static* and *kinetic* ones must be mentioned. In the static approach, the solution of the potential for a preset setup of the emitter-electrode combination will be computed only once. This is sufficient to explore ion trajectories originating from the modelled emitter. Details of the surface morphology are neglected. Hence, if one is mainly interested in exploring the general projective properties, this approach represents a good choice. The derived imaging characteristics may then later be used for conducting APT reconstructions which operate on real measurement data. Several authors have published studies which are based on this background [SW78; Gau+11; Loi+12] and some of the results presented in the next chapter have been derived in this way.

The disadvantage of the static approach is at least twofold. First, there is the question whether the considered shape of the evaluated field emitters is realistic. Usually, the applied shapes represent only an approximation to a supposed steady state shape (e.g. a cylinder with hemispherical cap). Irregular shapes evolving from inhomogeneous evaporation thresholds as well as trajectory aberrations originating from the atomic rough nature of the emitter surface are possibly not appropriately considered.

The second disadvantage addresses the fundamental difference between ion trajectories originating either from field ionization or field evaporation. In this view, the static approach is in principle not suited to predict the imaging properties. Field evaporation exclusively takes place at very well-defined surface sites with well-defined field conditions. In contrast, field ionization takes place at arbitrary locations somewhat above the emitter surface. Hence, respective ion trajectories are hardly comparable. Again, this point will be demonstrated in a later part.

An implementation of a kinetic approach accounts in contrast for the detailed atomic surface of the field emitter and its evolution in time. In consequence, shape changes, which evolve from the consecutive field evaporation of distinct surface sites, can be reproduced. Although this is at the cost of repetitively computing the solution for the potential, realistic fields and realistic trajectories may be considered by this approach. Both simulation models described next belong to this latter class.

4.1. Basic model according to Vurpillot's approach

The foundation of the kinetic approaches is made by the early work of Vurpillot et al. at the turn of the last century [Vur+99; VBB00; Vur+00]. By today, their approach still represents the standard on which other groups developed their own simulation packages. For this reason, details of Vurpillot's original framework are described here first and existing extensions will be addressed thereafter. Among one of these extensions is notably the ability to account for dielectricity which has been added by this work. Related results are summarized in section 4.1.4.

Vurpillot's basic model accounts for metallic sample structures. It is founded on the solution of the Laplace equation on the basis of a regular grid in 3D. The general setup of the simulation system is sketched in figure 4.1a, whereas figure 4.1b depicts a fully elaborated example. The emitter consists of a cylinder stub which is capped by a half-spherical apex. The size of the curvature radius is in the range between 10 nm to 30 nm. The resolution of the basic grid spacing matches the typical lattice spacing of metals (e.g. $d_0 \sim 5\,\text{Å}$). Each cubic cell of the emitter is identified with a single atom. By this treatment the potential is evaluated at the cube facets. In combination with fixed boundary conditions, the facets appear as contiguous equipotential surfaces.

Due to the limitation by the regular grid, only a small region within a short distance to the emitter sample is practically considered. More than two million nodes are needed already for a simulation box with the moderate size of

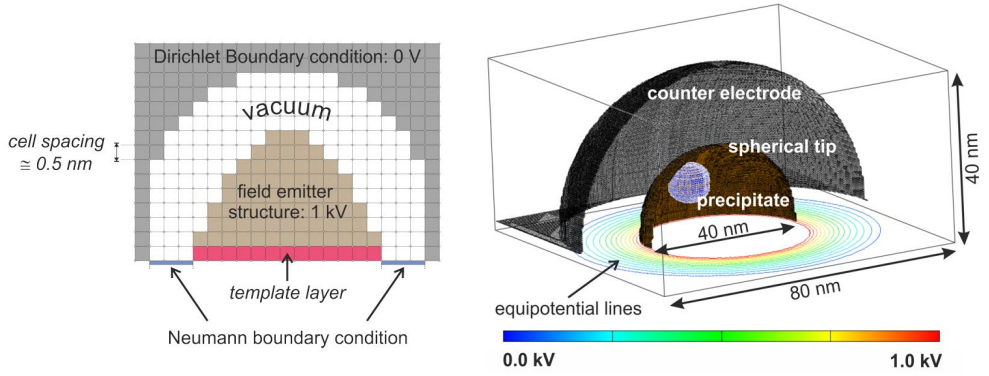

(a) 2D sketch highlighting the basic construction of the simulation grid composed of cubic cells.

(b) 3D view of a real setup used for computation. At the bottom, equipotential lines are plotted. [OS11].

Figure 4.1.: Setup of the regular computational mesh which is the basis for Vurpillot's simulation approach

$80\,\mathrm{nm} \times 80\,\mathrm{nm} \times 40\,\mathrm{nm}$. Thereof only a minor fraction ($\sim 15\,\%$) is allocated to the emitter structure. Facing this limitation by the grid, realistic field conditions comparable to experiments must be artificially imposed by means of a curved counter electrode opposite to the emitter. The alignment is such that both the emitter apex and the counter electrode are congruent to each other. The potential of the second electrode is grounded. At the bottom of the simulation mesh, the Neumann boundary condition with $\frac{\partial \varphi}{\partial n}\hat{\boldsymbol{e}}_n = \mathbf{0}$ is enforced. This choice mimics an infinitely continued emitter base with cylindric shape.

For this settings of the mesh, the Laplace equation will be solved. The Laplace equation derives from the Poisson equation if charge and dielectricity become neglected. Therefore, we set $q(i,j,k) \equiv 0$ and $\epsilon^{(i,j,k)} \equiv 1 \;\; \forall\, i,j,k$ in equation (3.30) and receive

$$\varphi(i,j,k) \cong \frac{\varphi(i \pm 1,j,k) + \varphi(i,j \pm 1,k) + \varphi(i,j,k \pm 1)}{6} \tag{4.1}$$

for the potential at one distinct node. The solution throughout the mesh is enabled by iterative application of equation (4.1) to all nodes. Let φ^t denote the potential at node (i,j,k) in the t*th* cycle, then the newly calculated value becomes

$$\varphi^{t+1} := \left[\varphi(i,j,k) - \varphi^t\right] \cdot \alpha + \varphi^t,\; \alpha \in [1;2] \subset \mathbb{R} \tag{4.2}$$

in the subsequent cycle. In the case with $\alpha > 1$ in equation (4.2), an "overrelaxation" for the newly assigned potential is introduced which leads to improved convergence [Hum93].

The asymptotic convergence rate of the scheme makes need for an exit condition of the relaxation process. For this, we track the maximum change of the recomputed potential within one iteration step by

$$\Delta\varphi^t := \max\left(\frac{\varphi^{t+1} - \varphi^t}{\alpha}\right) \;\; \forall\, i,j,k \tag{4.3}$$

If the change drops below a certain threshold, further computation stops. In addition, the convergence rate, $d\left(\Delta\varphi^t\right)/dt < 0$, may be considered for an automatic exit condition. This ensures termination even if the preset error threshold turns out to be unreachable due to numeric constraints. In this case, the best possible approximation is reached if the slope approaches zero.

Once the potential has been derived for the first time, the *kinetic* part of the simulation gets invoked. It consists in the management of all the necessary tasks

which allow the field evaporation of atoms from the emitter structure at a given stage. Essential for this venture is a maintained list with the surface atoms of the emitter. By definition, an atom cell is considered to be part of the surface, if it shares at least one of its facets with the vacuum. With this, the *kinetic* cycle proceeds as follows:

1) A surface atom is selected for evaporation. In the most simple approach, the average field at the eight corner sites of the cubic cell is evaluated according to equation (3.38). The cell exposed to the maximum field strength will be selected for evaporation. This choice resembles the experimental situation of APT measurements in which the voltage is adjusted for maintaining a critical evaporation field at the apex.

2) The selected atom is removed from the emitter structure. The selected cell at the surface changes its properties and becomes a vacuum cell. Thereafter, the list of surface atoms is updated.

3) The potential is recomputed. This is necessary in order to adopt for the altered field conditions. Accuracy of the relaxation is adjusted by the same termination condition which already controlled the initial relaxation step.

4) The ion trajectory is computed. Starting at the former surface site, a cation is injected and is accelerated by the actual field. The computed trajectory stops, if either the electrode or the boundary of the simulation mesh is reached. The respective end position is recorded.

This sequence of tasks is repeated for all successive atoms. If it happens that the atom at the topmost emitter site has been removed, the whole emitter structure is shifted upwards by one atomic layer in order to prevent a shrinkage. For this purpose a special "template layer" at the bottom of the emitter structure (fig. 4.1a) will be reproduced. In this way, an infinite proceeding is enabled.

An example of the obtained ion hit positions at a 2D detector plane placed directly beyond the counter electrode is shown in figure 4.2. The non-uniform distribution already reveals features which are qualitatively known from field desorption experiments.

4.1.1. Increasing numeric resolution

The basic model is entirely limited to the use of field emitters with the same sc ⟨100⟩ structure. This is a consequence of the underlying grid on which the potential is

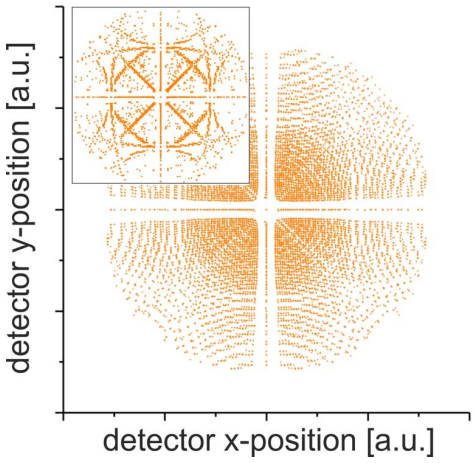

Figure 4.2.: Computed detector hits which have been obtained using an own implementation of Vurpillot's basic model [OS11]. The pattern reflects a sc ⟨100⟩ emitter structure with fourfold symmetry. If only a subset of those positions with elevated field of evaporation at the apex is shown, the pattern in the inset reveals.

solved. However, for practical purposes, this structure is only of limited interest. Almost all samples in the conducted APT experiments consist of bcc, fcc, and more complex lattices and are only in exceptional cases oriented in ⟨100⟩. In consequence, an one-to-one comparison of simulated and experimental results is not feasible.

A slightly more flexible representation of the emitter structure is enabled if a finer resolved mesh applies for the electrostatic solution. Instead of using eight potential nodes for one atomic cell, atoms will be constructed from n^3 ($n \geq 2$) cubic cells with $(n+1)^3$ grid points for the potential [Gru12]. This leads to an increased accuracy of the calculated potential and somewhat extends the range of possible lattice structures. In the implementation, the simulation code manages two grids at the same time: one for the atom cells and one for the mapping to the grid on which the potential is solved. Because of this complex treatment, the approach is in the generality difficult to apply.

4.1.2. Distinguished evaporation thresholds

Imaging artifacts in experiments may arise from heterogeneous evaporation properties of the analysed samples. Thus, there should be the possibility to account for distinguished evaporation thresholds of chemical species in simulated samples.

The critical threshold for evaporation is considered as the field which completely reduces the activation energy $Q(E)$ for field evaporation of a surface atom (eqn. 2.9, p. 12). For the field dependency, we see an approximately linear relationship close to the critical field strength E_{Crit} (eqn. 2.10):

$$Q(E) \cong \frac{Q_0}{2} \cdot \left(1 - \frac{E}{E_{\mathrm{Crit}}}\right)$$

where Q_0 denotes the activation energy without any field.

In terms of a probability for field evaporation, the probability becomes equal to one, once the critical field E_{Crit} is reached. Therefore, this material-specific constant is especially considered in the following to derive a general standard. In contrast to the experimental procedure, the supplied voltage to the emitter structure is not adjusted in the simulation. Instead, different evaporation probabilities for each surface atom

$$\omega_i \sim E_{\mathrm{Mod}}/E_{\mathrm{Crit,i}} \tag{4.4}$$

are introduced which depend on the calculated field strengths E_{Mod} in the simulation relative to the required field strength to evaporate the given atom. The surface atom with the highest probability will be selected for removal in each evaporation cycle. The consequence of this setting is immediately clear: Under comparable fields E_{Mod}, atoms of elevated evaporation threshold E_{Crit} are retained on the surface while atoms of lower threshold evaporate preferentially.

Although the setting by equation (4.4) seems to be an arbitrary choice, in this way derived probabilities for field evaporation appear justified if the process is considered as thermally activated. In this view, the probability is controlled by Boltzmann's factor

$$\omega_i \sim \exp\left\{-\frac{Q_{0,i}}{2k_BT}\cdot\left(1-\frac{E}{E_{\mathrm{Crit},i}}\right)\right\} \tag{4.5}$$

and the field dependence becomes

$$\left.\frac{d\omega_i}{dE}\right|_{E_{\mathrm{Crit},i}} \approx \frac{Q_{0,i}}{2k_BT}\cdot\frac{1}{E_{\mathrm{Crit},i}} \tag{4.6}$$

which is the same relation which would be derived from equation (4.4) if the first coefficient on the right-hand side of equation (4.6) keeps constant. As the activation energies $Q_{0,i}$ of different species are expected to have roughly the same value, the approach represents an acceptable approximation.

However, on the background of a geometric model for APT simulation which does not make explicitly use of an electric field, Boll et al. demonstrated that the calculation of activation energies $Q_{0,i}$ based on local next neighbour relations allows for an alternative treatment of distinguished evaporation thresholds [Bol+12; BA13].

4.1.3. Statistic evaporation

Up to this point, field evaporation has been modelled in a deterministic picture: Either the surface atom exposed to the highest field or the atom exposed to the highest specific field, $E_{\mathrm{Mod}}/E_{\mathrm{Crit}}$, is selected for evaporation. Clearly, this is hardly the case in reality. A more realistic treatment of the evaporation process should fully account for different evaporation probabilities in the framework of a Monte Carlo approach. In the former section such probabilities have been introduced in order to address different material properties of the emitter atoms. Here, we further elaborate on this approach as it is presumed that the kinetics of field evaporation is indeed appropriately described by the Boltzmann relation.

The main problem, which prevents a straight forward application of equation (4.5) with this objective, is the inherent scaling invariance of the potential in the model. The absolute magnitude of the calculated fields is arbitrary. It depends on the preset emitter voltage. But more severely, the field changes slightly during the simulation. This change is caused by the continuous erosion of the apex. In consequence, deduced probabilities from the field are inconsistent unless a fixed scale can be established.

In experiments, the usual procedure is to adjust the voltage in order to maintain a preset event rate at the detector. This corresponds in the microscopic picture to field strengths at the emitter surface which are very close to the threshold for evaporation. Thus, the adjusted field almost suffices for completely reducing the activation barrier (eqn. 2.10). In order to establish an analogue situation in the simulation, we consider the field E_{Mod} linked to this distinct experimental field by

$$E_{\mathrm{Exp}} = \gamma^* \cdot E_{\mathrm{Mod}} \tag{4.7}$$

The factor γ^* accounts for the scaling invariance.

Any ambiguity in the choice of γ^* is now resolved by the requirement that at least one surface atom in the simulation should always get exposed to such a high field that its evaporation probability becomes maximized. This is just the case if the activation energy vanishes:

$$\begin{aligned} Q(E_{\mathrm{Exp}}) &\cong \frac{Q_{0,i}}{2} \cdot \left(1 - \frac{\gamma^* \cdot E_{\mathrm{Mod}}}{E_{\mathrm{Crit},i}}\right) \stackrel{!}{=} 0 \\ \Rightarrow \gamma^* &:= \max\left(\frac{E_{\mathrm{Crit},i}}{E_{\mathrm{Mod}}}\right) \quad \forall\, i \end{aligned} \tag{4.8}$$

In this way, consistent probabilities

$$\omega_i \sim \exp\left\{-\frac{Q_{0,i}}{2k_BT}\cdot\left(1-\max\left(\frac{E_{\mathrm{Crit},j}}{E_{\mathrm{Mod}}}\right)\cdot\frac{E_{\mathrm{Mod}}}{E_{\mathrm{Crit},i}}\right)\right\},\ \forall\, j \tag{4.9}$$

may be derived as input for a Monte Carlo approach. Free parameters for the simulation are temperature, the respective activation energies, and the critical field strengths at each surface site.

4.1.4. Extension to include dielectricity

Atom probe experiments were for a long time restricted to the analysis of metallic samples, because poorly conducting materials prevent successful measurements under application of nano-second high-voltage pulses. This limitation seemed to be rather fundamental, but with the introduction of the new class of laser-assisted instruments, the full range of materials has been enabled for analysis regardless of their electrical properties. The analysis of dielectric samples brings up particularly new challenges. In this regard, theoretical investigations by APT simulation represent a promising approach and may enable new insights. For this purpose an extension of Vurpillot's model is introduced. A detailed description of the approach and of results which are not presented here has been published in an related article [OS11]. Only minor, but nevertheless decisive modifications to the basic model are made:

- Dielectric properties for the emitter structure are enforced by additionally attributing each atomic cell with a different value for dielectricity.

- Consequently, instead by the Laplace equation (4.1), the solution is determined by the Poisson equation (3.30). Even though this increases the numeric complexity, the additional numeric effort turns out to be almost negligible if multi-core processors are used.

- Instead by the application of a fixed potential, metallic properties of an atomic cell are mimicked by assigning extraordinary high values of dielectricity ($\epsilon_r \sim 10^6$). Attenuation of the field inside the metal is thereby appropriately ensured.

- The Dirichlet boundary condition only holds at the bottom layer of the emitter, which acts as electric contact.

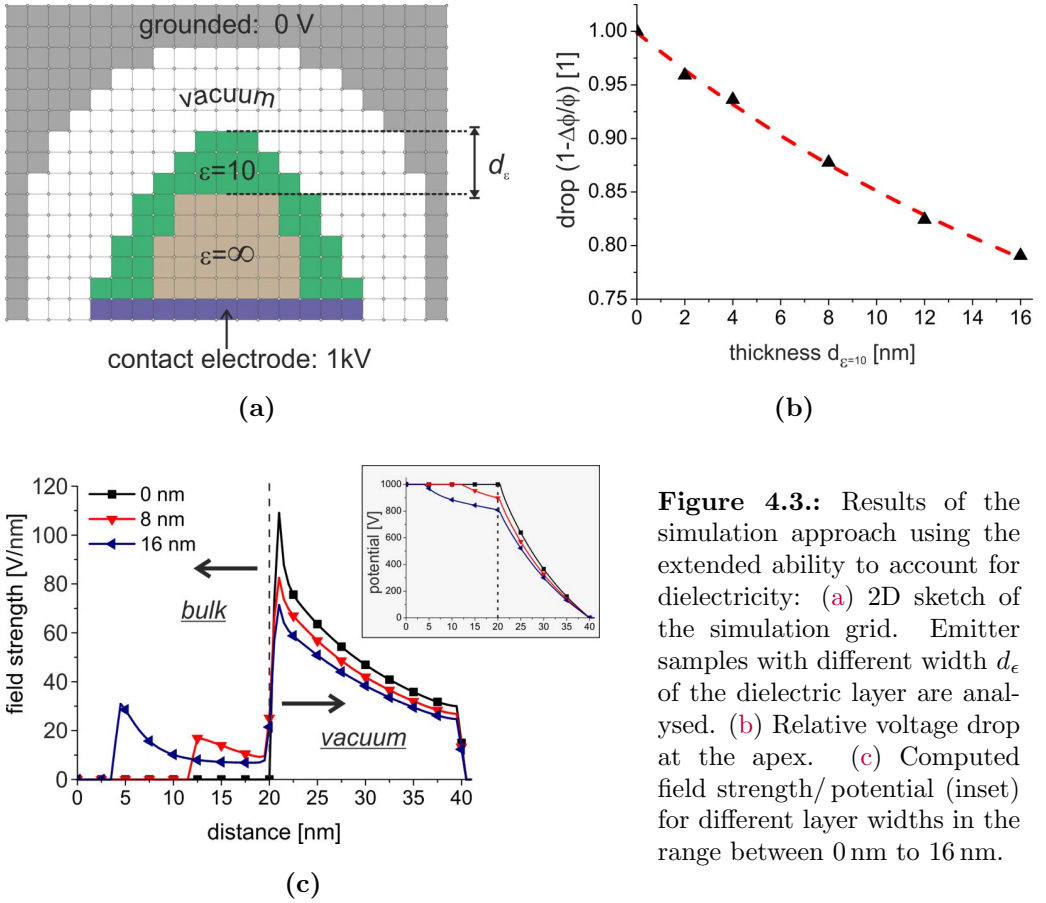

Figure 4.3.: Results of the simulation approach using the extended ability to account for dielectricity: (a) 2D sketch of the simulation grid. Emitter samples with different width d_ϵ of the dielectric layer are analysed. (b) Relative voltage drop at the apex. (c) Computed field strength/ potential (inset) for different layer widths in the range between 0 nm to 16 nm.

Figure 4.3a depicts the simplified setup for a dielectric sample structure. The emitter consists of a metallic core with a dielectric surface layer. In this example, a dielectricity of $\epsilon_r = 10$ applies, which corresponds to the typical value for oxide compounds, glasses or ceramics etc. Derived solutions of the field and the potential are shown in figure 4.3c. Different cases with a layer thicknesses d_ϵ in the range between 0 nm to 16 nm are considered. In all computations, the position of the emitter surface remained fixed at 20 nm. Clearly, field penetration into the dielectric bulk is visible. The result becomes confirmed by the presented voltage distributions in the inset. An analysis of the determined potential drop $(\frac{\Delta\varphi}{\varphi})(d_\epsilon)$ at the dielectric-vacuum surface shows an almost linear decrease as a function of the layer thickness (fig. 4.3b). If we assume that such an effect similarly takes part in experiments, an energy deficit of the detected ions would be expected. This deficit should decrease with progressing erosion of the dielectric layer until the voltage drop completely vanishes when the metal interface is finally reached. However, such an energy deficit has not yet been reported. Facing the extraordinary high field conditions

in APT, it is anyway questionable to which extent dielectricity is maintained. At least, effects like band bending will degrade the maximum penetration to a few nanometers [Tso79].

However, assuming a non-negligible field penetration takes nevertheless place, simulations as well as analytic calculations predict severe effects at the metal-dielectric-vacuum junction [OS11; Chu+13]. As an example the computed field distribution for a dielectric particle in a metallic matrix is presented in figure 4.4a. The approximate direction of field lines is indicated by the arrows. Because of the spherical shape, the field concentrates towards the particle core. In consequence, preferential evaporation is induced and a locally confined indention into the surface develops. The concave curvature causes significant aberrations of the ion trajectories. Since the reconstruction algorithm is not able to anticipate this change, we recognize an inhomogeneous atom density in the vicinity of the particle (fig. 4.4b). In addition, the originally spherical shape appears elongated.

Such a depressed evaporation threshold of the dielectric is a general effect. Figure 4.4c depicts another example which consists of several vertical layers with alternating dielectric and metallic properties. The steady state surface at the dielectric becomes again concave. In this case, even a crossing of trajectories is observed. The result are overlapping events at the detector and severe artifacts in the 3D reconstruction. A careful analysis for the concentration wrongly shows an enrichment of atoms from the dielectric in the metal bulk. Hence, we can learn from this example that artifacts in APT may be significant and hardly distinguishable from "proper" analysis results.

4.1.5. Discussion

Vurpillot's approach enables a numeric framework for accessing electric fields in the vicinity of modelled APT emitter structures. The dual use of a basic regular mesh for describing both the atomic structure and for computing the electrostatic solution turns out to be a pioneering concept.

The distinguished field acting on each surface atom of the emitter is considered. The surface exhibits an atomic rough morphology which originates from the arrangement of single cubic cells. This is in contrast to a static approach, in which a conventional finite-element solution of the potential is derived from an analytically prescribed emitter shape. In correspondence with the experimental observation, the roughness at the surface naturally leads to enhanced fields at protruding kinks and edges. As a result, these sites are more likely evaporated. Additionally, not

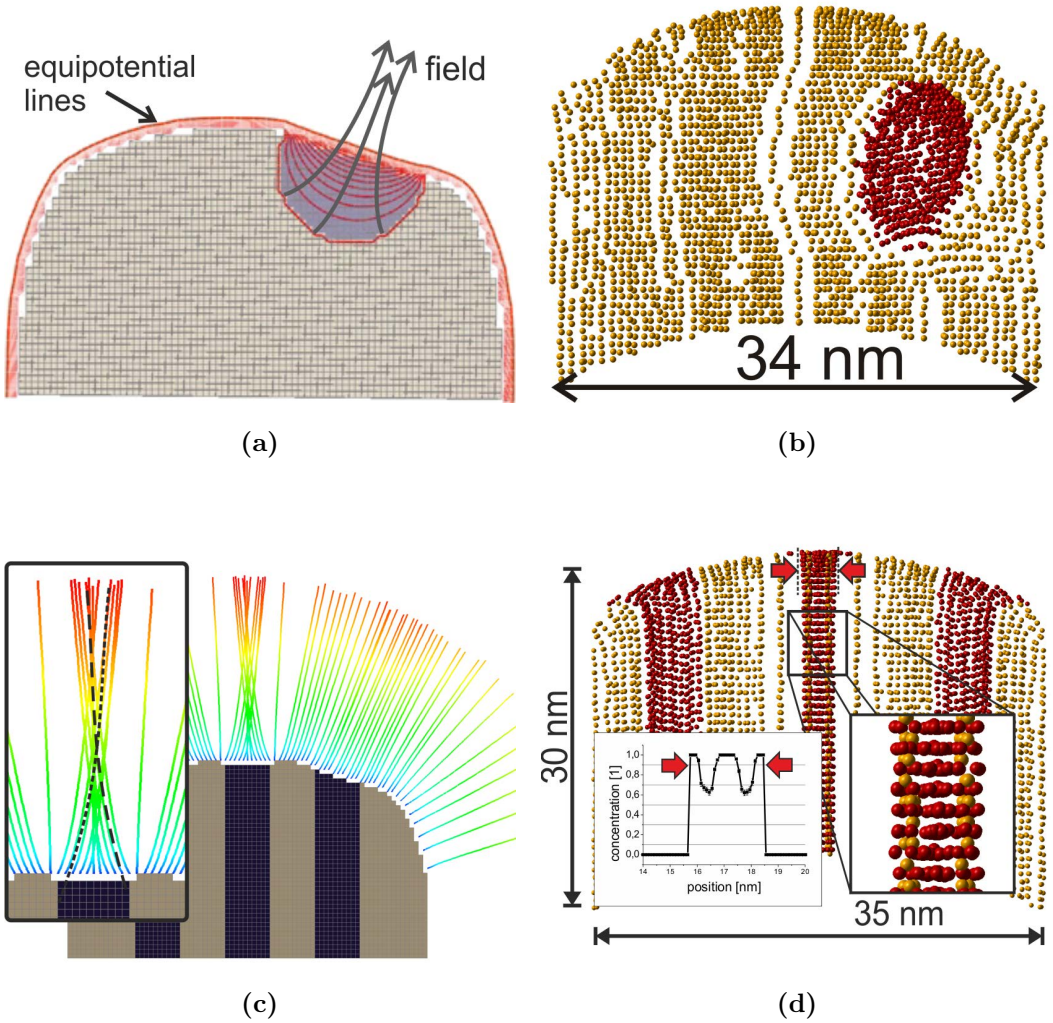

Figure 4.4.: Effect of field penetration at APT emitter structures with dielectric-metallic interfaces [OS11]: (a) The simulated evaporation of a dielectric particle reveals an enhancement of the surface field. (b) In consequence, an inhomogeneous atom density appears in the computed reconstruction. The particle shape is distorted. (c) Trajectory overlaps take part due to locally concave surface shapes. (d) The result are systematically displaced atoms in the 3D reconstruction.

only the field but also distinguished materials properties may be taken into regard. Thus, the obtained evaporation sequence of surface atoms becomes quite realistic.

The simulated trajectories are severely affected by the surface morphology. The ions initially start at rest. This makes them particularly sensitive for the field close to the emitter. Additionally, the magnitude of the field drops rapidly with increasing distance from the surface ($\sim 1/r$). For this reason, the trajectories compare quite well to experimental ones, although the possible size of the actual simulation box is way to small. However, in order to receive realistic impact positions at the detector, additional and possibly error-prone extrapolation is required. Anyway, at least for a qualitative analysis, the computed trajectories provide sufficient information, e.g. for the investigation of imaging artifacts.

Noteworthy, if the counter electrode necessarily moves to such close distances, a concentric curved electrode turns out to be mandatory. Otherwise, realistic fields in the free space around the emitter, corresponding to a regular flat electrode in the far distance, are not ensured because the shape of the applied electrode imprints to a noticeable degree the curvature at the emitter apex. Caution is needed about this point.

In summary, the approach along with the established extensions already addresses an important part of the physics which is expected to affect APT measurements. In fact, the main disadvantage of Vurpillot's extended model arises from its inflexibility which prevents the investigation of realistic emitter structures. Only simple, basically cubic lattice geometries are suited for simulation. Even with more computational effort or additional tricks, there is no way to carry out simulations of close to realistic emitter structures, since atoms are forced to be localized on a regular array. Ideally, possible input samples should not only reflect chemical inhomogeneity but should allow for arbitrary lattice defects as well. The use of the basic regular mesh clearly renders this latter feature impossible.

4.2. New generalized approach

In view of this limitation, a new simulation approach has been derived. Firstly, it overcomes the constraints by the grid of Vurpillot's model and enables simulations which truly reflect experimental conditions. Secondly, it permits a different description of the physics of field evaporation. Instead of the field, field induced polarization forces pulling at the surface atoms are considered for the simulated desorption. Details of this new treatment will be described in section 4.2.4.

4.2.1. Foundation by an irregular mesh

In order to overcome the restrictions by the regular grid, an irregular grid is used. In chapter 3 we have already seen how the potential (eqn. 3.34) and the field (eqn. 3.43) can be determined on this basis. In the new approach, the potential is accessible at arbitrary points in space (fig. 4.5a):

- In a dual view, nodes of the Delaunay tessellation represent at the same time the centre points of Wigner-Seitz (Voronoi) cells. This enables the nodes to directly correspond to atomic lattice sites inside the emitter structure. Different electrostatic properties such as dielectricity and charge density assign to individual nodes. In the linked Voronoi tessellation, attributed parameters hold for the domain of each Voronoi cell or atom.

- At the same time, the simulation environment is constructed from additional arbitrary distributed nodes in space. A network is established by the Delaunay tetrahedralization. At each node, a potential value will be computed. The nodes in this network do naturally act as support for the discrete electrostatic solution in the simulation domain.

Figure 4.5d depicts a sketch of the 3D simulation mesh which has the shape of a flat disc. The top face represents the APT detector. The emitter sample becomes embedded into the disc at the bottom center. In comparison, its size is considerably smaller. It amounts only to about 200 nm in diameter and 150 nm in height. Because there is no particular restriction for the placement of support points in the vacuum space, necessary nodes for computing the potential can be distributed randomly. Carefully computed trajectories with sufficient accuracy are possible if the node density decreases proportional to the field strength of the electric solution. By this choice, approximately the same number of nodes as in the case of the regular mesh is sufficient to cover a much larger length scale (1 nm $\rightarrow$ 1 cm, $\approx 0.5 \cdot 10^6$ nodes). In this way, realistic extents equal to experimental conditions are easily enabled. Thus, there is no need to apply a curved counter electrode as before in Vurpillot's original approach.

In figure 4.5b a highly magnified view of an exemplary emitter structure is presented. The height and diameter both amount to about 100 nm. Here, the whole emitter structure and not just the apex part is completely considered for the simulation. Hence, in this case, there is no need for compensating the shrinkage of the apex by shifting atoms from bottom to top.

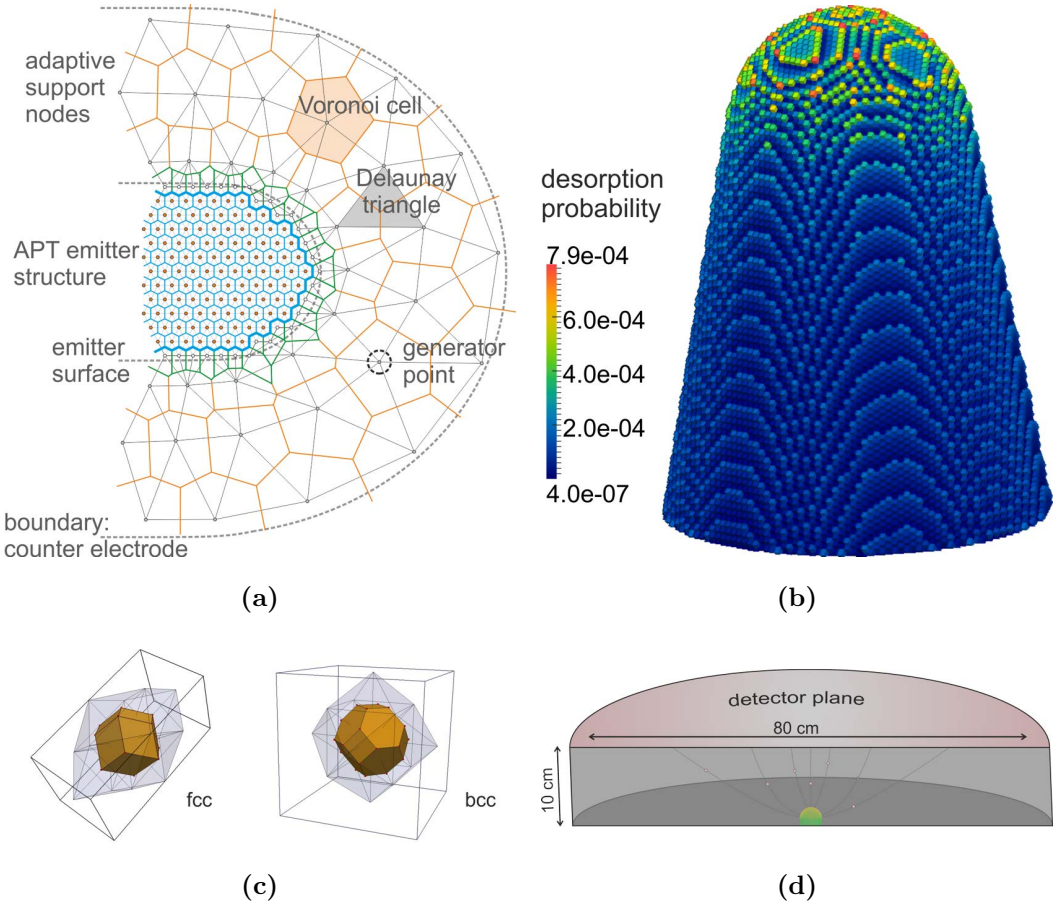

Figure 4.5.: Foundation of the generalized approach [OES13]: (a) Basis is an irregular distribution of nodes with one node at each lattice site of the field emitter and less dense nodes in the surroundings. (b) 3D model of an exemplary emitter structure. (c) Each atomic cell naturally represents as a Wigner-Seitz cell. Arbitrary lattice structures are possible. (d) The adaptive layout permits extents of the simulation box comparable with experiments.

Despite the changes, which originate from the used irregular mesh, the general procedure for simulating the field evaporation is preserved: Once the simulation environment has been constructed and the potential has been computed, the same evaporation cycle as before on the regular mesh (see p. 74) is processed. For instance, the color coding of the surface atoms in figure 4.5b resembles the desorption probability which has been derived in straight forward manner from the computed field at the centred generator point of each Wigner-Seitz cell. Inhomogeneous evaporation thresholds of atomic species (eqn. 4.4) are considered by rescaling calculated fields to evaporation probabilities. In the same way, different values for dielectricity may apply for the domain of the Wigner-Seitz cell and affect the potential of the

solution (eqn 3.34).

4.2.2. Assisted mesh generation

The simulation mesh on the basis of the regular grid could be easily established, since only the grid spacing must be set. In contrast, the application of the irregular mesh requires extra effort. Particularly, the adaptive distribution of nodes with a changing density makes the assembly difficult. Fortunately, tailored mesh generation is a common task in the field of computational geometry and we can make use of already available techniques. A ready-to-use solution suited for tetrahedral meshes is provided by the TetGen package [Si11]. Besides control of the density, the applied algorithm also ensures an appropriate numeric quality of the produced mesh. The construction of badly shaped tetrahedrons (e.g. slivers) is thereby mostly avoided.

An example of the realized mesh generation procedure is illustrated in figure 4.6. In order to bridge the scaling from microscopic to macroscopic dimensions, a set of four nested cylindric meshes is constructed, denoted by the roman numbers I to IV, respectively. The innermost basis of the constructed meshes is fixed by the user. The position of any atom in the field emitter must be provided as input. Arbitrary geometries are possible as long as the emitter geometry is of convex shape.

Using the input as a template, the first constructed mesh (I) fills the space between the provided geometry and a somewhat larger cylinder. The density of nodes is homogeneous. The remaining meshes (II to IV) each increase in size such that they perfectly nest inside each other. Despite some geometric restrictions for the tetrahedra, the density of nodes is set to drop exponentially. In order to avoid a too low density, a lower limit applies for the nodes in the most outward mesh (IV).

The complete simulation environment consists of the field emitter structure and the support mesh in the surroundings. It results from the combination of all constructed partial meshes. In a last step, distinct boundary conditions are set. The Neumann boundary condition holds for the bottom nodes, whereas the Dirichlet boundary condition holds for nodes at the sides and at the top.

Notably, only about half of the total required nodes are used for the support. The other half is used for the emitter structure. This emphasizes the enhanced efficiency compared to the former construction approach based on the regular mesh. Even if larger emitter structures are considered, the number of required nodes for the support mesh would remain almost unchanged.

From the viewpoint of a user, the automatic mesh generation completely re-

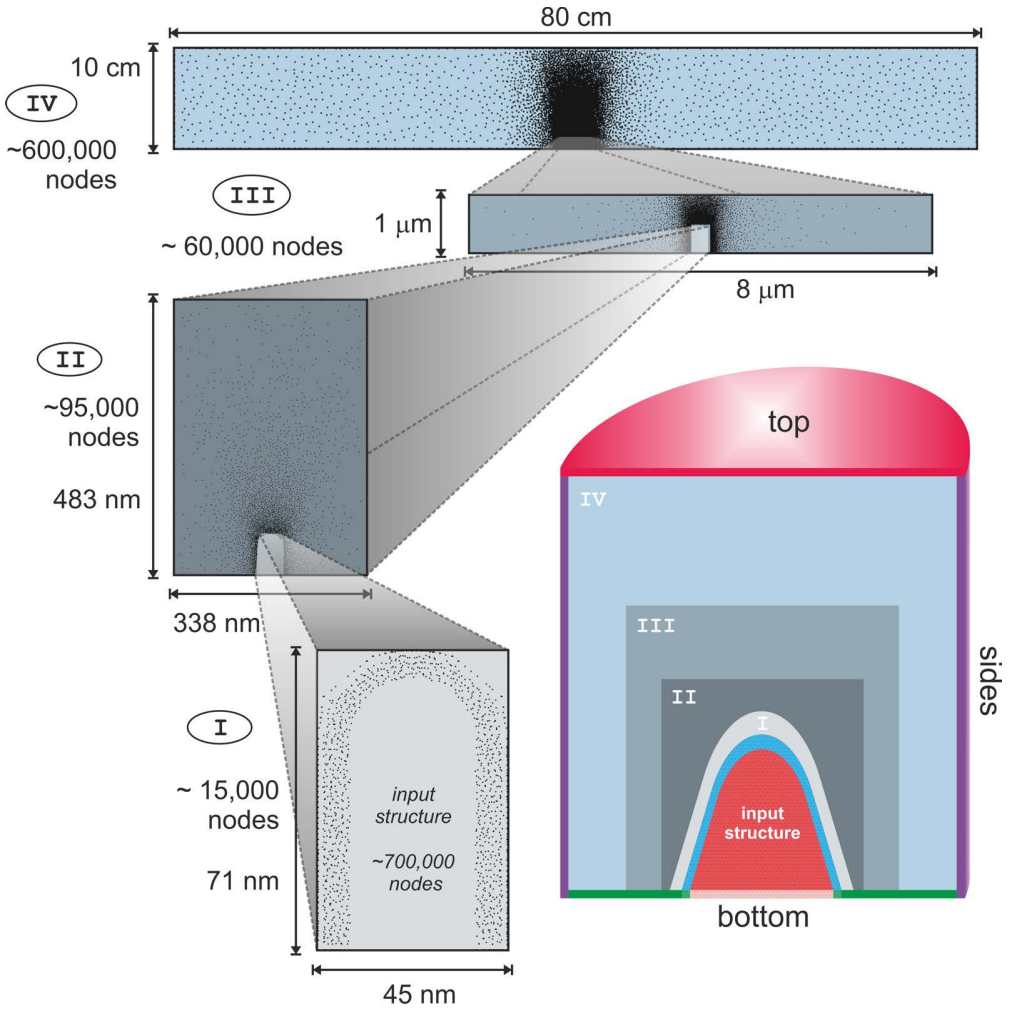

Figure 4.6.: Construction of the simulation mesh from an adaptive layout of four nested sub-meshes. Each dot represents a generator point of the Voronoi tessellation or a vertex in the Delaunay tessellation, respectively.

lieves from considering the support mesh. A tailored simulation environment is constructed only based on the provided input.

4.2.3. Properties of the electrostatic solution

The iterative numeric solution scheme for the potential turns out to be astonishingly stable. Convergence is achieved reliably for all provided input structures.

The accuracy of the numeric solution is limited by the machine precision [Suk03]. However, as the distinct potential in between two nodes of the mesh is accessed by linear interpolation, the density of nodes certainly affects the interpolation error.

In order to characterize the derived solution two questions are addressed in the following.

Of which quality are the solutions for the potential and the field close to the emitter structure?

The answer determines the possible quality of the predicted trajectories. Figure 4.7a depicts the potential in the vicinity of a field emitter (cylinder with 20 nm radius and 50 nm height). In this example, the simulation environment was set to be considerably smaller than usual (cylinder with 2 µm radius and 1 µm height). Two kinds of solutions have been calculated: Both the coloured potential in the background and the inscribed black equipotential lines refer to the solution of the new approach. A second solution has been derived by making use a commercial finite element software package[1]. This result is depicted by the white equipotential lines. The obtained solutions almost perfectly match each other. Little differences at the bottom boundary are visible which trace back to the particular implementation of the Neumann boundary condition.

However, for the trajectories, the field is decisive. In the case of the generalized approach, two distinct solutions are presented: The field in figure 4.7b depicts the derivative of the potential which is computed in first order accuracy (see sec. 3.3), while figure 4.7c shows the more accurate computation in second order (see ap. B). The enhanced accuracy of the latter approach is clearly revealed by the inscribed equi-field lines which appear more smooth. Directly at the bottom, the field is not computed. Instead, a fixed zero field applies. Although this artificial choice severely disturbs the equi-field lines, it is of almost no significance for any computed trajectories starting at the emitter apex. Apart from this, the computed fields do compare well with the reference field from the FEM solution presented in figure 4.7d. Quantitatively, this is demonstrated by the graphs along the z-direction (fig. 4.7e and fig. 4.7f).

Notably, the numeric effort for computing the second order field is about ten times higher. For this reason trajectories are by default computed with first order accuracy in this work. The introduced error is considered to be acceptable. This choice finds its confirmation in the detailed pattern of obtained field desorption maps which are presented in the next chapter (see p. 104).

[1] "Comsol Multiphysics", version 3.5

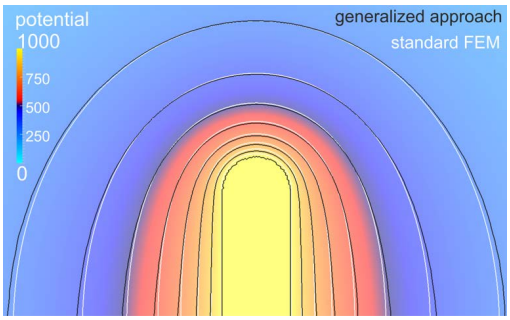

(a) Potential in the FEM and the new generalized approach.

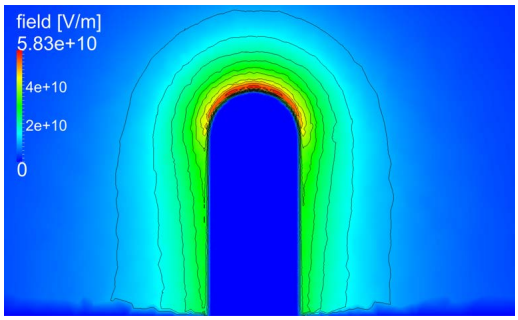

(b) Field distribution in the generalized approach using the first order approximation.

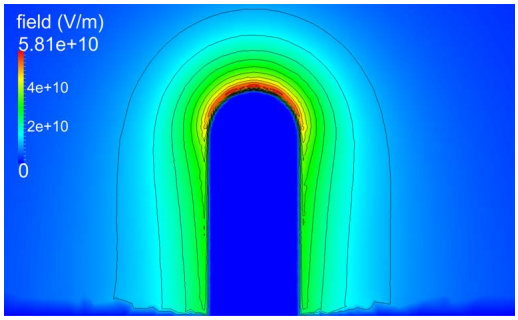

(c) Field distribution in the generalized approach using the second order approximation.

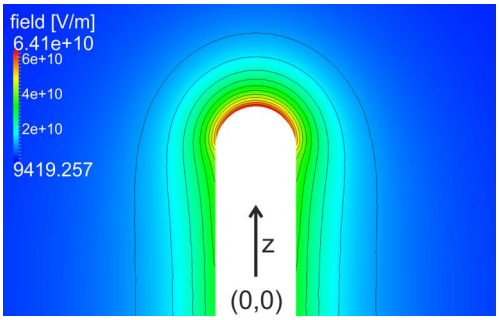

(d) Derived field from the FEM solution.

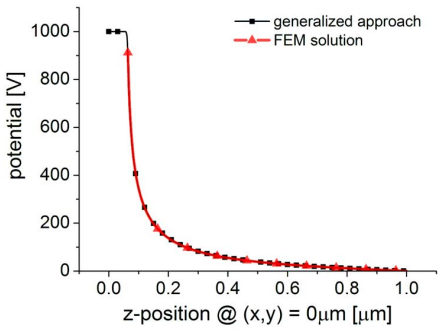

(e) Comparison of the potential along the z-axis in front of the apex.

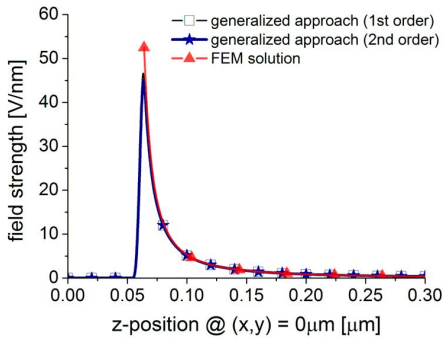

(f) Comparison of the field strength along the z-axis in front of the apex.

Figure 4.7.: Comparison of the numeric solutions derived from a standard finite-element approach with the solution derived from the irregular Voronoi mesh.

What are the general dependencies of the potential and the field on a larger length-scale?

For investigation in this regard, a simulation box with an emitter to detector distance of 10 cm is considered. Figure 4.8 presents the change of both the potential and the field along the centre axis. From the almost straight curve of the field, a general dependency according to

$$E(x) \cong A \cdot x^B \; A, B \in \mathbb{R} \tag{4.10}$$

is assumed which leads to

$$\varphi(x) = \varphi(x_0) + \frac{A}{B+1} \cdot x^{(B+1)} \tag{4.11}$$

for the potential. Here, A is a constant in units of $\mathrm{V\,nm^{-1}}$ and B denotes a dimensionless parameter. The applied fits match quite well, whereas the analytic solution on the basis of the paraboloidal model neither compares to the potential nor to the field.

The field directly at the detector at 10 cm shows a distinguished curvature. It smoothly approaches the outward boundary. Although this behaviour appears quite symmetric to the field change at the emitter surface at 100 nm, the reason for this feature is unclear. It may possibly be an artifact of the numeric approach.

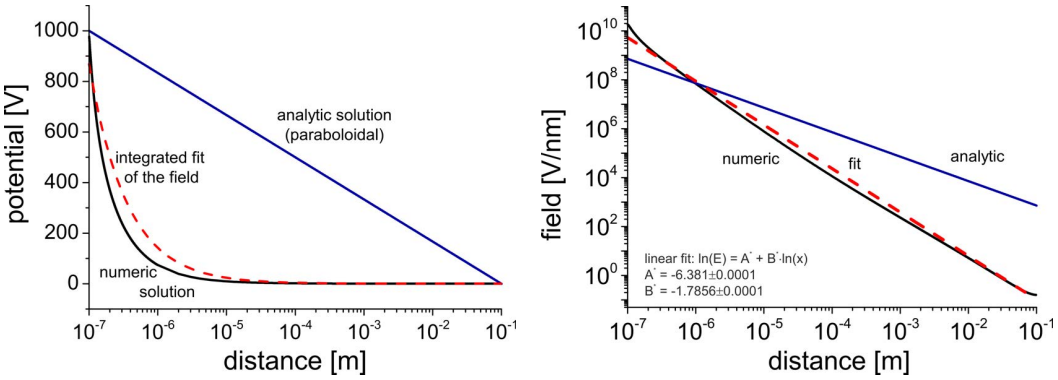

(a) (b)

Figure 4.8.: Change of potential and field in far distance of the emitter structure: comparison of the paraboloidal with the numeric solution.

4.2.4. Consideration of the polarization force for evaporation

The representation of the field emitter structure by an arrangement of Wigner-Seitz cells is a main characteristic of the new generalized approach. We will now fully adopt this concept and show how the description of the atoms by different Voronoi cells enables us to directly evaluate field-induced forces for the desorption from the emitter surface.

Although the idea of an acting force seems to be straight forward, this picture has not yet at all been followed in the APT community. Instead, the field magnitude is usually considered as the important parameter. This particularly results from the historic development of APT as the successor of the FIM technique. The often used terms "best image field" or "best image voltage" probably originate from the very early experiments and have determined the way of thinking since that early time.

In fact, a description on the basis of the field is not completely wrong. In the case of homogeneous materials, a uniform effect of the field on the charges may be assumed. Therefore, no special care must be taken and the force becomes proportional to the field. But in the case of inhomogeneous materials, a different effect of the field on the charges can no longer be neglected. In order to account for non-uniform polarizability, the force is considered as dependent on both a field induced charge $q(\boldsymbol{E})$ and the field:

$$\boldsymbol{F}(\boldsymbol{E}) = q(\boldsymbol{E}) \cdot \boldsymbol{E} \tag{4.12}$$

Then, already for the case of a linear polarization ($q(\boldsymbol{E}) \sim E$), this results in a parabolic dependency which enhances forces at an elevated field strength.

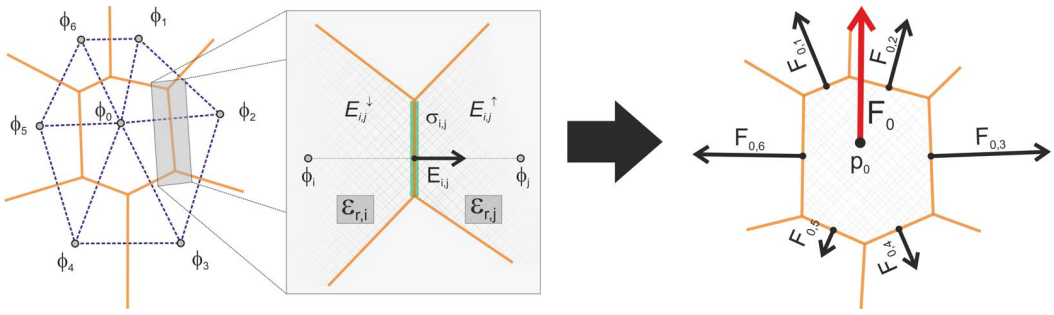

(a) **(b)**

Figure 4.9.: Sketch depicting the calculation of the exerted force on a Voronoi cell [OES13]. (a) Facets of the Voronoi cell are considered as electrostatic interfaces ($\epsilon_{r,i} \neq \epsilon_{r,j}$) at which the fields $E_{i,j}$ induce polarization charges $\sigma_{i,j}$. (b) The force, which pulls at the Voronoi cell, equates to the vector sum over all facets.

This idea is now applied to the simulation approach. In figure 4.9, the Voronoi cell of a single atom is depicted. Each of its six facets is linked to a pair of generator points in the Delaunay tessellation at which the potential has been calculated. On either side of the facets, different values of dielectricity are present, which give rise to the formation of a surface charge at the respective interfaces. Taking into account this surface charge and the constant field along the surface enables us to calculate the force. The actual situation for a single facet is shown in the magnified view. Based on equation (3.33), the displacement field in direction normal to the interface reads

$$D_{i,j} = \frac{\varphi_i - \varphi_j}{|\boldsymbol{p}_i - \boldsymbol{p}_j|} \cdot \epsilon_0 \cdot \frac{2 \cdot \epsilon_{r,i}\epsilon_{r,j}}{\epsilon_{r,i} + \epsilon_{r,j}} \tag{4.13}$$

In correspondence to the contiguity equation (3.22), $D_{i,j}$ remains constant across the interface whereas the effective electric field strengths $E_{i,j}^{\downarrow}$ and $E_{i,j}^{\uparrow}$ are different on either side of the interface according to the respective values for dielectricity:

$$\begin{aligned} E_{i,j}^{\downarrow} &= \frac{D_{i,j}}{\epsilon_0 \epsilon_{r,i}} = \left(\frac{\varphi_i - \varphi_j}{|\boldsymbol{p}_i - \boldsymbol{p}_j|} \cdot \frac{2}{\epsilon_{r,i} + \epsilon_{r,j}} \right) \cdot \epsilon_{r,j} \\ E_{i,j}^{\uparrow} &= \frac{D_{i,j}}{\epsilon_0 \epsilon_{r,j}} = \left(\frac{\varphi_i - \varphi_j}{|\boldsymbol{p}_i - \boldsymbol{p}_j|} \cdot \frac{2}{\epsilon_{r,i} + \epsilon_{r,j}} \right) \cdot \epsilon_{r,i} \end{aligned} \tag{4.14}$$

This finding is consistent with the field strength which derives directly from the potential difference between the nodes p_i and p_j:

$$E_{i,j} = -\frac{\varphi_j - \varphi_i}{|\boldsymbol{p}_j - \boldsymbol{p}_i|} = \frac{1}{2} \cdot \left(E_{i,j}^{\downarrow} + E_{i,j}^{\uparrow} \right) \tag{4.15}$$

The discontinuity in the field corresponds to the formation of an excess charge at the interface. The respective charge density $\sigma_{i,j}$ is obtained from the application of the Gaussian law and yields

$$\sigma_{i,j} = \frac{q_{i,j}}{||A_{i,j}||} = \left(E_{i,j}^{\uparrow} - E_{i,j}^{\downarrow} \right) \cdot \epsilon_0 = \frac{\varphi_i - \varphi_j}{|\boldsymbol{p}_i - \boldsymbol{p}_j|} \cdot 2\,\epsilon_0 \cdot \frac{\epsilon_{r,i} - \epsilon_{r,j}}{\epsilon_{r,i} + \epsilon_{r,j}} \tag{4.16}$$

We see, the charge decisively depends on the values of dielectricity at the interface. Combination of the results from equation (4.15) and (4.16) leads to the force in normal direction to the facet

$$\boldsymbol{F}_{i,j} = \sigma_{i,j}\, ||A_{i,j}|| \cdot E_{i,j} \cdot \frac{\boldsymbol{p}_j - \boldsymbol{p}_i}{\left(\boldsymbol{p}_j - \boldsymbol{p}_i\right)^2} \tag{4.17}$$

The total force on the Voronoi cell is then expressed by the vector sum

$$\boldsymbol{F}_i = \sum_j \left[\left(\frac{\varphi_j - \varphi_i}{|\boldsymbol{p}_j - \boldsymbol{p}_i|} \right)^2 \cdot 2\,\epsilon_0 \cdot \frac{\epsilon_{r,j} - \epsilon_{r,i}}{\epsilon_{r,j} + \epsilon_{r,i}} \cdot \frac{\boldsymbol{p}_j - \boldsymbol{p}_i}{|\boldsymbol{p}_j - \boldsymbol{p}_i|} \right] \tag{4.18}$$

over all present facets (fig. 4.9b).

For the final application to the simulation, we have to consider that the likelihood for a surface atom to become field evaporated should not depend on different volumes of the Voronoi cells in the model. This prevents a direct use of equation (4.18). In contrast, a measure, which is independent of the geometry, is obtained if the force gets divided by the surface area of the Voronoi cell $A_i = \sum_j ||A_{i,j}||$. With this, the evaporation probability is effectively computed by the deduced stress $\tau_i := \frac{F_i}{A_i}$ on the cell. Distinguished evaporation thresholds of different atomic species are normalized with the squared critical field values

$$\omega_i \sim \tau_i \,/\, E^2_{\mathrm{Crit,i}} \tag{4.19}$$

in analogy to the standard approach (eqn. 4.4). In the experiments, any field induced forces are counter-balanced by the solid bonding. If it gets too weak, field evaporation takes place. Related bonding forces may be derived from pair interaction potentials between the respective next neighbour atoms. Such a more realistic treatment of the physics may be introduced in a further development stage of the simulation approach but is not considered here. Like it was explained in section 4.1.2, equation (4.19) appears equally justified if an sufficiently homogeneous binding of different atoms can be assumed.

5. Imaging characteristics of detector events

Essential for the imaging characteristics in APT is the electric field. The microscopic field at the emitter surface triggers the desorption of atoms and is responsible for the detailed pattern in the ion projection at the detector. On the other hand, the mesoscopic field in between the emitter and the detector is comparably weak. Nevertheless, in little distance to the surface ($\ll 1\,\mu m$), the field is sufficiently strong and can affect the ion trajectories. For this field, the shape of the emitter shaft is important.

In this chapter, we address the effects of both the mesoscopic and the microscopic field conditions, and further demonstrate the impact of statistical desorption.

5.1. Field properties and trajectories

Reliable information on the ion projection constitutes the basis of the 3D reconstruction. Commonly, image formation is understood by considering a simple point projection (ch. 2). In this way, positions at the emitter apex become linked to distinct positions at the detector. The deviation from a radial projection is expressed by the image compression factor ξ (eqn. 2.16). Determination of this parameter together with the field factor β (eqn. 2.15) enables the inverse projection in the reconstruction.

Initially, both parameters were considered as independent constants which either depend on the instrumental setup or on the emitter geometry. But recent work of Loi et al. [Loi+12] and Vurpillot et al. [Vur+11] suggests that this is probably not the case. Ion trajectories for different emitter, electrode, and detector configurations have been tested. Results indicate that both parameters are coupled to each other by a cubic dependency with $\beta \sim \xi^3$. The detailed analysis of experimental wide angle atom probe data additionally reveals a clear dependency of both parameters on the estimated specimen shape [Gau+11].

In face of this existing work, a similar study is presented in the following. Besides the confirmation of the published results, the main objective is to characterize the imaging conditions with the new simulation approach and to demonstrate the comparability with experiments. Therefore, the basic geometry of a truncated cone with spherical apex is investigated (fig. 5.1). Different geometries with the taper half angle γ_{tip} in the range between 0° to 30° and the curvature radius of the apex r_{tip} between 5 nm to 40 nm are considered. All samples have a fixed length of 100 nm in order to minimize boundary effects in the simulation.

The detailed procedure is as follows: First, each sample is placed in a simulation box with extents of 40 cm × 40 cm × 10 cm. Subsequently, the electrostatic solution

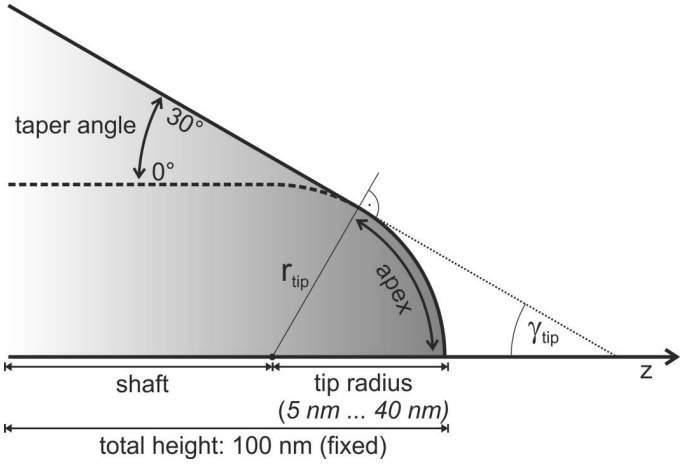

Figure 5.1.: Sketch of the sample geometry which applies for investigations of the emitter field and imaging properties of trajectories.

is computed and ion trajectories originating from the surface sites of the sample are calculated. The applied voltage is in all cases the same ($\Delta\varphi = 1\,\mathrm{kV}$) such that an effect of the different geometries on the field can be studied.

In order to get an impression of the obtained trajectory courses, the example of the emitter with $r_{\mathrm{tip}} = 20\,\mathrm{nm}$ and $\gamma_{\mathrm{tip}} = 15°$ is presented in figure 5.2. Initially at rest, the velocity of the ions reaches $50\,\mathrm{km\,s^{-1}}$ already in a distance of about 100 nm from the emitter. This amounts to about two thirds of the maximum speed. The magnified part in figure 5.2 reveals the sensitivity on the location at the apex surface. The distinct launch position at a kink site or the edge of a low indexed terrace leads to severe deflections. Some trajectories do even intersect with each other. This view at the microscopic scale suggests that the assumption of a radial projection law is probably error-prone and may not be best suited as basis of any reconstruction. However, in order to describe the formed image at the detector

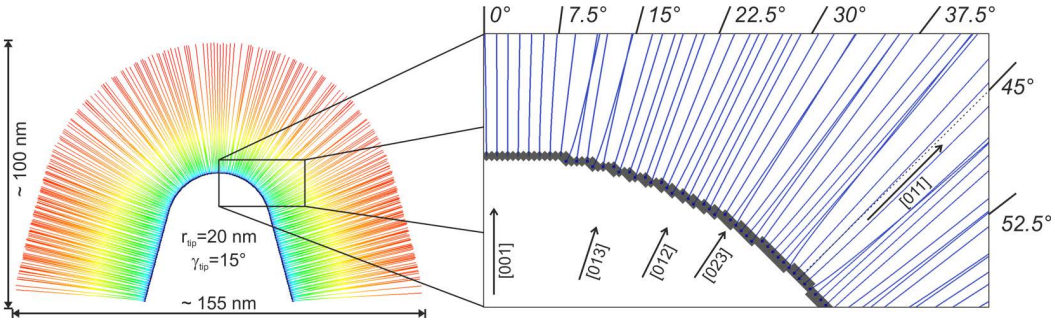

Figure 5.2.: Cross-section through the simulation space highlighting the course of computed trajectories. The colouring depicts different velocities. In the magnified view, a clear deviation from a straight line can be seen. For example, this is indicated by the dotted marker line at the [011] direction.

such a general projection law appears nevertheless justified.

In the experiments, the active imaging area of the emitter is constrained by the demand of a sufficient field strength. This condition approximately coincides with the presence of a sufficiently curved apex and cancels out the outer part of the trajectories plotted in figure 5.2. If the conical shaft is excluded, the imaged apex area depends on the taper angle and the tip radius as equated by

$$A_{\mathrm{tip}} = 2\pi r_{\mathrm{tip}}^2 \cdot (1 - \sin \gamma_{\mathrm{tip}}) \tag{5.1}$$

5.1.1. Field factor

With regard to this restriction, the surface field at the apex is analysed for different tip radii and taper angles. Figure 5.3a shows data of the microscopic field distribution. From the histogram, a single "macroscopic" field is derived based on the statistic measure of the percentile, e.g. $p_{99\%}$. This choice facilitates the comparison of the field for different geometries. It is preferred to the maximum field because the percentile is more robust against fluctuations originating from not so ideally equilibrated emitter shapes. In figure 5.3b and figure 5.3c this way extracted "macroscopic" fields are plotted against the inverse curvature radius and the taper angle, respectively.

In general, the field is expected to be inversely proportional to the curvature radius. This relation is reasonably confirmed although only four different radii for one taper angle are evaluated. The best match is seen for an taper angle of 0° whereas for 30° increased deviations from the linear relation occur. For the change with respect to the taper angle, we see a linear decrease. It seems that the taper angle has a particularly strong effect on the apex field for a small curvature radius.

In summary, both observations, the dependence of the apex curvature as well as on the taper angle of the shaft, may be taken into account by an extension to the standard field factor:

$$\beta(\gamma_{\mathrm{tip}}) = \beta_1/(1 - \beta_2 \cdot \gamma_{\mathrm{tip}}) \tag{5.2}$$

Accordingly, the classic equation (2.15) for the surface field is modified to

$$E(r_{\mathrm{tip}}, \gamma_{\mathrm{tip}}) = \frac{\Delta\varphi}{\beta(\gamma_{\mathrm{tip}})\, r_{\mathrm{tip}}} = \frac{\Delta\varphi}{r_{\mathrm{tip}}} \cdot \frac{1 - \beta_2\, \gamma_{\mathrm{tip}}}{\beta_1} \tag{5.3}$$

Here, β_1 refers to the classic definition equal to $\beta(\gamma_{\mathrm{tip}} = 0)$. For quantitative values, the expression $\left(\frac{E(r_{\mathrm{tip}},\gamma_{\mathrm{tip}})\cdot r_{\mathrm{tip}}}{\Delta\varphi}\right)^{-1}$ is plotted against the taper angle (fig. 5.3d). The slope of the plot reveals β_2. Each point represents the mean value from the data

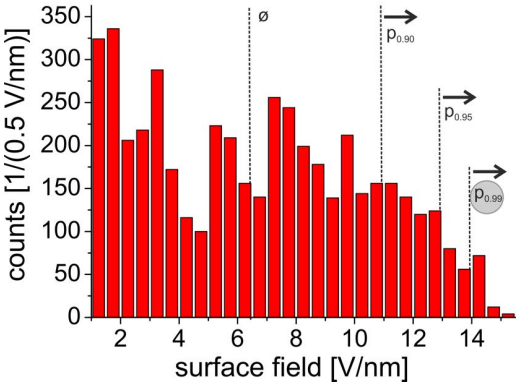

(a) Histogram of the surface field distribution at the sample with $r_{\mathrm{tip}} = 20\,\mathrm{nm}$ and $\gamma_{\mathrm{tip}} = 15°$. The percentile $p_{99\%}$ is located at about $14\,\mathrm{V\,nm^{-1}}$.

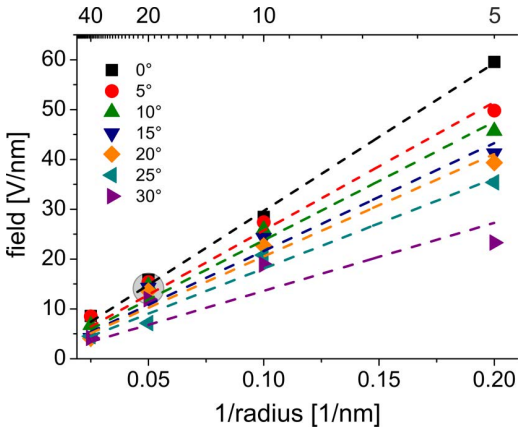

(b) Field versus curvature radius. The situation shown in (a) is indicated by the gray encircled data point.

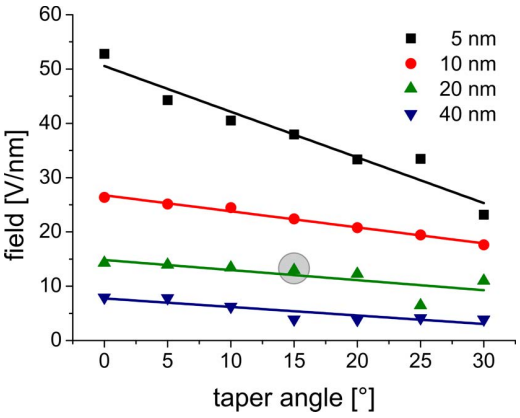

(c) Field versus taper angle. The situation shown in (a) is indicated by the gray encircled data point.

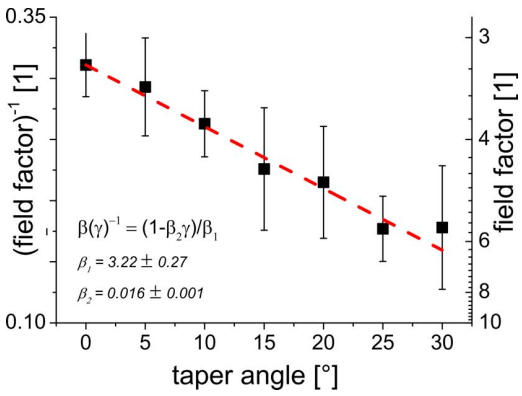

(d) Field factor versus taper angle

Figure 5.3.: Dependence of the surface field on the emitter geometry

with $r_{\mathrm{tip}} = const.$, error bars result from the standard deviation. As one can see, the field factor increases with the taper angle. The determined variation of the field factor in the range between 3 to 8 appears realistic and is comparable to experiments [Vur+11].

5.1.2. Image compression

Besides the field factor, the image compression represents the second ingredient for the 3D reconstruction. For quantitative values, the imaging angle

$$\vartheta_{\mathrm{img}} = \arctan\left(\frac{\sqrt{x_{\mathrm{Det}}^2 + y_{\mathrm{Det}}^2}}{d_{\mathrm{flight}}}\right)$$

of each ion trajectory is compared with the corresponding launch angle

$$\vartheta_{\mathrm{launch}} = \arccos\left(\frac{(\boldsymbol{p}_{\mathrm{tip}} - \boldsymbol{p}_{\mathrm{ctr}}) \cdot \hat{e}_z}{|\boldsymbol{p}_{\mathrm{tip}} - \boldsymbol{p}_{\mathrm{ctr}}|}\right)$$

of the initial surface site. The launch angle is derived by considering the centre of the constructed sphere about the apex at

$$\boldsymbol{p}_{\mathrm{ctr}} = (z_{\mathrm{max}} - r_{\mathrm{tip}}) \cdot \hat{e}_z$$

Figure 5.4a depicts again the case with $r_{\mathrm{tip}} = 20\,\mathrm{nm}$ and $\gamma_{\mathrm{tip}} = 15°$. About 5,000 trajectories are evaluated. The line fit indicates a proportionality between the imaging and the launch angle. It holds almost over the whole value range. Visible oscillations for $\vartheta_{\mathrm{launch}} \leq 20°$ trace back to atomic terraces at the apex (e.g. compare with fig. 5.2). In contrast, deviations for $\vartheta_{\mathrm{launch}} \geq 70°$ are probably caused by the transition from the apex to the shaft.

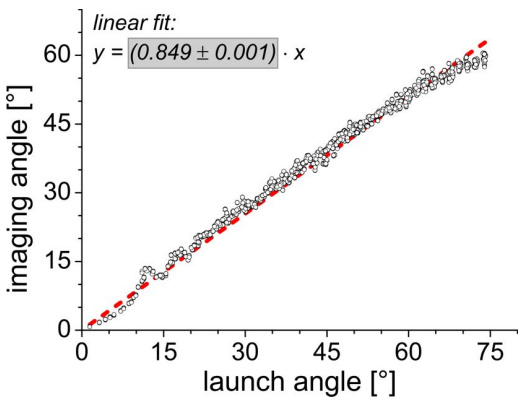

(a) Imaging angle versus launch angle for the emitter with $r = 20\,\mathrm{nm}$ and $\gamma = 15°$.

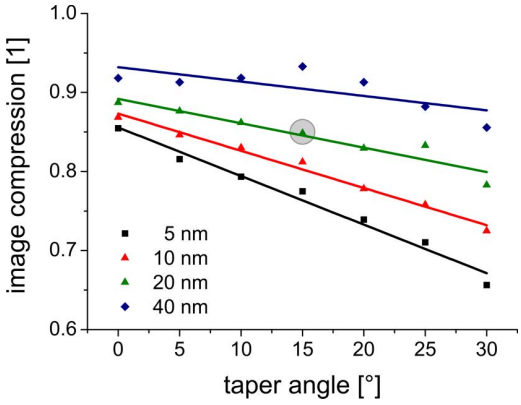

(b) Image compression versus taper angle. The gray encircled data point represents the slope from the line fit in (a).

Figure 5.4.: Dependence of the image compression on the emitter geometry

The fitted slope directly corresponds to the image compression. Results for different taper angles are shown in figure 5.4b. The image compression decreases linearly with increasing taper angle. Interestingly, the estimated maximum amounts approximately to about 0.9 in the case of the cylindric geometry ($\gamma_{\text{tip}} \equiv 0°$). Here, it appears to depend only weakly on the curvature radius.

5.1.3. Interdependence of surface field and image compression

Finally, the recently revealed connection of the emitter field to the image compression is shortly addressed as both parameters have already been evaluated. Although it is already clear from basic considerations that the field strength at the apex and the image projection properties are linked with each other, it is nevertheless astonishing that a simple cubic relation $E_{\text{Surf}} \sim \xi^3$ holds. Indeed, the data in figure 5.5 show this particular dependence clearly. The linear fits almost perfectly match. An exception is the case with 40 nm curvature radius where half of the data points barely fit to the line. In addition, it shows a negligible dependency of the image compression on the field. For this discrepancy, inaccuracies in the determined image compression (see fig. 5.4b) may be responsible. Regardless of this, overall results match reasonably well to those from the literature.

However, in this work as well as in the study of Vurpillot et al. [Vur+11], the Neumann boundary condition applies at the bottom of the simulation box. Since this choice seems appropriate if a cylindric emitter geometry is analysed, it appears questionable whether it is suited to approximate the field of an infinitely extended cone in a realistic manner.

In contrast, this conceptional weakness does not hold for the results by Loi et

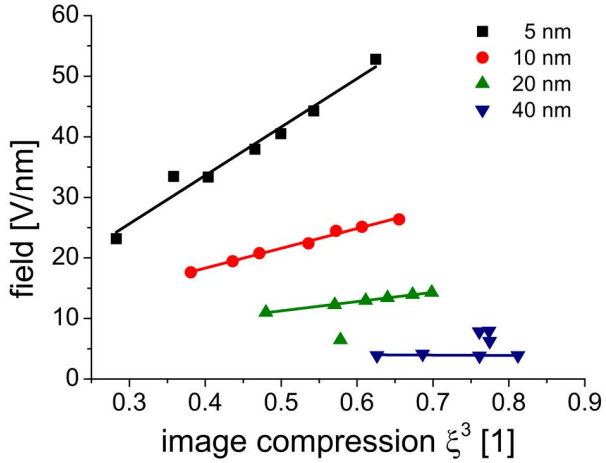

Figure 5.5.: Cubic relation of the field factor to the image compression.

al. [Loi+12]. In their work, the solution for the potential is founded on a full-scale boundary element method (BEM). In this way, they are able to consider the field for a quite realistic geometry. Investigated emitter samples were of up to 5 mm in length. This approach resulted in the same cubic dependence. Therefore, it appears unlikely that boundary conditions in the simulation are responsible for this finding.

Anyway, in future simulations, a possible effect of the boundary conditions can be avoided if an enlarged emitter shaft, e.g. with a length of hundred times the curvature radius, is considered.

5.2. Detector event maps

We will now change the focus of interest and take a look at the distribution of the hit events at the detector. Results from two different approaches are presented. In the static *surface imaging mode*, ion trajectories originating from all surface sites of the emitter sample are considered simultaneously. In contrast, in the kinetic *desorption mode*, trajectories of surface atoms field evaporating atom by atom are considered. The first approach mimics the imaging conditions in FIM experiments, the latter one accounts for APT experiments.

5.2.1. Surface imaging mode

Figure 5.6 depicts in detail the spherical curved apex of two distinguished bcc emitter structures. The preset lattice constant is 5 Å. The depicted diameter of 50 nm almost resembles the size of an experimental tip. In the illustration, more than 15,000 surface sites can be distinguished. Each surface atom of the emitter is represented by its Voronoi cell. Depending on how the lattice is oriented, different surface morphologies appear. The colour coding of single Voronoi facets denotes the surface field. Different colour contrast clearly emphasizes the location of prominent lattice planes which are revealed in the form of concentric rings. A close inspection of the morphology is enabled by the magnified insets. The shape of individual Wigner-Seitz cells becomes clearly visible. Even the specific orientation of the cells in correspondence to the lattice orientation, $\langle 011 \rangle$ or $\langle 111 \rangle$, is visible.

Very similar to this view at the plain apex is the 2D projection, which results from the computed trajectory hits in the detector plane. Data for the sc, bcc and fcc cubic lattices and for ordinary orientations are presented in figure 5.7. The imaging distance is 10 cm. For all emitter samples, the same lattice spacing as before, 5 Å, applies. An imaging contrast similar to the FIM is mimicked by plotting spheres

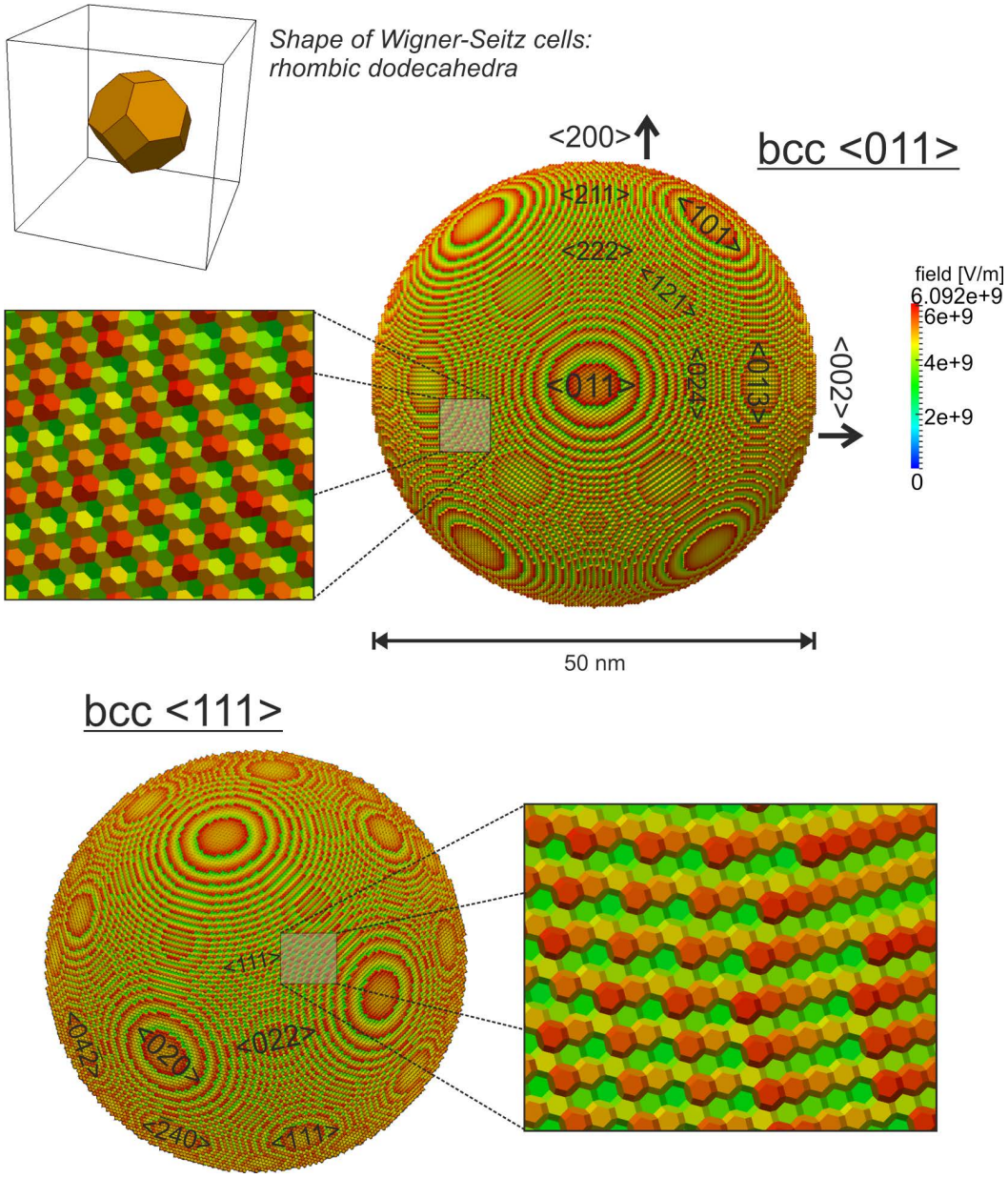

Figure 5.6.: Top view of the apex structures of a bcc ⟨011⟩ and bcc ⟨111⟩ emitter sample. The detailed structure consists of about 15,000 Voronoi cells. In this way, a distinct surface morphology depending on the lattice orientation is established.

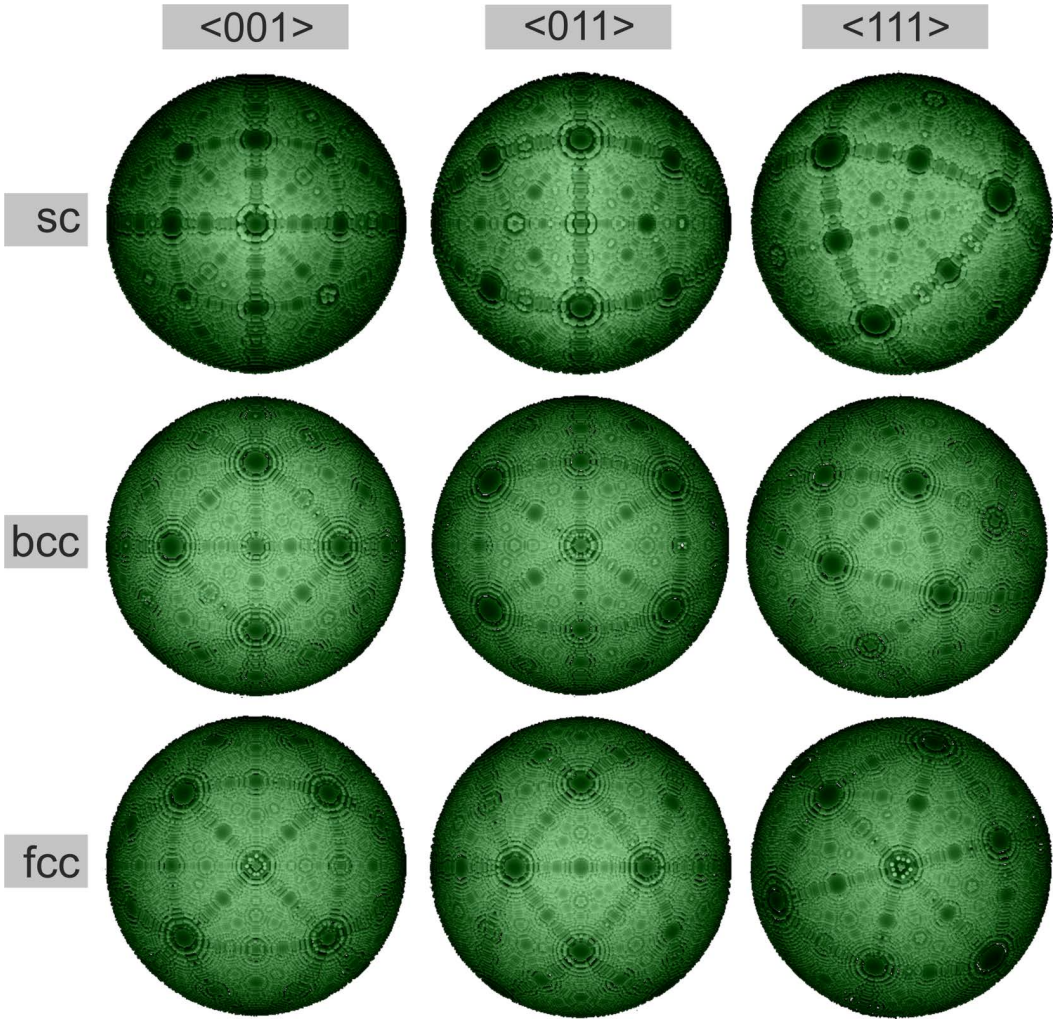

Figure 5.7.: Detector hit maps of calculated surface trajectories for various emitter structures. Results mimic those obtained from FIM experiments.

of different size and setting the colour intensity corresponding to the field strength. This way, terrace edges in the vicinity of poles appear pronounced by a strong bright contrast. But also single protruding surface atoms (e.g. in the centre of the fcc $\langle 111 \rangle$ projection) are particularly striking. Somehow astonishing is the darker appearance of the zone lines in between low indexed poles.

Apart from the visible contrast, the pattern of the poles exhibits the expected two-, three- and fourfold symmetry according to the respective $\langle 011 \rangle$, $\langle 111 \rangle$ and $\langle 001 \rangle$ orientations. The sizes of equivalent poles in the sc, bcc, and fcc lattices do not directly compare. In the microscopic picture, the apex region about the poles is flattened. The observed pole pattern resembles this kind of facetting. The apparent

size of the poles corresponds to the extents of the facets.

5.2.2. Desorption mode

Another situation emerges if trajectories in the desorption mode are analysed. In this case, the detector positions originate from simulated field evaporation at the emitter surface. According to the iterative procedure described in chapter 4.1, detector events are obtained one after the other. The sequence is controlled by the respective surface field. Results are therefore in clear contrast to that in the surface imaging mode.

For the analysis, the same set of emitter samples applies. More than 200,000 evaporation events from each emitter are simulated and the detector positions are recorded. Figure 5.8 presents the results in the form of 2D histograms. The colour scale denotes the hit intensity. As before, patterns which clearly relate to the lattice structure and the respective lattice orientation are observed. Distinct crystallographic features like poles and zone lines are immediately visible.

Distribution of the hit intensity

At first glance, the general distribution of the detector hits is particularly striking. The maximum intensity is located at the center with a strong outward decrease. Indeed, if the histogram of the detector hits is plotted against the imaging angle, the obtained distribution reveals excellently the expected relationship for the desorption flux described before in section 2.2.5 (eqn. 2.30).

As an example, the case of the fcc $\langle 110 \rangle$ emitter structure is shown in figure 5.9. The curve shows a dip at about 30° which is due to the visible depletion at the $\langle 111 \rangle$ pole in the field desorption map (see fig. 5.8).

Fitting of the hit distributions according to equation (2.30) enables an alternative approach for determining the image compression factor. In the depicted example, an image compression of $\xi = 0.83 \pm 0.01$ is estimated. Respective results for all combinations of the lattices and orientations are summarized in table 5.1. Astonishingly, results group nicely depending on the lattice type. An increase from 0.83 for bcc to 0.92 for sc is seen. A significant difference in the dependence of the lattice orientation is not recognized. The systematic shift shows that the estimated image compression depends on the lattice structure. Although, it is worth mentioning that the values for the image compression in table 5.1 are not far away from the previous results presented in figure 5.4., they do not coincide within the estimated

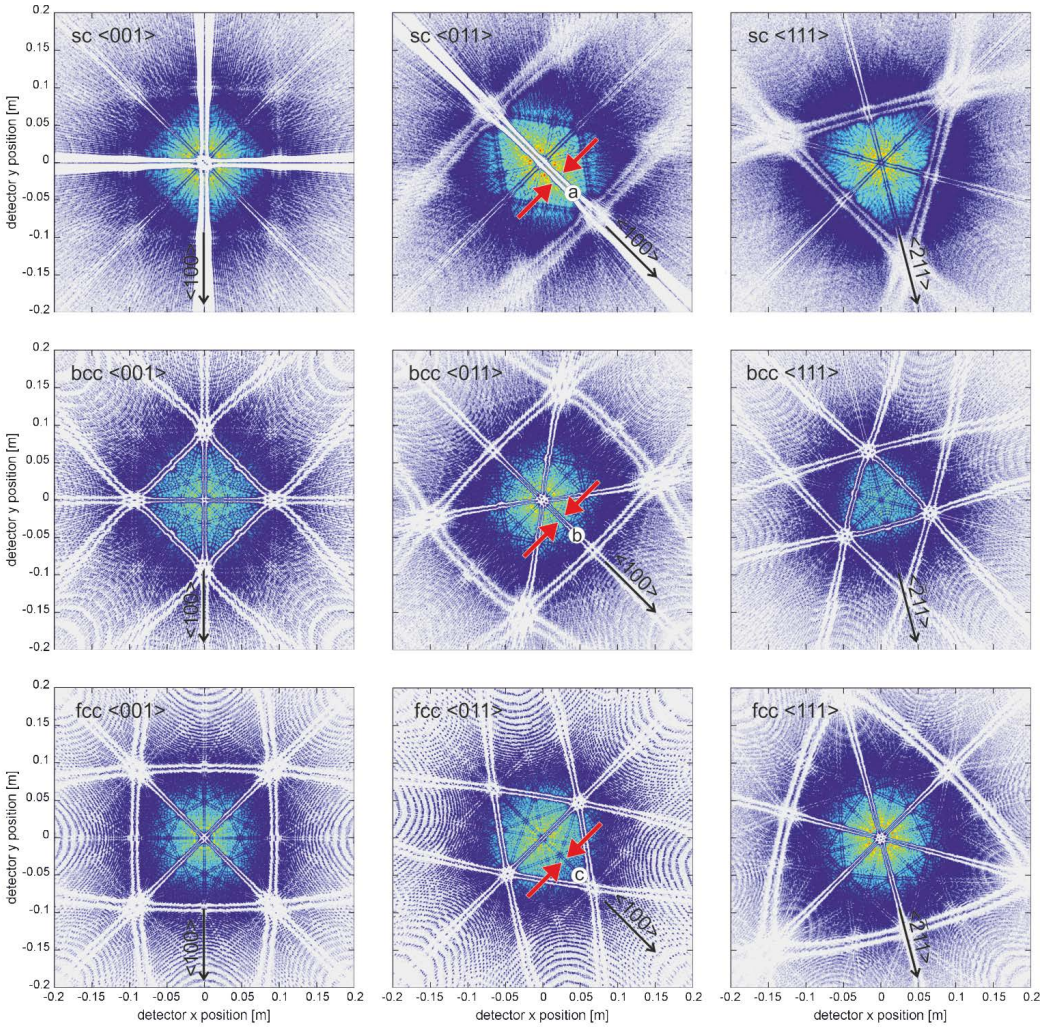

Figure 5.8.: Event positions in the desorption mode for various emitter structures [OES13]. The sequential field evaporation from the surface is determined by those sites which are exposed to the maximum field. Visible patterns of the 2D histograms are comparable to experimental field desorption maps. Labels (a), (b), and (c) in the centred column denote the [100] zone lines in the case of [011] orientation. The width for sc, bcc, and fcc changes by the ratio 4:2:1.

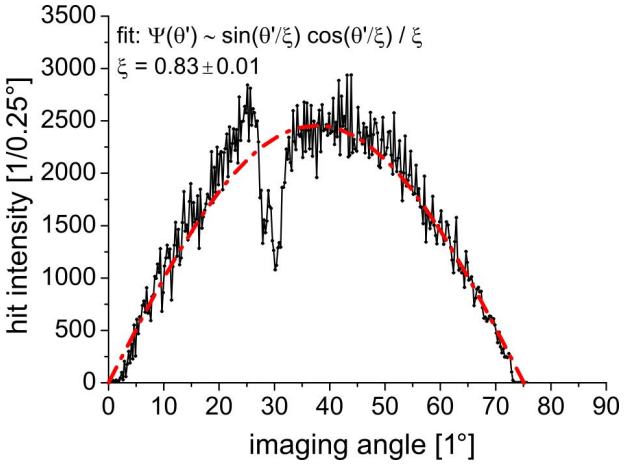

Figure 5.9.: Angular distribution of the hit intensity at the detector. The case for the fcc ⟨110⟩ structure is shown as an example of the general behaviour.

Table 5.1.: Values of the image compression derived from the desorption maps.

lattice	ξ
sc ⟨100⟩	0.91 ± 0.01
sc ⟨110⟩	0.93 ± 0.01
sc ⟨111⟩	0.92 ± 0.01
bcc ⟨100⟩	0.87 ± 0.01
bcc ⟨110⟩	0.86 ± 0.01
bcc ⟨111⟩	0.88 ± 0.01
fcc ⟨100⟩	0.84 ± 0.01
fcc ⟨110⟩	0.83 ± 0.01
fcc ⟨111⟩	0.83 ± 0.01
mean value	0.87 ± 0.04

error bounds.[1]

Particular features of the zone lines

Another striking feature of the desorption maps is the detailed structure of the zone lines. These are imaged by rows of atoms which are decorated by a depleted stripe to the left and to the right. As an outcome of the new simulations, the width of the depletion seems to depend on local neighbour distances in the lattice. E.g. for the case of the ⟨011⟩ structures, the depleted width at the ⟨001⟩ zone line is assumed to be given by $\sqrt{2}\,d_0$ for sc, $\sqrt{2}/2\,d_0$ for bcc, and $\sqrt{2}/4\,d_0$ for fcc (fig. 5.10). Thus, the expected ratio amounts to 4:2:1, which exactly matches the observed width in the corresponding desorption maps (fig. 5.8).

In this regard, another interesting observation is made if the field at desorption gets considered. For illustration, figure 5.11 depicts the example of a bcc ⟨100⟩ structure. The extents of the plotted apex are extraordinary huge.[2] Approximately

[1] The applied conical test structures have been assembled using a bcc lattice with 5 Å lattice spacing.

[2] The simulation was originally intended for testing the efficiency of the simulation code for dealing with huge data sets. The prepared emitter structure amounted to 150 nm in diameter and 125 nm in height. The lattice spacing matched to tungsten ($d_0 = 3.16$ Å). About 450,000 atoms are at the surface. In total, 28 million atoms are used to establish the complete structure. About one million of these have been eroded by simulated evaporation (equal to less than 20 surface layers). About 30 Gb of memory were consumed by the simulation at runtime. In conclusion, the speed of the simulation turned out to be almost acceptable (about 12 atoms/min). As a

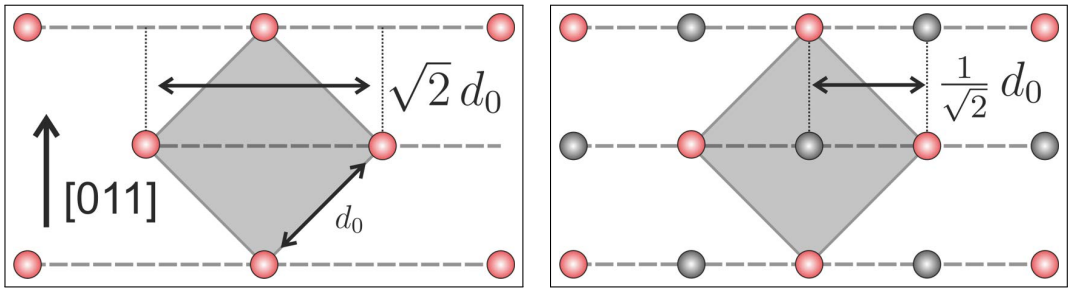

(a) sc [011] lattice

(b) bcc [011] lattice

(c) fcc [011] lattice

Figure 5.10.: The different widths of the [100] zone lines in figure 5.8 may be explained by considering local neighbour distances in the [011] projection of the cubic lattices.

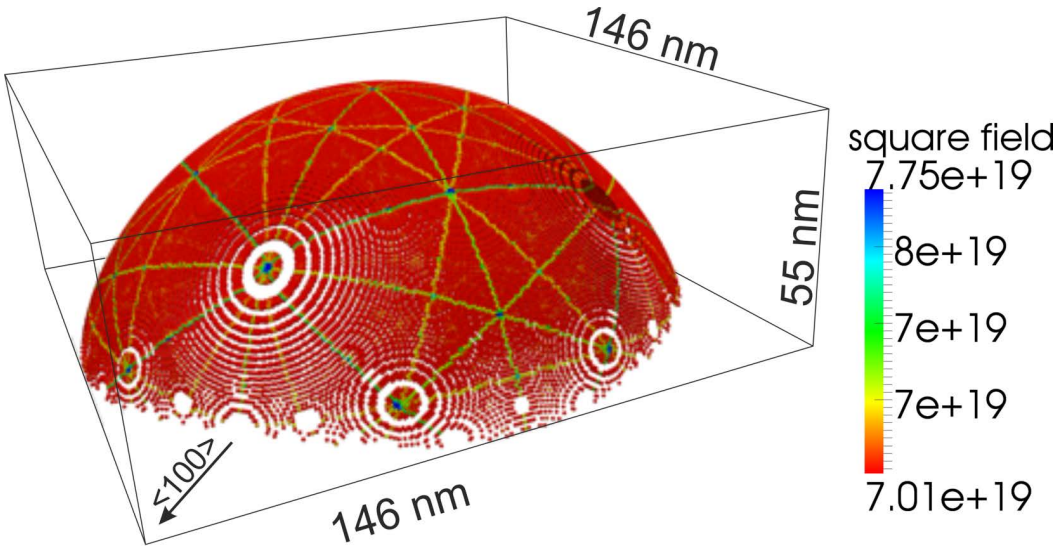

Figure 5.11.: Zone lines at the apex of a bcc ⟨100⟩ structure are revealed by their distinguished field strength during the simulated evaporation [OES13].

20,000 atoms are visible which belong to about one mono-layer. All of these have been first subjected to the simulated evaporation and the respective fields at desorption have been recorded. Subsequent to the simulated evaporation, atoms are placed back to their initial position at the apex which leads to the presented image. The color scale denotes the squared evaporation field strength. In this way, slightly elevated fields are clearly resolved. In detail, subtle differences between the zone lines become obvious. The field at the poles is highest (+5 %), the widest ⟨100⟩ zone lines reveal an increase of about +3 %, and approximately +1.5 % increase of the field is obtained for the narrower ones (e.g. ⟨112⟩).

Desorption pattern of a hexagonal lattice

The last striking feature of the presented desorption maps addresses the visible details in the pattern. Whereas for the sc structure, desorption maps appear in general a little blurred and, thus, do not show much crystallographic information, the bcc and fcc structures exhibit very detailed patterns. A natural explanation for the noticed difference would be the packaging density of the bcc-/ fcc-lattice on the one hand and of the sc-lattice on the other. However, a counter example which disproves this consideration is given by the desorption maps of a hcp emitter

major bottleneck, the calculation of the trajectories was identified. This task must be inevitably processed by a single thread and therefore cannot benefit from parallel computations.

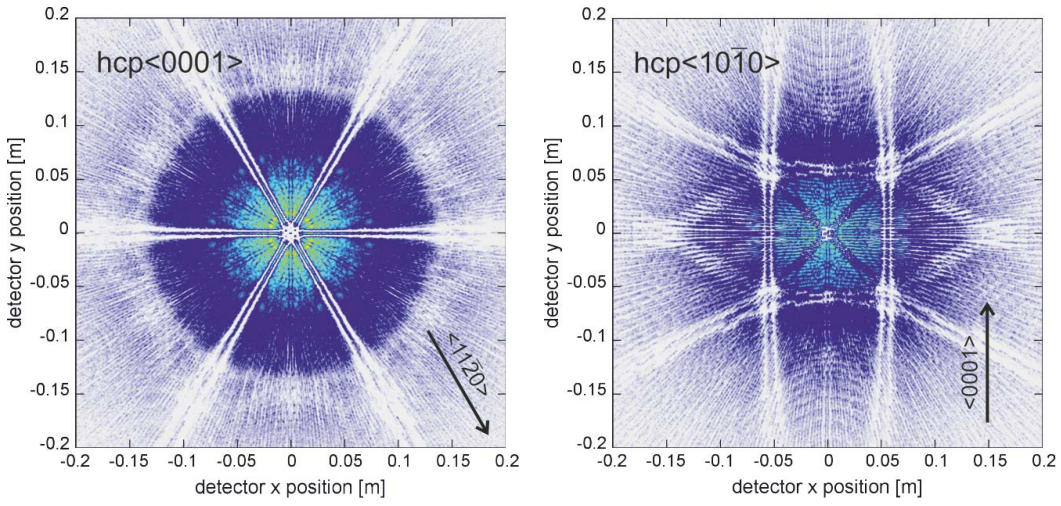

(a) **(b)**

Figure 5.12.: Desorption maps for hcp lattice structures. The orientation of the visible line pattern in the desorption map of the hcp ⟨10$\bar{1}$0⟩ are in correspondence with the alignment of the close-packed (0001) lattice planes.

(fig. 5.12) with the a/c-ratio of the lattice axes set to $\sqrt{3/8}$. Although the only difference between the hcp $\langle 0001 \rangle$ and the fcc $\langle 111 \rangle$ lattices consists in the stacking sequence, the respective patterns (fig. 5.12a and 5.8) look clearly different. The hcp desorption maps appear as blurred as in the case of the sc structure. Anyhow, poles and zone lines are visible as expected and confirm the prepared crystal orientation. In the tilted hcp $\langle 10\bar{1}0 \rangle$ orientation, a line pattern appears in the computed desorption map (fig. 5.12b). This feature is probably due to the different effect of local neighbour sites at the apex on the field. The orientation of the line pattern parallel to the close-packed (0001) planes is evident and supports this assumption. Outward at the detector the stripes are frayed and curved. For this observation, both the increasing error introduced by the projection and the change in the imaged surface orientation is responsible. The maximum imaging angle in the plots already amounts to about 60°.

5.2.3. Atom displacements in the desorption mode

The characteristic crystallographic features in the computed pattern are most likely a result of the different fields in the desorption mode. In general, the presence of depleted areas in the desorption pattern raises the question of their origin. In order to highlight this point, we consider the example of a fcc $\langle 100 \rangle$ field emitter sample. After the simulated evaporation of several mono-layers from the apex, processing is suspended. Trajectories starting from each of the actual surface atoms are calculated. The result is a first set of detector events (fig. 5.13a). Thereafter, processing continues until a second set with event positions, based on the field evaporation of the same surface atoms as before, completes (fig. 5.13b). By means of these two data sets, the comparison of event positions in the surface imaging mode with those in the desorption mode is enabled. The colouring in the event maps denotes the displacement

$$\Delta \boldsymbol{x}(\boldsymbol{x}_{\mathrm{Des}}) := \boldsymbol{x}_{\mathrm{FIM}} - \boldsymbol{x}_{\mathrm{Des}}$$

which is computed for each pair of linked positions $\boldsymbol{x}_{\mathrm{FIM}}$ and $\boldsymbol{x}_{\mathrm{Des}}$, respectively. Displacements in the range between 0.4 mm to 40 mm are determined. An alternative representation by a displacement field is seen in figures 5.13c and 5.13d. The arrows highlight the direction of the vectors. Due to the projection onto the flat detector, the absolute shift generally enlarges with increasing distance from the center (fig. 5.14). Nevertheless, at the center of the poles, a single atom with almost no shift appears regularly. Similarly, some of the atoms located at terrace

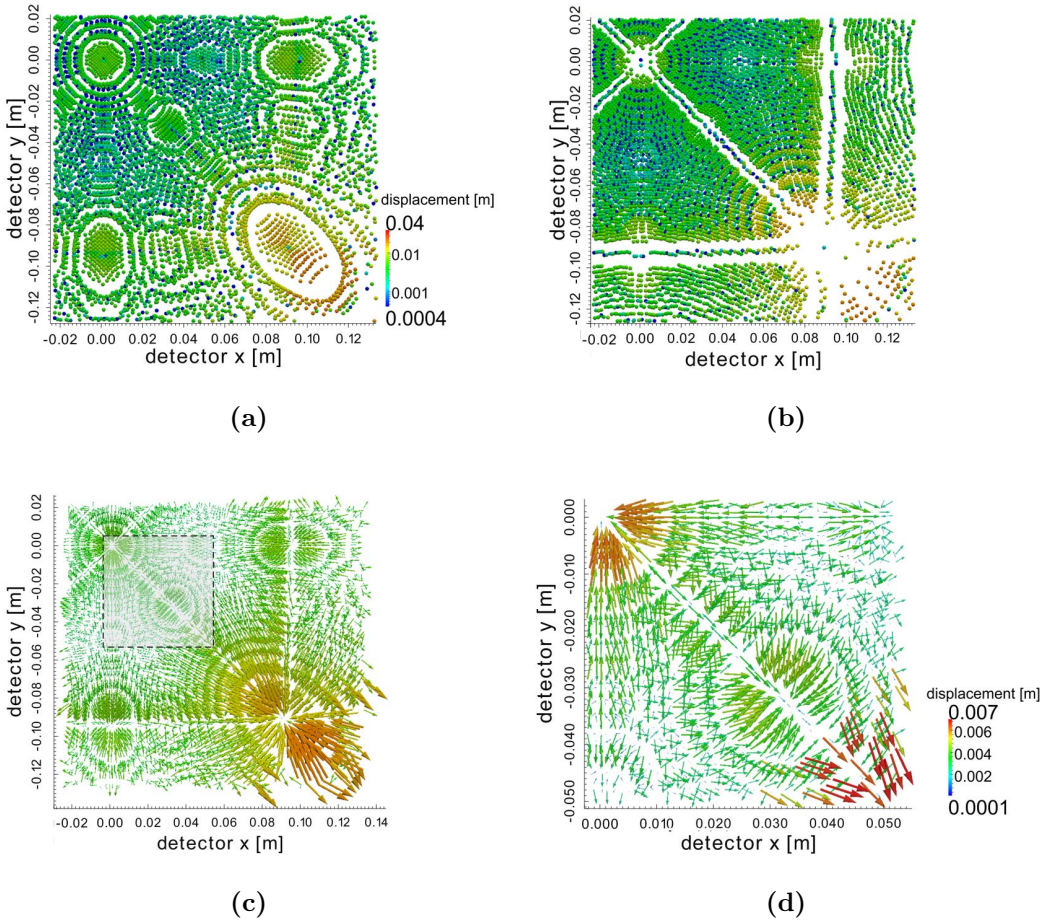

Figure 5.13.: Considering the same set of surface sites at a fcc ⟨100⟩ apex, simulated detector events in (a) the surface imaging mode and in (b) the desorption mode are computed. (c) The combination of both results enables the representation by a displacement field. The part inside the inscribed quadratic frame is shown in magnified view in (d). As it is seen by the colouring of the logscale, the magnitude of shifts generally increases with the distance to the center. This is an artifact and caused by the planar projection.

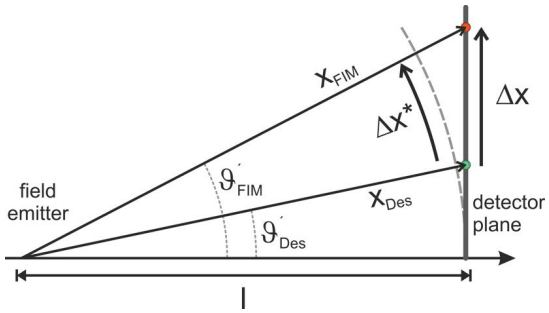

Figure 5.14.: Observed displacements Δx at the detector depend on the imaging angle. A comparison independent of the event position is enabled by the radian measure. For the conversion holds $\Delta x^{\star} = \Delta x(\vartheta'_{\mathrm{Des}}) \cdot \cos^2(\vartheta'_{\mathrm{Des}})$ accordingly.

edges about the poles also show a negligible shift. In general, the zone lines appear like a watershed which traces back to the crystal symmetry. Interestingly, displacements of neighboured positions do not surpass each other. Significant trajectory overlaps are not encountered. Instead, it seems as if an continuous shift of the event positions in analogy to an inflating balloon takes place.

In figure 5.15, a quantitative analysis for the distribution of the displacements is presented. A correction for the angle dependence of the shift amplitude must be applied. Therefore, corrected displacements $\Delta x^\star$ according to the equation written in the caption of figure 5.14 are evaluated. Besides, a second histogram based on the original displacements is shown in figure 5.15 in order to illustrate the effect of this correction.

The data can be well fitted by the Cauchy distribution[3] if the first part with very small displacements is neglected:

$$p(\Delta x^\star) \quad = \quad \frac{A}{\pi} \cdot \frac{w}{w^2 + (\Delta x^\star - x_c)^2} \tag{5.4}$$

This choice for the fitting function is in so far justified as the Cauchy distribution generally accounts for processes of random angular emission equal to that observed here [Mat13]. The function is symmetric about x_c, A denotes the amplitude, and w the width of the distribution, respectively. From the fitting we conclude that a shift of $(2.2 \pm 1.7)\,\mathrm{mm}$ is most likely determined. By taking into account the flight distance ($l = 10\,\mathrm{cm}$) and the image compression ($\xi \approx 0.87$), this results in an aiming error for the launch angle at the emitter apex of $\Delta\vartheta = (1.1 \pm 0.1)°$. For comparison, such a value is already sufficient to introduce an error in the APT

[3] The alternate naming is *Lorentzian distribution*.

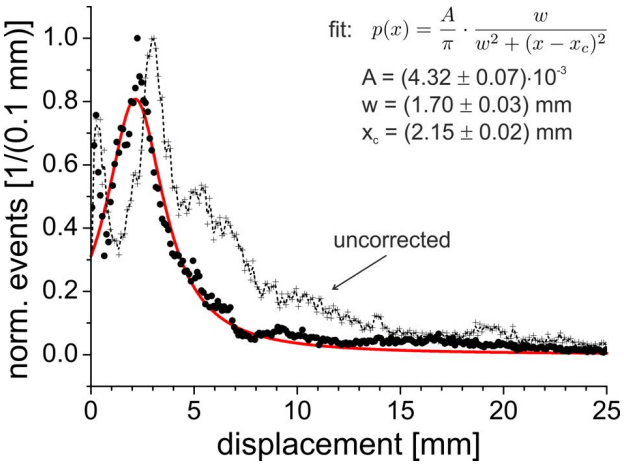

Figure 5.15.: Histogram of the obtained displacement amplitudes. The original and the corrected distribution according to Δx and $\Delta x^\star$ is shown, respectively. Fitting by the Cauchy distribution is enabled if events with displacements less than 0.5 mm are neglected.

reconstruction of about 5 Å for the calculated atom positions if a tip curvature of 25 nm is assumed.

5.3. Statistic desorption under the influence of temperature

Similar to the different imaging conditions which are revealed by the direct comparison of surface imaging and desorption mode, elevated emitter temperatures lead to a variation in the desorption sequence. In a complementary study to the report published by Gruber et al. [Gru+11], the influence of temperature is here investigated for the special case of a bcc ⟨110⟩ and fcc ⟨111⟩ sample structure ($d_0 = 5$ Å).

Like in the section before, the basic geometry of a cylinder with hemispherical apex (50 nm in diameter, 65 nm in height) is prepared. But in contrast to before, the desorption sequence gets now controlled by equation (4.9) as a Monte Carlo approach. Thus, besides temperature, an evaporation threshold field and an activation energy needs to be provided: for the threshold field a common value of 57.1 V nm^{-1} is preset, whereas for the activation energy different values of 2.0 eV for the bcc and 1.0 eV for the fcc apply, respectively. These values for the activation energy are taken from the study of Gruber et al. in order to facilitate comparability. Unfortunately, it turns out that this choice is (almost) arbitrary. In consequence, the temperature scale which is investigated in a nominal range between 1 K and 320 K is not realistic. This point must be kept in mind for all presented results in the following.

The immediate application of equation (4.9) enables to assign different evaporation probabilities to the apex sites. Respective histograms with the calculated probabilities in dependence on temperature are presented in figures 5.16a and 5.16c. Irrespective of the lattice type, only very specific lattice sites allow evaporation at 1 K. This situation resembles the maximum field condition used before for determining the evaporation sequence. At elevated temperatures, the distributions decisively broaden. So, at $T = 320$ K an increased number of emitter sites show a significant evaporation probability. Due to the smaller activation energy, the broadening is stronger for the fcc than for the bcc sample. In figures 5.16b and 5.16d, the spatial distribution of the evaporation probability about the apex is shown. Distinguished emitter sites appear clearly separated. Bright contrast is located at the edges of terraces and is particularly enhanced at kink sites.

In a next step, such calculated probabilities are fed into the Monte Carlo approach and the simulated evaporation of some 100,000 events from the emitter is processed. In this way, data sets for different temperatures are recorded. Fig-

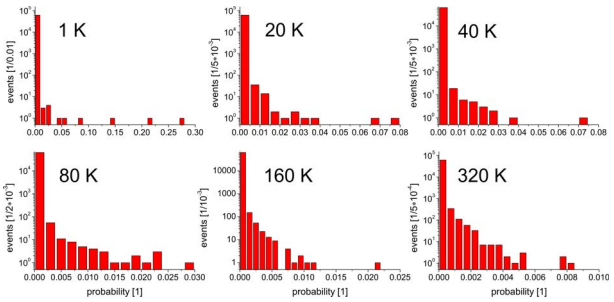

(a) Histogram for the bcc ⟨110⟩ emitter type.

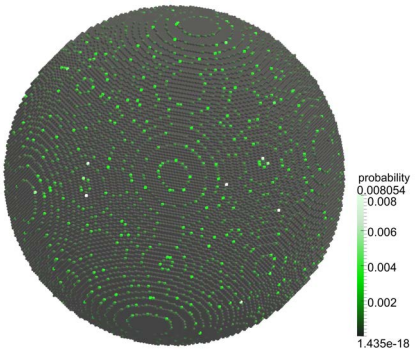

(b) Spatial distribution at the bcc apex at $T = 320\,\mathrm{K}$.

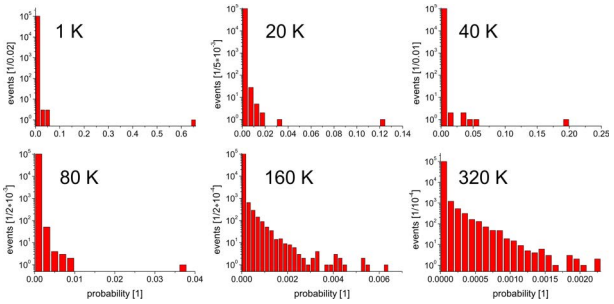

(c) Histogram for the fcc ⟨111⟩ emitter type.

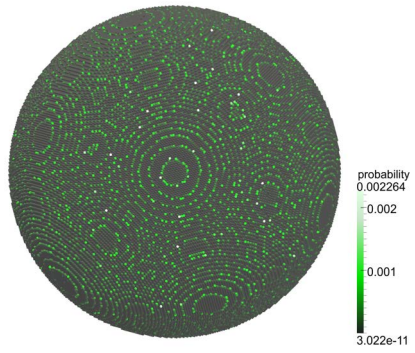

(d) Spatial distribution at the fcc apex at $T = 320\,\mathrm{K}$.

Figure 5.16.: Evaporation probabilities of the apex atoms in the simulated temperature range.

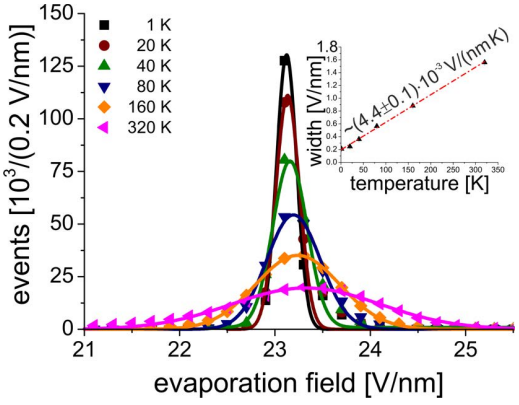

(a) bcc sample with $Q_0 = 2\,\mathrm{eV}$

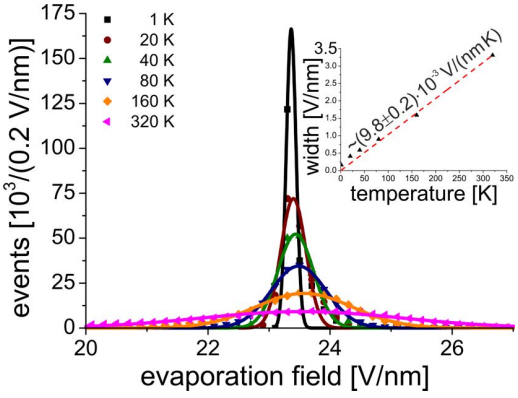

(b) fcc sample with $Q_0 = 1\,\mathrm{eV}$

Figure 5.17.: Field strengths at evaporation of evaporating atoms from the apex. In correspondence with equation (4.9), the distributions show a clear dependence of temperature. Data in the insets proves a linear increase of the respective widths.

ure 5.17 shows histograms which have been compiled considering the respective "field at evaporation" for each event.[4] The determined probabilities follow a Gaussian distribution. In the insets, the fitted width of the curves is plotted against temperature. As expected from the applied approach, the width depends linearly on the temperature which confirms the general reliability of the implementation of the statistic desorption mode.

Besides, the distribution shifts slightly towards increased fields for elevated temperatures. Probably, this shift is the consequence of changes in the general surface morphology. This assumption is underpinned by figures 5.18a to 5.18e which show the emitter surface of the fcc sample after the simulated evaporation at various temperatures. The magnified insets in the figures depict the centred ⟨111⟩ pole. As indicated by the dashed lines, facetting at the edges of atomic terraces according to the threefold symmetry of the lattice is present at low temperatures below approximately 80 K. This faceting decreases at elevated temperatures. The terrace continuously deforms with temperature and increasingly deviates from a circular shape. At the highest considered temperature, $T = 320\,\mathrm{K}$, the edges already appear decisively frayed. Finally, desorption even from the interior sites within the terraces can be observed (see circle in fig. 5.18e).

In view of the changing tip morphology, it is not surprising that the computed field desorption maps also show significant variation with temperature. Predominantly, we observe a fading of crystallographic details as it can be seen in figures 5.19 and 5.20 for the bcc and the fcc case, respectively. E.g. depletion at the zone lines almost vanishes at sufficiently elevated temperatures. The depleted zone around prominent poles reduces, but remains present even in the case of the fcc ⟨111⟩ at $T = 320\,\mathrm{K}$ where the effect is generally enhanced because of the lower activation energy.

In the insets of the desorption maps, displacements of the same atoms with regard to the obtained position at $T = 1\,\mathrm{K}$ are plotted. From the symmetry, one can conclude that preferential directions for the displacements are a result of local next neighbour positions in the lattice. The displacement appears predominantly in between the directions of the low indexed poles of the desorption maps.

The observations are quantitatively confirmed by the more detailed analysis of the displacements. In figure 5.21a and figure 5.21b histograms of the magnitude of the calculated shifts are shown. Most displacements are constrained to some millimeters which corresponds to a change in the launch angle of less than 2°. Solid

[4] The *field at evaporation* is the field which is present immediately before the respective surface atom is going to be field evaporated in the simulation.

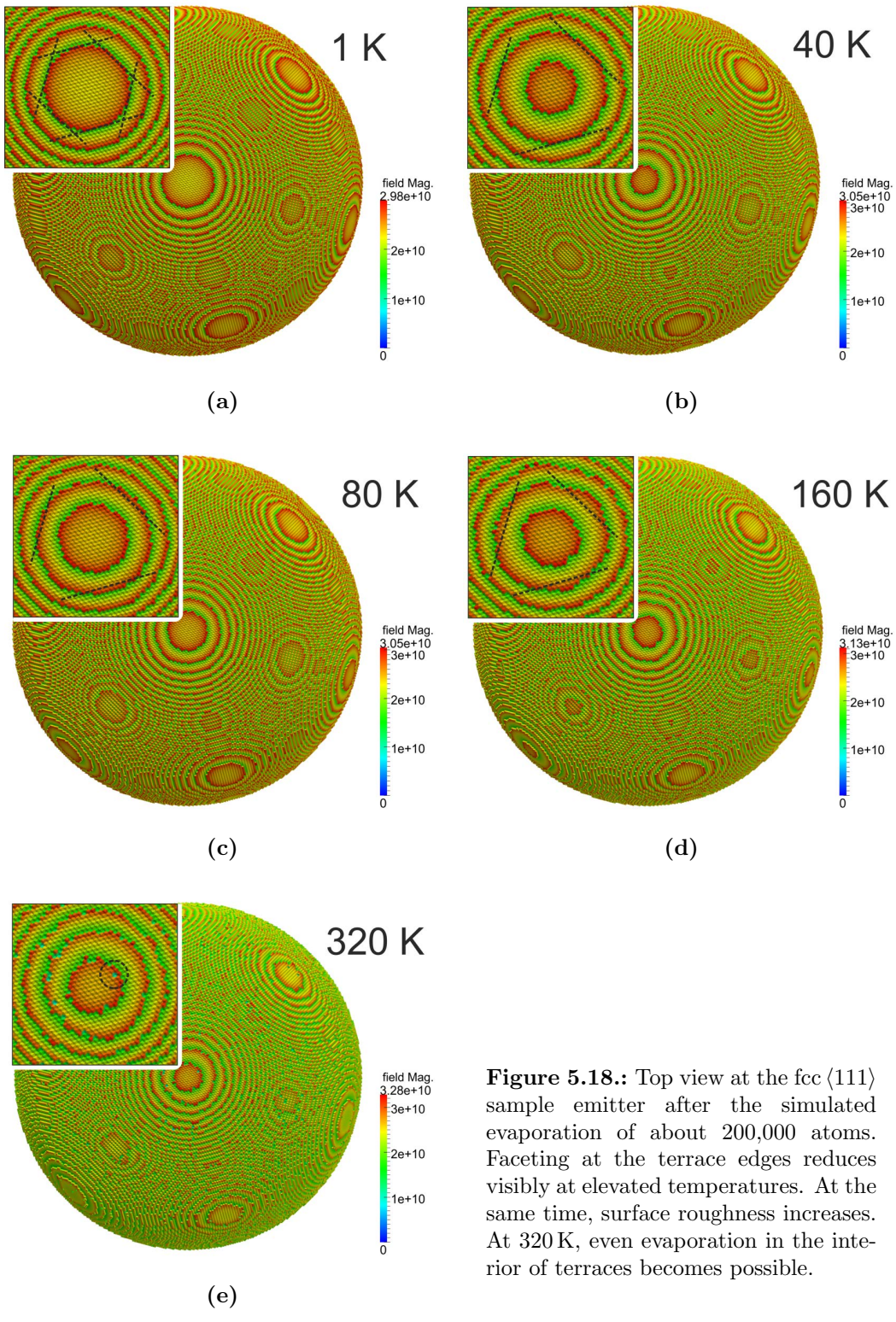

Figure 5.18.: Top view at the fcc ⟨111⟩ sample emitter after the simulated evaporation of about 200,000 atoms. Faceting at the terrace edges reduces visibly at elevated temperatures. At the same time, surface roughness increases. At 320 K, even evaporation in the interior of terraces becomes possible.

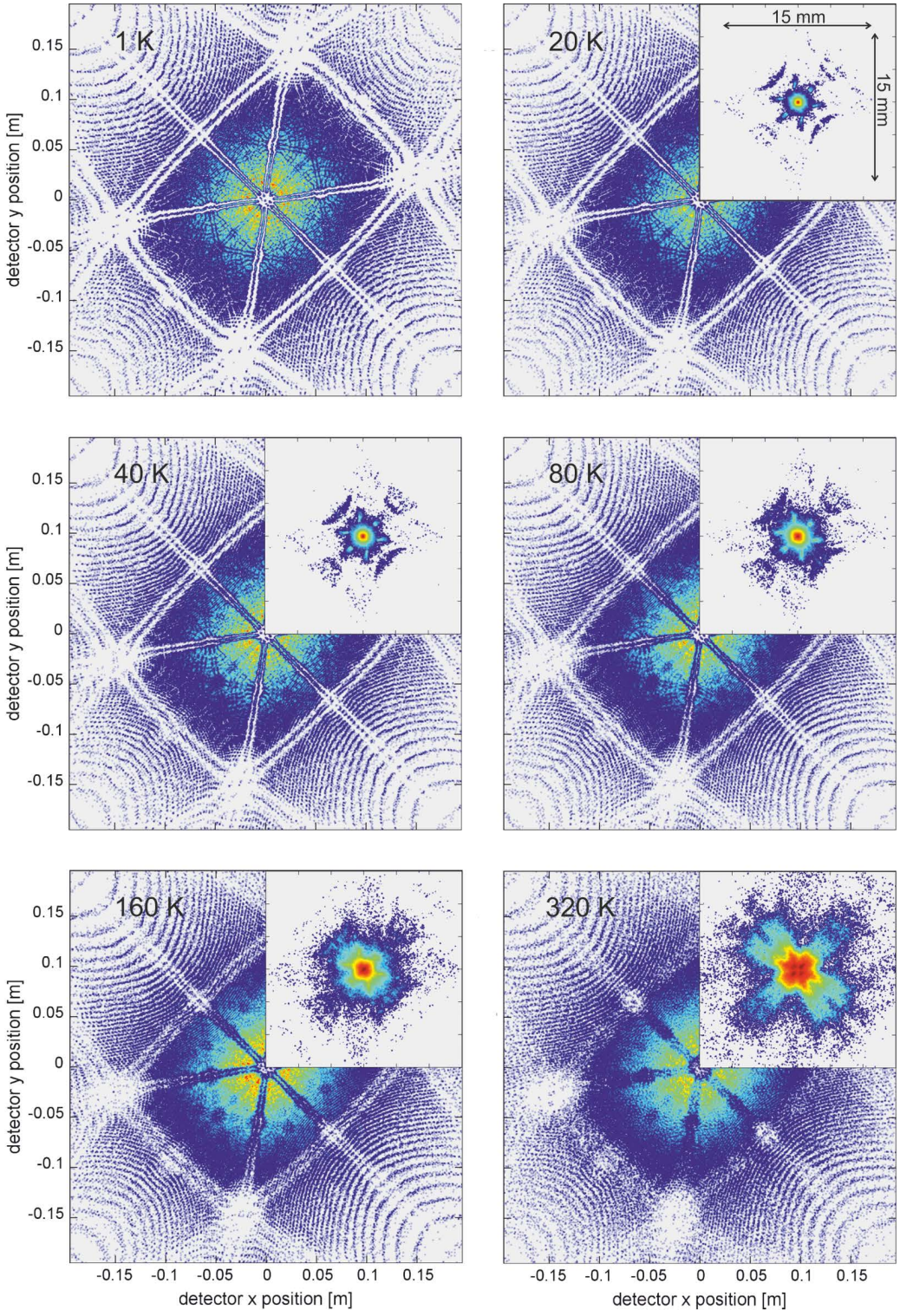

Figure 5.19.: Bcc ⟨110⟩ desorption maps as a function of on temperature. Insets depict event displacements at the detector in comparison to the computed positions of the same atoms at 1 K.

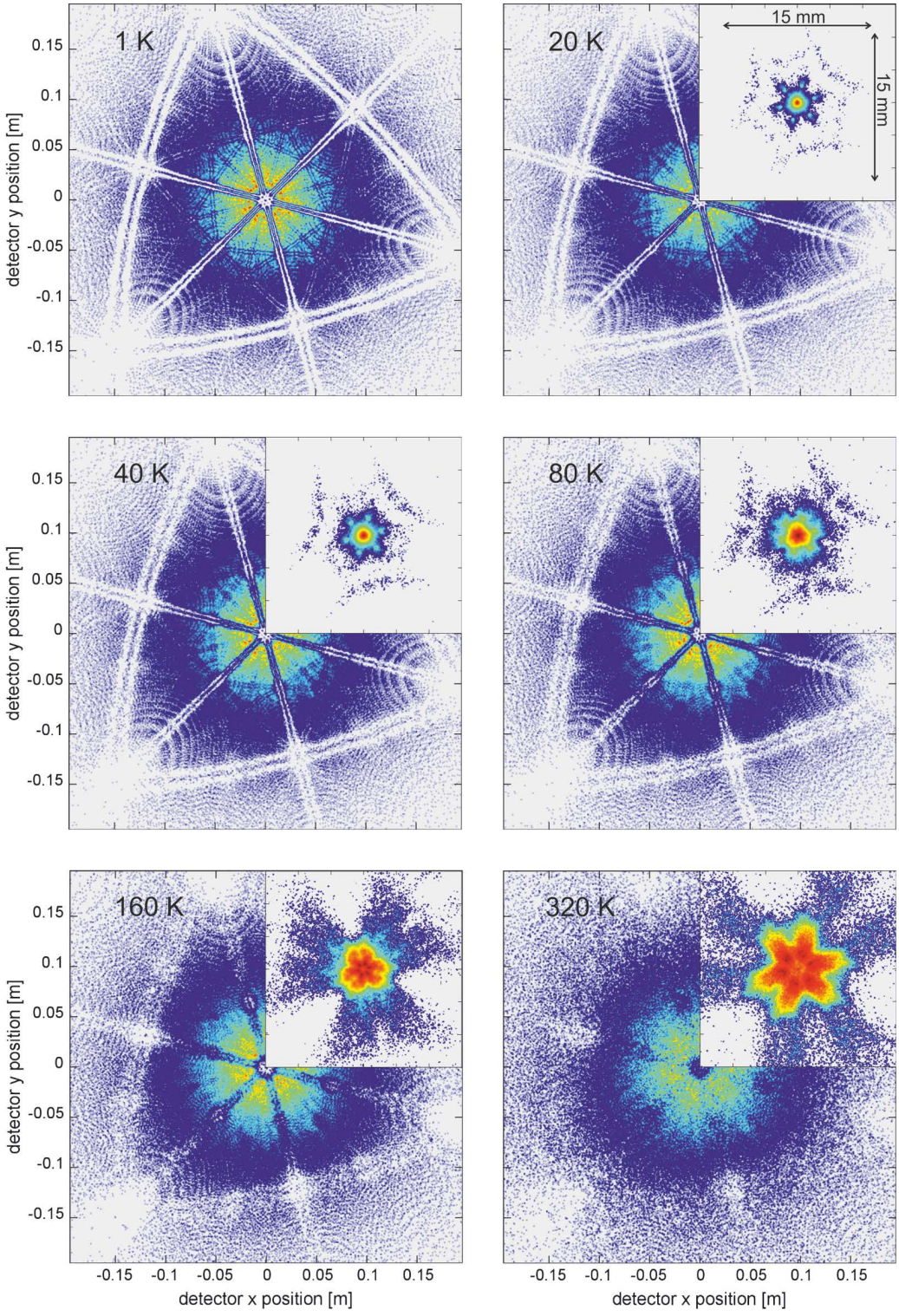

Figure 5.20.: Fcc ⟨111⟩ desorption maps as a function of temperature. Insets depict event displacements at the detector in comparison to the computed positions of the same atoms at 1 K.

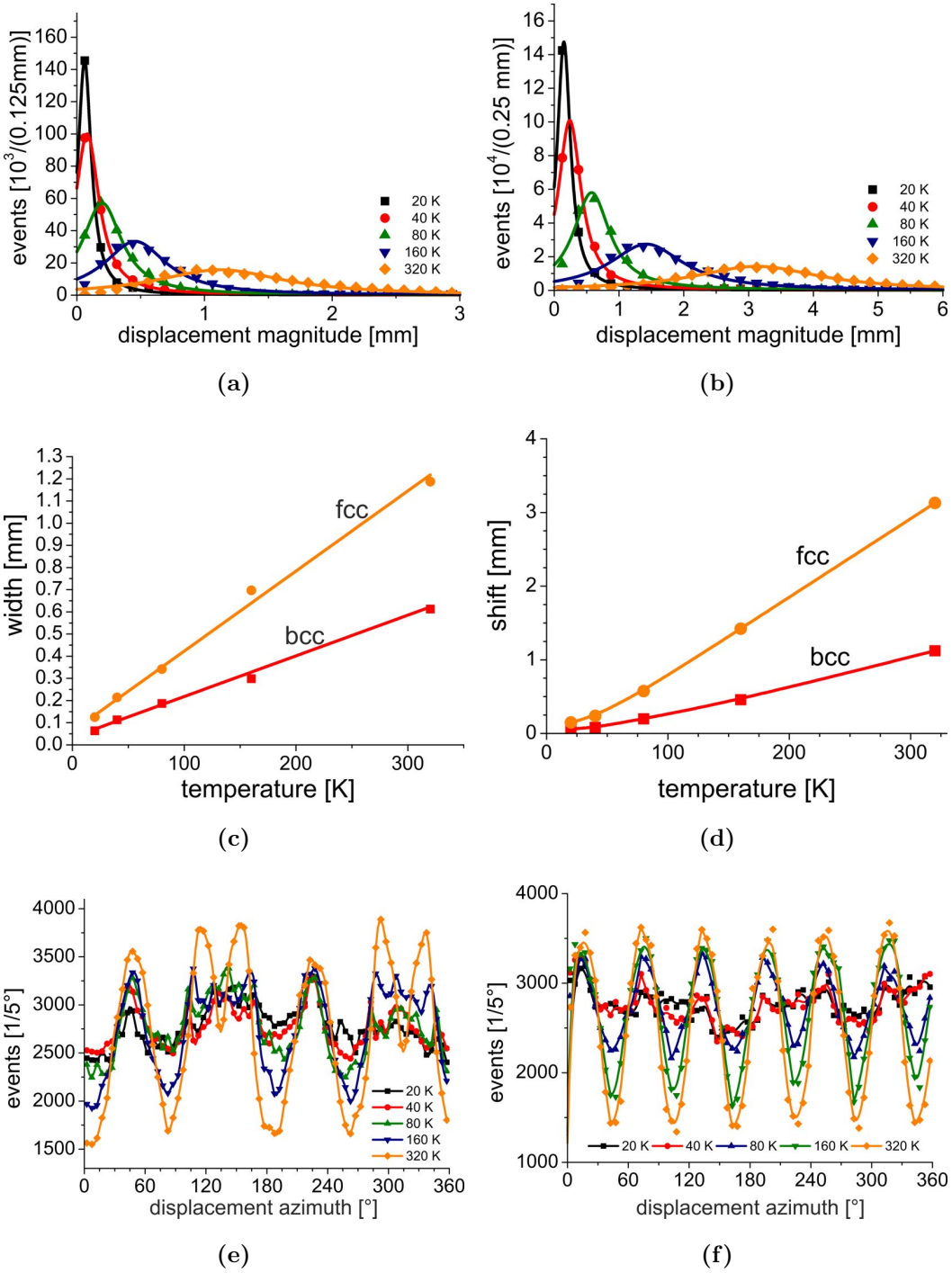

Figure 5.21.: Analysis of the (spatial) displacements at the detector: (a) - (b) Histograms of the displacement magnitude for bcc and fcc, respectively. Fitting by the Cauchy distribution reveals (c) an increase of the width and (d) a slightly stronger increase of the shift against temperature. (e) - (f) Histogram of the angular directions of the displacements. With increasing temperature, predominant angels in correspondence to the two- and threefold symmetry of the bcc ⟨011⟩ and fcc ⟨111⟩ lattices develop.

curves in the plots already represent fits using the Cauchy distribution as it has been applied before (see sec. 5.2.3). Interestingly, the fitted widths for the bcc as well as for the fcc increase proportional to the temperature. The proportionality factor reflects the ratio corresponding to the activation energies (fig. 5.21c). In contrast, a slight curvature appears for the fitted shift (fig. 5.21d). The origin for this may be speculated to lie in the described changing of the surface morphology, e.g. the combination of increasing field strength with an increasing temperature. The next two graphs, figures 5.21e and 5.21f, depict the evolution of preferential directions of the displacements. The symmetry constraints due to the bcc and fcc lattices, become particularly clear in this representation.

At last, figure 5.22 depicts particular interesting information which is not already included in the data of the desorption maps: The increased randomness in the desorption sequence causes not only spatial displacements in the imaging position at the detector, but also preferred or delayed desorption with respect to the computed sequence at $T = 1\,\mathrm{K}$ is increasingly pronounced. The insets in the figures depict the stepwise shrinkage of the emitter apex. About every 9.500 or 12.500 desorbed atoms, the apex shrinks by one atomic terrace, which is equal to an amount of $d_{\langle 110\rangle} = 3.5\,\text{Å}$ and $d_{\langle 111\rangle} = 2.9\,\text{Å}$ for the bcc and fcc, respectively. Thus, with regard to the APT reconstruction, the documented shift in the evaporation sequence can induce an displacement in the z-coordinate of five to ten mono-layers in dependence on the temperature.

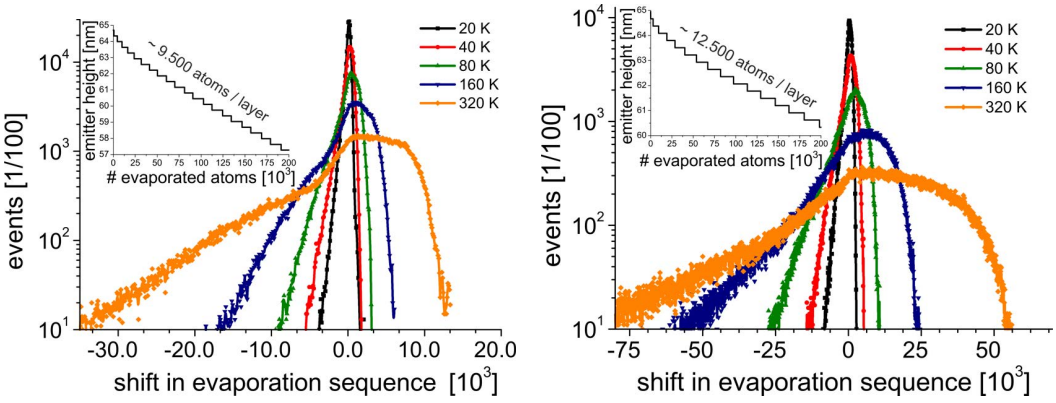

(a) bcc **(b)** fcc

Figure 5.22.: Analysis of the (temporal) displacements in the detection sequence: The order, in which atoms become evaporated from the emitter, broadens with temperature. Insets depict the shrinkage of the apex with the number of evaporated atoms. From this, we conclude that changes in the evaporation sequence can amount to several mono-layers in depth in computed reconstructions.

We complete this part with a final remark. We have seen that the consideration of temperature leads to spatial and temporal displacements of events at the detector. The effect will be at least responsible for a degraded resolution in derived 3D reconstructions. But moreover, it turns out that the magnitude of these displacements follows in particular a Cauchy distribution. By this description, the displacements appear to be of statistic nature. Notably, this is only true from a macroscopic point of view when just hit events at the detector are evaluated. In contrast, if the microscopic condition at the emitter apex close to the launch site of the trajectories would be taken into regard, a description in a deterministic frame should remain possible.

6. Quality of the 3D reconstruction

Access to the stoichiometric information in APT measurement data is achieved on the basis of produced reconstructions. Just like it is the case with experimental measurements, the applied procedure is not free from introducing errors into the compiled 3D maps, since an only presumed emitter geometry is considered.

At the most sophisticated level of development, the reconstruction would enable full 3D structural information combined with chemical information of analysed samples ("Atom probe crystallography" [Gau+12b]). Currently, this ultimate goal is only reached under particular experimental conditions. A well-defined evaporation sequence at a very low temperature is demanded. Almost identic evaporation thresholds of the analysed samples are beneficial.

Most measurements do not meet these optimal conditions which renders any application of more advanced analysis techniques for determining crystallographic features useless. In the common case, already the input to the reconstruction suffers from artifacts. E.g. in the laser assisted measurement mode, spatial resolution often degrades to such a degree that lattice planes become hardly visible.

In the following, the quality of the reconstruction as it is obtained from simulated field evaporation sequences is addressed. Data for the single case of a bcc $\langle 001 \rangle$ emitter structure, 65 nm in height and 25 nm in diameter, are presented. The preset lattice spacing amounts to $d_0 = 5\,\text{Å}$.

6.1. Geometric consistency

In order to fully explore the information from the experiments, every reconstruction is calibrated based on a particular set of parameters. Initially, only an appropriate atom density and the image compression are preset. Provided that lattice planes are resolved, further parameter values for the curvature radius of the apex and the shaft angle are adjusted such that the nominal lattice spacing is matched (see sec. 2.2.4, p. 25).

Usually, the best resolved planes are aligned perpendicular to the z-axis. With a proper calibration along this direction, the diameter of the reconstruction follows from the conservation of volume.

Problems with this procedure arise from the simple fact that the in this way adjusted parameters are not necessarily linked to the original geometry of the analysed samples. Appropriate values depend in first instance on the reconstruction model. It is indeed common practice that the applied parameters differ from those which would be expected on the basis of the original sample geometry, e.g. like it can be determined by TEM. At this point, the use of simulated data allows for the first

time to test the self-consistency of the 3D reconstruction procedure. Therefore, the input of the simulation is compared with the output of the reconstruction.

Figure 6.1 depicts two different results that have been derived to this end. For figure 6.1a the standard approach (Bas et al. [Bas+95]) is used, whereas for figure 6.1b the enhanced approach (sec. 2.2.5) is used. Atoms rendered in blue describe equidistant marker lines. Horizontal marker have a spacing of $\Delta_z = 5\,\mathrm{nm}$ whereas vertical ones are each separated by $\Delta_{xy} = 2\,\mathrm{nm}$. In the background of the depicted reconstructions, the original shape of the initially prepared bcc emitter structure from the simulation is visible. The maximum field of view has been set to an angle of 64.3° (equal to 15 cm detector radius), which constrains the maximum diameter in the reconstruction to 22.5 nm.

We see that the first reconstruction following the Bas et al. approach appears completely distorted. This is the case even though nominal correct parameters for the curvature radius and the atom density have been applied. The discrepancy in comparison to the original structure is appalling. In textbooks, the insufficiency of this approach is referred to be the result of "small angle approximations" without giving any further explanation [Gau+12a]. Clearly, in the application to measurement data of enlarged field of view, these must severely diminish the usability. However, facing this example here, it is clear that it is not a problem of angle

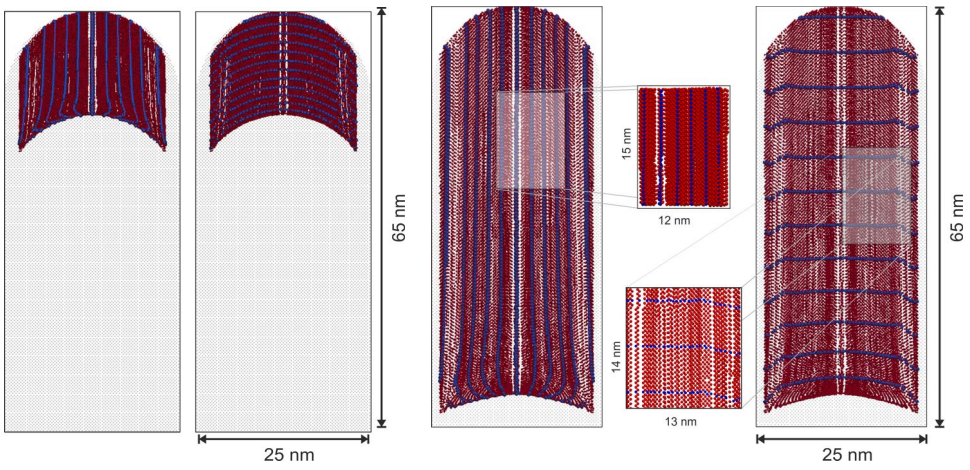

Figure 6.1.: Slices through the reconstructions which resulted from (a) the Classic approach (Bas et al.) and (b) the dedicated wide angle approach (sec. 2.2.5). For both computations, the same values for atom density, image compression, and curvature radius have been considered. Equidistant vertical and horizontal marker lines at distances of 2 nm and 5 nm are depicted in blue color, respectively.

approximation. Instead, it is a wrong estimation of the depth increment. The reconstructed atom density in figure 6.1a does not at all match the preset values. As the standard approach does not preserve the conservation of volume, it is simply incorrect in this regard.

In contrast, correcting for the depth increment, as it is done in the second wide-angle approach, immediately leads to an almost correctly aligned reconstruction. Visible misalignments close to the bottom in figure 6.1b are probably a side-effect of the simulation approach: once the emitter height gets below the curvature radius of 12.5 nm in the progressing simulation, irregular curvature changes take part due to the geometric constraints at the lower boundary of the simulation box.

This is the first time that such a self-consistent test of the basic assumptions for the reconstruction is performed. It has been only possible owing to the unique capability of the generalized APT simulation approach to consider the realistic experimental extents for the trajectories appropriately.

Particular distortions appear in the reconstruction which are not due to a mismatch in the density: In the vicinity to the $\langle 011 \rangle$ poles, a bending of the horizontal marker lines similar to an edge is visible (see the lower magnified excerpt in fig. 6.1b). This bending is clearly an original artifact of the reconstruction. It is probably caused by a varying onset for the evaporation of the atoms at the poles which results in a shift of the z-position. This assumption is confirmed by the otherwise perfect alignment of the vertical marker lines.

6.2. Spatial resolution determined by 3D Fourier analysis

Besides the general proper calibration of the reconstructed volumes, the regularity with which individual atoms are positioned is of particular interest. The question is: How good becomes the initial bcc lattice structure restored in terms of resolution?

In order to study this question, a Fourier analysis similar as described by Vurpillot et al. [Vur+01; Vur+04a] may be computed. For this purpose, each atom in the real space is equated by means of the δ-distribution. Thus, we write

$$R(\boldsymbol{x}) = \sum_i \delta(\boldsymbol{x} - \boldsymbol{x}_i) \tag{6.1}$$

for all the atomic positions $\boldsymbol{x}_i$ in the reconstruction. With this, the transformation simply becomes

$$\tilde{R}(\boldsymbol{k}) = \sum_i e^{-2\pi i\,(\boldsymbol{k}\cdot\boldsymbol{x}_i)} \tag{6.2}$$

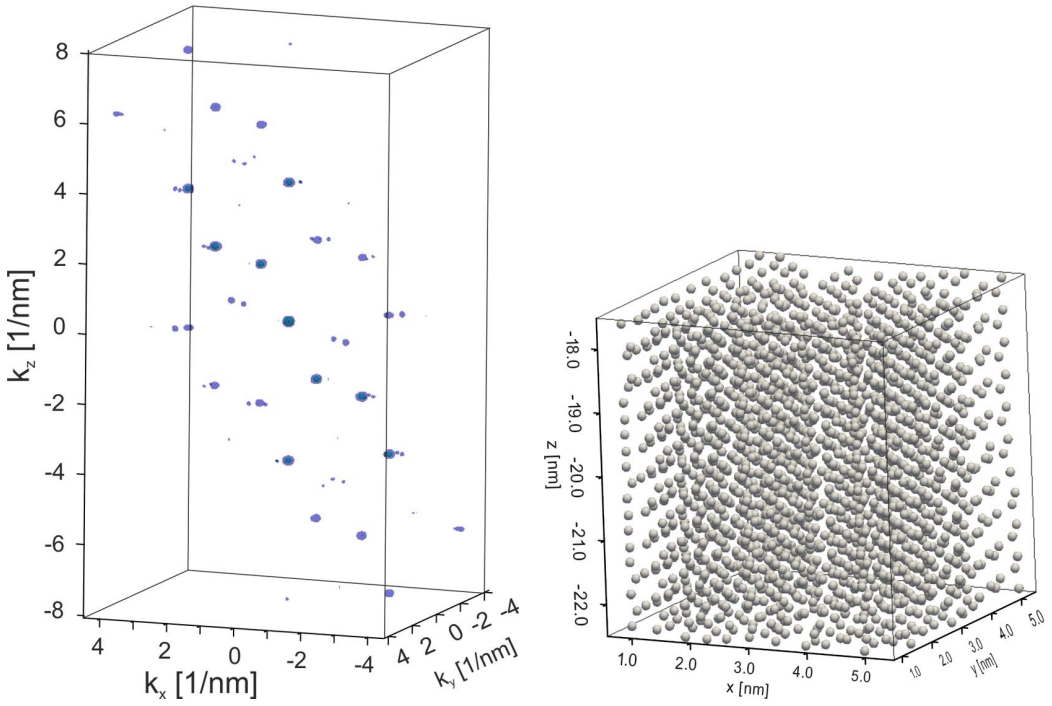

(a) **(b)**

Figure 6.2.: 3D Fourier transformation of an APT reconstruction derived from the simulated data of a bcc lattice. (a) The position of reflexes in the reciprocal space is revealed by iso-intensity surfaces. The transformation has been computed using a resolution of $\Delta k = 0.05\,\mathrm{nm}^{-1}$. Hence, the intensity at about 8 million discrete frequencies is evaluated. (b) Source showing the considered atoms in real space. The cubic volume was cut from the reconstruction shown in figure 6.1b. It contains about 3,500 atoms.

in the frequency domain. For the detailed analysis, the reciprocal space is probed at discrete frequencies

$$\boldsymbol{k}_i = (l, m, n)^\top \cdot \Delta k;\ l, m, n \in \mathbb{Z}$$

using a screen width of Δk ($\leq 1\,\mathrm{nm}^{-1}$). The result is a 3D map of (complex) intensities. Notably, the complete sum of equation (6.2) must be evaluated for each frequency which implies a severe computational effort. For this reason, only a representative subsection, $6\,\mathrm{nm} \times 6\,\mathrm{nm} \times 6\,\mathrm{nm}$ in size, has been Fourier analysed (fig. 6.2).

An analysis of the resolution is enabled by a look at different slices through the reciprocal space (fig. 6.3). Reflexes in the Fourier transformation are expected to appear only at those positions for which the frequency vector equals a reciprocal

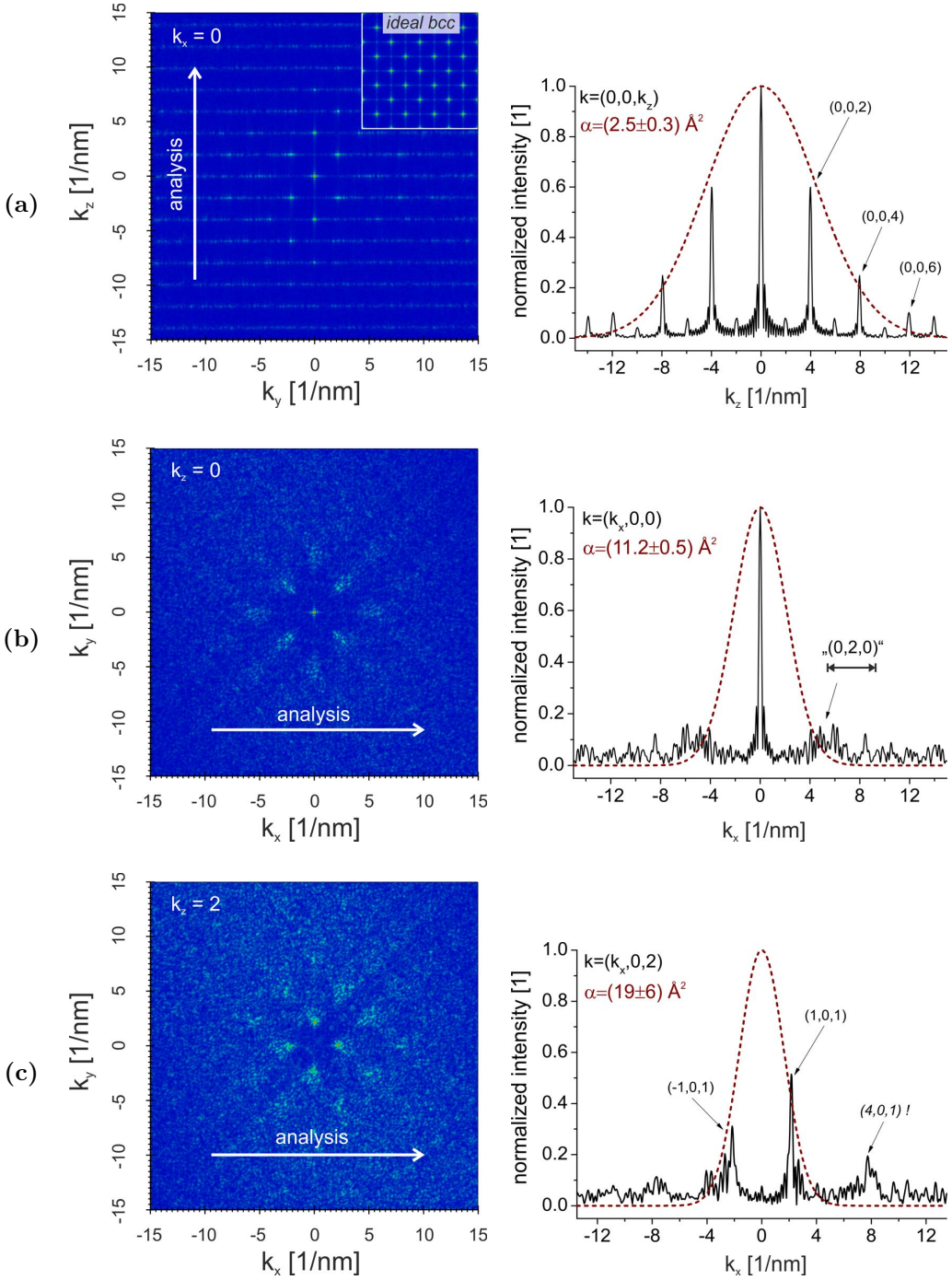

Figure 6.3.: Detailed analysis of the Fourier transformation: Maps on the left represent slices through the reciprocal space. Different orientations corresponding to planes with (a) $k_x = 0$, (b) $k_z = 0$, and (c) $k_z = 2$ are considered. Colouring denotes the intensity $|\tilde{R}|$. For comparison, the inset in the top right corner of the map with $k_x = 0$ shows reflexes for an ideal bcc structure. Further analysis is enabled by the line plots on the right. Here, intensity peaks are marked with Miller indices corresponding to the real space. Fitting is enabled by a Gaussian envelope equated with $\tilde{G}(\boldsymbol{k}) = e^{-\alpha \boldsymbol{k}^2}$.

lattice position

$$\boldsymbol{k}_{\max} = (l, m, n)^\top \cdot d_0^{-1};\ l, m, n \in \mathbb{Z}.$$

In this example, the reciprocal lattice constant amounts to $d_0^{-1} = 2\,\mathrm{nm}^{-1}$. In addition, the elimination rule for the bcc lattice applies[1] such that the 3D "diffraction" pattern resembles the structure of a fcc lattice. Indeed, analysed slices match well to these expectations. In particular, the z-direction shows many clear reflexes with sharp contrast (fig. 6.3a). Corresponding peaks in the intensity up to the sixth order are recognized. The determined reflex positions prove the proper calibration of the reconstruction in real space. In contrast, reflexes in the lateral directions appear less sharp and may be hardly distinguished from noise in the background (fig. 6.3b and 6.3c). This highlights that the positioning of atoms is by far not as regular as before. In addition, also exceptional reflexes may be recognized. For instance, the line plot in figure 6.3c shows an elevated intensity at a position corresponding to the Miller indices $\{0, 4, 1\}$. The sum is not even. This should not be there and it may be evidence for the presence of systematic microscopic shifts in the reconstruction.

In general, misalignments in the reconstruction prevent the occurrence of long ranging regularities. The consequence of these positioning errors in the real space is the degradation of the reflex intensity for elevated frequencies in the reciprocal space. Assuming a Gaussian blurring

$$G(\boldsymbol{x}) = \frac{1}{\sqrt{2\pi}\sigma} \cdot e^{-\frac{\boldsymbol{x}^2}{2\sigma^2}}$$

with σ denoting the standard deviation of position, we have to consider the convolution $G \otimes R$ in the Fourier space which results in another Gaussian envelope:

$$\begin{aligned} \widetilde{(G \otimes R)}(\boldsymbol{k}) &= \tilde{G}(\boldsymbol{k}) \cdot \tilde{R}(\boldsymbol{k}) \\ &= e^{-\alpha \boldsymbol{k}^2} \cdot \tilde{R}(\boldsymbol{k}),\ \ \alpha := 2\pi^2\sigma^2 \end{aligned} \tag{6.3}$$

This allows us to specify the resolution, defined by $\epsilon = |2\sigma|$ or $\epsilon = |\sqrt{2\alpha}/\pi|$, respectively. Dashed curves in the line plots on the right in figure 6.3 represent fittings of the envelope to the respective reflexes. In this way, different widths denoted by α are determined.

For the depth resolution, a value of $\epsilon_z = (0.72 \pm 0.06)\,\text{Å}$ is estimated . This is about a factor of two better than for the lateral resolution for which a value of

[1] The sum of the Miller indices $l + m + n$ must be even.

$\epsilon_{xy} \geq (1.50 \pm 0.04)$ Å results. However, fitting the Gaussian envelope here already suffers from the poorly resolved reflexes in the Fourier spectrum. The (0,2,0) reflex may be hardly recognized in figure 6.3b. Therefore, the given lateral estimate represents a lower limit. The resolution may be even worse. Similar constraints apply for the fitted curve in figure 6.3c. In this case, only the $\{0, 1, 1\}$ reflexes are clearly identified. However, the estimated resolution of $\epsilon_{xy} = (1.96 \pm 0.32)$ Å) does confirm the before defined range.

For comparison, the same approach has been used to determine the resolution of experimental data. In the case of a NiCrAl alloy, analysed by a voltage pulsed instrument, reported values were $\epsilon_z = 0.6$ Å for the depth and $\epsilon_{xy} = (2 \pm 1)$ Å for the lateral resolution [Vur+01].

In face of these results, we do conclude:

- Data from experiments and simulations show the same trend. The reconstructed depth resolution is about twice as good as the lateral resolution. This is not surprising, since the depth resolution is basically an outcome of a low counting error. In contrast, disturbed event positions at the detector essentially affect the lateral resolution.

- The simulation does not account for temperature. Nevertheless, the lateral resolutions appears quite comparable with the experiment. This implies that in experiments the temperature effect on the resolution can be negligible as far as high-voltage pulses and a sufficient low temperature (≤ 50 K) are used.

- Generally, the estimated resolution coincides fairly well with the reported one from the experiment.

This latter point is indeed surprising. Naively, a much better resolution would have been expected. The simulation approach is deterministic and therefore should not suffer from noisy contributions as they are present in experiments. But even under such optimum conditions, the lateral resolution does not significantly improve.

On the other hand, limitations due to numeric inaccuracies could be a reasonable explanation. The argument against this assumption is, however, the observed pattern in simulated field desorption maps. Particularly because this pattern looks very detailed for the here tested bcc lattice (see fig. 5.8 on p. 104), we exclude this explanation.

Instead, we want to give here another interpretation. By the Fourier analysis, the reconstruction is explored for regularities. Obviously, lateral regularity of the bcc lattice is barely restored by the reconstruction. Only a degraded resolution is obtained. We believe that this finding links to a general lack of the geometric back projection approach for reconstruction. We have indicated before in chapter 5 that the considered approach may not be best suited to describe the imaging process at a macroscopic level because important microscopic details are neglected. Significant improvements of the 3D resolution should therefore indeed be possible if a physically reconstruction approach based on a microscopic model of the sample apex similar to that in the simulation applies. Only in this way, the particular field conditions at the microscopic scale may be appropriately taken into account.

7. Evaluation of model emitter structures

In the proceeding chapters, the foundation and the basic properties of the new generalized simulation approach have been elaborated. In this chapter, we change the focus and demonstrate the new capabilities of the simulation approach. Therefore, we address three intuitive examples which refer to real APT measurement problems and show how complementary information to the experiments are enabled by simulations.

7.1. Exerted stress on an embedded particle

Already in the early publications about the simulation of field evaporation, coherent embedded particles have been investigated [VBB00]. If heterogeneous evaporation properties apply, a severe change of the local emitter curvature is observed which gives rise to trajectory aberrations. A focusing or de-focusing of the ions is noticed ("local magnification") [Mil87; Vur+04b]. In consequence, not only the local atom density but also the size of features may appear decisively modified in derived APT reconstructions [OS11].

Let us consider here again a particle but with different focus. The general premise for successful APT reconstructions is that all collected atoms in a measurement do originate from a coherent part of the sample. Although this seems rather trivial, this condition is not necessarily ensured in the experiments: In a conventional atom probe, a standing voltage applies to the sample which is periodically superimposed by short high voltage pulses for triggering the field evaporation. Provided the emitter is metallic, we can expect the respective surface charge density to be proportional to the acting fields. A rough estimate of the exerted stress is given by

$$\tau_{\mathrm{Apex}} \approx \epsilon_0 \, E_{\mathrm{Crit}}^2$$

Here, E_{Crit} denotes the critical evaporation threshold and ϵ_0 the vacuum permittivity. From this, a significant tensile stress of about 1 GPa is conceivable in experiments. With regard to the pulsed measurement conditions, an additional dynamic stress contribution of about two orders in magnitude below, e.g. in the range of 50 MPa affects the sample tip if a typical pulse ratio of about 20 % of the standing voltage is assumed. Indeed, experimental evidence for the present stress are specimen ruptures that are routinely encountered and usually cause the emitter to fail afterwards.

With particular regard to the particles, the question arises whether there is a distinguished force which pulls on the particle and, provided this is the case, whether

the arising stress is sufficient so that a complete loss of particles may happen.

As it is demonstrated in the following, this problem can be directly addressed in the frame of the new simulation approach by tracking the respective forces at the sample apex according to equation (4.18). Figure 7.1 depicts the sample geometry in these considerations. In order to closely match typical experimental samples, a complex structure is assumed consisting of a substrate tip coated by a matrix layer in which the particle is embedded. Three different cases with critical evaporation thresholds of the particle are regarded: (a) reduced by 40 %, (b) equal field strength, and (c) elevated by 40 % in comparison to the matrix. For instance, in the measurement of Al precipitates in Cu about the same difference is expected ($19\,\mathrm{V\,nm^{-1}}$:$30\,\mathrm{V\,nm^{-1}}$).

Snapshots of the field and force distributions at an intermediate stage of the simulated desorption sequence are shown in figures 7.2a to 7.2c for the three cases, respectively. In (a) and (c), modified curvature radii at the particles are visible. Consequently, fields become locally reduced or increased. Estimated forces are in the range between 10 pN to 100 pN. They are generally enhanced at terrace edges. Most remarkable, the forces depend decisively on the contrast in evaporation thresholds. Different stress curves with respect to the number of removed atoms are shown in figure 7.3. These quantitative values have been derived by considering the vector sum of induced force at the surface atoms separately for each species. As effective area on which the force acts, the maximum extents of the desired atom positions in lateral direction, perpendicular to the specimen axis have been used. So, the plotted curves represent the mean stress that applies.

The visible increase of the stress in the matrix ("layer" + "substrate") is due to an artificial effect of the boundary of the simulation mesh which would not appear for tips of realistic length. The matrix stress shows in addition a small indent when the particle atoms are evaporating. This is probably an artifact of the separate

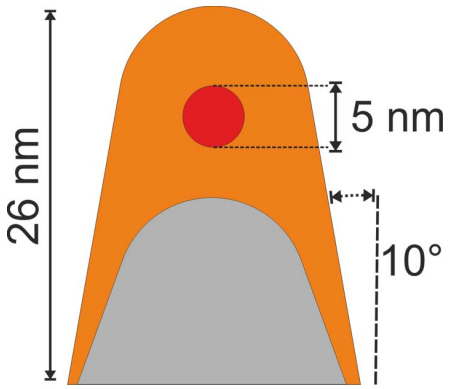

Figure 7.1.: Considered emitter geometry for the investigation of the exerted force on an embedded particle.

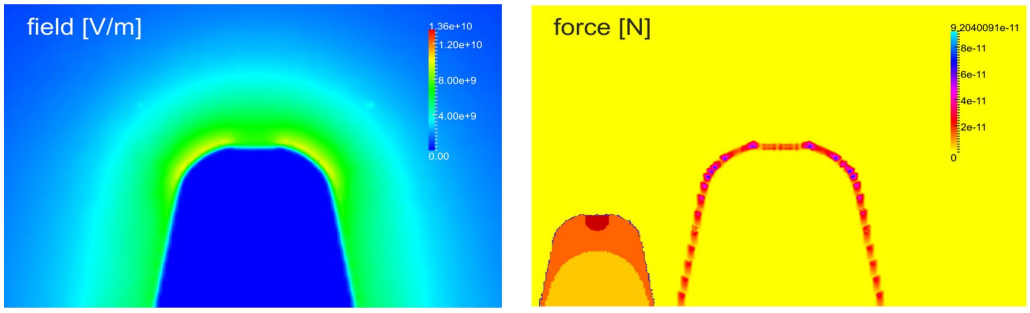

(a) 40 % reduced threshold

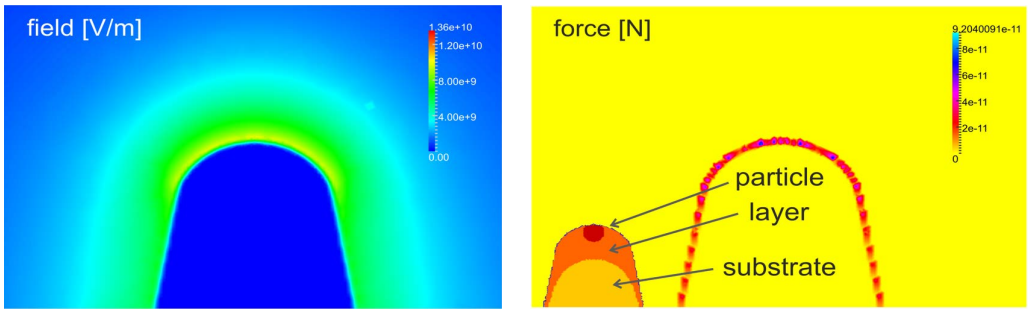

(b) equal threshold

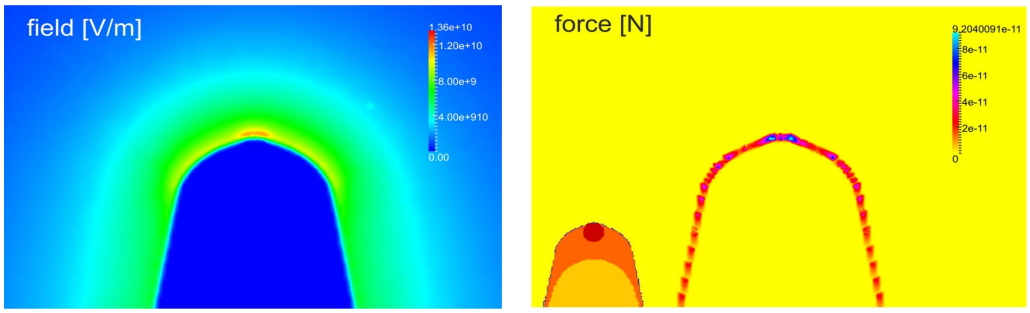

(c) 40 % elevated threshold

Figure 7.2.: Distribution of the field (left column) and the force (right column) at the emitter during the simulated evaporation of a particle. Three cases with different relative evaporation thresholds in comparison to the matrix are investigated. The intermediate stage with an already partially field evaporated particle is depicted.

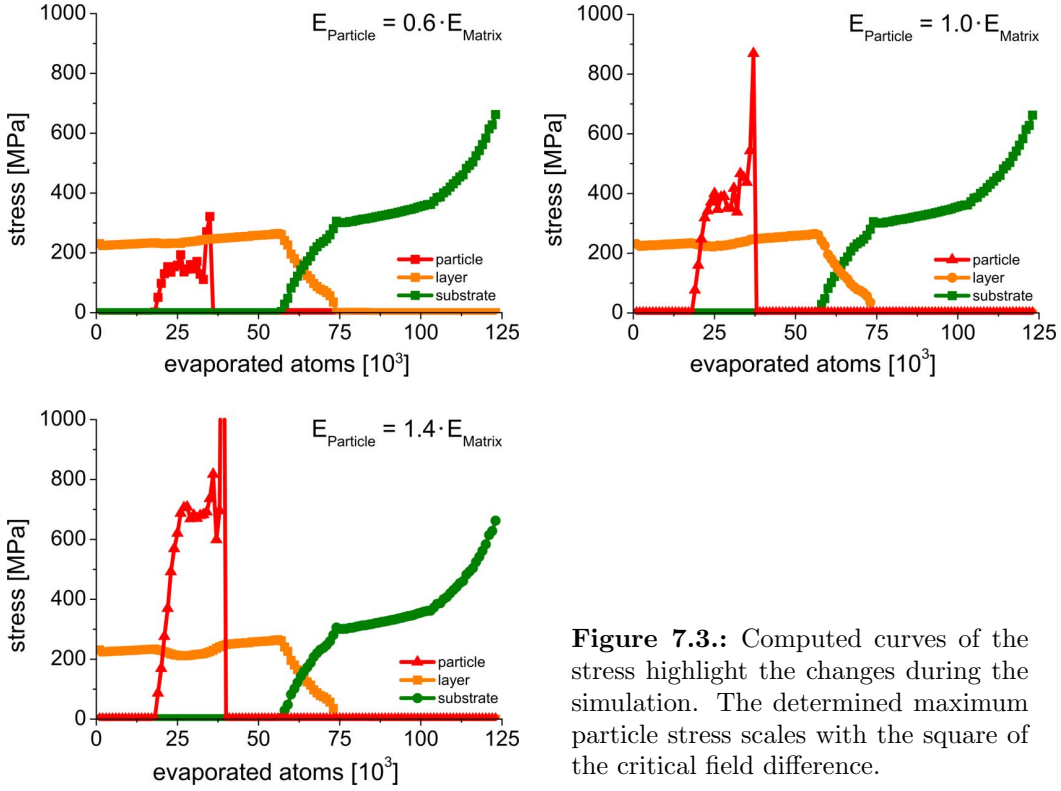

Figure 7.3.: Computed curves of the stress highlight the changes during the simulation. The determined maximum particle stress scales with the square of the critical field difference.

calculation of stresses for the particle and the matrix.[1]

Mostly due to the used estimate for the considered area, the particle stress gets already elevated in the case of equal evaporation properties. But besides this limitation, the determined absolute values nicely scale with the square of the preset evaporation thresholds in the three depicted cases, e.g. according to 0.6^2 and 1.4^2, respectively. This is a remarkable finding, because in experiments even stronger differences in evaporation thresholds are possible, e.g. Al:W= 30 %. Hence, a significant additional load can be present which demands a strong fixture of the particle to the matrix. If it is too weak, a major part of the particle may elute and is lost for the analysis. Even worse, such kind of a "nano rupture" cannot be expected to have a visible effect on the recorded voltage curve and therefore may even remain undetected at all.

In conclusion, this example not only illustrates the capability of the simulation in view of the additionally enabled force information. It also emphasizes that besides imaging artifacts, concerns with regard to the selective loss of atom data are indeed justified. Cohesion between the precipitate and matrix may get even poor if

[1] The contribution to the force acting on the particle atoms is not taken into account. The force at the (interior) particle to matrix interface equates to zero.

field penetration becomes possible. Under these circumstances, interior forces due to heterogeneous dielectricity build up in addition. However, this more complex situation is out of the scope here and may be the subject of future investigation.

7.2. Simulated evaporation of a complex multi-layer structure

Following the special example with the stresses, the full capabilities of the simulation approach are explored in this section. For this, the simulated evaporation of a tri-layer structure shall be investigated (fig. 7.4). The bottom layer has a bcc structure equal to that of tungsten. It is covered by an amorphous AB alloy which consists of two different atom species. The top layer is again crystalline and represents the fcc lattice of Al.

For the construction of the amorphous layer, the model of hard spheres has been considered: An initially random distribution of atom positions with 50 % A and 50 % B is set up. Subsequently, this structure gets relaxed to a meta-stable equilibrium configuration by a molecular dynamics (MD) calculation. Lennard-Jones pair potentials and different equilibrium distances $r_A = 2.5\,\text{Å}$ and $r_B = 5.0\,\text{Å}$ for both species are applied. For the AB interaction the equilibrium distance $(r_A + r_B)/2 = 3.75\,\text{Å}$ is chosen.

By the MD approach, a realistic atom structure is received which possesses irregularly shaped Wigner-Seitz cells (see the inset in fig. 7.4b). The amorphous structure represents the ultimate test for the implementation of the new simulation

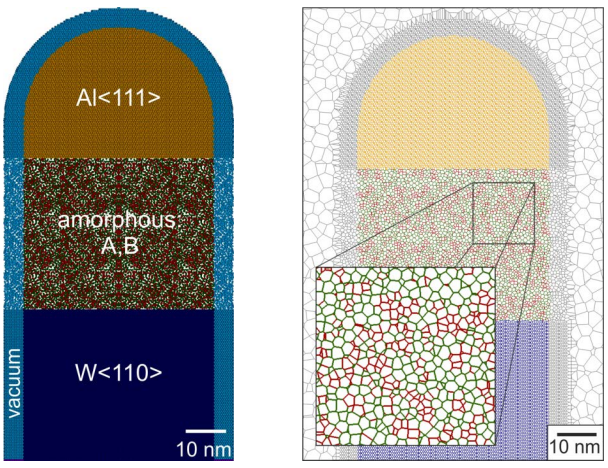

(a) **(b)**

Figure 7.4.: Sketch of the simulation mesh for the investigation of the tri-layer emitter structure [OES13]: (a) atom distribution, (b) geometric dual representation by Wigner-Seitz cells. Marked orientations of the crystalline layers are parallel to the sample axis.

Table 7.1.: Applied parameter values and properties of the layer stack

parameter	Al	amorphous (A + B)	W
lattice constant and equilibrium distance, respectively (Å)	4.05	2.5, 5.0, 3.75	3.16
atom mass (u)	27.0	14.0, 32.0	183.9
atomic density (nm^{-3})	60.2	21.2 (mean)	63.4

approach that allows for arbitrary atom positions. The full set of basic parameters is listed in table 7.1.

7.2.1. Curvature changes at the apex

Based on this well-defined structure, different simulation runs with different critical evaporation thresholds for Al, W, and the amorphous species (A,B) are processed. The computed evaporation probabilities are scaled according to equation (4.19) which ensures a realistic control of the evaporation sequence. Field induced forces and differently shaped Wigner-Seitz cells at the emitter structure are appropriately taken into account by this approach. The successful application is proven by the series of emitter shapes taken at different stages of the simulation (fig. 7.5). In this first example, equal critical evaporation thresholds apply for all species. As expected, a steady apex curvature develops that is independent of the respective layers.

In clear contrast are the results for the case with inhomogeneous thresholds

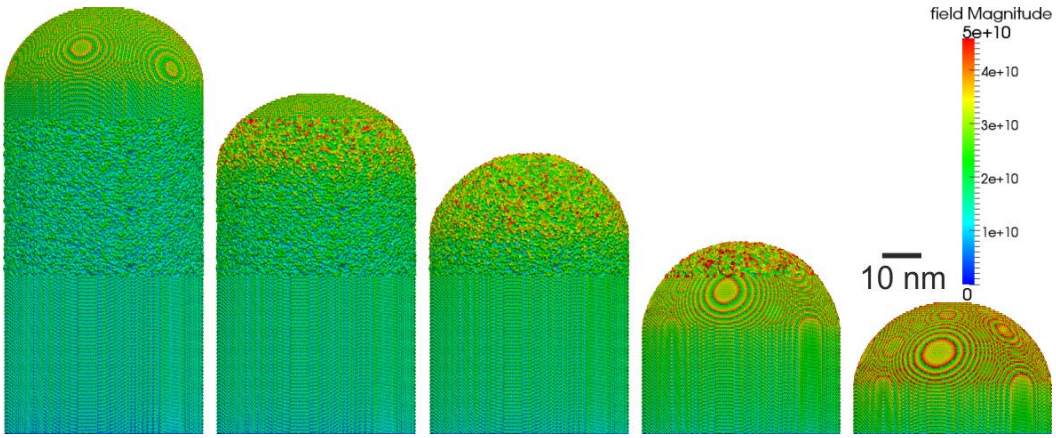

Figure 7.5.: Series of emitter shapes during the simulated field evaporation of the tri-layer structure. If equal critical thresholds apply for all species, a steady emitter curvature develops in consequence.

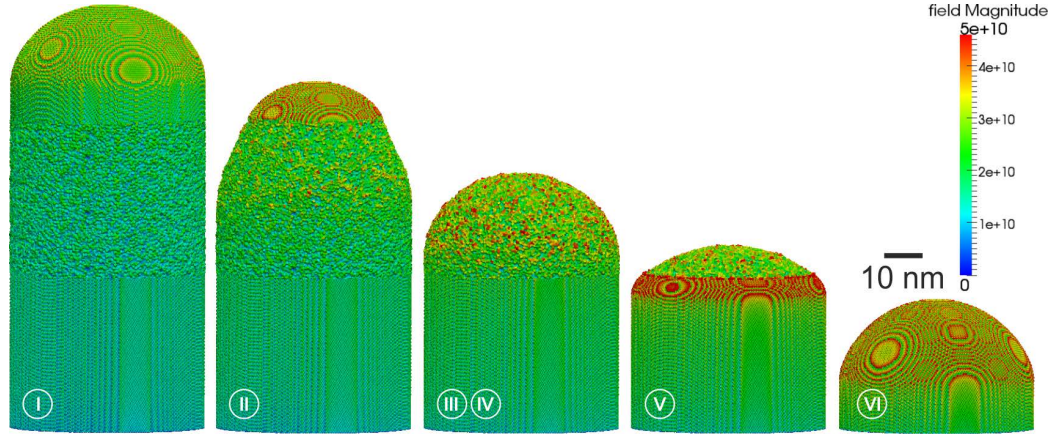

(a) shape of the emitter apex

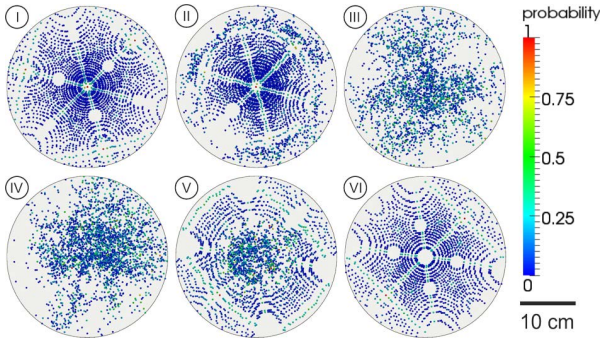

(b) detector hit distribution

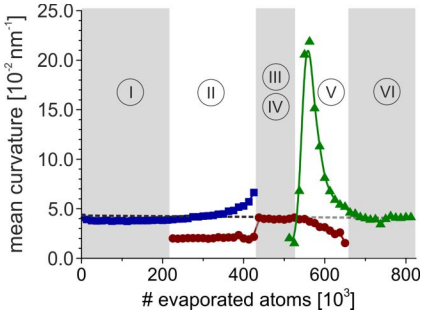

(c) evolution of the apex curvature

Figure 7.6.: Results of the simulation with the critical evaporation fields of the amorphous layer set to 20 V nm^{-1} and 17 V nm^{-1} for A and B, respectively [OES13]. By the latin numerals, different stages presented in (a) are linked to the observed detector hit events presented in (b). Attributed colours in (b) denote the evaporation probability in the moment of desorption. Determined curvature changes are shown in (c).

(fig. 7.6). In this second example critical thresholds of the amorphous are set to 20 V nm^{-1} (A) and 17 V nm^{-1} (B), while for the Al and W 19 V nm^{-1} and 57 V nm^{-1} apply, respectively. As before, figure 7.6a presents different stages of the simulation. In addition, figure 7.6b shows associated maps of the observed detector hits.

The first stage (I) represents the situation after the first few atomic layers of Al have been desorbed. An equilibrium surface has evolved and the expected fcc ⟨111⟩ desorption pattern is visible on the detector. Number (II) depicts the transition to the amorphous layer. Although the critical thresholds for A and B are almost comparable to Al, a clear effect is noticed. Due to the different thresholds that apply, the apex remains no longer spherical. Instead, it becomes a cone with a

hemispherical Al cap at the top. Accordingly, the Al desorption pattern in figure 7.6b appears now confined to the centre of the detector while outside a ring of randomly distributed atoms appears. The next snapshots with labels (III) and (IV) represent the steady shape within the amorphous phase. Remarkably, no steady detector image evolves in these stages. Instead, correlated density fluctuations are moving around on the detector. This simulated behaviour resembles indeed the experimental observation with atom probe analyses of e.g. glassy structures. At the transition to tungsten, the hits of the amorphous atoms become more and more confined to the centre (V). At the same time, the pattern of crystalline tungsten appears from the outside until the complete area is covered (VI). Because of the strong difference in the applied evaporation threshold between W and the amorphous layer, the change in surface morphology is even more severe than at the previous interface (compare (II) and (V) of fig. 7.6a).

It is instructive to track the progressive modification of the apex shape in more detail. We extract quantitative values of the curvature by fitting the apex contour in 2D. Figure 7.6c shows the curvature for each layer plotted versus the number of evaporated atoms. The computed mean curvature $\overline{R}^{-1}$ results from the fitted principal curvatures and equates as the harmonic average

$$\overline{R}^{-1} = \frac{1}{2}\left(\frac{1}{R_1} + \frac{1}{R_2}\right)$$

A steady curvature appears at all stages when only a single layer is evaporating (I, III+IV, VI). This steady curvature is preset by the radius of the cylindric shaft. In this example, the value amounts to $25^{-1}\,\mathrm{nm}^{-1}$ and is marked by the long dashed line in the plot. At the transition stages (II) and (V), the curvature radius of the layer with the higher critical threshold for evaporation decreases ($\overline{R}^{-1}\uparrow$), whereas it increases ($\overline{R}^{-1}\downarrow$) for the layer with the lower critical evaporation threshold. Quantitatively, it is not clear how the determined changes do depend on each other. A fixed ratio in the curvature is hardly seen. For instance, in (II) the curvature of the amorphous is depressed and it remains the same, while the curvature of the Al on top increases in time. However, we do notice that the determined increase in curvature corresponds to a clearly elevated surface field for the Al and W as it is depicted by the colouring in figure 7.6a. This finding reflects the usual relation between curvature and field ($E_{\mathrm{Crit}} \sim \overline{R}^{-1}$). During the transition from one layer to the other, atoms of higher threshold field are retained at the emitter apex. Curvature increases. The other way around, atoms with the lower critical field show preferential evaporation during the transition. Therefore, the curvature decreases.

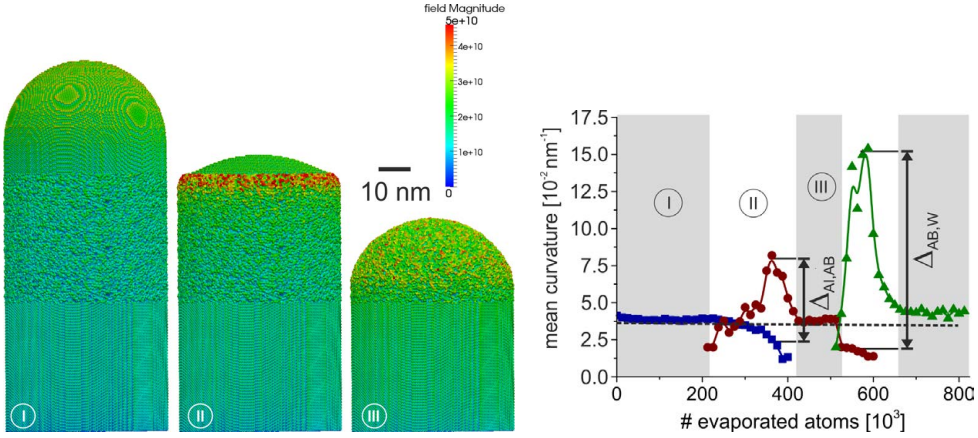

(a) shape of the emitter apex **(b)** evolution of the apex curvature

Figure 7.7.: Results of the simulation with the critical evaporation fields of the amorphous layer set to $30\,\mathrm{V\,nm^{-1}}$ for both A and B, respectively. The latin numerals refer to the analogue situation depicted in figures 7.6a and 7.6c before. Labels $\Delta_{\mathrm{Al,AB}}$ and $\Delta_{\mathrm{AB,W}}$ mark the curvature difference at the respective transition stage.

Results of another simulation are presented in figure 7.7. Here, the critical threshold is set to $30\,\mathrm{V\,nm^{-1}}$ for both of the amorphous species, A and B, respectively. For Al and W the same values as before apply. The results confirm the already described tendency. Again an elevated curvature for the material with higher evaporation threshold develops at the transition stages, while the curvature for the material with the lower evaporation threshold decreases at the same time.

In addition, a comparison of the curvature changes is obtained in this case (fig. 7.7b). The difference approximately amounts to $\Delta\overline{R}^{-1}_{\mathrm{Al,AB}} \approx 5.6 \cdot 10^{-2}\,\mathrm{nm^{-1}}$ at the first transition and to $\Delta\overline{R}^{-1}_{\mathrm{AB,W}} \approx 13.3 \cdot 10^{-2}\,\mathrm{nm^{-1}}$ at the second transition. The ratio $\Delta\overline{R}^{-1}_{\mathrm{AB,W}} : \Delta\overline{R}^{-1}_{\mathrm{Al,AB}}$ equates to about 2.4 which is astonishingly close to the expectation on the basis of the preset evaporation thresholds:

$$\frac{E_{\mathrm{Crit,W}} - E_{\mathrm{Crit,AB}}}{E_{\mathrm{Crit,AB}} - E_{\mathrm{Crit,Al}}} = 2.5$$

Although the fitting approach for determining the curvatures yields presumably a rough estimate, this good correspondence nevertheless suggests that the predicted changes at the apex due to heterogeneous evaporation thresholds are indeed realistic.

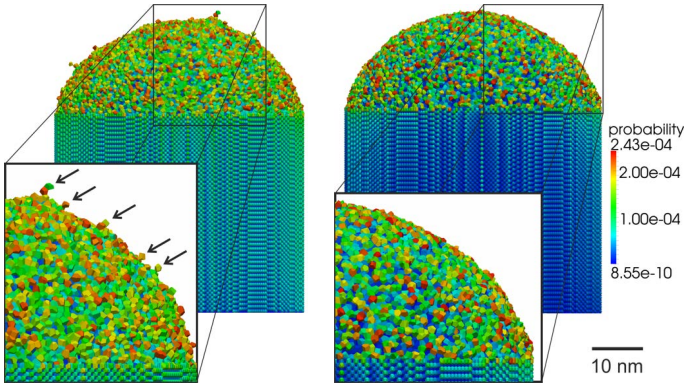

Figure 7.8.: Irregular surface contour of the amorphous layer as result of the considered approach for controlling the evaporation sequence [OES13].

(a) controlled by the *field*, equation (4.4)

(b) controlled by the *force*, equation (4.19)

7.2.2. Consistent control of the evaporation sequence

In the introduction to this chapter, it has been mentioned that the investigation of the amorphous structure provides a critical check for the reliability of the simulation approach. Indeed, severe differences of the surface morphology are encountered if the desorption sequence is controlled either by the conventional field approach or the alternative new approach based on the force (sec. 4.2.4). In figure 7.8, a magnified view of the different surface morphologies is presented. In the case of purely field controlled evaporation (fig. 7.8a), chains of atoms stick out from the surface. This may be seen as a qualitative evidence that the field approach is not appropriate. In contrast, if the field induced forces are considered to control the evaporation sequence, a smooth surface is seen.

Such different morphologies only appear if an disordered structure is processed. For instance, in the case of the regular lattices both approaches turn out to be equally applicable. Nevertheless, we consider the force approach as more generally applicable to a broader range of problems.

7.2.3. Additional information required for direct comparison with experimental data

Besides the detector hit position, data sets from atom probe experiments usually contain the actual emitter voltage and the determined time-of-flight. Although in the simulation approach neither the voltage at the emitter nor the interdependence with the flux of desorbing atoms is particularly regarded, complete data sets resembling real measurements can nevertheless be extracted. In this way, a comparison of data from the simulations with experimental observations becomes possible.

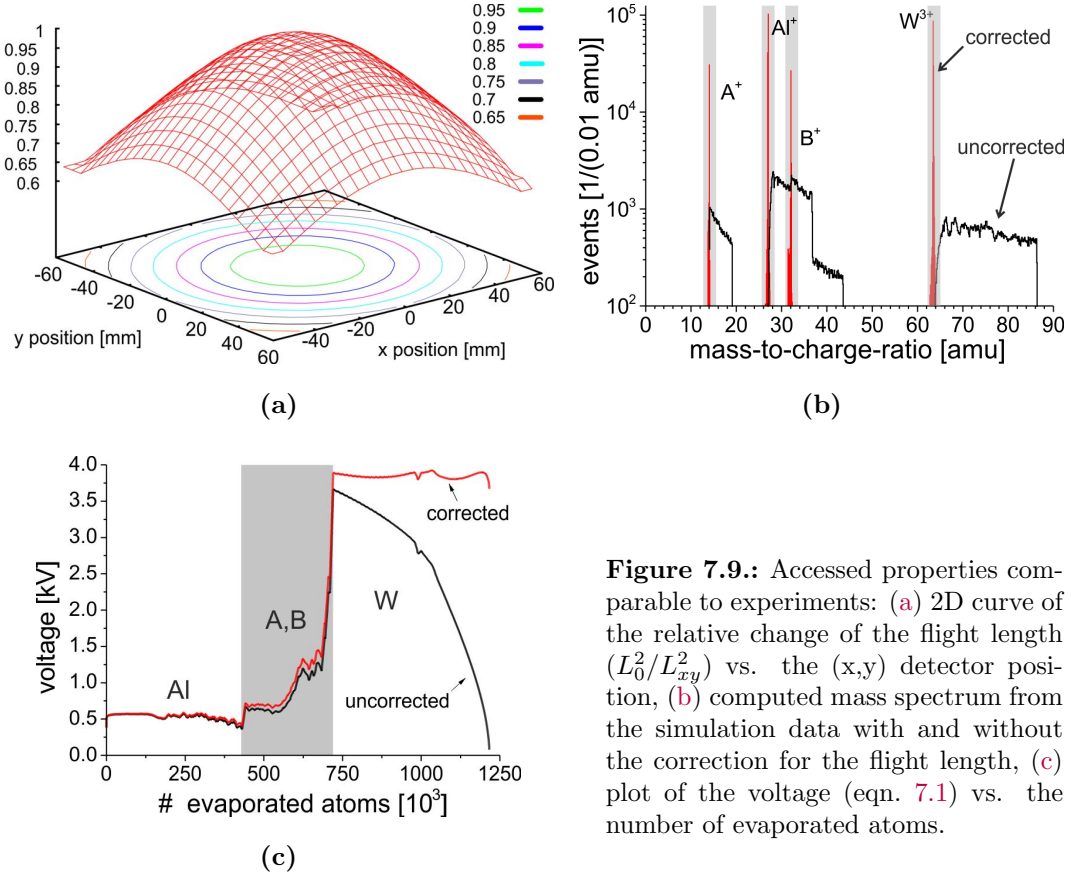

Figure 7.9.: Accessed properties comparable to experiments: (a) 2D curve of the relative change of the flight length (L_0^2/L_{xy}^2) vs. the (x,y) detector position, (b) computed mass spectrum from the simulation data with and without the correction for the flight length, (c) plot of the voltage (eqn. 7.1) vs. the number of evaporated atoms.

The missing information is derived by making use of the general scale invariance of the electric field and the equation of motion. The field E_i determined in the simulation and the preset evaporation threshold $E_{\mathrm{Crit,i}}$ for desorbed specimen i are regarded as a scaling factor for the voltage

$$U' := \left(\frac{E_i}{E_{\mathrm{Crit,i}}}\right)^{-1} \cdot U \tag{7.1}$$

In consequence, the rescaled time-of-flight equates to

$$t' := \sqrt{\frac{E_i}{E_{\mathrm{Crit,i}}}} \cdot t \tag{7.2}$$

The graph in figure 7.9c shows the evolution of the rescaled voltage for the already discussed example of the complex layer structure. Unfortunately, no clear voltage plateaus are present. This is an effect of the boundary conditions at the bottom of the simulation box. If the field emitter shrinks in the simulation, the field at

the surface of the emitter increases and the computed voltage from equation 7.1 decreases. In particular, this can be seen for the W part, but the decrease is present already from the beginning. Anyhow, the superimposed distortion of the voltage curve can be corrected for[2] and curves almost comparable to the experiments are obtained.

The time-of-flight information does not suffer from the previous artifact. Instead, another problem is encountered as in the case of real experiments. Figure 7.9a shows the relative change of the squared flight length in dependence on the detector position. Due to the curved trajectories, the actual flight length severely depends on the detector position. It may become significantly elongated ($\leq 20\,\%$). Therefore, the classic equation for the mass to charge ratio

$$\frac{m}{n} = \frac{2\,e\,U}{L^2} \cdot t^2 \tag{7.3}$$

does not offer sufficient precision. Peaks in the computed histograms appear broadened (fig. 7.9b). In the case of experimental data, this problem is addressed by the introduction of a correction function which accounts for the mass in dependence on the determined detector position. If the same correction is applied to the simulated data, sharp mass peaks in the mass spectrum at the expected position become visible. — Although this is a rather technical point, this example nicely demonstrates how data from the simulation and experimental approaches combine.

7.3. Investigation of a grain boundary in copper

The last part of this chapter deals with the analysis of a $\Sigma5[010](\bar{1}02)$ tilt boundary in copper. This example is chosen in order to demonstrate the new ability of the simulation approach to investigate field emitter samples with structural defects.

From the experimental side, the analysis of grain boundary segregation is of particular interest. In comparison to other methods, the outstanding ability of APT lies in the native access to true 3D chemical information. This advantage becomes even more pronounced with the advent of wide-angle instruments. By the enlarged field of view, the analysis of grain boundaries has been decisively facilitated.

However, with regard to the investigation of GB segregation, the possible accuracy of determined concentration profiles is limited by the counting statistics.

[2] E.g. by fitting the general decrease of the voltage if we require the voltage plateaus in the parts with only Al or W to be flat

Already half the atoms get lost during the measurement due to the limited detection efficiency of the instruments. If a nano-sized volume is investigated, this loss of information may be severe. Particularly, in the case of segregation, the number of atoms becomes small and limits the accuracy.

In addition, misplacing of atoms in the reconstruction is observed. In the case of heterogeneous evaporation conditions or exceptional emitter curvatures, this contributes to chemical inaccuracy. Marquis et al. demonstrated by the investigation of small precipitates that these artifacts are systematic in space but also depend on chemistry [MV08]. Obviously, such artifacts are particularly fatal for the careful analysis of segregation. In general, artifacts in APT either originate in the measurement process or they are introduced by the reconstruction. Simulations can help to reveal such artifacts and can in this way improve the interpretation of experimental results.

For the example of the grain boundary, investigations are conducted into two different directions. The next section shows simulation results for different alignments of the GB plane in the range from 0° inclination (parallel to the emitter axis) to 90° inclination (perpendicular to the emitter axis). In all cases, homogeneous evaporation thresholds are assumed in order to work out the mere effect of the GB geometry. A varying evaporation threshold for the GB is most likely to appear if segregation is investigated. Effects of inhomogeneous evaporation properties are described in a second part. A single orientation of the GB with 0° inclination is considered therefor.

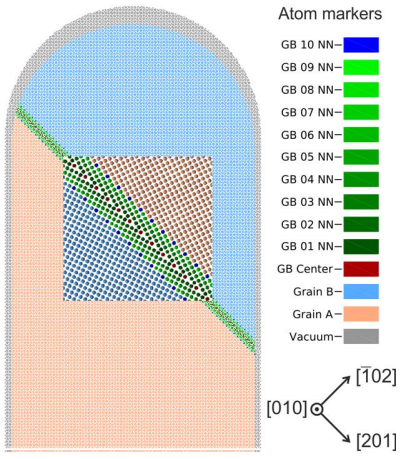

Figure 7.10.: Prepared sample structure with a Σ5 grain boundary depicting 45° inclination of the GB plane to the emitter axis. The distance of atoms to the GB core is independently colour coded .

7.3.1. Different inclination angles

The geometric structure of a relaxed $\Sigma5[010](\bar{1}02)$ boundary at 0 K in copper has been obtained by using a MD approach. Details of this procedure are outlined in [SM03]. However, due to the high symmetry of the $\Sigma5$, relaxed atom positions from this approach almost match the positions which would be derived from the coincidence lattice. Figure 7.10 shows an example of the prepared emitter sample with 45° inclination of the GB plane. The greenish coloured atoms denote atoms close to the GB core. Different distances up to the tenth nearest neighbour (NN) are distinguished. Atoms at the GB core are drawn in red. The general geometry of each emitter sample is the cylinder with half-spherical cap, 70 nm in height and 50 nm in diameter. Simulated samples consist of more than 1.5 million individual atoms.

Details for 45° inclination

In the following, we focus at the sample with 45° inclination. In figure 7.11, maps of the detector events at two different stages of the simulation are presented. Events corresponding to the grain located above the GB (fig. 7.11a) and events corresponding to the grain located below the GB (fig. 7.11b) are shown. Both patterns look the same except that they are mirrored along the y-axis reflecting the symmetry of the evaluated $\Sigma5$ GB.

The intermediate stage just when atoms at the grain boundary start field evaporating and just before the GB vanishes is shown in figure 7.12. The grain boundary reveals itself by the narrowly confined area in between the two different desorption patterns of the upper and lower grains. According to the projection of the curved apex onto the detector, the GB is imaged as a curved line.

Once a sufficient volume of the emitter structure with the GB inside has been evaporated, the 3D reconstruction of the collected data is processed. The result is plotted in figure 7.13. In the depicted cross section, the GB plane no longer appears as a straight line. Instead, distinguished distortions are visible. The width of the GB zone up to the tenth NN appears alternately compressed or expanded. It changes between 2 nm, which almost corresponds to the size of the geometrical core, and 4 nm. In consequence, the atom density is not homogeneous (a detailed analysis referring to this will be presented subsequently in sec. 7.3.2). Different zone lines are revealed by the depleted area in the reconstruction. At locations where the GB crosses a zone line, kink like artifacts are visible. Next to the GB, lattice planes with different orientation may be recognized within both depicted grains.

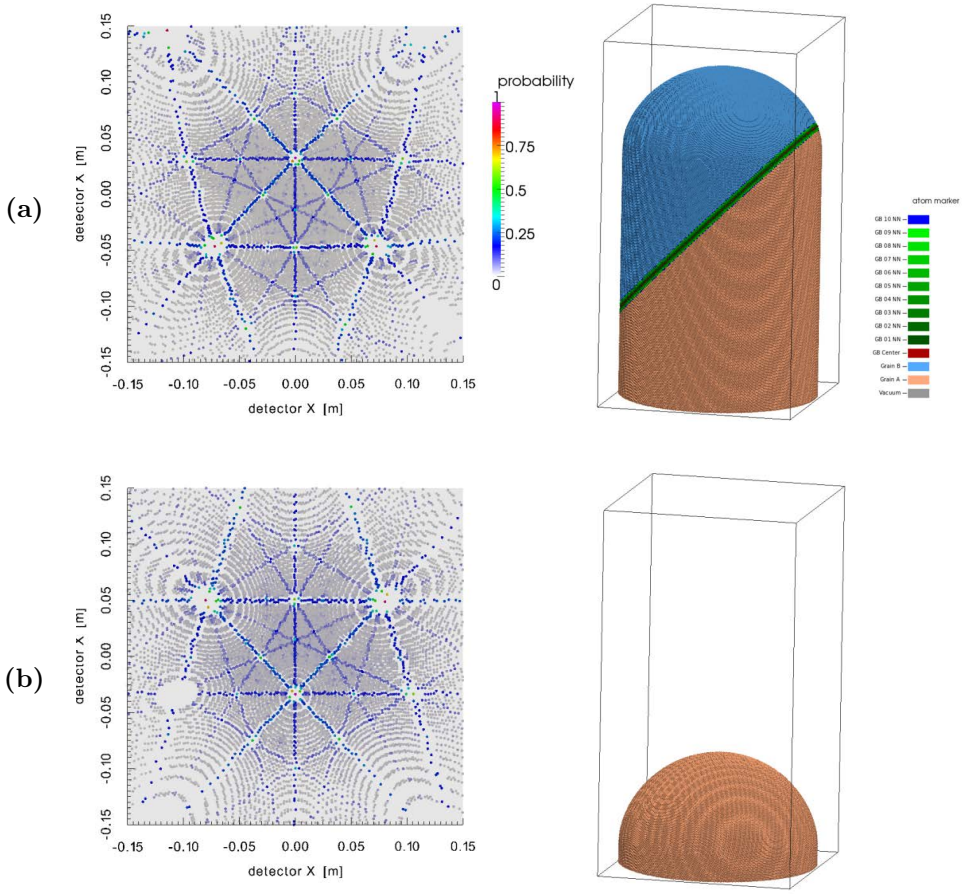

Figure 7.11.: Obtained detector hit map and shape of the emitter structure: (a) depicts the detector pattern for the first grain at the top, (b) shows the detector pattern of the second grain. The colouring depicts the evaporation probability of the atoms in the moment of desorption.

On the basis of the reconstruction, we can consider why the comparably confined defect of a GB leads to such striking artifacts. In the presented detector maps, displacements of the trajectories from GB atoms seem to be negligibly small. On the other hand, the GB in the sample has been set up as a flat plane. The observed kinks in the reconstruction are interpreted as systematic displacements of the computed z-coordinates. For this reason the GB plane appears similar to a creased sheet of paper. So, the seen displacements can only be explained by a significant disturbance of the evaporation sequence. As an explanation, we consider the zone lines. These correspond to distinct lattice orientations. In the desorption maps they appear as poles. The emitter apex in the vicinity of the poles is faceted. If it comes to the transition from one grain to the other, in the case of a GB, the faceting changes.

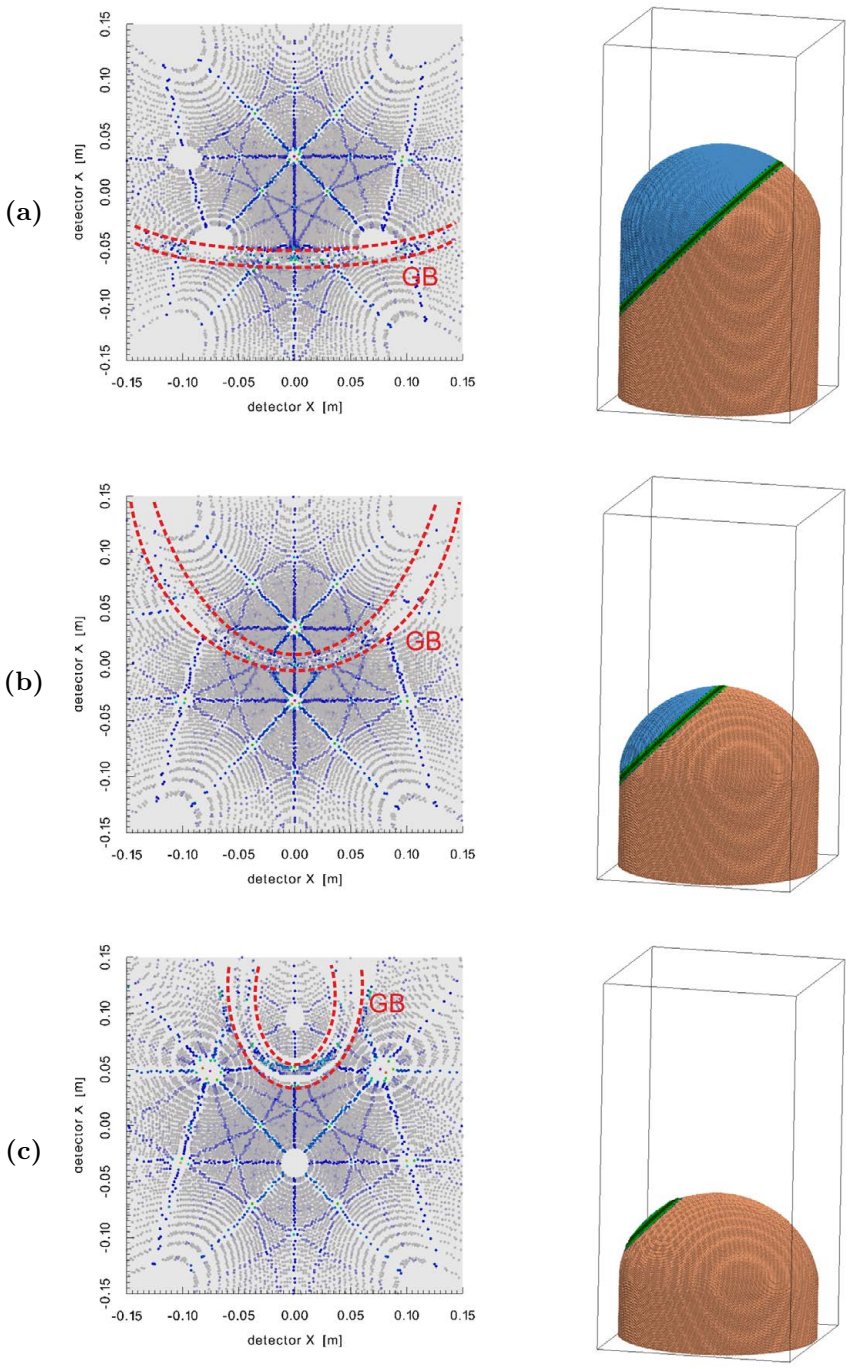

Figure 7.12.: Detector hit map and shape of the emitter structure. Three intermediate states (a)-(c), when the GB comes to evaporation, are shown.

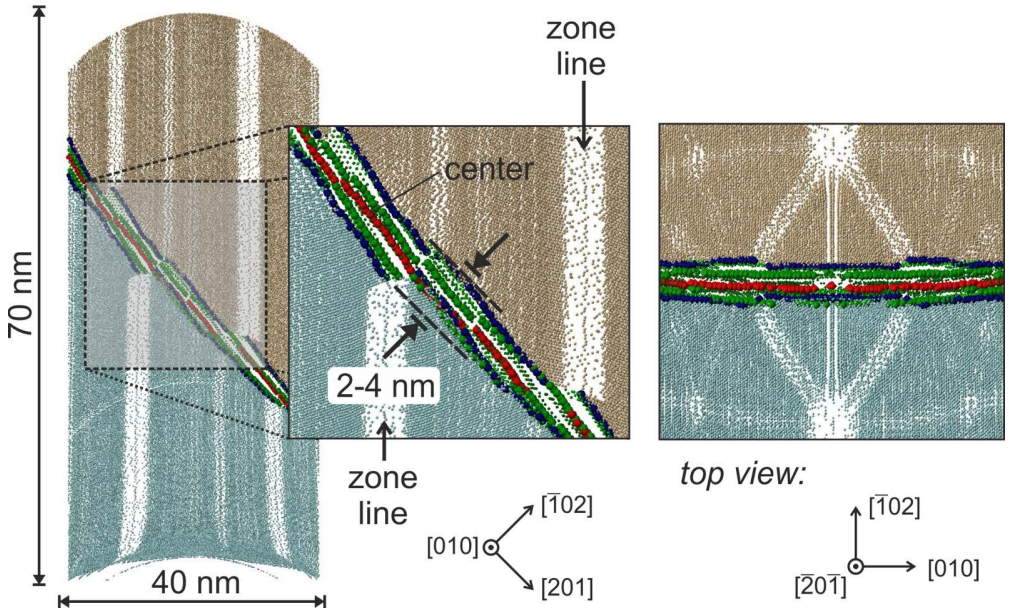

Figure 7.13.: Reconstruction of the Σ5 GB with 45° inclination

From this, we conclude that atoms evaporate preferentially or are retained at the apex if an existing facet vanishes or a new facet forms, respectively.

Results for additional inclinations: 0° – 90°

Reconstructions computed from inclinations of the GB other than 45° show qualitatively the same artifacts (fig. 7.14); namely the reduced atom density and the kink like distortions at the changing zone lines. Even in the case of a perpendicular alignment (fig. 7.14d), clear artifacts are present. In this case, marked GB atoms are reconstructed as curved planes. The only exception is the reconstruction with the horizontal alignment of the grain boundary (fig. 7.14a), which exhibits almost no distortions at all. Since there is no lateral transition between distinguished orientations of the grains, kink like artifacts do not develop. Notably, this is the only set up of the GB which ensures an undisturbed evaporation sequence at the apex. Therefore, any observed distortions in this example can only be due to displaced trajectories. Indeed, we will see in the subsequent section that the determined atom density in the GB core is lower than in the matrix.

Although such small displacements of the trajectories cannot be excluded, they seem to be of minor importance here. Rather the discussed error in the z-positioning of the atom is predominant. These deviations in depth explain on the one hand the curved GB surfaces in figure 7.14d and are also responsible for the varying width

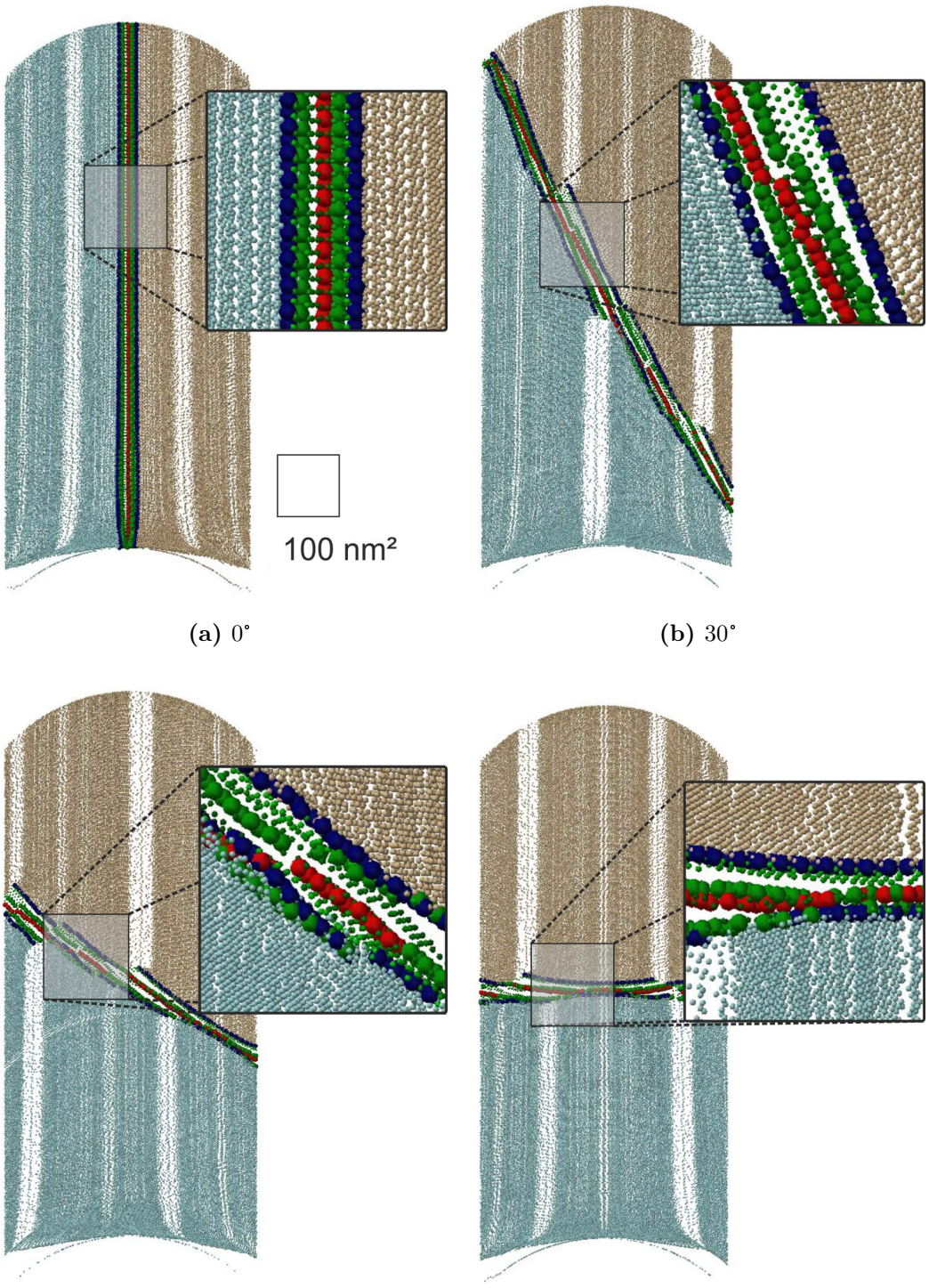

(a) 0˚ **(b)** 30˚

(c) 60˚ **(d)** 90˚

Figure 7.14.: Reconstructions of the Σ5 GB for different inclination angles

of the GB in the reconstructions with inclinations from 30° to 90°.

7.3.2. Segregation effects

Up to this point, only simulations with equal evaporation thresholds for all atoms were presented. Now, we extend the analysis and allow different evaporation thresholds. Two cases either with a reduction in the evaporation threshold by 20 % or with an elevation by 20 % with respect to the matrix are addressed. Only the vertical alignment of the GB plane which before turned out to be only weakly affected by artifacts is studied. Figure 7.15 depicts the steady surface shapes of the respective field emitter which develop. Clear changes in the local surface curvature can be seen. If reduced thresholds apply, a ridge like shape evolves. In contrast, a bulge is formed for elevated ones.

We expect that this emitter shape will cause severe aberrations of the trajectories. And indeed, computed reconstructions show clear artifacts in (fig. 7.16a and 7.16c). The GB zone is either broadened in the case where the bulge develops (elevated evaporation thresholds) or is slightly compressed if the ridge is present (reduced thresholds).

A quantitative analysis is enabled by determination of concentration and density profiles across the GB plane (fig. 7.16b and 7.16d). The additional broadening of the segregation zone amounts to about 1 nm which means almost doubling the original width. If reduced thresholds apply, no significant reduction of the width is seen. But more severe, here atoms of the GB center intermix with atoms of the neighboured bulk. This mixing is caused by trajectory overlaps between evaporated atoms of the bulk with segregated atoms close to the GB core. In consequence, the maximum determined concentration is reduced to about 50 %.[3]

[3] Qualitatively, this effect may be seen with the naked eye in the lower half of figure 7.16c.

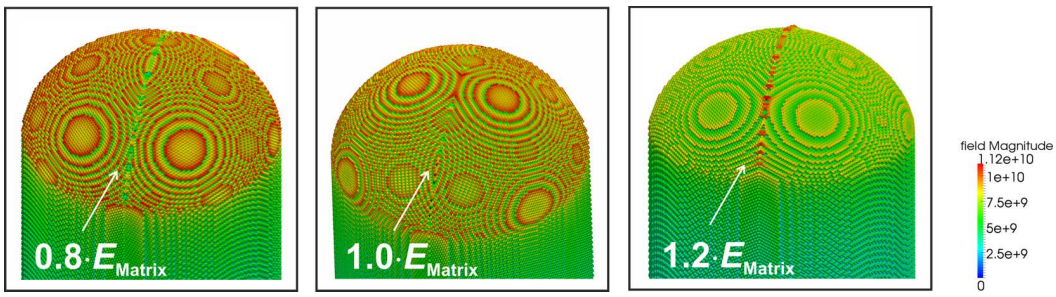

Figure 7.15.: Different emitter shapes in dependence on the applied evaporation threshold for segregated atoms at the GB develop [OES13].

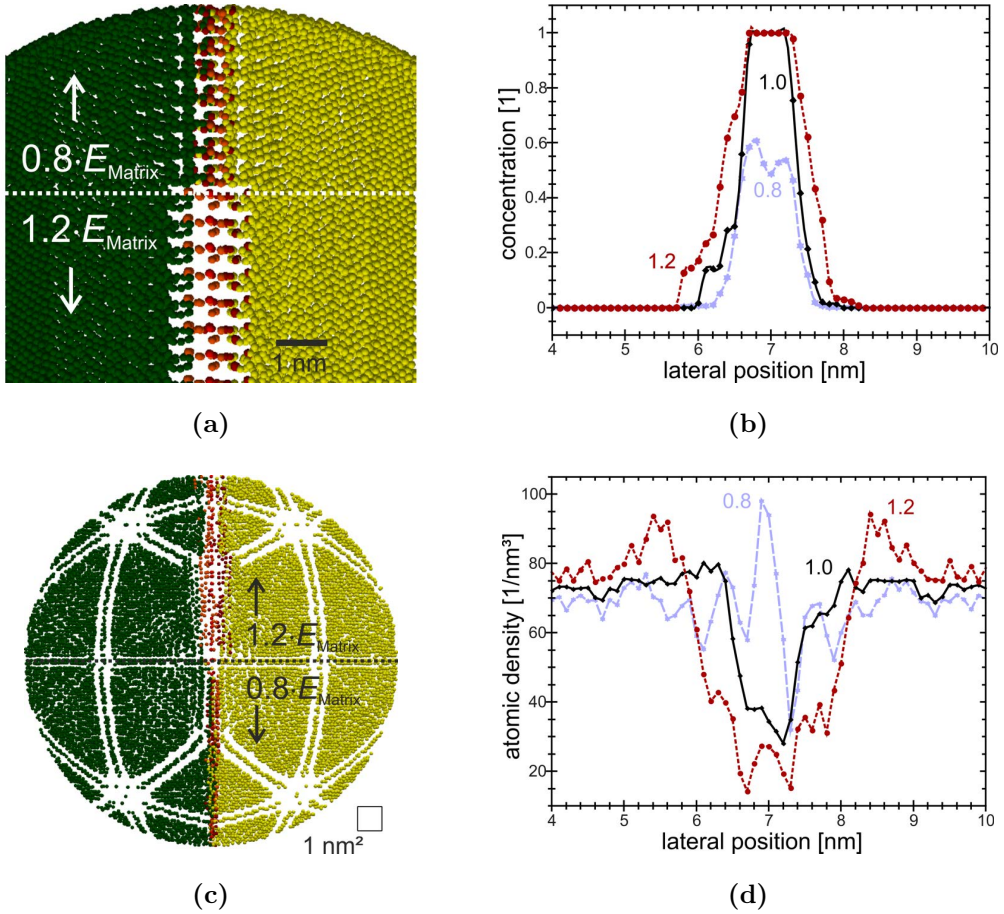

Figure 7.16.: Analysis of the impact of the simulated GB segregation on the reconstruction [OES13]: In (a) and (c) cross-sections through the computed reconstructions in directions parallel and perpendicular to the emitter axis are shown. Results for the cases both with reduced and elevated evaporation thresholds at the segregation zone are depicted. Atoms of the grains and of the segregation zone are drawn with different colours. (b) and (d) show plots of the concentration $c = \frac{N_{\mathrm{Seg}}}{N_{\mathrm{Seg}}+N_{\mathrm{Mat}}}$ and of the atom density versus the lateral position, perpendicular the GB plane, respectively.

Similarly, an analysis for the reconstructed atom density also shows significant effects. A depletion in the atom density around 50 % of the nominal value is determined for already homogeneous evaporation properties. This depletion is further enhanced in the case of elevated thresholds (∼28 %) of the segregating element and is less for the case with reduced thresholds (∼66 %). As a consequence of the described trajectory overlaps, the atom density at the GB core becomes increased.

8. Conclusion

In the process of this work, a theoretical investigation of APT experiments by means of a new numeric simulation approach is conducted. The applied approach has been termed the *generalized approach for APT simulation* because of its outstanding capabilities in the way it does reflect the real measurement conditions in APT.

In contrast to other existing simulation approaches before, this new approach is in particular characterized by the following features:

- The 3D simulation space is constructed from an adaptive mesh of irregular shaped Voronoi cells.
- Based on the well-defined partitioning of space by the cells, the Poisson equation is solved on a large range of length scales. The electric field information both in the vicinity to an embedded field emitter sample and at the mesoscopic scale is enabled.
- Trajectories of field emitted ions are computed at full-scale comparable to experiments.
- In a dual use, the detailed atomic bulk structure of the emitter sample is established by adopting the same Voronoi (Wigner-Seitz) cells which are already considered for the solution of the potential.
- The Voronoi cells in the emitter structure are explicitly attributed with different values of dielectricity. In this way, the sequence of field evaporating atoms from the emitter surface may be determined by considering field induced forces which directly take effect on the cells and literally pull at the respective atoms.

The forces are calculated unambiguously based on the Voronoi mesh. Therefore, they represent a reliable measure for controlling the evaporation sequence. In an example calculation of reduced size, the computed potential and field by this new approach is shown to be in accordance with results from an otherwise established FEM solver. Contrary, the analytic model of two confocal paraboloids does only poorly compare to the obtained solution of the potential.

The general imaging characteristics of ion trajectories in the new approach are investigated. Ions start from rest at the simulated emitter surface and are accelerated by the present field. The hit position on a detector plane is analysed. For the evaluation, a distinction is drawn between trajectories analysed in the *surface imaging* mode and those analysed in the *desorption* mode:

In the surface imaging mode, trajectories from the apex sites are probed all at the same time using the field which is computed once. Here, different emitter geometries with different parameters for the taper angle of the emitter shaft and the curvature radius at the emitter apex are considered. Qualitatively, the same dependence of the image compression on geometry as it is published in the literature is seen. Quantitatively, the determined image compression seems to be comparably weak. Presumably, this is due to the lack of an additional counter electrode in the conducted calculations. For the field factor, values in the range between 3 to 8 are determined. The image compression changes in between 0.65 and 0.93 dependent on the taper angle of the field emitter. The recently discovered cubic dependency by Vurpillot et al. could be confirmed.

In the desorption mode, detector events result from the consecutive shrinkage of the emitter apex atom by atom. Respective fields are repetitively updated after each event. The simulated detector hit positions are collected and subsequently analysed. The computed desorption maps for different emitter structures are investigated. For the cubic and hexagonal lattices in different orientations, a typical pattern with characteristic symmetry similar to experimental results is seen. In detail, it turns out that for a given atom the imaging position at the detector is in general not unique and depends on the field conditions at the moment of evaporation. Severe displacements may appear. E.g. in the comparison of identical atoms imaged both in the surface imaging mode and in the desorption mode, these displacements correspond to a shift in the launch angle of about 1.1° or more. Similarly, displacements are determined if a statistic evaporation sequence controlled by temperature is taken into regard. Due to a shift in the position of the recorded evaporation sequence, the depth resolution in the 3D reconstructions may then additionally degrade in the range of a few angstrom.

Astonishing results are furthermore obtained from the spatial analysis of the computed 3D reconstructions. Based on the data from the simulated evaporation of an exemplary bcc emitter structure, a test for the geometric consistency of the common reconstruction approach by Bas et al. clearly failed. It is demonstrated that this approach in general does not preserve the volume of reconstructions as it does not correctly account for the hit distribution of the events at the detector. In contrast, a modified reconstruction approach is proposed which corrects for this error. By considering such a well-calibrated reconstruction, a 3D Fourier analysis for the spatial resolution is conducted. The depth resolution is estimated to about 0.8 Å. A lateral resolution not better than about 1.5 Å is determined. Remarkably, these values are close to results of computed reconstructions obtained from

experimental data. This suggests that the possible resolution may be limited by the applied reconstruction approach itself. In contrast to present approaches on the basis of geometric relations, a significant improved resolution can probably only be achieved if a more extensive physical model of the sample apex is considered.

In order to emphasize the practical benefit of the proposed simulation approach, three different applications are described.

The first focuses on a spherical precipitate with distinguished evaporation threshold. Simulations with the critical threshold lower, equal, and elevated to that of the matrix are processed. Accordingly, particular apex shapes with heterogeneous fields at the surface evolve when the precipitate comes to evaporation. Field induced stresses show a significant load in the range between 200 MPa to 800 MPa. Interestingly, the different load on the particle in comparison to the matrix scales like the square of the difference in the preset evaporation thresholds. In the case of an elevated threshold, the elevated stress may indeed be responsible for a partial fail out of the precipitate in the analysis.

The second application highlights the new possibility to consider arbitrary emitter structures for simulation. A cylindric emitter sample with three different layers is used. Layers at the top and at the bottom are crystalline, the intermediate part is amorphous. Again simulations with different critical evaporation thresholds are conducted. It is demonstrated that the emitter curvature changes differently as a function of the applied thresholds. A physically consistent evaporation sequence is only achieved if field induced forces at the emitter surface are considered.

The third application depicts the case of a field emitter which contains a $\Sigma 5$ grain boundary. Simulations with different inclinations of the GB show a common result. The grain boundary is reconstructed with an artificially depleted atom density. At the transition to zone lines, displaced atoms forming a kink are observed. If different evaporation thresholds apply for atoms within a segregation zone to the GB core, the depletion in atom density broadens or narrows but does not vanish. Similarly, an analysis of the atom concentration shows severe artifacts.

These results demonstrate that the newly introduced simulation approach is well suited as a decisive tool for the complementary analysis of conducted APT measurements. Practically, simulations may help to reveal artifacts in the 3D reconstructions and to quantify their possible impact on the extracted results. Simulated data may also be used to double check other sophisticated analysis methods which are regularly applied to the APT reconstructions of experimental data (e.g. cluster search algorithms). By its conception, the simulation approach resembles as closely as necessary the important physics. This becomes particularly clear by the example

of the calculated field desorption maps which otherwise would not compare so well to those seen in the experiments. In regards to the essential physics, the foundation by Voronoi cells represents a sophisticated and obviously a sufficient approximation. By the consequent assignment of electrostatic properties to the Voronoi cells (and consideration of its geometric dual, the Delaunay mesh) not only the numeric solution for the potential and the electric field is enabled, but furthermore even electrostatic forces may get considered. In the future, these forces may be used not only to predict the evaporation sequence in a reliable manner, but also to account for site specific critical evaporation thresholds of evaporating atoms. It is well known that finally the local chemistry in terms of a binding force is decisive for the evaporation. Thus, this description based on the Voronoi partition may lastly also turn out to be fruitful in light of an improved understanding with regards to basic field evaporation theory which has not made any significant progress since about thirty years.

A. Derivation of the discrete Poisson equation on the regular mesh

Derived from the Poisson equation, we obtain

$$\sum_{\partial V(i,j,k)} \Psi_{\{x,y,z\},\{\uparrow,\downarrow\}} - q(i,j,k) = 0 \tag{A.1}$$

$$\sum_{\partial V(i,j,k)} \left(\oiint_{\{x,y,z\},\{\uparrow,\downarrow\}} \epsilon_r(\boldsymbol{r})\, \boldsymbol{E}(\boldsymbol{r})\, d^2 r \right) - \frac{q(i,j,k)}{\epsilon_0} = 0 \tag{A.2}$$

for the balanced flux over the centred cube about the potential node $\varphi(i,j,k)$. The cube volume amounts to $V = (\Delta a)^3$. Referring to figure 3.19b, the enclosed charge writes as

$$q(i,j,k) = \left(\frac{\Delta a}{2}\right)^3 \cdot \left[\rho^{(i,j,k)}_{\bar{1}\bar{1}\bar{1}} + \cdots + \rho^{(i,j,k)}_{111)} \right]. \tag{A.3}$$

From the contiguity equation for the electric field, the surface field may be considered as constant across each facet. For this reason, we can replace the surface integral by the respective product of field, dielectricity, and area:

$$(\Delta a)^2 \cdot \sum_{\partial V(i,j,k)} \epsilon_{\{x,y,z\},\{\uparrow,\downarrow\}}\, \boldsymbol{E}_{\{x,y,z\},\{\uparrow,\downarrow\}} - \frac{q(i,j,k)}{\epsilon_0} = 0. \tag{A.4}$$

An approximation for the field is enabled by first order finite-differences. According to the six-point-stencil for the regular grid in 3D, six neighboured potential nodes contribute to the potential node $\varphi(i,j,k)$ in the center of the stencil:

$$\begin{aligned} \boldsymbol{E}^{(i,j,k)}_{x,\downarrow} &\equiv -\operatorname{grad}\varphi\Big|_{\boldsymbol{r}-\frac{\Delta a}{2}\hat{e}_x} \cong -\frac{\varphi(i-1,j,k) - \varphi(i,j,k)}{\Delta a} \\ &\cdots \\ \boldsymbol{E}^{(i,j,k)}_{z,\uparrow} &\equiv -\operatorname{grad}\varphi\Big|_{\boldsymbol{r}+\frac{\Delta a}{2}\hat{e}_z} \cong -\frac{\varphi(i,j,k+1) - \varphi(i,j,k)}{\Delta a}. \end{aligned} \tag{A.5}$$

Since the electric field remains contiguous across the interfacial area, an effective dielectricity is accessed directly by the sum of the four present values at each facet:

$$\begin{aligned} \epsilon_{x,\downarrow}^{(i,j,k)} &= \epsilon_{\bar{1}\bar{1}\bar{1}}^{(i,j,k)} + \epsilon_{\bar{1}\bar{1}1}^{(i,j,k)} + \epsilon_{\bar{1}1\bar{1}}^{(i,j,k)} + \epsilon_{\bar{1}11}^{(i,j,k)} \\ &\dots \\ \epsilon_{z,\uparrow}^{(i,j,k)} &= \epsilon_{\bar{1}\bar{1}1}^{(i,j,k)} + \epsilon_{\bar{1}11}^{(i,j,k)} + \epsilon_{1\bar{1}1}^{(i,j,k)} + \epsilon_{111}^{(i,j,k)}. \end{aligned} \tag{A.6}$$

After insertion, the detailed flux becomes

$$\begin{aligned} \Psi_{x,\downarrow} &= \epsilon_0 \cdot \epsilon_{x,\downarrow}^{(i,j,k)} \cdot E_{x,\downarrow}^{(i,j,k)} \cdot (\Delta a)^2 \\ &= \epsilon_0 \cdot \left(\epsilon_{\bar{1}\bar{1}\bar{1}}^{(i,j,k)} + \dots + \epsilon_{\bar{1}11}^{(i,j,k)} \right) \cdot \Big(\varphi(i,j,k) - \varphi(i-1,j,k) \Big) \cdot \Delta a \\ &\dots \\ \Psi_{z,\uparrow} &= \epsilon_0 \cdot \epsilon_{z,\uparrow}^{(i,j,k)} \cdot E_{z,\uparrow}^{(i,j,k)} \cdot (\Delta a)^2 \\ &= \epsilon_0 \cdot \left(\epsilon_{\bar{1}\bar{1}1}^{(i,j,k)} + \dots + \epsilon_{111}^{(i,j,k)} \right) \cdot \Big(\varphi(i,j,k) - \varphi(i,j,k+1) \Big) \cdot \Delta a \end{aligned} \tag{A.7}$$

From this, we derive finally the discrete approximation of the potential by rearranging after $\varphi(i,j,k)$:

$$\varphi(i,j,k) \cong \frac{\epsilon_{x,\{\uparrow,\downarrow\}}^{(i,j,k)} \varphi(i \pm 1,j,k) + \epsilon_{y,\{\uparrow,\downarrow\}}^{(i,j,k)} \varphi(i,j \pm 1,k) + \epsilon_{z,\{\uparrow,\downarrow\}}^{(i,j,k)} \varphi(i,j,k \pm 1) + \frac{q(i,j,k)}{\epsilon_0}}{\epsilon_{x,\{\uparrow,\downarrow\}}^{(i,j,k)} + \epsilon_{y\{\uparrow,\downarrow\}}^{(i,j,k)} + \epsilon_{z,\{\uparrow,\downarrow\}}^{(i,j,k)}} \tag{A.8}$$

B. Computing the electric field on the irregular mesh (2nd order)

Here, a more smooth approximation for determining the electric field in the case of an irregular mesh is presented. Compared to the approach, which has already been presented in section 3.3 before, this approach is based on a second order fitting to the potential. Accordingly, we write

$$\begin{aligned}\varphi(\boldsymbol{p}) &= \varphi(\boldsymbol{p_0}) + \sum_{i=1}^{3} \underbrace{\left.\frac{\partial\varphi}{\partial \boldsymbol{r}_i}\right|_{\boldsymbol{r}=\boldsymbol{p_0}}}_{\alpha_i} \cdot \underbrace{\Delta\boldsymbol{p}_i}_{(\boldsymbol{p}-\boldsymbol{p_0})_i} + \frac{1}{2}\cdot \sum_{i=1}^{3}\sum_{j=1}^{3} \underbrace{\left.\frac{\partial^2\varphi}{\partial \boldsymbol{r}_i \partial \boldsymbol{r}_j}\right|_{\boldsymbol{r}=\boldsymbol{p_0}}}_{\beta_{ij}} \cdot \Delta\boldsymbol{p}_i \cdot \Delta\boldsymbol{p}_j + \mathcal{O}(3) \\ &\cong \varphi(\boldsymbol{p_0}) + \boldsymbol{\alpha}\cdot\Delta\boldsymbol{p} + \sum_{i=1}^{3}\sum_{j=i}^{3} \beta_{ij} \cdot \frac{\Delta\boldsymbol{p}_i \cdot \Delta\boldsymbol{p}_j}{1+\delta_{ij}}\end{aligned} \tag{B.1}$$

for the fitting function. This ansatz is equal to the second order Taylor expansion of the potential. For the potential $\varphi(\boldsymbol{p})$ in the vicinity of a given node $p_0 \in \mathbb{R}^3$, we see that it depends on the values of the unknown derivatives at p_0, abbreviated by α_i and β_{ij}, respectively. The parameters β_{ij} represent the nine elements of the 3×3 Hessian matrix, accordingly.

Next we take into account the N neighbour nodes of p_0 as local support points for the fitting. Therefore, we demand the least squares error defined by

$$\chi^2(\alpha_i, \beta_{ij}) := \sum_{n=1}^{N} \Big(\varphi_n - \varphi(\boldsymbol{p}_n)\Big)^2 \tag{B.2}$$

to be at minimum. As it has already been demonstrated in section 3.3, this requirement directly translates into a necessary condition for the differential $d\chi^2$ with

$$d\chi^2(\alpha_i, \beta_{ij}) = \sum_{i=1}^{3} \frac{\partial\chi^2}{\partial\alpha_i}\, d\alpha_i + \sum_{i=1}^{3}\sum_{j=i}^{3} \frac{\partial\chi^2}{\partial\beta_{ij}}\, d\beta_{ij} \overset{!}{=} 0 \tag{B.3}$$

Obviously, a solution for this equation is only possible if all the partial derivatives become zero.

A first set of three equations is received by

$$\begin{aligned}\frac{\partial\chi^2}{\partial\alpha_i} = &-2\cdot\sum_{n=1}^{N}\Big(\varphi_n-\varphi(\boldsymbol{p_0})\Big)\cdot\Delta\boldsymbol{p}_{n,i}+2\cdot\sum_{k=1}^{3}\alpha_k\cdot\left(\sum_{n=1}^{N}\Delta\boldsymbol{p}_{n,k}\cdot\Delta\boldsymbol{p}_{n,i}\right)\\ &+2\cdot\sum_{k=1}^{3}\sum_{l=k}^{3}\beta_{kl}\cdot\left(\sum_{n=1}^{N}\frac{\Delta\boldsymbol{p}_{n,k}\cdot\Delta\boldsymbol{p}_{n,l}\cdot\Delta\boldsymbol{p}_{n,i}}{1+\delta_{kl}}\right)\end{aligned} \tag{B.4}$$

which takes into regard the derivatives with respect to $\partial\alpha_i$. If we introduce the following abbreviations

$$\begin{aligned}A_{0,\partial\alpha_i} &:= \sum_{n=1}^{N}\Big(\varphi_n-\varphi(\boldsymbol{p_0})\Big)\cdot\Delta\boldsymbol{p}_{n,i}\\ A_{\alpha_k,\partial\alpha_i} &:= \sum_{n=1}^{N}\Delta\boldsymbol{p}_{n,k}\Delta\boldsymbol{p}_{n,i}\\ A_{\beta_{kl},\partial\alpha_i} &:= \sum_{n=1}^{N}\frac{\Delta\boldsymbol{p}_{n,k}\cdot\Delta\boldsymbol{p}_{n,l}\cdot\Delta\boldsymbol{p}_{n,i}}{1+\delta_{kl}}\end{aligned}$$

a clarified form of the same equations yields

$$A_{0,\partial\alpha_i} = \sum_{k=1}^{3}\alpha_k\cdot A_{\alpha_k,\partial\alpha_i}+\sum_{k=1}^{3}\sum_{l=k}^{3}\beta_{kl}\cdot A_{\beta_{kl},\partial\alpha_i} \tag{B.5}$$

With this, we continue and write

$$\begin{aligned}\frac{\partial\chi^2}{\partial\beta_{ij}} = &-2\cdot\sum_{n=1}^{N}\Big(\varphi_n-\varphi(\boldsymbol{p_0})\Big)+2\cdot\sum_{k=1}^{3}\alpha_k\cdot\left(\sum_{n=1}^{N}\Delta\boldsymbol{p}_{n,k}\cdot\frac{\Delta\boldsymbol{p}_{n,i}\cdot\Delta\boldsymbol{p}_{n,j}}{1+\delta_{ij}}\right)\\ &+2\cdot\sum_{k=1}^{3}\sum_{l=k}^{3}\beta_{kl}\cdot\left(\sum_{n=1}^{N}\frac{\Delta\boldsymbol{p}_{n,k}\cdot\Delta\boldsymbol{p}_{n,l}}{1+\delta_{kl}}\cdot\frac{\Delta\boldsymbol{p}_{n,i}\cdot\Delta\boldsymbol{p}_{n,j}}{1+\delta_{ij}}\right)\end{aligned} \tag{B.6}$$

for the derivatives with respect to $\partial\beta_{ij}$. Again we introduce appropriate abbrevia-

tions by

$$B_{0,\partial\beta ij} := \sum_{n=1}^{N} \Big(\varphi_n - \varphi(\boldsymbol{p_0})\Big) \cdot \frac{\Delta \boldsymbol{p}_{n,i} \cdot \Delta \boldsymbol{p}_{n,j}}{1+\delta_{ij}}$$

$$B_{\alpha_k,\partial\beta ij} := \sum_{n=1}^{N} \Delta \boldsymbol{p}_{n,k} \cdot \frac{\Delta \boldsymbol{p}_{n,i} \cdot \Delta \boldsymbol{p}_{n,j}}{1+\delta_{ij}}$$

$$B_{\beta_{kl},\partial\beta ij} := \sum_{n=1}^{N} \frac{\Delta \boldsymbol{p}_{n,k} \cdot \Delta \boldsymbol{p}_{n,l}}{1+\delta_{kl}} \cdot \frac{\Delta \boldsymbol{p}_{n,i} \cdot \Delta \boldsymbol{p}_{n,j}}{1+\delta_{ij}}$$

This leads us to a second set of nine equations:

$$B_{0,\partial\beta_{ij}} = \sum_{k=1}^{3} \alpha_k \cdot B_{\alpha_k,\partial\beta_{ij}} + \sum_{k=1}^{3}\sum_{l=1}^{3} \beta_{kl} \cdot B_{\beta_{kl},\partial\beta_{ij}} \tag{B.7}$$

As before, the form appears equally clear here.

Finally, we express the complete result by a system of nine linear equations:

$$\left(\begin{array}{ccc|ccc} A_{\alpha_1,\partial\alpha_1} & \dots & A_{\alpha_3,\partial\alpha_1} & A_{\beta_{11},\partial\alpha_1} & \dots & A_{\beta_{33},\partial\alpha_1} \\ \vdots & \ddots & \vdots & \vdots & & \vdots \\ A_{\alpha_1,\partial\alpha_3} & \dots & A_{\alpha_3,\partial\alpha_3} & A_{\beta_{11},\partial\alpha_3} & \dots & A_{\beta_{33},\partial\alpha_3} \\ \hline B_{\alpha_1,\partial\beta_{11}} & \dots & B_{\alpha_3,\partial\beta_{11}} & B_{\beta_{11},\partial\beta_{11}} & \dots & B_{\beta_{33},\partial\beta_{11}} \\ \vdots & & \vdots & \vdots & & \vdots \\ B_{\alpha_1,\partial\beta_{33}} & \dots & B_{\alpha_3,\partial\beta_{33}} & B_{\beta_{11},\partial\beta_{33}} & \dots & B_{\beta_{33},\partial\beta_{33}} \end{array}\right) \cdot \begin{pmatrix} \alpha_1 \\ \vdots \\ \alpha_3 \\ \beta_{11} \\ \vdots \\ \beta_{33} \end{pmatrix} = \begin{pmatrix} A_{0,\partial\alpha_1} \\ \vdots \\ A_{0,\partial\alpha_3} \\ B_{0,\partial\beta_{11}} \\ \vdots \\ B_{0,\partial\beta_{33}} \end{pmatrix} \tag{B.8}$$

which may be solved by means of standard numeric algorithms (LU decomposition for example). Although the solution matrix reveals a high degree of symmetry, e.g. $A_{\alpha_k,\partial\alpha_i} = A_{\alpha_i,\partial\alpha_k}$ and $B_{\beta_{ij}} = B_{\beta_{ji}}$, the computational effort decisively increases compared to the first order approach presented earlier in section 3.3.

However, as a benefit the solution yields on the one hand the desired field vector which is essentially equal to $\boldsymbol{\alpha}$ except for the sign:

$$\boxed{\boldsymbol{E}(\boldsymbol{p}_0) = -\nabla\varphi\big|_{\boldsymbol{r}=\boldsymbol{p_0}} = -\begin{pmatrix} \alpha_1 \\ \alpha_2 \\ \alpha_3 \end{pmatrix}} \tag{B.9}$$

But additionally, we see that we can gain even more information if we inspect the initial equation (B.1) for the second time. Here, we split up the matrix elements

β_{ij} into two parts:

$$\varphi(\boldsymbol{p}) = \varphi(\boldsymbol{p_0}) + \boldsymbol{\alpha} \cdot \Delta\boldsymbol{p} + \frac{1}{2}\left(\sum_{i=1}^{3} \beta_{ii}\right) \cdot (\Delta\boldsymbol{p})^2 + \sum_{i=1}^{3}\sum_{j=i+1}^{3} \beta_{ij} \cdot \Delta\boldsymbol{p}_i \cdot \Delta\boldsymbol{p}_j \quad \text{(B.10)}$$

Written in this alternative form, we immediately recognize that the trace of the matrix elements β_{ii} reflects the components of the Laplace-operator. Hence, due to equation (3.19) a local charge value

$$\boxed{\frac{\rho(\boldsymbol{p}_0)}{\epsilon_0} = \nabla^2\varphi\big|_{\boldsymbol{r}=\boldsymbol{p_0}} = -\left(\beta_{11} + \beta_{22} + \beta_{33}\right)} \quad \text{(B.11)}$$

may be obtained from the second order solution. In particular, this charge represents the present microscopic charges including the polarization charges due to different dielectricity.

Bibliography

[Aud+09] P. Audsumilli et al. “An atom-probe tomography primer”. In: *MRS Bulletin* 34 (2009), pp. 717–724. DOI: 10.1557/mrs2009.194 (cit. on p. 2).

[Bas+95] B. Bas et al. “A general protocol for the reconstruction of 3D atom probe data”. In: *Applied Surface Science* 87/88 (1995), pp. 298–304. DOI: 10.1016/0169-4332(94)00561-3 (cit. on pp. 18, 25, 123).

[Beg13] Stephen Begin. *Photograph of the wing structure from a dragon fly.* Online source (“http://www.flickr.com”). Creative Commons licence: “Attribution-NonCommercial-Share-Alike 2.0 Generic” (CC BY-NC-SA 2.0). Ottava, Canada, 2013 (cit. on p. 50).

[Ber+08] Mark de Berg et al. “Computational Geometry: Algorithms and Applications”. In: Springer, Berlin Heidelberg, 2008. Chap. Delaunay Triangulations, pp. 191–218 (cit. on p. 43).

[BF82] R. K. Biswas and Richard G. Forbes. “Theoretical arguments against the Müller-Schottky mechanism of field evaporation”. In: *Journal of Physics D* 15 (1982), pp. 1323–1338. DOI: 10.1088/0022-3727/15/7/026 (cit. on p. 12).

[Bla+93] D. Blavette et al. “The tomographic atom probe: A quantitative three-dimensional nanoanalytical instrument on an atomic scale”. In: *Review of Scientific Instruments* 64 (1993), pp. 2911–2919. DOI: 10.1063/1.1144382 (cit. on p. 22).

[Bla+99] D. Blavette et al. “Three-Dimensional Atomic-Scale Imaging of Impurity Segregation to Line Defects”. In: *Science* 286 (1999), pp. 2317–2319. DOI: 10.1126/science.286.5448.2317 (cit. on p. 28).

[BA13] T. Boll and T. Al-Kassab. “Interpretation of atom probe tomography data for the intermetallic TiAl+Nb by means of field evaporation simulation”. In: *Ultramicroscopy* 124 (2013), pp. 1–5. DOI: 10.1016/j.ultramic.2012.09.003 (cit. on p. 76).

[Bol+12] T. Boll et al. "Atom Probe Tomography Simulations and Density Functional Theory Calculations of Bonding Energies in Cu_3Au". In: *Microscopy and Microanalysis* 18 (2012), pp. 964–970. DOI: dx.doi.org/10.1017/S1431927612001365 (cit. on p. 76).

[Bow81] A. Bowyer. "Computing Dirichlet tessellations". In: *Computer Journal* 24 (1981), pp. 162–166. DOI: 10.1093/comjnl/24.2.162 (cit. on p. 44).

[CK90] J. R. Cash and A. H. Karp. "A variable order Runge-Kutta method for initial value problems with rapidly varying right-hand sides". In: *ACM Transactions on Mathematical Software* 16 (1990), pp. 201–222. DOI: 10.1145/79505.79507 (cit. on p. 65).

[CGS88] A. Cerezo, T. J. Godfrey, and G. D. W. Smith. "Application of a position-sensitive detector to atom probe microanalysis". In: *Review of Scientific Instruments* 59 (1988), pp. 862–866. DOI: 10.1063/1.1139794 (cit. on p. 22).

[CWS99] A. Cerezo, P. J. Warren, and G. D. W. Smith. "Some aspects of image projection in the field-ion microscope". In: *Ultramicroscopy* 79 (1999), pp. 251–257. DOI: 10.1016/S0304-3991(99)00071-6 (cit. on p. 19).

[Chu+13] M. S. Chung et al. "Dielectric effect on electric fields in the vicinity of the metal-vacuum-dielectric junction". In: *Ultram* 132 (2013), pp. 41–47. DOI: 10.1016/j.ultramic.2012.12.014 (cit. on p. 80).

[DMZ98] L. Devroye, E. P. Mücke, and Binhai Zhu. "A Note on Point Location in Delaunay Triangulations of Random Points". In: *Algo* 22 (1998), pp. 477–482. DOI: 10.1007/PL00009234 (cit. on p. 48).

[For86] S. Fortune. "A sweepline algorithm for Voronoi diagrams". In: *ACM* (1986), pp. 313–322. DOI: 10.1145/10515.10549 (cit. on p. 43).

[FN28] R. H. Fowler and L. Nordheim. "Electron Emission in Intense Electric Fields". In: *Proceedings of the Royal Society of London* 119 (1928), pp. 173–181. DOI: 10.1098/rspa.1928.0091 (cit. on p. 9).

[Gau+09] Baptiste Gault et al. "Origin of the spatial resolution in atom probe microscopy". In: *Applied Physics Letters* 95 (2009), p. 034103. DOI: 10.1063/1.3182351 (cit. on p. 28).

[Gau+12a] Baptiste Gault et al. *Atom Probe Microscopy*. Springer, New York, 2012. DOI: 10.1007/978-1-4614-3436-8 (cit. on pp. 8, 30, 123).

[Gau+06] B. Gault et al. "Investigation of an oxide layer by femtosecond-laser-assisted atom probe tomography". In: *Applied Physics Letters* 88 (2006), p. 114101. DOI: 10.1063/1.2186394 (cit. on p. 13).

[Gau+11] B. Gault et al. "Advances in the reconstruction of atom probe tomography data". In: *Ultramicroscopy* 111 (2011), pp. 448–457. DOI: 10.1016/j.ultramic.2010.11.016 (cit. on pp. 3, 71, 94).

[Gau+12b] B. Gault et al. "Atom probe crystallography". In: *Materialstoday* 15 (2012), pp. 378–386. DOI: 10.1016/S1369-7021(12)70164-5 (cit. on p. 122).

[Gau+12c] B. Gault et al. "Influence of surface migration on the spatial resolution of pulsed laser atom probe tomography". In: *Journal of Applied Physics* 108.044904 (2012). DOI: 10.1063/1.3462399 (cit. on p. 28).

[Gei+09] B. P. Geiser et al. "A System for Evaluation of Tip Evolution Under Field Evaporation". In: *Microscopy and Microanalysis* 15 (2009), pp. 302–303. DOI: 10.1017/S1431927609098298 (cit. on pp. 21, 22).

[Gle89] H. Gleiter. "Nanocrystalline Materials". In: *Progress in Materials Science* 33 (1989), pp. 223–315. DOI: 10.1016/0079-6425(89)90001-7 (cit. on p. 2).

[Gle00] H. Gleiter. "Nanostructured materials: basic concepts and microstructure". In: *Acta Materialia* 48 (2000), pp. 1–29. DOI: 10.1016/S1359-6454(99)00285-2 (cit. on p. 2).

[Gom59] Robert Gomer. "Field Desorption". In: *Journal of Chemical Physics* 31 (1959), pp. 341–345. DOI: 10.1063/1.1730354 (cit. on p. 11).

[GS63] Robert Gomer and Lynn W. Swanson. "Theory of Field Desorption". In: *Journal of Chemical Physics* 38 (1963), pp. 1613–1629. DOI: 10.1063/1.1776932 (cit. on p. 11).

[GS78] P. J. Green and R. Sibson. "Computing Dirichlet Tessellations in the Plane". In: *The Computer Journal* 21 (1978), pp. 168–173. DOI: 10.1093/comjnl/21.2.168 (cit. on p. 48).

[Gru12] Maria Gruber. "Étude de l'évaporation par effet de champ en sonde atomique tomographique : Application à la métrologie de l'instrument". PhD thesis. GPM Rouen, 2012 (cit. on p. 75).

[Gru+11] Maria Gruber et al. "Field evaporation: A kinetic Monte Carlo approach on the influence of temperature". In: *Surface Science* 605 (2011), pp. 2025–2031. DOI: 10.1016/j.susc.2011.07.022 (cit. on p. 111).

[GKS92] Leonidas J. Guibas, Donald E. Knuth, and Micha Sharir. "Randomized Incremental Construction of Delauany and Voronoi Diagrams". In: *Algorithmica* 7 (1992), pp. 381–413. DOI: 10.1007/FBF01758770 (cit. on p. 43).

[Hum93] Stanley Humphries. *Field solutions on Computers*. CRC Press Boca Raton, 1993 (cit. on p. 73).

[JS02] T. Jeske and G. Schmitz. "Influence of the microstructure on the interreaction of Al/Ni investigated by tomographic atom probe". In: *Materials Science & Engineering, A: Structural Materials: Properties, Microstructure and Processing* 327 (2002), pp. 101–108. DOI: 10.1016/S0921-5093(01)01886-X (cit. on p. 27).

[AlK+03] T. Al-Kassab et al. "High-Resolution Imaging and Spectrometry of Materials". In: ed. by F. Ernst and M Rühle. Springer, Berlin, 2003. Chap. Tomography by Atom Probe Field Ion Microscopy, pp. 290–293 (cit. on p. 18).

[Kel84] G. L. Kellogg. "Measurement of activation energies for field evaporation of tungsten ions as a function of electric field". In: *Physical Review B* 29 (1984), pp. 4304–4312. DOI: 10.1103/PhysRevB.29.4304 (cit. on pp. 13, 21).

[KT80] G. L. Kellogg and T. T. Tsong. "Pulsed laser atom probe field ion microscopy". In: *Journal of Applied Physics* 51 (1980), pp. 1184–1193. DOI: 10.1063/1.327686 (cit. on p. 13).

[KL12] T. F. Kelly and D. J. Larson. "Atom probe tomography 2012". In: *Annual Review of Materials Research* 42 (2012), pp. 1–31. DOI: 10.1146/annurev-matsci-070511-155007 (cit. on p. 17).

[KM07] T. F. Kelly and M. K. Miller. "Invited Review Article: Atom probe tomography". In: *Review of Scientific Instruments* 78 (2007), p. 031101. DOI: 10.1063/1.2709758 (cit. on p. 2).

[Kin82a] David R. Kingham. "A new view of field evaporation". In: *Vacuum* 32 (1982), pp. 471–476. DOI: 10.1016/0042-207X(85)90425-7 (cit. on p. 11).

[Kin82b] David R. Kingham. "The post-ionization of field evaporated ions: a theoretical explanation of multiple charge states". In: *Surface Science* 116 (1982), pp. 273–301. DOI: 10.1016/0039-6028(82)90434-4 (cit. on p. 11).

[KN87] H. J. Kreuzer and K. Nath. "Field Evaporation". In: *Surface Science* 183 (1987), pp. 591–608. DOI: 10.1016/S0039-6028(87)80230-3 (cit. on p. 11).

[KMM77] S. V. Krishnaswamy, M. Martinka, and E. W. Müller. "Multilayer field evaporation patterns". In: *Surface Science* 64 (1977), pp. 23–42. DOI: 10.1016/0039-6028(77)90255-2 (cit. on p. 21).

[Lar+10] D. J. Larson et al. "Improvements in planar feature reconstructions in atom probe tomography". In: *Journal of Microscopy* 243 (2010), pp. 15–30. DOI: 10.1111/J.1365-2818.2010.03474.x (cit. on p. 28).

[Lar+11a] D. J. Larson et al. "From the store shelf to device-level atom probe analysis: An exercise in feasibility". In: *Conference Proceedings from the International Symposium for Testing and Failure Analysis*. 2011 (cit. on p. 3).

[Lar+11b] D. J. Larson et al. "Toward atom probe tomography of microelectronic devices". In: *Journal of Physics: Conference Series* 326 (2011), p. 012030. DOI: 10.1088/1742-6596/326/1/012030 (cit. on p. 3).

[Lar+13] D. J. Larson et al. "Atom probe tomography spatial reconstruction: Status and directions". In: *Current Opinion in Solid State and Materials Science* 17 (2013), pp. 236–247. DOI: 10.1016/j.cossms.2013.09.002 (cit. on p. 3).

[Loi+12] Shyeh Tjing Loi et al. "Electrostatic simulations of a local electrode atom probe: The dependance of tomographic reconstruction parameters on specimen and microscope geometry". In: *Ultramicroscopy* (2012). DOI: 10.1016/j.ultramic.2012.12.012 (cit. on pp. 71, 94, 100).

[MV08] E. A. Marquis and F. Vurpillot. "Chromatic Aberrations in the Field Evaporation Behavior of Small Precipitates". In: *Microscopy and Microanalysis* 14 (2008), pp. 561–570. DOI: 10.1017/S1431927608080793 (cit. on pp. 3, 30, 144).

[Mar+10] E. A. Marquis et al. "Evolution of tip shape during field evaporation of complex multilayer structures". In: *Journal of Microscopy* 241 (2010), pp. 225–233. DOI: 10.1111/J.1365-2818.2010.03421.x (cit. on p. 30).

[Mat13] Wolfram Mathworld. *Information on query for "Cauchy distribution"*. Online source ("http://mathworld.wolfram.com"). June 2013 (cit. on p. 110).

[Mel13] Allan J. Melmed. *Biographical memoirs*. Online source ("http://www.nasonline.org"). US National Academy of Sciences, 2013 (cit. on p. 8).

[Mil87] M. K. Miller. "The effects of local magnification and trajectory aberrations on atom probe analysis". In: *J. Phys. Colloques* 48 (1987), pages. DOI: 10.1051/jphyscol:1987692 (cit. on pp. 3, 132).

[Mil00] M. K. Miller. *Atom Probe Tomography - Analysis at the Atomic Level*. Kluwer Academic/ Plenum Publishers, New York, 2000. DOI: 10.1046/j.1365-2818.2001.00847.x (cit. on p. 8).

[MH91] M. K. Miller and M. G. Hetherington. "Local magnification effects in the atom probe". In: *Surface Science* 246 (1991), pp. 442–449. DOI: 10.1016/0039-6028(91)90449-3 (cit. on p. 3).

[MS89] M. K. Miller and G. D. W. Smith. *Atom Probe Microanalysis: Principles and Applications to Material Problems*. Materials Research Society, Pittsburg, 1989. DOI: 10.1002/jemt.1070200209 (cit. on pp. 8, 13, 31).

[Moo65] Gordon E. Moore. "Cramming more components onto integrated circuits". In: *Electronics* 38 (1965). DOI: 10.1109/JPROC.1998.658762 (cit. on p. 2).

[MSZ99] Ernst P. Mücke, Isaac Saias, and Binhai Zhu. "Fast randomized point location without preprocessing in two- and three-dimensional Delaunay triangulations". In: *Computational Geometry* 12 (1999), pp. 63–83. DOI: 10.1016/S0925-7721(98)00035-2 (cit. on p. 50).

[Mül36a] E. W. Müller. "Versuche zur Theorie der Elektronenemission unter der Einwirkung hoher Feldstärke". In: *Physikalische Zeitschrift* 37 (1936), p. 838 (cit. on p. 10).

[Mül36b] Erwin W. Müller. "Die Abhängigkeit der Feldelektronenemission von der Austrittsarbeit". In: *Zeitschrift für Physik* 102 (1936), pp. 734–761. DOI: 10.1007/BF01338540 (cit. on p. 10).

[Mül51] Erwin W. Müller. "Das Feldionenmikroskop". In: *Zeitschrift für Physik* 131 (1951), pp. 136–142. DOI: 10.1007/BF01329651 (cit. on p. 10).

[Mül56] Erwin W. Müller. "Field Desorption". In: *Physical Review* 102 (1956), pp. 618–624. DOI: 10.1103/PhysRev.102.618 (cit. on p. 12).

[OS11] C. Oberdorfer and G. Schmitz. "On the Field Evaporation Behavior of Dielectric Materials in Three-Dimensional Atom Probe: A Numeric Simulation". In: *Microscopy and Microanalysis* 17 (2011), pp. 15–25. DOI: 10.1017/S1431927610093888 (cit. on pp. 3, 62, 72, 75, 78, 80, 81, 132).

[OES13] Christian Oberdorfer, Sebastian Eich, and Guido Schmitz. "A full-scale simulation approach for atom probe tomography". In: *Ultramicroscopy* 128 (2013), pp. 55–67. DOI: 10.1016/j.ultramic.2013.01.005 (cit. on pp. 3, 62, 84, 90, 104, 106, 136, 138, 141, 150, 151).

[Obe+07] Christian Oberdorfer et al. "Laser-Assisted Atom Probe Tomography of Oxide Materials". In: *Microscopy and Microanalysis* 13 (2007), pp. 342–346. DOI: 10.1017/S1431927607070274 (cit. on pp. 3, 13).

[Pan74] John A. Panitz. "The Crystallographic Distribution of Field-Desorbed Species". In: *Journal of Vacuum Science & Technology* 11 (1974), pp. 207–210. DOI: 10.1116/1.1318570 (cit. on p. 22).

[Pre+07] William H. Presse et al., eds. *Numerical Recipes – The Art of Scientific Computing*. Camb, 2007 (cit. on p. 67).

[Pro+13] T. J. Prosa et al. "Analysis of implanted silicon dopant profiles". In: *Ultramicroscopy* 132 (2013), pp. 179–185. DOI: 10.1016/j.ultramic.2012.10.005 (cit. on p. 3).

[Ric24] O. W. Richardson. "Electron Emission from Metals as a Function of Temperature". In: *Physical Review* 23 (1924), pp. 153–155. DOI: 10.1103/PhysRev.23.153 (cit. on p. 9).

[Sch+10] R. Schlesiger et al. "Design of a laser-assisted tomographic atom probe at Münster University". In: *Review of Scientific Instruments* 81 (2010), p. 043703. DOI: 10.1063/1.3378674 (cit. on pp. 18, 24).

[Sch23] W. Schottky. "Über kalte und warme Elektronenentladungen". In: *Zeitschrift für Physik* 14 (1923), pp. 63–106. DOI: 10.1007/BF01340034 (cit. on p. 9).

[She97] Jonathan Richard Shewchuck. "Adaptive Precision Floating-Point Arithmetic and Fast Robust Geometric Predicates". In: *Discrete & Computational Geometry* 3 (1997), pp. 305–363 (cit. on p. 45).

[She12] Jonathan Richard Shewchuck. "Unstructured Mesh Generation". In: *Combinatorial Scientific Computing*. Ed. by Uwe Neuman and Olaf Schenk. Chapman & Hall / CRC Computational Science, 2012. Chap. 10, pp. 259–299 (cit. on p. 44).

[Si11] Hang Si. *TetGen — A Quality Tetrahedral Mesh Generator and a 3D Delaunay Triangulator*. Online source ("http://www.tetgen.org"). Version 1.4.3. Mohrenstr. 39, 10117 Berlin, Germany: Weierstrass Institute for Applied Analysis and Stochastics (WIAS), Jan. 2011 (cit. on pp. 44, 85).

[SW78] R. Smith and J. M. Walls. "Ion trajectories in the field-ion microscope". In: *Journal of Physics D: Applied Physics* 11 (1978), pp. 409–419. DOI: 10.1088/0022-3727/11/4/005 (cit. on pp. 14, 71).

[Ste66] P. Stein. "A Note on the Volume of a Simplex". In: *The American Mathematical Monthly* 73 (1966), pp. 299–301 (cit. on p. 37).

[Ste+07] P. Stender et al. "New tomographic atom probe at University of Muenster, Germany". In: *Ultramicroscopy* 107 (2007), pp. 726–733. DOI: 10.1016/j.ultramic.2007.02.032 (cit. on p. 15).

[Sto00] Prof. Dr. Horst Stoecker, ed. *Taschenbuch der Physik*. Verlag Harry Deutsch, Thun und Frankfurt am Main, 2000 (cit. on p. 13).

[Suk03] N. Sukumar. "Voronoi cell finite difference method for the diffusion operator on arbitrary unstructured grids". In: *International Journal for Numerical Methods in Engineering* 57 (2003), pp. 1–34. DOI: 10.1002/nme.664 (cit. on p. 86).

[SB03] N. Sukumar and J. E. Bolander. "Numeric Computation of Discrete Differential Operators on Non-Uniform Grids". In: *CMES – Computer Modeling in Engineering and Sciences* 4 (2003), pp. 691–705 (cit. on p. 63).

[SM03] A Suzuki and Y. Mishin. "Atomistic modeling of point defects and diffusion in copper grain boundaries". In: *Interface Science* 11 (2003), pp. 131–148. DOI: 10.1023/A:1021599310093 (cit. on p. 145).

[Tso79] T. T. Tsong. "Field penetration and band bending near semiconductor surfaces in high electric fields". In: *Surface Science* 81 (1979), pp. 28–42. DOI: 10.1016/0039-6028(79)90503-X (cit. on pp. 30, 80).

[Tso90] Tien Tzou Tsong. *Atom-Probe Field Ion Microscopy: Field Emission, Surfaces and Interfaces at Atomic Resolution*. Cambridge University Press, New York, 1990. DOI: 10.1017/CBO9780511599842 (cit. on pp. 8, 13).

[Vel+06] A. Vella et al. "Evidence of field evaporation assisted by nonlinear optical rectification induced by ultrafast laser". In: *Physical Review B* 73 (2006), p. 165416. DOI: 10.1103/PhysRevB.73.165416 (cit. on p. 13).

[VBB00] F. Vurpillot, A. Bostel, and D. Blavette. "Trajectory overlaps and local magnification in three-dimensional atom probe". In: *Applied Physics Letters* 76 (2000), pp. 3127–3129. DOI: 10.1063/1.126545 (cit. on pp. 3, 30, 72, 132).

[Vur+13] François Vurpillot et al. "Reconstructing Atom Probe Data: A review". In: *Ultramicroscopy* (2013). in press. DOI: 10.1016/j.ultramic.2013.03.010 (cit. on p. 3).

[Vur+99] F. Vurpillot et al. "Trajectories of field emitted ions in 3D atom-probe". In: *The European Physical Journal Applied Physics* 6 (1999), pp. 217–221. DOI: 10.1051/epjap:1999173 (cit. on pp. 3, 72).

[Vur+00] F. Vurpillot et al. "The spatial resolution of 3D atom probe in the investigation of single-phase materials". In: *Ultramicroscopy* 84 (2000), pp. 213–224. DOI: 10.1016/S0304-3991(00)00035-8 (cit. on pp. 3, 72).

[Vur+01] F. Vurpillot et al. "Structural analyses in three-dimensional atom probe: a Fourier transform approach". In: *Journal of Microscopy* 203 (2001), pp. 295–302. DOI: 10.1046/j.1365-2818.2001.00923.x (cit. on pp. 124, 128).

[Vur+04a] F. Vurpillot et al. "Application of Fourier transform and autocorrelation to cluster identification in three-dimensional atom probe". In: *Journal of Microscopy* 216 (2004), pp. 234–240. DOI: 10.1111/j.0022-2720.2004.01413.x (cit. on p. 124).

[Vur+04b] F. Vurpillot et al. "Modeling Image Dirstortions in 3DAP". In: *Microscopy and Microanalysis* 10 (2004), pp. 384–390. DOI: 10.1017/S1431927604040486 (cit. on pp. 30, 132).

[Vur+06] F. Vurpillot et al. "Estimation of the cooling times for a metallic tip under laser illumination". In: *Applied Physics Letters* 88 (2006), p. 094105. DOI: 10.1063/1.2181654 (cit. on p. 13).

[Vur+11] F. Vurpillot et al. "Pragmatic reconstruction methods in atom probe tomography". In: *Ultramicroscopy* 111 (2011), pp. 1286–1294. DOI: 10.1016/j.ultramic.2011.04.001 (cit. on pp. 94, 97, 99).

[WK90] L. C. Wang and H. J. Kreuzer. "Kinetic theory of field evaporation of metals". In: *Surface Science* 237 (1990), pp. 337–346. DOI: 10.1016/0039-6028(90)90546-K (cit. on p. 13).

[WCS98] P. J. Warren, A. Cerezo, and G. D. W. Smith. "Observation of atomic planes in 3DAP analysis". In: *Ultramicroscopy* 73 (1998), pp. 261–266. DOI: 10.1016/S0304-3991(97)00165-4 (cit. on p. 28).

[Wat81] D. F. Watson. "Computing the n-dimensional Delaunay tessellations with application to Voronoi polytopes". In: *Computer Journal* 24 (1981), pp. 167–172. DOI: 10.1093/comjnl/24.2.167 (cit. on p. 44).

[WDJ75] A. R. Waugh, Boyes E. D., and Southon M. J. "Field-desorption microscopy and the atom probe". In: *Nature* 253 (1975), pp. 342–343. DOI: 10.1038/253342a0 (cit. on p. 21).

[WDJ76] A. R. Waugh, Boyes E. D., and Southon M. J. "Investigations of field evaporation with a field-desorption microscope". In: *Surface Science* 61 (1976), pp. 109–142. DOI: 10.1016/0039-6028(76)90411-8 (cit. on p. 21).

[WSS74] T. J. Wilkes, G. D. W. Smith, and D. A. Smith. "On the quantitative analysis of field-ion micrographs". In: *Metallography* 7 (1974), pp. 403–430. DOI: 10.1016/0026-0800(74)90041-X (cit. on p. 18).

Danksagung

Zuerst möchte ich mich bei Prof. Schmitz für die Aufgabenstellung und die gute Betreuung in all den Jahren bedanken.

Einige der Abbildungen in Kapitel 2 wurden mir liebenswürdigerweise zur Verfügung gestellt. Dafür an dieser Stelle noch einmal herzlichen Dank!

Mein Dank gilt aber auch allen anderen, die ich nennen möchte: Andrè, Andreas, Britta, Christoph, Daniel, Dietmar, Fabian, Fabian, Frank, Gerd, Houari, Isabell, Jan, Jens, Jens, Lars, Mohammed, Lei, Lea, Lea, Manuel, Maria, Martin, Martin, Mathias, Michael, Reza, Ralf, Patrick, Sebastian, Susann, Tobias, Tobias, Vitaliy, Yaser sowie Zoltan; Frank, Michael, Nicole, Sylvia, Patrick und Willi; Alexander, Doris, Jonas, Kirsten, Ludwig, Sabine, Sebastian, Stefan und Thomas; Andreas, Burkhard, Claas, Helmut, Jürgen, Margot, Norbert, Günter, Sabine, Sabine und Tilman; Patrizia; und ganz besonders meiner Familie.